Characterisation of Dust Sources in Central Asia Using Remote Sensing

PhD in Environmental Science

School of Archaeology, Geography and Environmental Science (SAGES)

Mohamad Nobakht

September 2017

Declaration of original authorship

Declaration: I confirm that this is my own work and the use of all material from other sources has been properly and fully acknowledged.

Mohamad Nobakht

Acknowledgement

This thesis was carried out at the Department of Geography and Environmental Science of the University of Reading, from 2013 to 2017. It was financed by the University of Reading International Research Studentships Award.

I wish to express my sincere appreciation to those who have contributed to this thesis and supported me in one way or the other during this amazing journey. Firstly I would like to express my special appreciation and gratitude to my supervisors Dr. Maria Shahgedanova and Dr. Kevin White for the continuous support during my PhD study and their guidance, patience and immense knowledge. I also remain indebted for Maria's understanding and support during the times when I was really down due to personal family problems. Her advice and encouragement has allowed me to grow both professionally and personally and this has been priceless.

Besides my supervisors, I would like to thank my thesis examiners for their insightful comments and for letting my viva be an enjoyable experience. My sincere gratitude is reserved for Dr. Matthew Baddock for his invaluable insights and suggestions.

A very special thanks goes out to the University of Reading for giving me the opportunity to carry out my doctoral research and for their financial support.

And finally, last but by no means least, I would like to thank my family for their support, especially my wife, Sarah. Words cannot express how grateful I am for all of the sacrifices that you have made. I am truly thankful for having you in my life.

Abstract

Central Asian deserts are a significant source of dust in the middle latitudes, where economic activity and the health of millions of people are affected by dust storms. Detailed knowledge of sources of dust, controls on their activity, seasonality and atmospheric pathways are of crucial importance but to date, these data are limited. This thesis presents a detailed database of sources of dust emissions in Central Asia, from western China to the Caspian Sea, obtained by a multi-scale analysis of the Moderate Resolution Imaging Spectroradiometer (MODIS) satellite data. The multi-scale approach consists of the following steps: 1) MODIS Deep Blue Aerosol Optical Depth (DB AOD) at 10 km resolution, acquired between 2003 and 2014, is used to investigate the spatiotemporal distribution of dust hotspots. 2) A dust enhancement algorithm was employed to obtain two composite images (Dust Enhancement Product, DEP) per day at 1 km resolution from MODIS Terra/Aqua acquisitions between 2003 and 2012, from which dust point sources (DPS) were detected by visual analysis of dust plumes and recorded in a database together with meteorological variables at each DPS location derived from the ERA-Interim reanalysis dataset. In all, more than 13500 DPS were identified. Using this multi-scale approach we provided a high resolution inventory of dust sources at sub-basin scale for Central Asia. Our analysis revealed several active source regions, the most active of which are the eastern part of the Taklmakan desert. An important finding was an increase in dust activity in the newly-formed desert of the Aralkum. Several of the identified dust source regions were not previously identified (e.g. sources in northern Afghanistan) or were not widely discussed in literature before (e.g. the Pre-Aral region in western Kazakhstan). Investigation of land surface characteristics and meteorological conditions at each source region revealed mechanisms for the formation of dust sources, including rapid desiccation of water bodies (e.g. Aral Sea), deflation of dust from fluvial sources (e.g. the Upper Amudarya region) and post-fire wind erosion (e.g. Pre-Aral and Lake Balkhash basins). Different seasonal patterns of dust emissions were observed as well as inter-annual trends. Comparison of DB AOD and DPS revealed a noticeable spatial bias in the AOD-based methods for detection of dust sources which is attributed to the fact that the highest atmospheric dust loadings are not always observed over the dust point sources.

Table of Contents

List of Tables

List of Figures

Chapter 1. Introduction

1.1. Overview

Aeolian mineral dust is a key component of the climate system and represents an important natural source of atmospheric particulate matter (Goudie, 1983). Each year, megatons of dust are emitted from the surface of arid and semi-arid regions into the atmosphere, making it the most important atmospheric aerosol by mass (Knippertz, 2014). Atmospheric dust particles significantly impact the energy balance of the Earth system not only through absorbing and scattering the solar radiation but also by modifying the optical properties of clouds and snow and ice surfaces on which they are deposited (Shen *et al.*, 2016). In addition, atmospheric dust is considered to be a harmful air pollutant causing respiratory and lung diseases (Indoitu *et al.*, 2012). Wind erosion of the soils is a major problem in agriculture, impacting the crop yield through reducing the soil productivity and also sandblasting the plant tissue (Stefanski *et al.*, 2009). Reduced visibility caused by significant dust events can also have a substantial economic impact by affecting air traffic, road transportation and military operations (Knippertz, 2014).

Central Asian deserts are a significant source of dust in the middle latitudes, where economic activity and health of millions of people are affected by dust storms (Orlovsky *et al.*, 2005). More than 75% of the territory in Central Asia is desert lowland varying from sandy to stony, salt, and clay deserts (Lewis, 2003). The frequency of dust emissions, dust storms and transportation of dust from the deserts in this region have increased during the last decades due to extensive anthropogenic desertification in the Central Asian states of Kazakhstan, Uzbekistan and Turkmenistan (Groll *et al.*, 2013). It has been shown that the drylands of Central Asia experience the most frequent dust storms in the world (Orlovsky *et al.*, 2005; Shen *et al.*, 2016).

Although the significance of Central Asian dust sources has been repeatedly highlighted in dust studies at the global scale (e.g. Goudie, 1983; Middleton *et al.*, 1986; Herman *et al.*, 1997; Prospero *et al.*, 2002; Liu *et al.*, 2008; Ginoux *et al.*, 2012; Choobari *et al.*, 2014), only a few studies investigated the spatiotemporal distribution of Central Asian dust sources in detail (e.g. Orlovsky *et al.*, 2005; Micklin, 2007; Indoitu *et al.*, 2012; Groll *et al.*, 2013). Most of these studies relied on weather station records as the primary source of data for investigation of spatiotemporal variation of dust storms (Indoitu *et al.*, 2012; Issanova *et al.*, 2014) and dust deposition rates (Groll *et al.*, 2013) and are hampered by the scarcity of meteorological stations, unaccessibility of many areas and difficulties in organising continuous sampling.

During the last 50 years, the primary focus of studies of atmopshric dust in Central Asia has been on the desiccation of the Aral Sea, one of the most staggering ecological disasters of the last century. Several studies demonstrated the increasing trend of dust emission from the Aral Sea dry bed (now called the Aralkum), using remote sensing (Kozhoridze *et al.*, 2012; Indoitu *et al.*, 2015), dust observation (Groll *et al.*, 2013) and dust modelling (Singer *et al.*, 2003; Darmenova *et al.*, 2007). The land surface characteristics of the Aralkum was also the subject of several research projects (Argaman *et al.*, 2006; Micklin, 2007; Starodubtsev *et al.*, 2007). However, detailed knowledge of sources of dust and their charactristics in other regions, perhaps with the exception of the Taklamakan which received attention recently (Rittner *et al.*, 2016), is very limited. To date, very little is known about the distribution and evolution of dust sources in Central Asia at the sub-basin scale. Consecuently, the contemporary literature on land surface characteristics, seasonality of dust emision and controls over their activity is limited and highly fragmented.

Precise mapping of active dust sources at sub-basin scale is the first step in understanding the driving factors of dust emissions, which is a key part of the dust cycle (Shao *et al.*, 2011). One particular benefit of accurate information on spatial variability of dust sources could be in modelling of dust emission, transportation and deposition and in the numerical weather and climate models which benefit from the accurate data on position of dust sources and dust emissions. Detailed knowledge on spatiotemporal distribution of dust sources at sub-basin scale enables more accurate characterisation of dust emitting surfaces and their geomorphology, which can improve the results of dust models (Parajuli *et al.*, 2017. It can also be useful for more rigorous validation of dust modelling results. Previous studies have shown that inaccurate information on the spatial characteristics of dust sources can lead to large biases in estimated dust loadings (Raupach *et al.*, 2004; Shao, 2004), leading to further errors in models which use this information. This is of great importance in Central Asia, where there are fewer studies of the spatiotemporal variability of dust emissions at sub-basin scale, compared to the well-known dust sources such as the Sahara desert.

1.2. Research Questions and Thesis Structure

This research addresses the identified research gaps by taking advantage of advanced remote sensing and geo-spatial analysis techniques. It addresses the following research questions:

1. What are the spatiotemporal characteristics of dust emissions?
2. What are the land surface characteristics of active dust sources?
3. What are the synoptic controls on dust emissions?

4. What are the direction of dust entrainments at the time of dust emission?

The thesis aims to provide detailed information on Question 1 which is in the focus of this research. These data inform Questions 2, 3 and 4 which are addressed and thereby set the directions for further research. Each of these questions as well as detailed studies of each of the identified dust-emitting regions can form basis for future research projects.

The structure of the thesis is as follows. Following the Introduction, the second chapter of the thesis reviews the existing literature on the main dust sources in Central Asia and methods for monitoring of dust with emphasis on research conducted in Central Asia. Description of the data and methodology to address these research questions is provided in Chapter 3. Detailed inventory of the dust source regions and their land surface characteristics, inter-annual and intra-annual variation of dust outbreak frequency and synoptic climatology of dust emissions are presented in Chapters 4 and 5. It is followed by discussion on the results, as well as a cross-comparison of the major dust source regions in Chapter 6. Finally an overview on the main findings and concluding remarks are outlined in Chapter 7.

Chapter 2. Literature Review

2.1. Dust in the Climate System

Atmospheric aerosols, also known as particulate matter, are produced by both natural and anthropogenic processes. The main components of the atmospheric aerosols are inorganic species (such as sulphate, nitrate, ammonium and sea salt), black carbon (formed from the incomplete burning of fossil and biomass based fuels under certain conditions), mineral dust, organic species and primary biological aerosol particles (IPCC, 2013). Dust as an aerosol impacts the energy balance of the Earth system via absorption and scattering of radiation in the atmosphere and through the mechanism by which aerosols modify the optical properties of clouds and land surfaces (Sokolik *et al.*, 1996; Shao *et al.*, 2011).

The importance of aerosols in the Earth system has been highlighted in the Fourth and Fifth Assessment Report of Intergovernmental Panel on Climate Change (IPCC, 2013). It is reported that the net global cooling effect of aerosols compensates, in part, for the global warming effect of the greenhouse gases (Figure 2-1). But the impact of dust on the radiation balance is not the only role of dust in the Earth system. It also includes the interactions with other physical, chemical and biogeochemical processes on global scales. For instance, interactions between aerosols and clouds, which themselves have a major influence on Earth's energy budget, are one of the most important indirect radiative effects of aerosols, as illustrated in Figure 2-2. Aerosols serve as cloud condensation nuclei upon which cloud droplets form. As a result, for fixed water content, a cloud formed from a mass of polluted air contains more droplets than a cleaner cloud. Although the droplets will be smaller, the cloud will be more reflective than air mass without any aerosols. This is just one indirect, cooling effect. Moreover, since the droplets are smaller, they do not reach the critical size required to precipitate, thus extending the cloud's average lifetime, increasing the altitude at which clouds develop and modifying radiative forcing of clouds (IPCC, 2013).

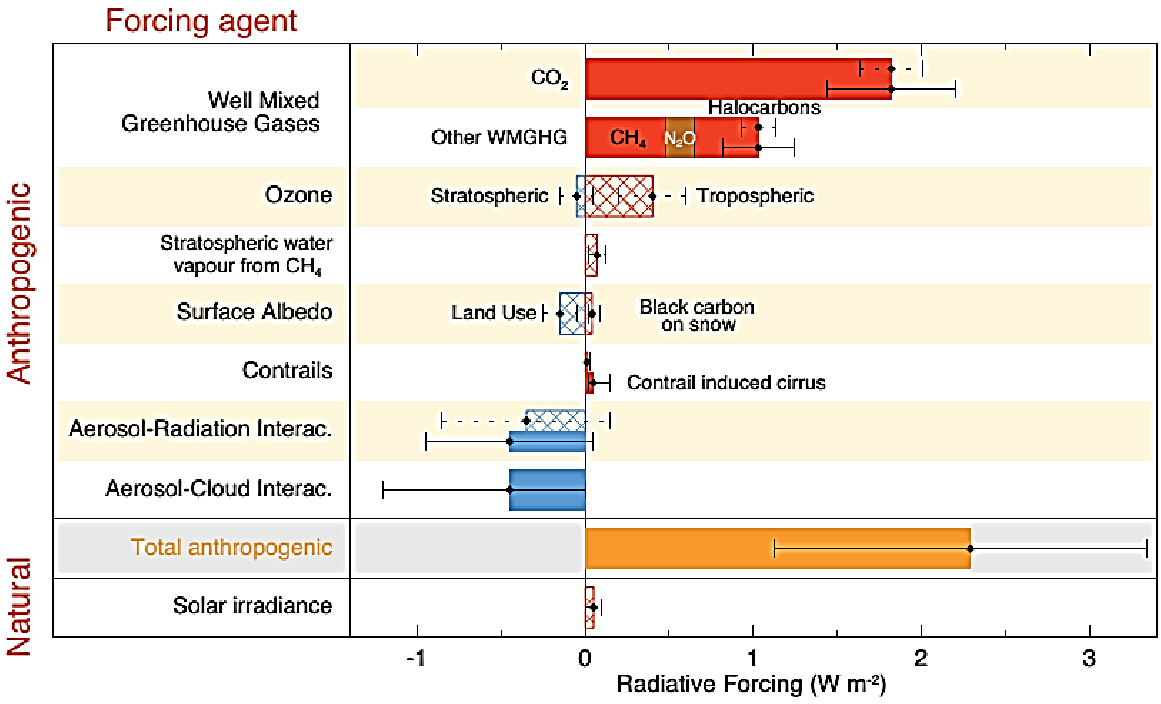

Figure 2-1. Bar chart for radiative forcing (hatched) and effective radiative forcing (solid) for the period 1750–2011. Uncertainties (5 to 95% confidence range) are given for radiative forcing (dotted lines) and effective radiative forcing (solid lines) (IPCC, , 2013)

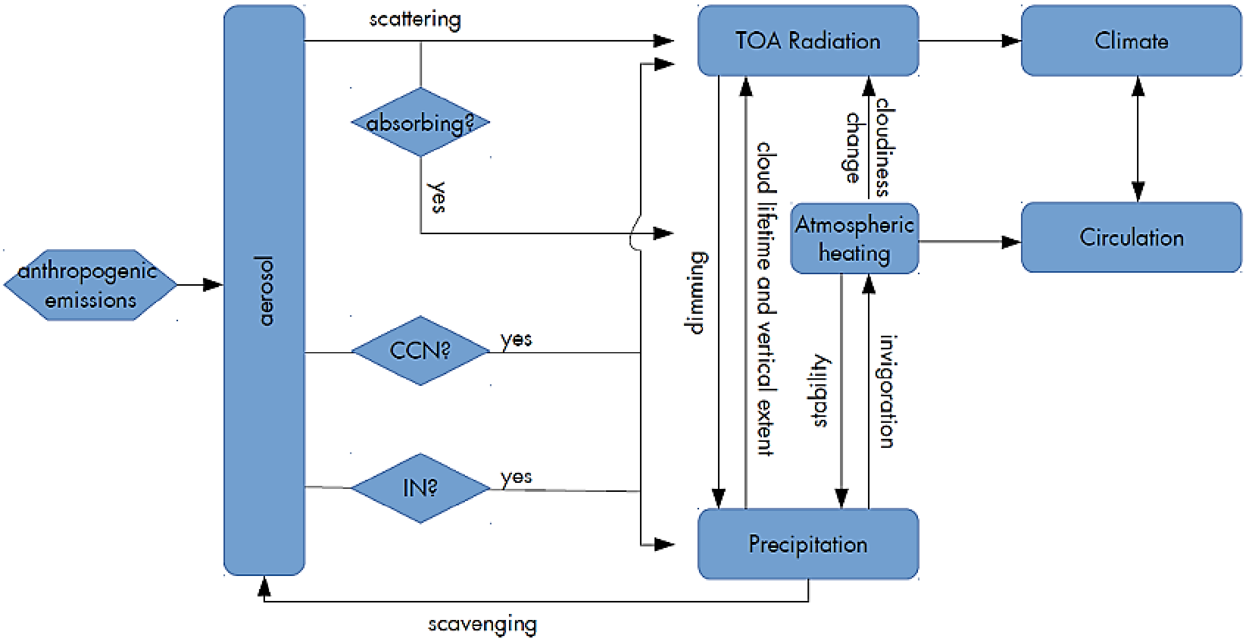

Figure 2-2. Illustrations of role of aerosol particles in decrease or increase of local precipitation, alteration of thermal radiation and latent heating profiles, thus altering the hydrological cycle and climate. Adapted from Rosenfeld *et al.* (2014).

During the last three decades, several attempts have been made to estimate the global dust emission to the atmosphere. However, because of great diversity in implemented models and applied methods, these estimations vary significantly from 500 Mt a^{-1} by Peterson *et al.* (1971) to 2073 Mt a^{-1} by Ginoux *et al.* (2004). Based on recent literature, mostly published after advances in the field of satellite remote sensing in early 21st century, each year about 2000 Mt dust is emitted into atmosphere. It is estimated that around one fourth of the emitted dust is deposited on the surface of oceans and almost 75% (equal to 1500 Mt a^{-1}) is deposited on land (Shao *et al.*, 2011). The dust cycle is closely related to the carbon and energy cycles. In addition to its impact on radiative forcing, mineral aerosol is also the main source of iron which fertilizes the oceans, affecting ocean productivity, and subsequently the ocean-atmosphere CO_2 exchange (King *et al.*, 2003). These cycles and their interactions are schematically illustrated in Figure 2-3.

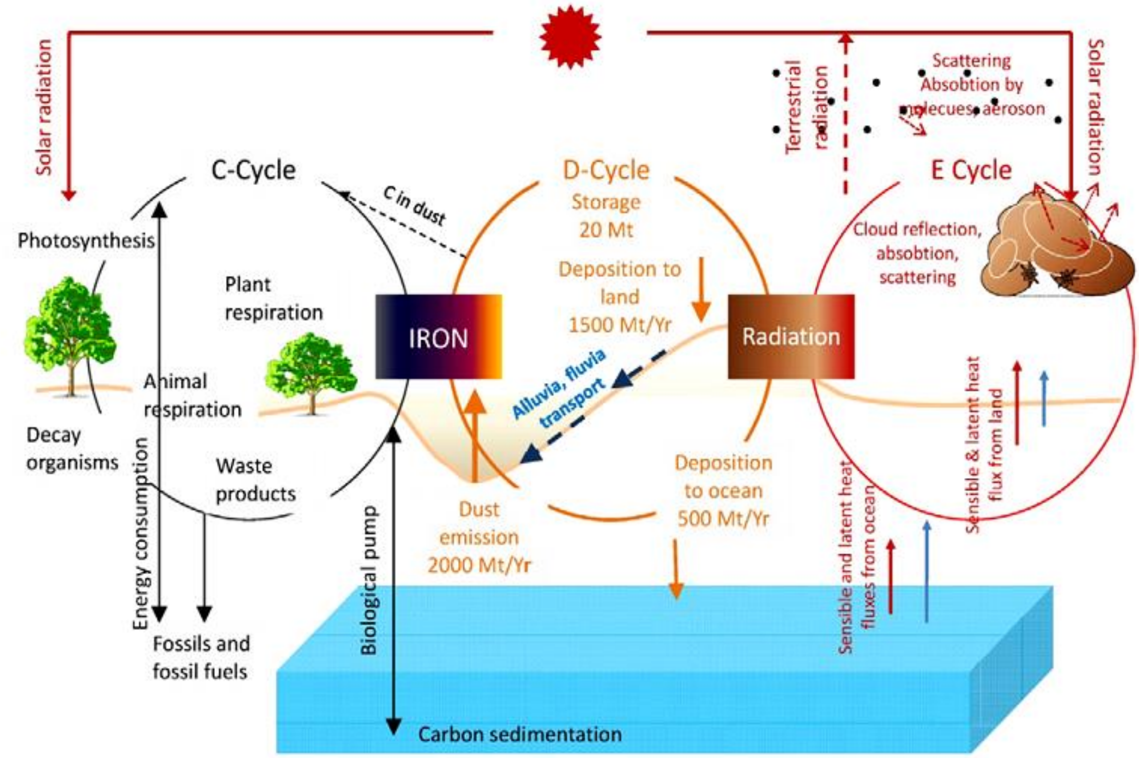

Figure 2-3. Interactions between mineral dust , carbon and energy cycles (Shao *et al.*, 2011).

2.1.1. Dust Impacts on Glaciated Environments

Globally, about 30% of the total land area is a potential source of mineral dust for the atmosphere, and this area is predicted to increase in size in response to human activities (Sokolik *et al.*, 1996; Ginoux *et al.*, 2010). As a result, mineral dust emissions are projected to grow, potentially leading to stronger impacts in distant regions. It is now established that the deposition of mineral dust significantly affects high-altitude environments, including both snow pack and glacier ice (Painter *et al.*, 2007; Painter *et al.*, 2012). The impact is twofold. Firstly, mineral dust deposition changes the reflectance of snow pack and glacier surfaces affecting energy balance and melt rates of glaciers and seasonal snow cover, through the provision of additional at-surface radiative forcing (Brock *et al.*, 2000; Painter *et al.*, 2007; Dozier *et al.*, 2009; Oerlemans *et al.*, 2009; Painter *et al.*, 2010; Painter *et al.*, 2012). Secondly, mineral dust affects the geochemical cycle of glaciated and high-altitude environments (Casey, 2012). Analyses of ice cores have shown that mineral dust originating in deserts is deposited on glaciers in the most remote regions such as Antarctica (e.g. Grousset *et al.*, 1992), Greenland (e.g. Biscaye *et al.*, 1997; Steffensen *et al.*, 2008) and the Himalayas (e.g. Xu *et al.*, 2007; Gautam *et al.*, 2013). An example of dust deposition on snow is shown in Figure 2-4, obtained by Painter *et al.* (2007) during field observations in San Juan Mountains, Colorado.

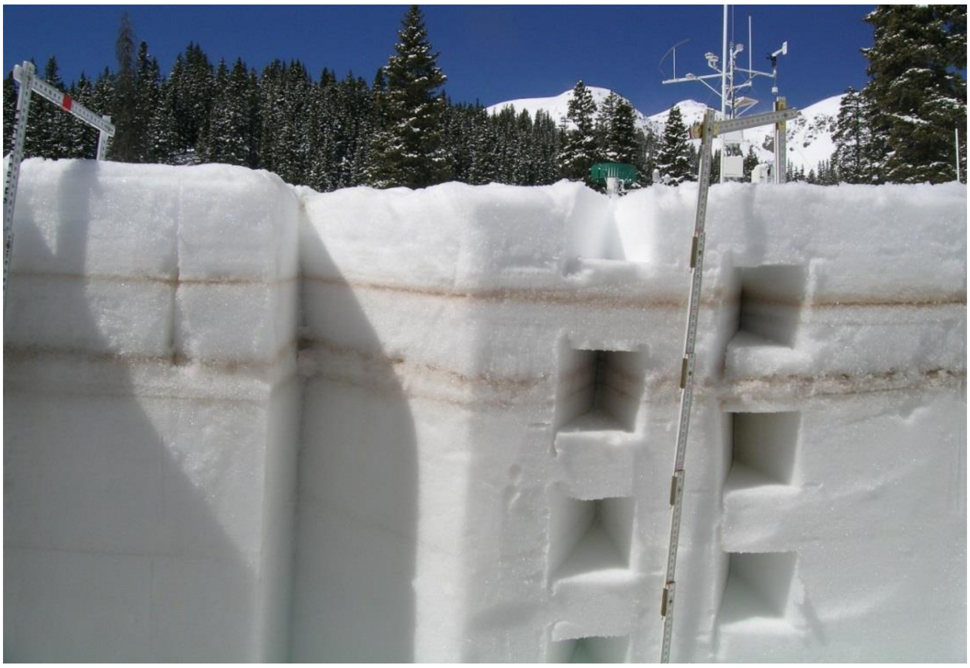

Figure 2-4. Evidence of deposition of desert dust from the Colorado Plateau onto Colorado's mountain snowpacks. Image from http://www.codos.org (Painter *et al.*, 2010).

The link between dust emission and its impact on physical and geochemical characteristics of glaciers has been explored in several studies. Painter *et al.*, (2007), investigated the effect of desert soil on shortening the duration of mountain snow cover in the western US by 18 to 35 days, by deposition of dust originated from Arizona deserts. In another study, darkening of snow cover and accelerated snowmelt in western Himalaya mountains was studied by Gautam *et al.*, (2013). Their remote sensing observations revealed a significant reduction of west Himalayan snow albedo as a result of mineral dust deposition originating from adjacent deserts. Transport of dust from the Sahara to the glaciers in the European Alps and Caucasus has also been investigated in numerous studies (Schwikowski *et al.*, 1999; Sodemann *et al.*, 2006; Oerlemans *et al.*, 2009; Kutuzov *et al.*, 2013; Shahgedanova *et al.*, 2013).

2.2. Satellite and ground-based remote sensing of dust

Sensors on board satellites detect radiation of different wavelengths, both reflected by, and emitted from, the Earth to allow the monitoring of dust events, to identify dust hot-spots, to derive land-surface parameters required for dust modelling and to derive dust-related quantities such as optical thickness, particle size, etc. (Washington *et al.*, 2003; White, 2009; Ginoux *et al.*, 2012; Schepanski *et al.*, 2012). Mineral aerosol can be detected and mapped through remote sensing via inversion of radiative transfer models which operate in the following wavelengths: (a) ultraviolet (UV 0.315–0.4 μm) via absorption (e.g. TOMS AI; Torres *et al.*, 1998), (b) visible (VIS 0.38–0.79 μm) via scattering (e.g. Tanré *et al.*, 1991a), and (c) thermal infrared (TIR 8–15 μm) via contrasting land/aerosol emissivity and/or temperature (e.g. Ackerman, 1997).

The ability to use remote sensing data to detect a dust plume and identify emission sources is affected by several factors including the radiative transfer properties of the emitted dust, radiative properties of land or ocean surface over which the plume is transported, size and density of the dust plume, time of satellite overpass relative to dust emission, the presence or absence of clouds, horizontal and vertical plume trajectory, and sensor characteristics and radiative transfer model used to detect dust (Baddock *et al.*, 2009). The following sections review the remote sensing products and algorithms used in the detection of dust in the atmosphere, identification and characterisation of emission sources, and quantification of the global dust budget.

2.2.1. AERONET (Aerosol Robotic Network)

AERONET (Aerosol Robotic NETwork) is a global network of automated ground-based sun/sky scanning radiometers established by NASA and PHOTONS (Univ. of Lille 1, CNES, and CNRS-INSU) and has been greatly developed by partners from national agencies, institutes, universities and individual scientists. AERONET has been running since 1993 and has been performing routine measurements at around 150 stations distributed globally (Figure 2-5). The combination of satellite and ground based networks, such as AERONET, provides an extremely powerful tool for monitoring of the dust cycle. Long term, mostly continuous and readily accessible database of aerosol radiative properties provided by AERONET program has been broadly used for aerosol research and characterization (e.g. Ginoux *et al.*, 2001; Holben *et al.*, 2001; Dubovik *et al.*, 2002), validation of satellite retrievals (e.g. Fan *et al.*, 2008; Carboni *et al.*, 2012; Schuster *et al.*, 2012) and in combination with other databases (e.g. Sano *et al.*, 2003). AERONET provides globally distributed observations of spectral aerosol optical depth (AOD), inversion products, and precipitable water in diverse aerosol regimes (Holben *et al.*, 1998).

Only a few sites have carried out aerosol optical property observations using the AERONET on and around known dust sources in Central Asia such as Issyk-Kul (42N,76E) in northern Tian Shan (Semenov *et al.*, 2005; Aref'ev *et al.*, 2008), Muztagh Ata (38N,75E) in eastern Pamir (Yan *et al.*, 2015), Dushanbe (38N,68E) in Tajikistan (Abdullaev *et al.*, 2014) and Tazhong station (39N,83E) in the centre of Taklamakan desert (Che *et al.*, 2013). There is a gap in AERONET spatial coverage over the post-Soviet Central Asia in the major Kyzylkum, Karakum and Aral Kum deserts (See Figure 2-5 and Figure 2-6). Analysis of aerosol optical depth measurements at Issyk-Kul station by Semenov *et al.* (2005) over the period of 2000 to 2003, showed a seasonal pattern with a maximum AOD observed during summer. Time series analysis of multi instrument observations by Aref'ev *et al.* (2008) at the same station over a longer time span, revealed a steady increase in atmospheric transparency (decrease in AOD) during 1982-1995 time period followed by a gradual increase in mean AOD from 1995 to 2007. They observed the same seasonal pattern with AOD maxima in the summer season. Summer peak in AOD is very important because this station is located in the borders of the Tian Shan mountain system and clean glacier ice exposed in summer time can be strongly affected by deposition of mineral aerosol.

In addition to uneven spatial distribution and limited number of sites, a major limitation of AERONET data is that the sun-photometer cannot measure the particle backscatter coefficient, but estimates it from products of inversions (Mona *et al.*, 2012). This leads to not negligible uncertainty especially in cases of large non-spherical dust particles. In addition, the AERONET climatological study is based on column measurements and therefore assumes that a single type of aerosol is present in the column, which in most cases is unlikely (Mona *et al.*, 2012). Figure 2-6 shows the distribution of AERONET sites in Central Asia. Discontinuity in data records and the short period of availability of data in some of AERONET sites must be considered as a limitation to their use in long-term dust monitoring.

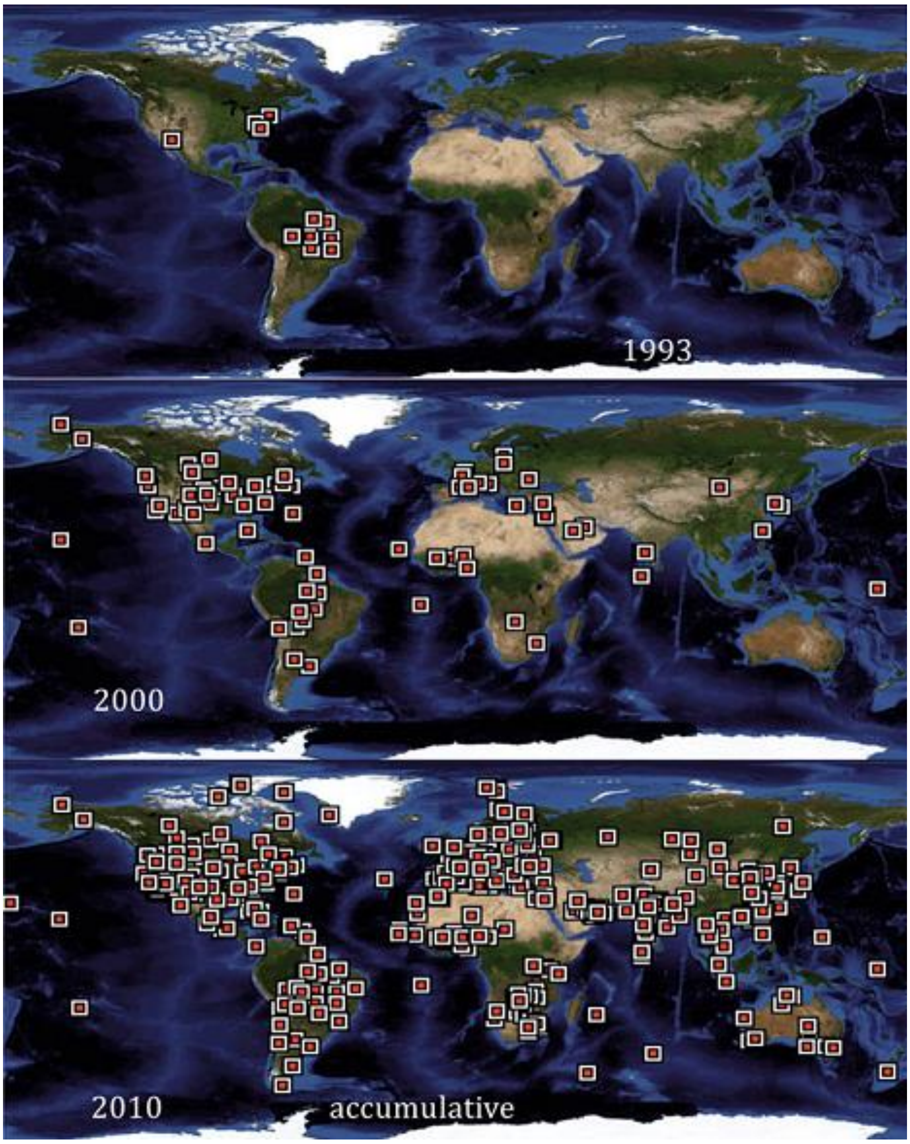

Figure 2-5. The distribution of AERONET station locations in 1993, 2000 and the total accumulative location of stations from 1993 to 2010.

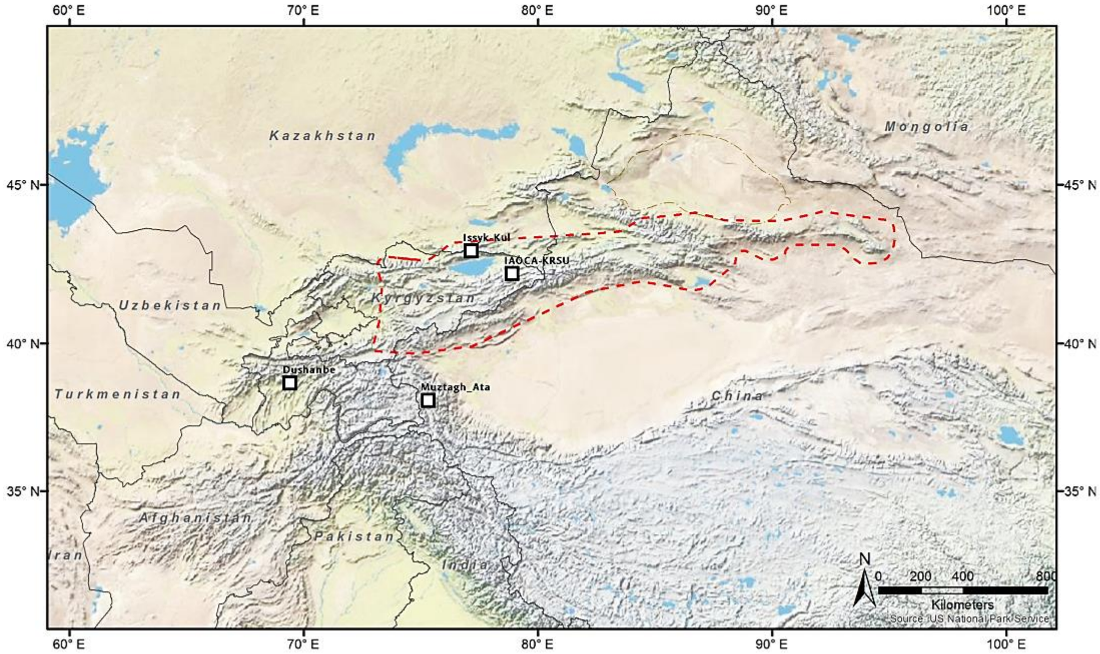

Figure 2-6. Distribution of AERONET sites in Central Asia. Tian Shan mountain range is depicted by red dashed line.

Availability of data for AERONET sites shown in Figure 2-6 are as follow:

- Dushanbe : Start Date: 08 JUN 2010; Latest Date: 18 DEC 2013
- Muztagh_Ata: Start Date: 06 JUN 2011; Latest Date: 11 MAY 2012
- Issyk_Kul: Start Date: 18 AUG 2007; Latest Date: 25 JAN 2014
- IAOCA-KRSU: Start Date: 28 OCT 2013; Latest Date: 03 SEP 2014

2.2.2. TOMS (Total Ozone Mapping Spectrometer)

The early attempts to retrieve aerosol characteristics using satellite remote sensing were made by using data from the Advanced Very High Resolution Radiometer (AVHRR) sensor on board of the National Oceanic and Atmospheric Administration (NOAA) satellite. While AVHRR images have been useful in characterizing dust transport over the oceans (e.g. Husar *et al.*, 1997; Evan *et al.*, 2006), they cannot be readily used to identify sources because of difficulties associated with the large temporal and spatial variability of albedo of land surface (Prospero *et al.*, 2002). Due to the similar spectral properties of dust and bare soil at visible wavelengths, airborne dust cannot be distinguished from the surface with sufficient accuracy. At ultra-violet (UV), near-UV (deep blue), and infra-red (IR), the radiative properties of dust can be separated from the signature of bare soil (Schepanski *et al.*, 2012). As the UV albedo of continental surfaces is low and relatively invariant, using measurements that are made in the ultraviolet (UV) spectrum make it possible to readily detect absorbing aerosols over land surfaces as well as water (Herman *et al.*, 1997; Washington *et al.*, 2003; Ginoux *et al.*, 2012).

The Total Ozone Mapping Spectrometer (TOMS) is a satellite instrument that was designed to provide accurate global estimates of total column ozone and can detect UV-absorbing aerosol. Of the five TOMS instruments which were built, four entered successful orbit. The first two satellites of the TOMS series, Nimbus-7 and Meteor-3, provided global measurements of total column ozone on a daily basis and together provide a complete data set of daily ozone from November 1978 to December 1994. After an eighteen month period when the program had no on-orbit capability, ADEOS TOMS was launched on August 17, 1996 and provided data until the satellite which housed it lost power on June 29, 1997 (www.nasa.gov). Earth Probe TOMS was launched on July 2, 1996 to provide supplemental measurements, but was boosted to a higher orbit to replace the failed ADEOS satellite and circularized to optimize global coverage. The result is an Earth Probe TOMS data set of eighteen months of high resolution data taken at the expense of full global coverage, and a continuing data set beginning in December of 1997 that provides nearly global coverage (McPeters *et al.*, 1998).

The transmitter for the Earth Probe TOMS failed on December 2, 2006 (White, 2009).

Since January 1, 2006 data from the Ozone Monitoring Instrument (OMI) has replaced Earth Probe TOMS. OMI is flown on the Aura spacecraft which is part of the NASA's long-term Earth Observing System (EOS) mission and was launched July 15, 2004. The heritage of OMI are the European ESA instruments GOME and SCIAMACHY, which introduced the concept of measuring the complete spectrum in the ultraviolet/visible/near-infrared wavelength range with a high spectral resolution. This enables retrieval of several trace gases from the same spectral measurement.

TOMS has the advantage of a relatively small ground-pixel size (50 km × 50 km) combined with daily global coverage. OMI combines the advantages of GOME and SCIAMACHY with the advantages of TOMS, measuring the reflected solar radiation in the ultraviolet and visible part in the spectral range between 270 and 500 nm, using two channels with a spectral resolution of about 0.5 nm, relatively high spatial resolution (13 km × 24 km) and daily global coverage (Levelt *et al.*, 2006). Table 2-1 shows the availability of different TOMS satellite data and Ozone Monitoring Instrument (OMI) data.

Table 2-1. Availability of TOMS and OMI data

Instrument	Data Availability	
OMI	(July 2004 - present)	
TOMS	Nimbus-7	(11/1/1978 - 5/6/1993)
	Meteor-3	(8/22/1991 - 11/24/1994)
	Earth Probe	(7/25/1996 - 12/31/2005)

A study of dust storm source areas by Washington *et al.* (2003) using 14.5 years of TOMS Nimbus-7 data and field observations revealed the dominance of the Sahara, and also highlighted the importance of some other dryland regions, such as the Middle East, Taklamakan, central and southwest Asia and central Australia. The OMI absorbing aerosol index (AAI) is also used to detect major dust sources, as it takes near-zero values for clouds and weakly absorbing aerosols and positive values for dust and biomass burning aerosols (Torres *et al.*, 1998; Torres *et al.*, 2007). Wang *et al.* (2013) used 5 years (June 2006 to May 2011) of AAI data to study the horizontal and vertical distributions of dust over northern China and compared it with MODIS AOD and dust aerosol occurrence (OCC) from CALIOP, reporting a good agreement between MODIS AOD and OMI AAI.

In addition to the effect of aerosol physical and optical properties on quality of TOMS results, the main drawback to TOMS and OMI products is that the AAI depends on the height of the aerosol layer above the ground (Herman *et al.*, 1997; Torres *et al.*, 1998). Absorbing aerosols above the boundary layer yield positive AAI values (>1), but in the boundary layer they may produce low AAI values (<0.5) that make it difficult to separate their signal from the background noise (Wang *et al.*, 2013). For that reason, this type of data can be used for investigating the presence of dust above the boundary layer at global level, but it is less useful in detection of dust sources and the origins of individual dust plumes.

2.2.3. MODIS (Moderate Resolution Imaging Spectroradiometer)

The Moderate Resolution Imaging Spectrometer (MODIS) is one of the most widely and successfully used sensors for identification of dust source locations (e.g. Miller, 2003; Hsu *et al.*, 2006; Bullard *et al.*, 2008; Ginoux *et al.*, 2012; Wang *et al.*, 2013). The MODIS instrument is part of the NASA Earth Observing System (EOS) mission. MODIS was launched onboard the Terra and Aqua spacecrafts in December 1999 and May 2002 respectively. This sensor measures radiation in 36 narrow spectral bands situated between 0.4 to 14.4 µm. All infrared channels are available at 1 km sub-satellite resolution, with a subset of visible and shortwave infrared channels at native resolutions of either 500m (5 channels) or 250m resolutions (2 channels). In sun-synchronous orbits, Terra and Aqua provide 10:30 and 13:30 local Equatorial crossing times, respectively.

Multispectral dust enhancement techniques using satellite radiometer measurements in visible/reflective infrared (0.4 – 1.6 µm), shortwave/infrared (2 – 5 µm), and thermal infrared (8 – 12 µm) channels have been widely used in dust studies including dust event frequency (e.g. Schepanski *et al.*, 2007) and accurate mapping of dust sources for use in mesoscale dust storm forecasting (e.g. Walker *et al.*, 2009). Although mineral aerosol is sometimes detectable on visible MODIS images (particularly over the dark ocean), it can be difficult to detect over land because dust can have similar reflectivity to the bright desert surfaces from which it is originated (Levy *et al.*, 2007). In addition, it is often hard to differentiate dust from cloud, sea salt and anthropogenic pollution. Mineral dust shows different emissive and tranmissive behaviour within multiple thermal infrared (TIR) wavelength ranges. Hence, a great number of studies have used methods based on brightness temperature difference (BTD) in either two or three wavelength ranges in order to enhance entrained dust in satellite imagery (e.g. Tanré *et al.*, 1991a; Ackerman, 1997; Schepanski *et al.*, 2007). BTD based methods are based on temperature differences between the land surface and elevated dust, which is cooler than the ground surface, and are principally unaffected by absorption from other atmospheric gases (Park *et al.*, 2014). However, there are several limitations associated with these techniques which are (1) the conventional BTD methods often fail to distinguish between dust and thin cirrus, (2) the depressed infrared method is hindered by requiring accurate background surface emissivity (particularly at 8.5 μm), and (3) the visible channel contrast reduction method is of limited use over bright desert backgrounds.

2.2.3.1. Dust Enhancement Product

A new robust technique for enhancing desert dust storms over land and ocean using MODIS imagery was introduced by Miller (2003). The algorithm, which combines near and thermal infrared measurements with colour information from visible channels, provides the ability to distinguish areas of dust from different types of clouds and bright desert backgrounds in enhanced false colour imagery. In this method, dust enhancement over land is based on three premises: (i) elevated dust is cooler than the background land, resulting in a lower brightness temperature against the hot skin temperature of the desert background, (ii) coloration properties of dust can be used in order to distinguish dust from water clouds having the same radiometric temperature, and (iii) unlike the cirrus, mineral dust often produces a positive 12 – 11 μm difference.

Walker *et al.* (2009) utilized the MODIS Dust Enhancement Product (DEP) imagery to distinguish elevated dust over land and water from other components of the scene. A high resolution (1-km) Dust Source Database (DSD) was created for southwest Asia using 5 years (2001–2005) of 1km resolution DEP imagery. This product allowed them to identify the point sources at scales of 1 to 10 km that erode to form point source plumes. An example of MODIS DEP is presented in Figure 2-7, showing the benefit of the DEP over true colour images for identifying small dust plumes. The dust plume within the white rectangle in this figure is barely visible in the true colour image while it is clearly seen in the DEP imagery.

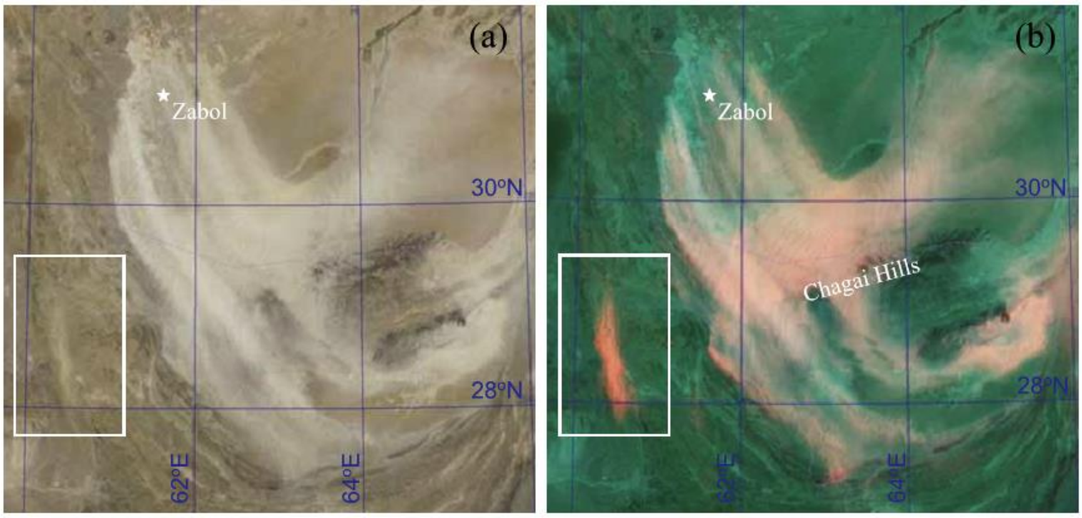

Figure 2-7. MODIS true colour image (a) is compared to the MODIS dust enhancement product (b), revealing several dust plume for 20 August 2003 of southern Afghanistan, southwestern Pakistan, and eastern Iran (From Walker *et al.*, 2009).

The utility of MODIS DEP for dust source identification was evaluated by Baddock *et al.* (2009) for four significant dust events from the Lake Eyre Basin, Australia. MODIS DEP was found to be visually very effective for all events observed in their study. In particular, a clear distinction between dust and cloud was observed using this technique. However, dust/non-dust threshold suggested by Miller (2003) had to be tuned for different dust events as this enclosed basin contained multiple dust sources with different geochemical signatures.

One of the limitations of applying BTD based algorithms, including DEP, for dust enhancement over land is that cold terrain may result in a false enhancement of dust. This limitation is more prominent in winter observations, especially over mountain ranges, and in early morning observations (Walker *et al.*, 2009). Another major shortcoming is that these methods cannot detect dust beneath clouds (Miller, 2003).

2.2.3.2. MODIS Deep Blue AOD (M-DB AOD)

Radiative transfer model inversion of aerosol observations made within (or via combinations of) each of the three wavelength ranges (UV, VIS, IR) often provides either a relative indication of aerosol concentration (e.g. via TOMS AI), or a calibrated measure of wavelength-dependent total aerosol optical thickness/depth (AOT/D). Hsu *et al.* (2004) developed the "Deep Blue AOD" algorithm with the aim of obtaining comprehensive properties of aerosol optical thickness and Angstrom exponent using multiple narrow-band channels at the near-UV (DB – Deep Blue) part of the wavelength spectrum (412 and 490 nm for SeaWiFS; 412 and 470 nm for MODIS). The retrieval is developed for the MODIS instrument flying aboard Aqua and Terra, and for the SeaWiFS (Sea-viewing WIde Field-of-View) sensor aboard OrbView-2. As a result of utilizing wavelength at the DB part of the visible spectrum, the dependency between aerosol layer height and AOT intensity (e.g. OMI AI retrieval for UV wavelengths) is avoided. The DB algorithm uses a pre-calculated surface reflectance database developed by employing the minimum reflectivity technique to determine the surface boundary condition.

DB AOD products were evaluated by Hsu *et al.* (2006) in a study of sources, pathways, and transport of dust and anthropogenic pollution aerosols in East Asia. Using this technique, they indicated that the major dust sources in East Asia are the Taklamakan Desert, the Gobi Desert in China and southern Mongolia and deserts in Inner Mongolia. Comparisons of DB AOD and Angstrom exponent values with direct sunphotometers measurements at five different AERONET sites in China and Mongolia during the ACE-Asia experiment, has shown that this algorithm can provide high quality AOD over reflective desert surface and is capable of separating fine mode from coarse mode particles, even for the mixed aerosol environments. The size distribution of an aerosol is one of its most important properties, as it governs its impact on many processes, e.g. its radiative impact and removal processes efficiencies (Knippertz, 2014). It was also shown that, among the observations taken from MODIS, SeaWiFS and MISR, the good spatial coverage provided by MODIS, with almost no gaps between orbits at mid and high latitudes, is an important advantage for identifying source regions over very large areas, while global coverage by SeaWiFS and MISR is achieved once every two days and once every nine days respectively.

Ginoux *et al.* (2012) investigated the global distribution and emission rates of anthropogenic and natural dust sources using MODIS imagery. They employed the DB algorithm to estimate AOD and extract dust optical depth (DOD) over arid regions worldwide. To extract DOD from M-DB AOD, a screening method comprising three criteria was established; Namely, (1) AOD values with negative Angstrom exponent ($\alpha < 0$), (2) absorption of solar radiation in the green (550 nm), and (3) Increasing single scattering albedo with wavelength. In their study, a good agreement between M-DB products and field measurements at most AERONET sites was achieved over the period 1 January 2003 to 31 December 2009. Their findings were consistent with global dust sources detected by Prospero *et al.* (2002) using the Nimbus 7 TOMS aerosol index and it was also shown that the inefficiency of TOMS AI for making quantitative measurements of AOD can be overcome using M-DB products.

The effect of varying dust mineralogy on the capability of Deep Blue to detect dust plumes is among the most substantial drawbacks of this algorithm. In the Deep Blue algorithm, it is assumed that surface reflectivity over desert regions is low in blue wavelengths, where dust aerosol is more reflective (Hsu *et al.*, 2004). However, dust reflectivity is variable depending on its chemical characteristics and can diminish considerably with increased iron concentration. As a result, red (iron-rich) dust will have relatively low blue reflectivity and therefore potentially lower contrast with respect to background reflectance, while white dust (composed of carbonates, bleached quartz or evaporite minerals) will have higher reflectance in the VIS and significantly higher contrast relative to underlying ground (Baddock *et al.*, 2009). The spatial resolution of 1km of BTD dust enhancement products is another key advantage over the relatively coarse resolution of Deep Blue AOD products (~10 Km).

2.2.4. **CALIOP (Cloud-Aerosol Lidar with Orthogonal Polarization)**

The CALIPSO satellite, launched in April 2006, carries a two-wavelength polarization-sensitive lidar, named the Cloud-Aerosol Lidar with Orthogonal Polarization (CALIOP). CALIPSO is an integral part of NASA's A-Train of Earth Observing System (EOS) remote sensing satellites. CALIOP is an elastic backscatter lidar that transmits linearly polarized laser light at 532 nm and 1064 nm and measures range-resolved backscatter intensities at both wavelengths using a three channel receiver. This instrument provides information on the vertical distribution of aerosols as well as clouds which greatly helps to determine the height of dust layer. This knowledge is crucial for the study of dust pathways through the atmosphere, and also is of great help to refine their radiative studies on a global scale (Winker *et al.*, 2007). The main advantages of the CALIOP sensor can be summarised as follows:

- By receiving the laser light backscattered from different layers of the atmosphere along the transmitted laser beam, CALIOP can accurately measure the global vertical distribution of aerosol and cloud and, unlike all other products, enable detection of aerosols under the cloud cover;
- The capability of CALIOP to measure the depolarization ratio makes it possible to distinguish dust aerosols from other types of aerosol;
- Third, CALIOP can detect dust aerosols over any terrestrial surfaces during day and night (Liu *et al.*, 2008).

There are three types of CALIPSO Lidar Level 2 products; layer products (cloud and aerosol), profile products (backscatter and extinction) and a vertical feature mask (cloud and aerosol locations and type). The Lidar Level 2 aerosol layer products are generated at 5 km horizontal resolution (Anselmo *et al.*, 2006). Figure 2-8 shows an example of CALIOP data, demonstrating the capability of CALIOP to track dust long-range transport during a dust event that originated in the Sahara desert on 17 August 2007 and was transported to the Gulf of Mexico.

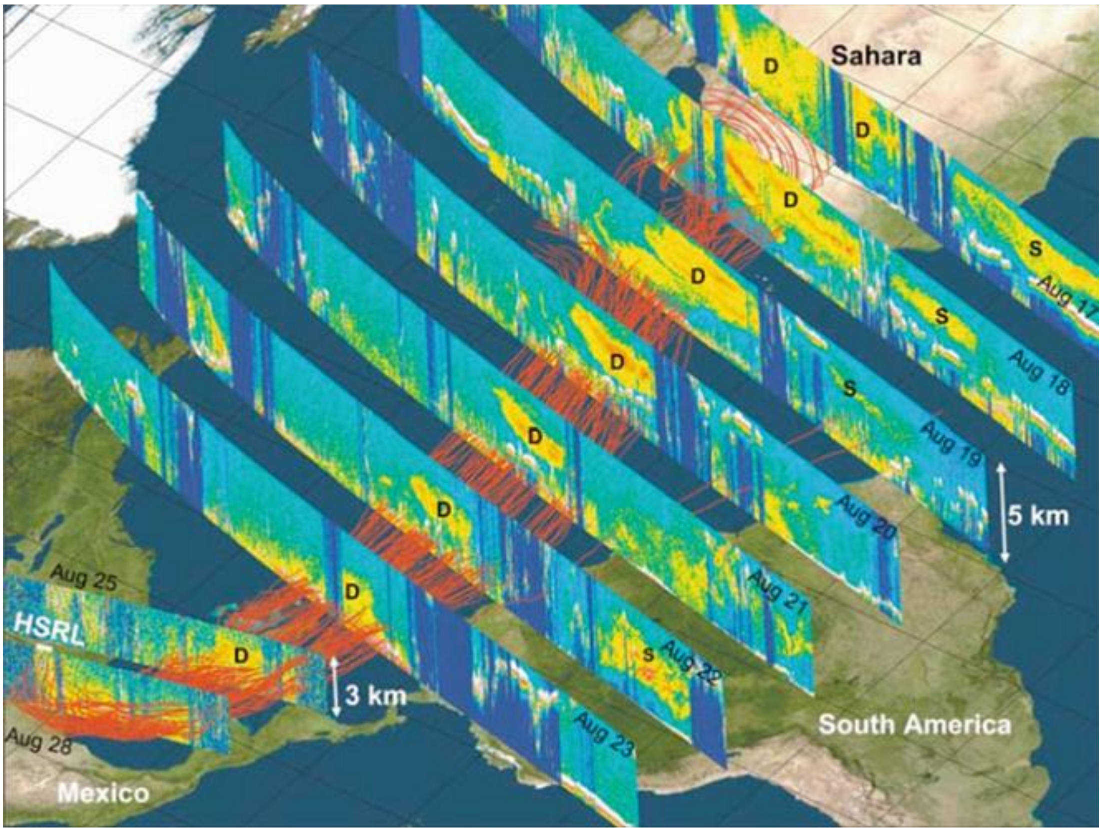

Figure 2-8. 532-nm attenuated backscatter coefficients measured by CALIOP when passing over the dust transport track (From Liu *et al.*, 2008)

A study of seasonal change in maximum elevation of dust plumes was carried out by Liu *et al.* (2008) using CALIOP data. They provide in-depth analysis of the elevation of dust layer tops based on the first year of CALIOP measurements. They showed that dust layers reach their highest elevations in the summer and lowest in the winter over North Africa and the Arabian Peninsula, while in the spring the highest elevations are observed over the Taklamakan and Gobi deserts. Using the 1 km layer average depolarization ratio, different types of dust events including dust storms, blowing dust and even optically thin dust layers were distinguished. The results of this and several other studies (e.g. Winker *et al.*, 2007; Liu *et al.*, 2008; Wang *et al.*, 2013) clearly illustrate the value of CALIPSO data in improving our understanding of dust production and transport.

Although CALIPSO vertical profiles improve our understanding of dust transport, due to the narrow measurement swath of CALIPSO, it is still not feasible to characterise the spatial extent of the dust emission sources from these data. Uncertainties in CALIPSO products were also analysed in several studies. CALIPSO-derived AOD was compared with AERONET measurements by Schuster *et al.* (2012) showing that the assumed lidar ratio (40 sr) for the CALIPSO dust retrievals is too low and that the CALIPSO-derived AOD is on average 20% lower the AERONET AOD in North Africa. Similarly, a number of analyses of lidar measurements by the European Aerosol Research Lidar Network (EARLINET) and observations by the Saharan Mineral Dust Experiment (SAMUM) suggested that the given lidar ratio for the CALIOP dust model is not applicable to all dust scenarios (e.g. Tesche *et al.*, 2009; Pappalardo *et al.*, 2010). Based on their findings it was suggested that multiple dust models for CALIPSO that are based upon source locations, transport times, and dust loading could improve dust optical depth retrievals from the CALIPSO product.

2.2.5. POLDER (POLarization and Directionality of the Earth Reflectance)

The PARASOL (Polarization and Anisotropy of Reflectances for Atmospheric science coupled with Observations from a Lidar) mission, whose purpose is to characterize radiative properties of clouds and aerosols, was launched in December 2004 as a part of the A-Train formation. PARASOL carries a POLDER-type instrument (POLarization and Directionality of the Earth Reflectance) which provides spectral, directional and polarized radiances (Fan *et al.*, 2008; Peyridieu *et al.*, 2010). This sensor provides optical depth at 670 and 865 nm for fine and coarse mode aerosols over the oceans, and for fine mode aerosols over land (Torres *et al.*, 2007). Polarization capability of POLDER enables discrimination between spherical and non-spherical particles in the coarse mode, as non-sphericity is an indicator of the presence of mineral aerosol. The individual foot-print of the instrument is 5.0×6.5 km and the aerosol product is averaged over a 3×3 pixel grid, which results in AOD products of 15×19.5 km resolution. Over ocean, the inversion algorithm is able to discriminate small spherical particles (accumulation mode) from large spherical or non-spherical particles (coarse mode).

Several studies have attempted to retrieve aerosol over land surfaces (e.g. Qu *et al.*, 2006; Fan *et al.*, 2008) and above cloud (e.g. Lee *et al.*, 2012b). Although the performance of PARASOL is satisfactory over oceans, retrieval of aerosol over land from total radiances is difficult because the signal is generally dominated by the surface contribution (Deuzé *et al.*, 2001). However, thanks to the polarization measurement capability of POLDER, retrieval of dust over land can be achieved using polarized reflectance. In this method the polarized reflectance of the land surfaces is assumed to be moderate and spectrally constant, although with a very strong directional signature. Scattering by submicron aerosol particles generates highly polarized radiance, which makes it possible to estimate the corresponding load. The performance of the retrieval increases with more polarizing aerosols and less polarizing underlying surfaces. This is why the method is sensitive to the small mode of the aerosol size distribution. It is, therefore, limited to aerosol with size less than 0.35 μm (Tanré *et al.*, 2011). Larger aerosol particles, such as desert dust, do not nearly polarize sunlight and are therefore not accessible by quantitative inversion from POLDER measurements (Carboni *et al.*, 2012).

2.2.6. SEVIRI (Spinning Enhanced Visible and Infrared Imager)

Imagery obtained by the Spinning Enhanced Visible and Infrared Imager (SEVIRI) onboard the Meteosat Second Generation (MSG) series of geostationary satellites is widely used to investigate dust generation mechanism and transport of dust (e.g. Liu *et al.*, 2006; Schepanski *et al.*, 2009). MSG satellite takes measurements every 15 min with a spatial resolution of 3×3 km at nadir (over the Sahara) and ~5×7 at off-nadir (over the Middle East). Mineral aerosol sources can be inferred using a qualitative dust index, which is retrieved based on brightness temperatures of three different IR channels (8.7 μm, 10.8 μm, and 12.0 μm) (Schepanski *et al.*, 2007). This tri-spectral approach as proposed by Ackerman (1997), uses the brightness temperature difference of two adjacent wavelength channels both within the atmospheric window (wavelength at which the transmittance through the atmosphere is highest and thus the atmosphere is relatively transparent). Elevated dust is enhanced and appears as pink colour in the derived RGB composition (Figure 2-9). Atmospheric dust can be detected by MSG during daytime and night time at high temporal and spatial resolutions using these wavelength channels.

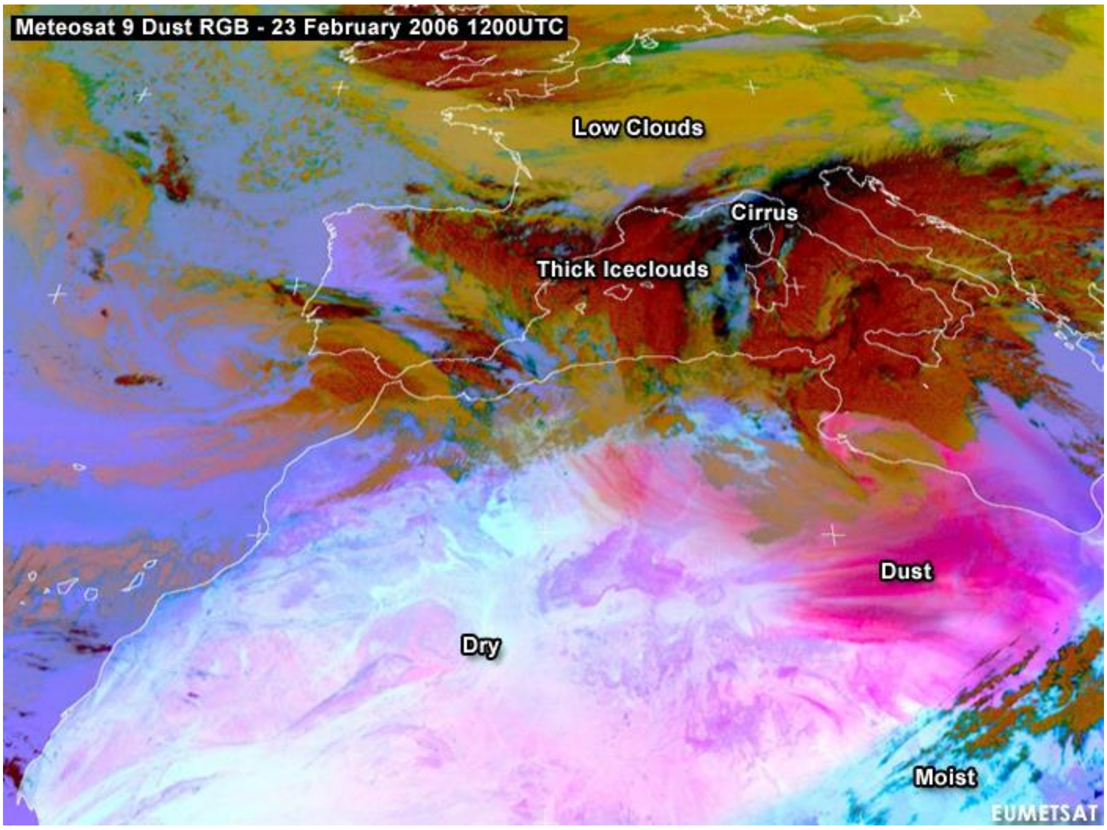

Figure 2-9. SEVIRI dust RGB composition obtained on 23 Feb 2006,12:00 UTC, over North Africa. (from Schepanski *et al.*, 2007)

The most significant advantage of using data obtained by a geostationary satellite is the improved detection of atmospheric dust close to its source due to the higher temporal resolution of the retrievals compared to daily retrievals from polar-orbiting instruments like OMI and MODIS. High temporal resolution of SEVIRI allows dust plumes to be tracked forward or backward in time. Additionally, the relatively high spatial resolution of SEVIRI allows for a comprehensive analysis of dust processes.

SEVIRI data was used by Schepanski *et al.* (2009) in a comprehensive study of the diurnal characteristics of dust storm activity in Sahara and Sahel over 2 years. This data set was used to identify the most active dust source areas and the time of day when dust source activation occurs most frequently. Taking advantage of the 15 minutes temporal resolution of SEVIRI, dust storms in the Sahara were found to be highest frequency in the early hours after sunrise. A major limitation for using SEVIRI imagery is that the dust index is affected by vertical temperature gradient in the lower troposphere (i.e. boundary-layer inversions) and atmospheric moisture content, as the index is purely referring to the spectral varying emissivity at thermal wavelengths (Brindley *et al.*, 2012). Another shortcoming of this type of data is that no information on dust can be retrieved from underneath optically thick clouds (Schepanski *et al.*, 2012). Moreover, due to the geostationary position of the satellite, MSG data are only provided for the domain centred at the Prime Meridian and the Equator. This covers Africa to Arabia, but unfortunately does not cover the deserts of Central Asia.

2.2.7. Summary

Table 2-2 gives a brief overview of the remote sensing data most widely for dust studies, their characteristics and availability. As discussed in the literature, each type of remote sensing data and methods have their own limitations but a combination of different remote sensing products and techniques can be a reliable tool to study the dust emission mechanism and to detect dust sources. We also reviewed the characteristics of different passive and active spaceborne sensors, highlighting their advantages and limitations.

Both spaceborne and ground based remote sensing data have their own advantages and limitations. Some databases benefit from a long record of dust observations (e.g. TOMS), while some other products have the advantage of fine temporal resolution (e.g. 15 minutes for SEVIRI). Considering the availability of remote sensing products and mineralogy of dust sources in Central Asia, Aqua/MODIS products seem to be a suitable dataset to study the dust emission sources in Central Asia. The main advantage of MODIS data can be summarised as follows: (i) relatively good spatial and temporal resolution of atmosphere products, (ii) continuous availability of data and (iii) diversity of archived standard products, from Deep Blue AOD to Level 1 land surface radiance.

Table 2-2. Overview of remotely sensed products and their availability

DATA		Temp. Res.	Spatial Res.	Wavelength	Availability
TOMS	OMI AI	1 Day	13×24 km nadir 28×150 km extremes	270 to 500 nm	Jan. 2006 – Now
	Nimbus-7	1 Day	50×50 km nadir 150×250 km extremes	340, 360, and 380 nm	Nov 1978 – Dec 1994
	Earth probe				Jul 1996 – Dec 2006
MODIS	Deep Blue AOD	1 Day	10×10 km (level 2)	412 and 470 nm	Mar 2000 - Dec 2007 (Terra) Aug 2002 – Now (Aqua)
	DEP	1 Day	1×1 km	0.645 to 12 μm	
SEVIRI Dust RGB		15 Minutes	3×3 km	8.7, 10.8, 12.0 μm	Aug 2002 - Now
CALIOP		12 hours	5×5 km	Laser, 532 & 1064 nm	Apr 2006 - Now
POLDER		1 Day	5×6.5 km	670 & 865 nm	Dec. 2004 – Oct. 2013

2.3. Central Asia

Central Asia, the area extending from the Caspian Sea in the west to China in the east and from Afghanistan in the south to Russia in the north, hosts some of the largest temperate deserts in the world. Traditionally In the Russian literature Turkmenistan, Uzbekistan, Tajikistan, and Kyrgyzstan are usually defined as "Middle Asia", while the term "Central Asia" includes Kazakhstan, as well as parts of China and Mongolia (Lioubimtseva *et al.*, 2009). The landscape of Central Asia is dominated by large desert and semi-deserts. The glaciated mountain ranges of Central Asia represent one of the greatest concentrations of permanent snow and ice in the mid-latitudes of the Northern Hemisphere, including Tian Shan, Pamir and Karakoram (Figure 2-10).

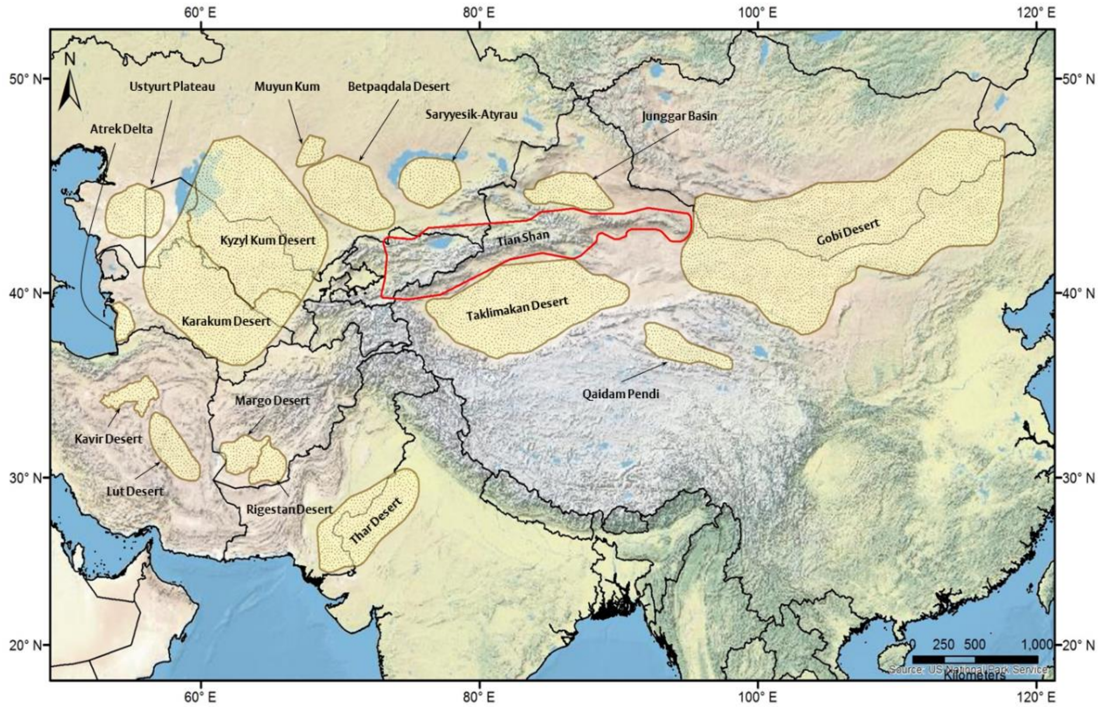

Figure 2-10. Location of the Tian Shan Mountains (red polygon) and surrounding deserts. Desert outlines are from http://www.naturalearthdata.com

More than 75% of the territory in Central Asia is desert lowland, varying from sandy deserts to stony, salt, and clay deserts (Lewis, 2003). These lowlands contain large deserts such as the Taklamakan, Junggar Pendi, and Gobi desert in east and south, as well as deserts of Turkmenistan, Uzbekistan and Kazakhstan in north and west of Tian Shan (See Figure 2-10). The deserts of Central Asia form the second major source of mineral dust in the world, which supply up to 25% of desert aerosol to the atmosphere (Ginoux *et al.*, 2004). These deserts are characterized by severe weather, sparse vegetation cover, long dry summers and frequent recurrence of droughts (Indoitu *et al.*, 2012). Meteorological data since the beginning of the 20th Century registered a steady increase of the mean annual and mean winter temperatures in Central Asia (Groll *et al.*, 2013). In the Tian Shan Mountains, the increase of the mean annual air temperature was 0.94 °C between 1940 and 1991 (Aizen *et al.*, 1997). At the same time, the frequency of dust storms, dust emission and transportation of dust from the deserts in this region have increased due to extensive increase in anthropogenic dust emission in the Central Asian states of Kazakhstan, Uzbekistan and Turkmenistan (Groll *et al.*, 2013).

Dust emission in Central Asia has been traditionally monitored using ground based observations at meteorological stations (Orlovsky *et al.*, 2002; Indoitu *et al.*, 2012) and AERONET (Semenov *et al.*, 2005; Aref'ev *et al.*, 2008) providing data with low spatial resolution. More recent research relied on the use of the satellite remote sensing. For instance, maps of dust sources were produced by Walker *et al.* (2009) for the Middle East covering the westernmost part of Central Asia. A global assessment of anthropogenic and natural dust sources by Ginoux *et al.* (2012) included Central Asia, provided a useful resource for the identification of dust sources in this region (Figure 2-11). However, these assessments either do not cover the whole region or are of low spatial and temporal resolution.

The spatiotemporal distribution of dust sources at sub-basin scale have been studied for several major dust source regions around the world, e.g. the Lake Eyre Basin in Australia (Bullard *et al.*, 2008), West Texas in USA (Lee *et al.*, 2012a), the Namib Desert in Africa (von Holdt *et al.*, 2017) and Southwest Asia (Walker *et al.*, 2009). To date there is no detailed information on dust source regions at sub-basin scale for Central Asian deserts and their temporal variations in terms of dust emission and meteorological conditions leading to dust emission have not been investigated.

In the following section of this chapter the existing literature on the main dust sources in Central Asia and methods for monitoring of dust with emphasis on researches conducted in Central Asia are reviewed. A review of ground based and remote sensing methods for retrieval of AOD and detection of dust sources will be presented and the advantages and limitations associated with each method will be discussed. Finally an outline of the existing methods and selected strategy for this research is presented.

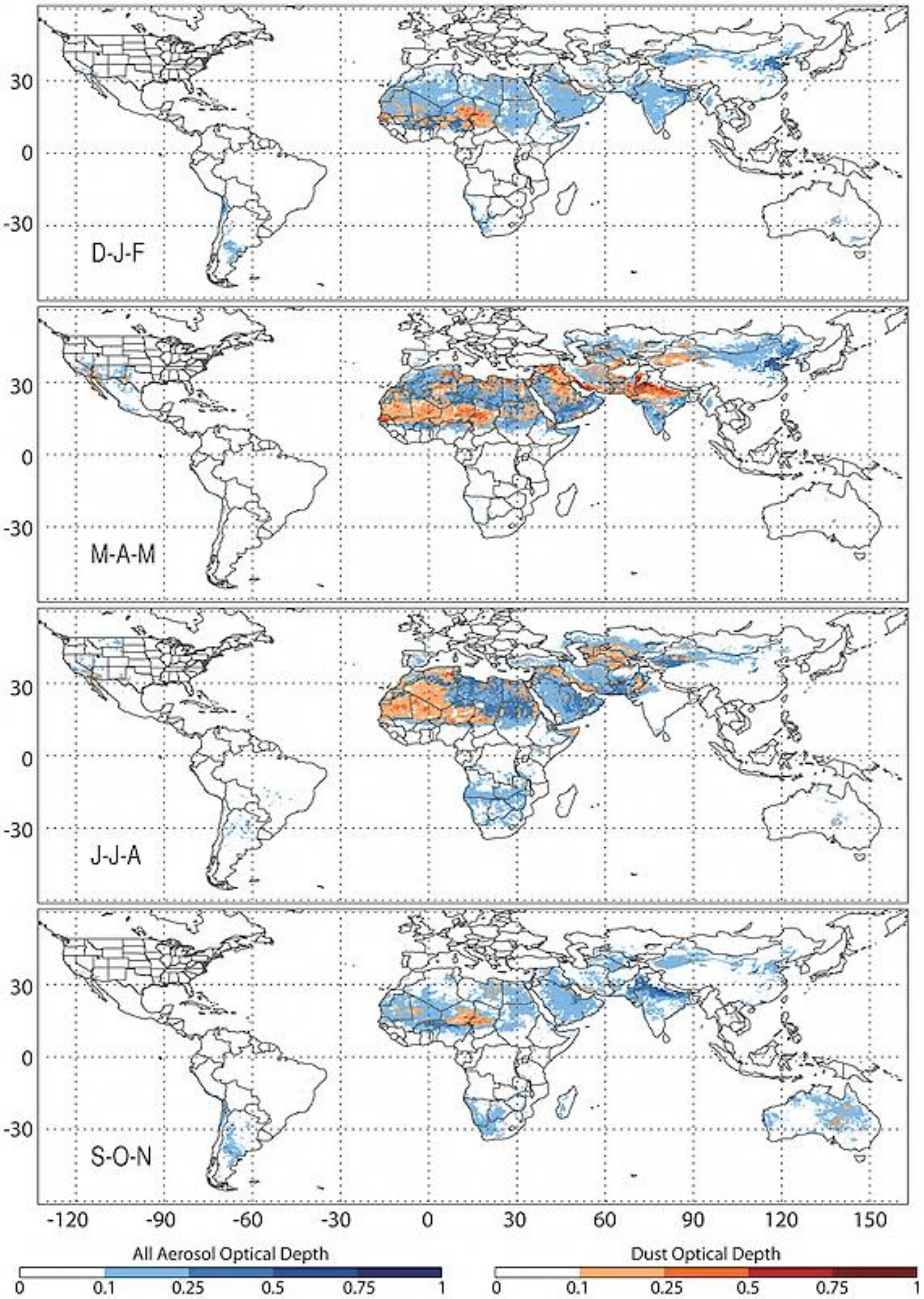

Figure 2-11. Global distribution of MODIS DB seasonal mean aerosol optical depth (blue) overplotted by dust optical depth (red) (from Ginoux *et al.* 2012).

2.4. Dust source regions in Central Asia

Figure 2-10 presents the location of the major deserts in Central Asia and west China. These deserts are the most prominent dust sources according to previous research carried out in this region. While several studies at global and continental scale have highlighted the high rate of dust emission from the Central Asian dust sources, the sub-basin distribution of dust sources within these large deserts have not yet been investigated. This section presents an overview of the most important deserts, their geographical extent and a review of main dust studies carried out in them.

2.4.1. Karakum Desert

The Karakum Desert covers almost 80 percent of the Central Asian republic of Turkmenistan. To the south it is bounded by the Kopet-Dag Mountains and to the north and east lies the Amudarya river, which runs down from the Pamir Mountains (Figure 2-12). The desert owes its names to its greyish sands (Karakum means 'Black Sand' in Turkic). The Karakum covers a total area of around 300,000 km^2, making it the 12th largest desert in the world.

Land surface characteristic of the Kara-Kum, particularly in the southern part of the central region, are partially vegetated sand ridges that may reach up to 90 meters height and sometimes can be more than 10 km long (Babaev, 1994). To the south-east are areas of salt marsh, while to the north is a region of windswept plateau. Absolute elevations vary from 20 m a.s.l in the west to 200 m a.s.l. in the east. The Karakum has a continental type climate, characterised by cool winters and long hot summers. Average summer temperatures in the central part of the Karakum are as high as 34°C. Average temperatures in the north part and areas adjacent to the Caspian Sea are lower than central parts (Figure 2-12). In January average temperatures are 4°C in the south and −4°C in the north, although temperatures can drop as low as −20°C (Harris, 2003). The aridity of the climate is represented by very low precipitation (100–250 mm), low air humidity, low cloudiness, high evaporation rates (2000–2700 mm), and frequent droughts (Orlovsky *et al.*, 2004).

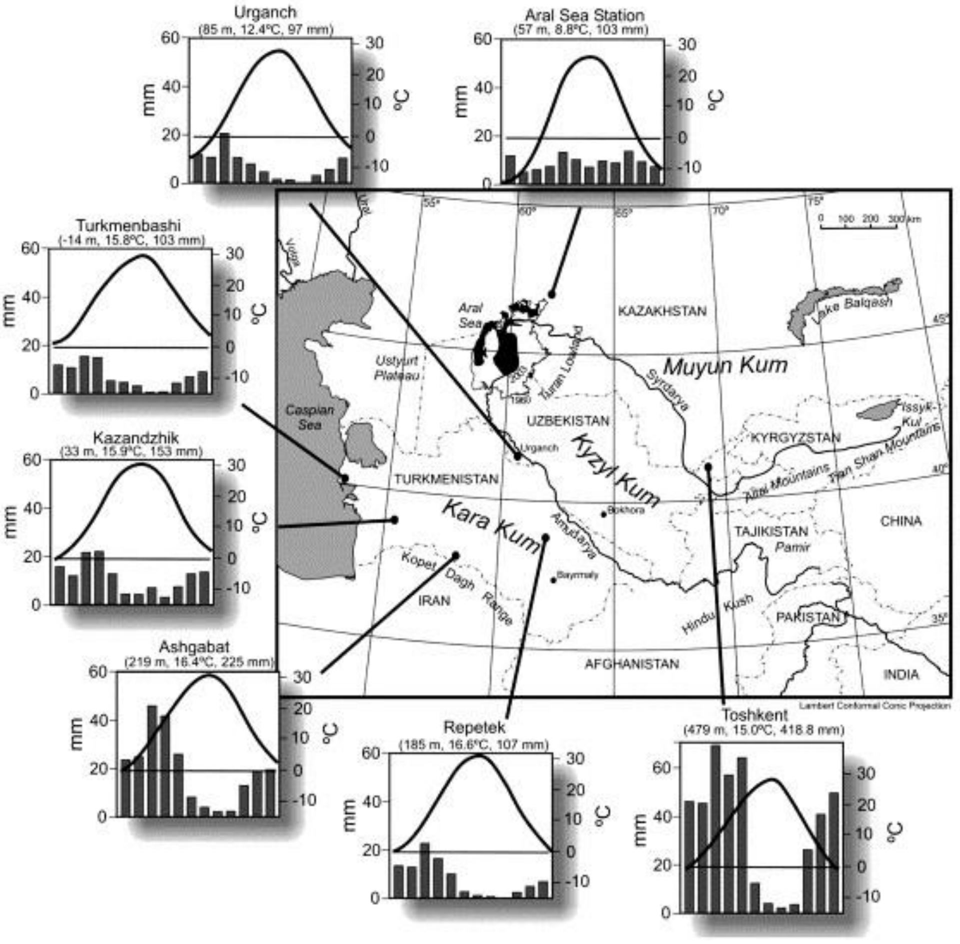

Figure 2-12. The climate of Central Asia. Adapted from Goudie, 1983; Lioubimtseva *et al.* (2005).

During the warm period, cold air invasions may occur from the northwest and north, usually under cloudless skies and accompanied by strong wind, dust storms, a temperature drop of 4 to 6°, and increased humidity. In periods of strong winds, dust storms appear in lowland Turkmenistan, especially in spring and summer. The annual number of days with dust storms ranges from 30 to 40 days in the Central Karakum and in the Southeast Karakum. Dust storms are rare in the southern mountains and oases of Karakum (Fet *et al.*, 1994).

In a comprehensive study of dust storms in Turkmenistan by Orlovsky *et al.* (2005), 60 years of weather records from 56 meteorological stations were analysed to obtain the spatial distribution, frequency, seasonality and diurnal variation of the dust storms. The highest mean annual frequency of dust storms was observed in the spring season. Central Karakum desert experienced a maximum average of 67 dust storm days in spring, while the maximum number of dust storm days was registered at 146 days in western Turkmenistan. An analysis of diurnal variation in dust storms revealed that dust storms over Turkmenistan occur in most cases during daylight, reaching their peak at 11:00–12:00 hrs in the plains, and around 15:00 hrs in the piedmont areas.

2.4.2. Kyzylkum Desert

The Kyzylkum desert, 15th largest desert in the world, lies between two major rivers in this region Amudarya and Syrdarya. It covers an area of about 298,000 km^2, spreading across northern Uzbekistan and up into neighbouring Kazakhstan. The Kyzylkum (meaning "Red Sand" in Turkic), occupies roughly two-thirds of Uzbekistan and borders the Karakum in the south (Figure 2-12). Except for the pre-Aral lowland, the Kyzylkum is characterised by higher elevations and more complex landscape than the Karakum. Monadnocks, with elevations over 500 meters, can be found toward its centre (Lewis, 2003).

Kyzylkum like Karakum has a continental climate. However, winters are colder with a mean January temperature ranging between -3°C and -9°C. The mean July temperature ranges from 22°C to 25°C and the annual precipitation from 155 mm to 270 mm (Figure 2-12). Precipitation in this region is mainly associated with the predominant westerlies and reaches its maximum in spring–summer as the influence of the Siberian high decreases and convective activity becomes stronger (Lioubimtseva *et al.*, 2005). Since the humid season in Kyzylkum lasts typically from November to March, the dust sources are less active in those months. The surface experiences rapid evaporation of precipitation due to rise of temperatures and high wind speeds in the spring, which leads to development of dust events. In the summer and autumn seasons, desiccation of the sandy and clay-rich surface sediments, together with very strong winds, favour the occurrence of dust storms in the Kyzylkum (Indoitu *et al.*, 2012).

Indoitu *et al.* (2012) studied the spatial distribution of dust storms over Central Asia based on statistical analysis of meteorological observations from 400 meteorological stations for the period of 1936 to 2000. Their analysis showed that dust storm occurrence in this region generally decreased during the last century. However, since 1980 a tendency for an increase in dust storm activities has been registered in stations located in Kyzylkum. Groll *et al.* (2013) have also investigated the dust deposition in Central Asian deserts using data from meteorological stations. The highest maximum deposition intensity between all stations in their study was observed in the corresponding source area of the Kyzylkum, with 9,616 g m^2 in September 2009.

2.4.3. Aral Kum

The Aral Sea was a closed lake lying between Kazakhstan in the north and Uzbekistan in the south. The Amudarya in the south and the Syrdarya in the east provided 87% of the Aral inflow, with the rest coming from precipitation and groundwater discharges (Figure 2-13). Formerly the 4th largest lakes in the world with an area of 68,000 km^2, the Aral Sea has been steadily shrinking since the

1960s after the incoming rivers were diverted for irrigation projects (Micklin, 2007). As a result of development of extensive cotton plantations, and abstraction of water from the Amudarya and Syrdarya Rivers for irrigation, the inflow into the Aral Sea was significantly decreased, resulting in loss of almost 74.3% of the surface area of the lake and 90% of the lake water volume. (Ginoux *et al.*, 2012; Indoitu *et al.*, 2012; Groll *et al.*, 2013). The Southern part of the Aral Sea is now the Aral Kum desert. Figure 2-14 shows stages of the formation of the Aral Kum between 1960 and 2008.

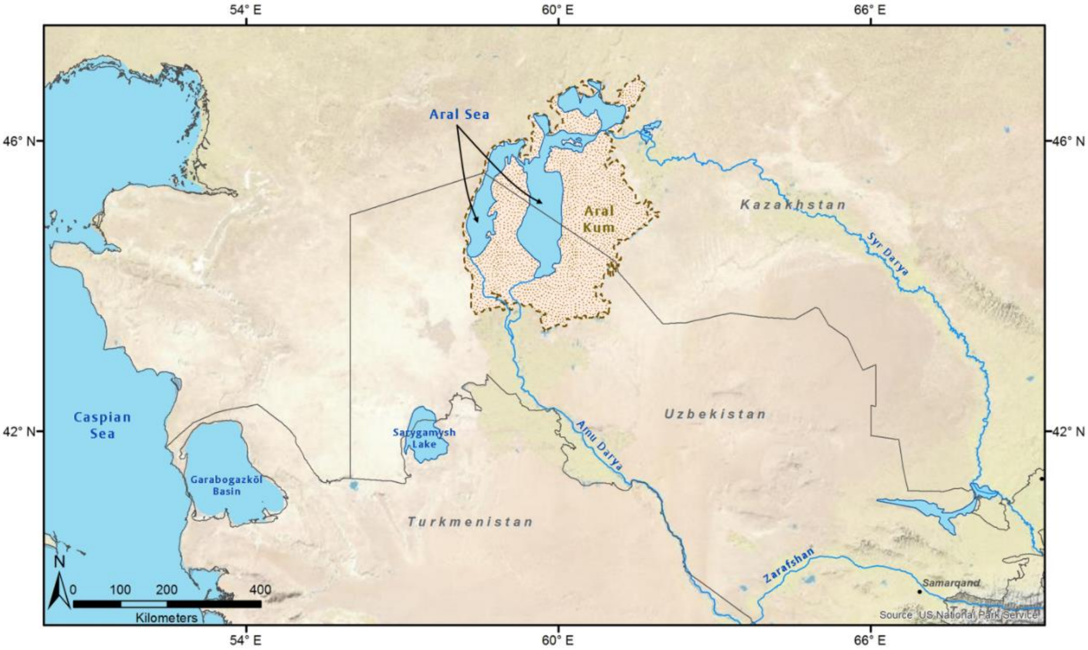

Figure 2-13. Geographical location of the Kyzylkum desert in Central Asia

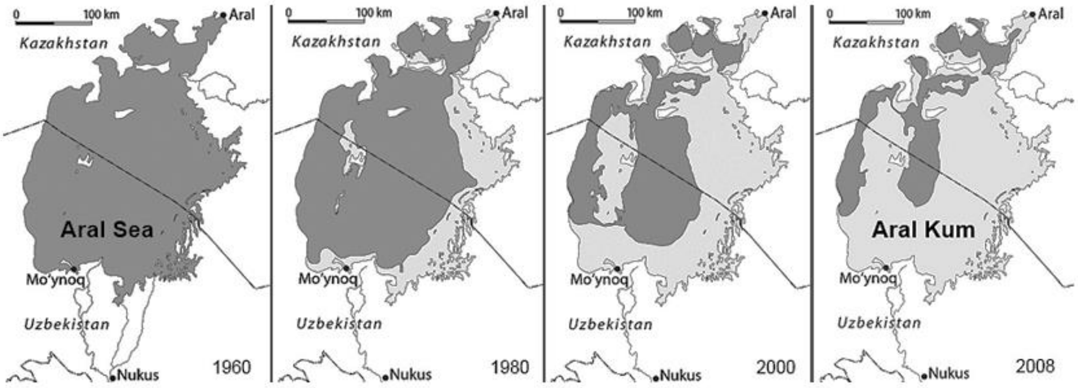

Figure 2-14. Formation of the Aral Kum (1960–2008) – The dark grey shows water surface and light grey shows dry area. From Groll *et al.* (2013).

Groll *et al.* (2013) carried out dust monitoring at 21 meteorological stations in the Aral Sea basin. The Kyzylkum, Karakum, and Aral Kum were identified as the main sources for aeolian dust in the western part of Central Asia. They concluded that transportation of aeolian dust from Aral Kum occurs mainly towards the south. The highest average monthly deposition rate was registered in Uzbekistan

(56.2 g m^{-2}), while the percentage of months with a very intense (and potentially harmful) dust deposition flux was highest in Turkmenistan (36.4%). The highest average dust deposition was registered in June, and a secondary maximum occurred in February. A slight increase in frequency of dust storms and dust deposition was registered between 2003 and 2010 with a strong inter-annual variability.

While most of hotspots of high dust storm activity showed decreasing trend of dust emissions, the new Aral Kum Desert became very active in the last two decades of the 20th Century (Indoitu *et al.*, 2012). Observations suggest that dust from the Aral Kum is deposited relatively close to the source areas; within about 120–140 km from the Aral Kum, dry dust deposition has been reported to be 96% lower than at the former seashore, thus the dust from the Aral Kum affects an area of no more than 200 km around the former seashore (Groll *et al.*, 2013). However, there are still dust entrainments in synoptic scale depressions over this region which are yet to be studied.

2.4.4. Taklamakan Desert

The Taklamakan Desert is located in the Tarim Basin, surrounded by the Pamir Mountains in the west, Tibetan Plateau in south and the Tian Shan Mountains in the north. The Taklamakan extends for about 1400 km from west to east and for about 550 km from north to south with a very limited number of meteorological stations located at the edge of the desert (Uno *et al.*, 2005). This desert of unstable sand dunes occupies about 323,750 km^2 in the Tarim Basin, western China. Aridity of this continental desert is largely caused by its sheer distance from the sea. Additional cause of its aridity is that Tarim Basin lies in the rain shadow of the high mountain ranges that bound the desert on three sides (see Figure 2-15). The Taklamakan rainfall is predominantly in the summer months with about 30% from local convective showers. Some parts of the desert receive only 10 mm of rainfall a year, and nowhere gets more than 38 mm, which indicates an extremely arid climate (Warner, 2004).

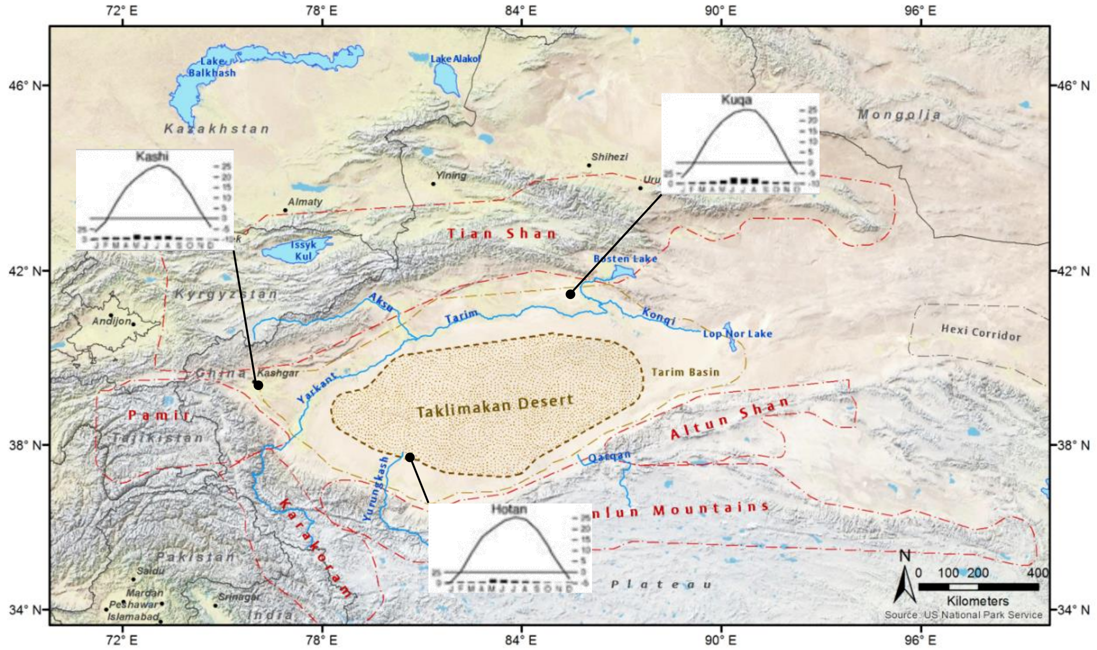

Figure 2-15. Geographical location of the Taklamakan desert in China and its climograph.

The complex winds of the region have created a great diversity of sand bedforms, including longitudinal, transverse and star dunes (Harris, 2003). Crescent shaped dunes are mostly formed on the eastern side of the desert and on the western side they are transverse and longitudinal. The dunes in general are 250 m to 500 m wide and can reach 30 to 150 min high, though some pyramidal shaped star dunes, reaching 200-300 m high, can also be found (Mares, 1999).

The Tarim Basin is characterised by a very high frequency of dust events (Aoki *et al.*, 2005; Shao *et al.*, 2011). In the Taklamakan, dust uplift occurs mainly in late spring (53% of annual dust storms) with a secondary maximum (35% of annual dust storms) in summer (Wang *et al.*, 2004). Dust from the Taklamakan as well as from the Gobi Desert is mainly transported toward the southeast and then the northeast, following the Mongolian cyclones and the East Asian trough (Shao *et al.*, 2011). The large-scale dust storms in the Taklamakan Desert are strongly affected by topographical characteristics of the surrounding areas and source elevation significantly affects dust transport as shown by Kai *et al.* (2008). The predominant elevation of the Tarim Basin is about 1000 m a.s.l. but it is surrounded by mountains rising more than 3000 meters. Dust from the Taklamakan can be uplifted by convection and basin-scale mountain-valley circulation to 8–10 km altitude and transported by the westerly flow in the upper atmosphere around the Earth (Uno *et al.*, 2009; Shao *et al.*, 2011).

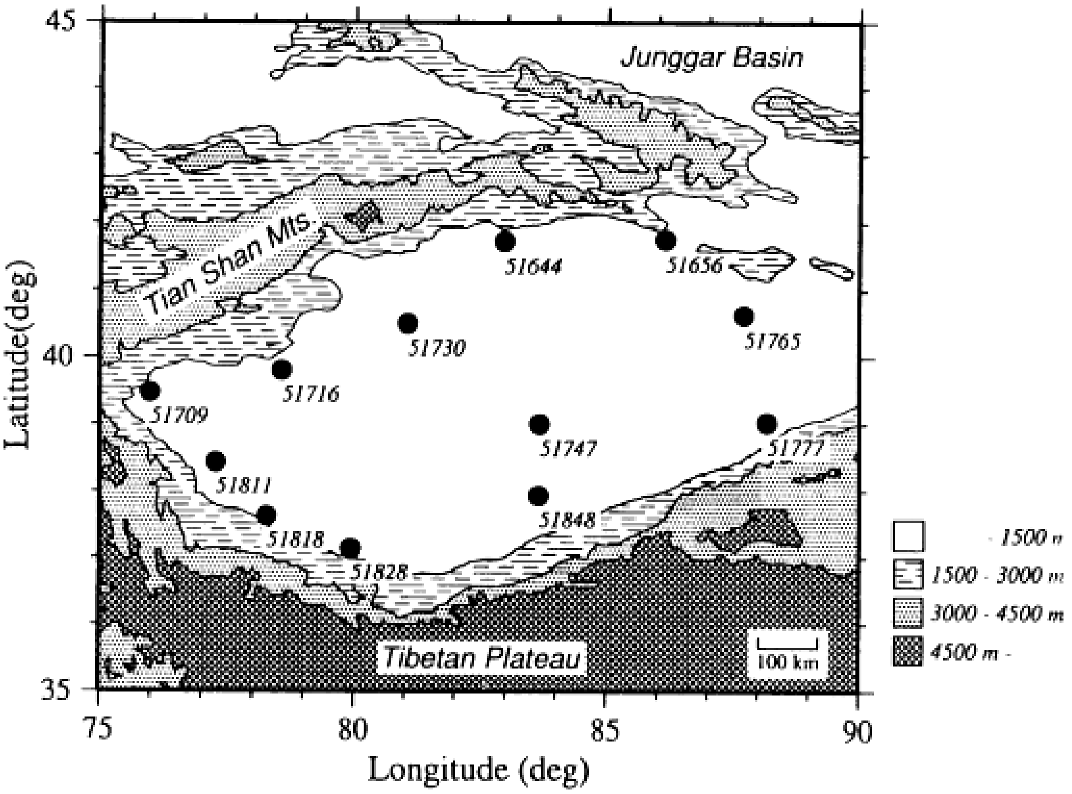

Figure 2-16. Topographic map showing locations of the ADEC stations (Yasunori *et al.*, 2002).

Yasunori *et al.* (2002) set up a network observation of the Taklamakan dust including dust emission, transport and deposition, during the "Aeolian Dust Experiment impact on Climate (ADEC)" project in 2000 (Figure 2-16). An extended version of RAMS/CFORS regional meteorology and dust emission/transport model has been applied over Taklamakan using data from these stations by Uno *et al.* (2005). Model calculation was conducted over the period of April 2001 to compare the typical springtime meteorology with that associated with dust episodes in the Taklamakan Desert. The period of April 2001 was selected because five dust storms were reported from this region.

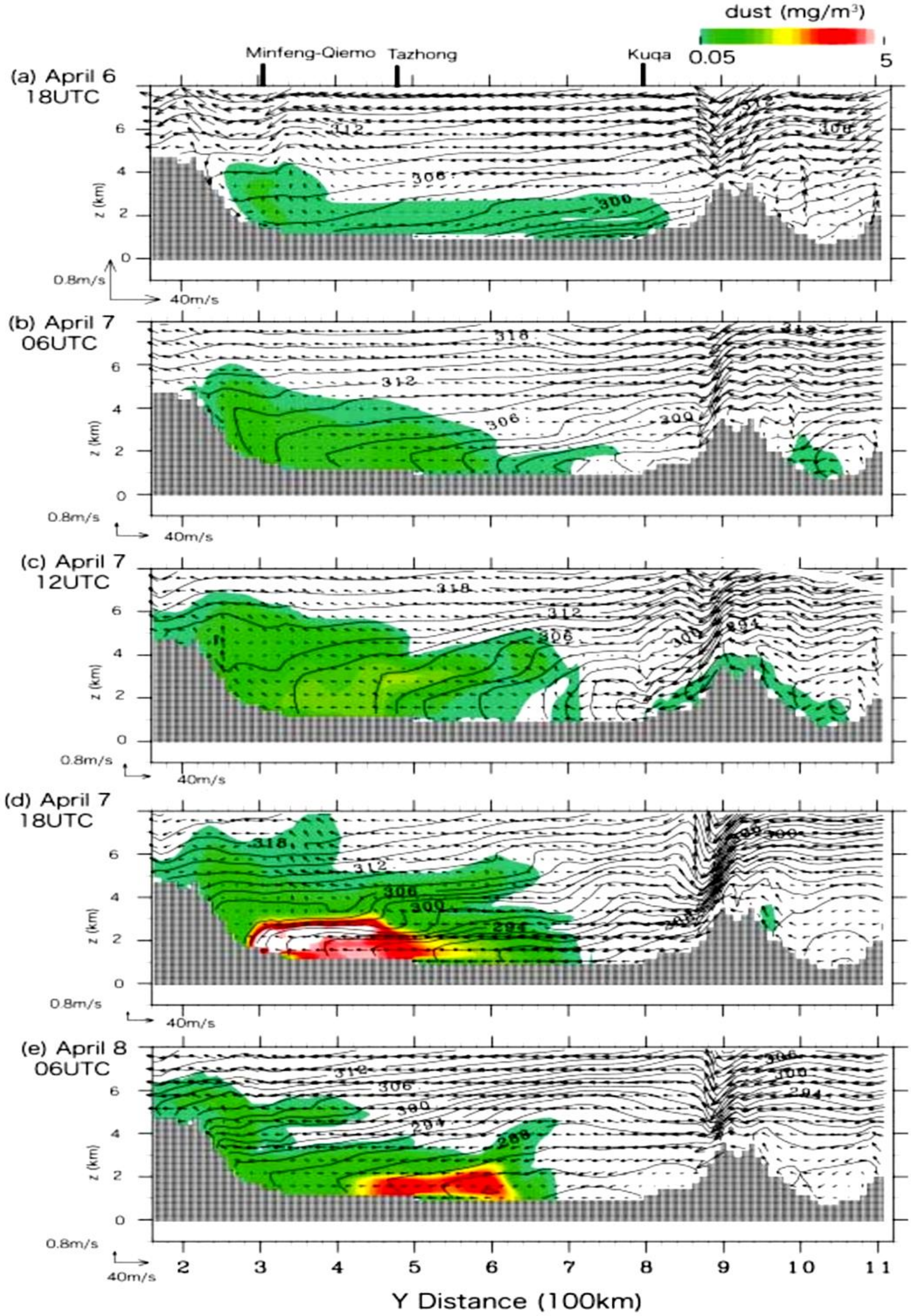

Figure 2-17. Vertical Y cross section along south-north on the Julian days 96 to 98. It shows the wind vectors (v and w), potential temperature (K: contour) and dust concentration (tone). The vertical velocity is scaled as shown in wind scale (Uno *et al.*, 2005).

Their model results reproduced complicated airflows within the Tarim Basin, strong downslope winds from the Tian Shan Mountains when meteorological disturbances cross over the Taklamakan (Figure 2-17), and a strong easterly flow from the Hexi Corridor side. Figure 2-18-a shows that the easterly flow is frequently simulated over the eastern part of the Taklamakan.

(a) suface wind (easterly case) and dust concentration

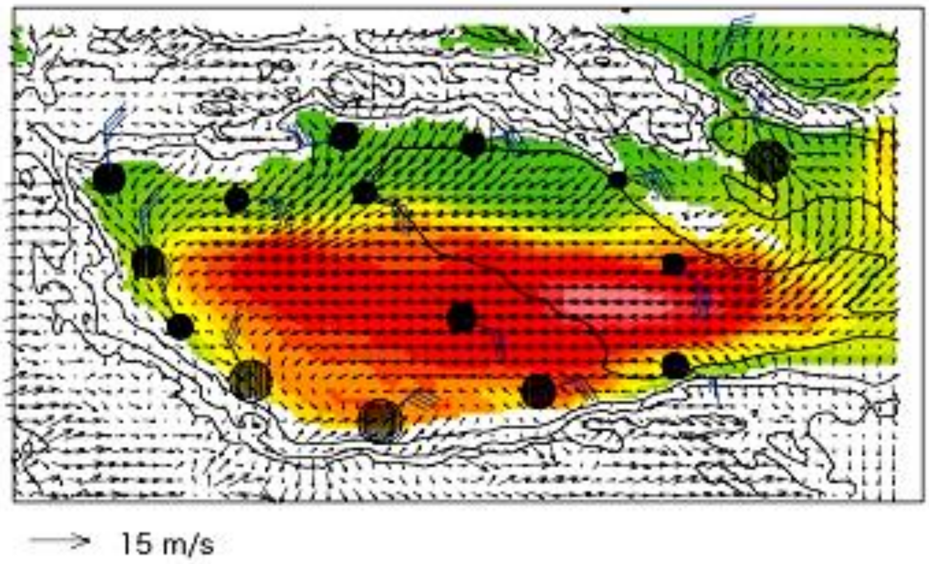

(b) wind, dust and potential temperature at z=3000m

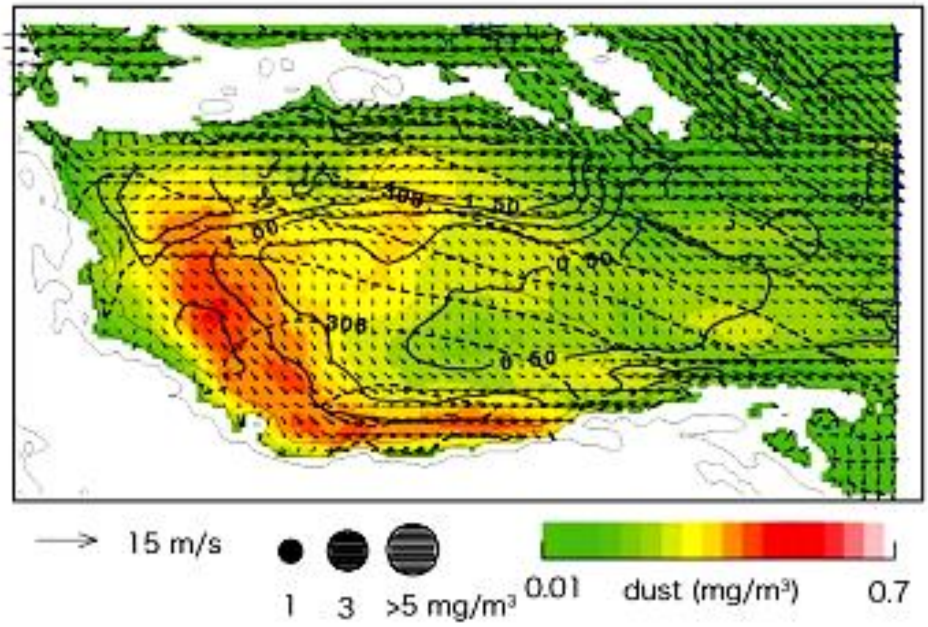

Figure 2-18. Result of composite analysis of the easterly wind case. (a) and (b) show the horizontal wind flow and dust concentration at the surface and z = 3000 m, respectively.

Atmospheric stratification is stronger (more stable) in the northern and eastern parts of the Tarim Basin (i.e., colder areas) and weakly stable in the southern and western parts of the Basin (warmer areas). Dust concentration ratio at the height of 3000 meters indicates that the relatively shallow dust layer from the eastern side of the Taklamakan Desert is transported to the south and western parts (Figure 2-18-b). During this transport process, the dust layer becomes thicker and tends to produce a uniform concentration profile. Such a vertical dust structure is important for penetration of boundary layer dust into the free atmosphere and for its long-range eastward transport to Korea and Japan.

2.4.5. Gurbantunggut Desert

The Gurbantunggut desert occupies a large part of the Junggar Basin in northern Xinjiang, in the northwest of China. This region is bounded by the Tian Shan to the south, the Altai Mountains to the northeast and the Tarbagatai Mountains to the northwest (Figure 2-19). The southern Junggar Basin is one of the important source regions of dust events in China (Wang *et al.*, 2004). Gurbantunggut covers an area of approximately 50,000 km^2, elevated around 300 to 600 meters a.s.l. Weather patterns and dust generation in this region are controlled mainly by westerly air currents. For example, a sand-dust storm event of 18 April 1998, which was captured on SeWiFS satellite images, showed that the dust originated from this desert, passed across the Pacific ocean and reached the west coast of North America (Qian *et al.*, 2007).

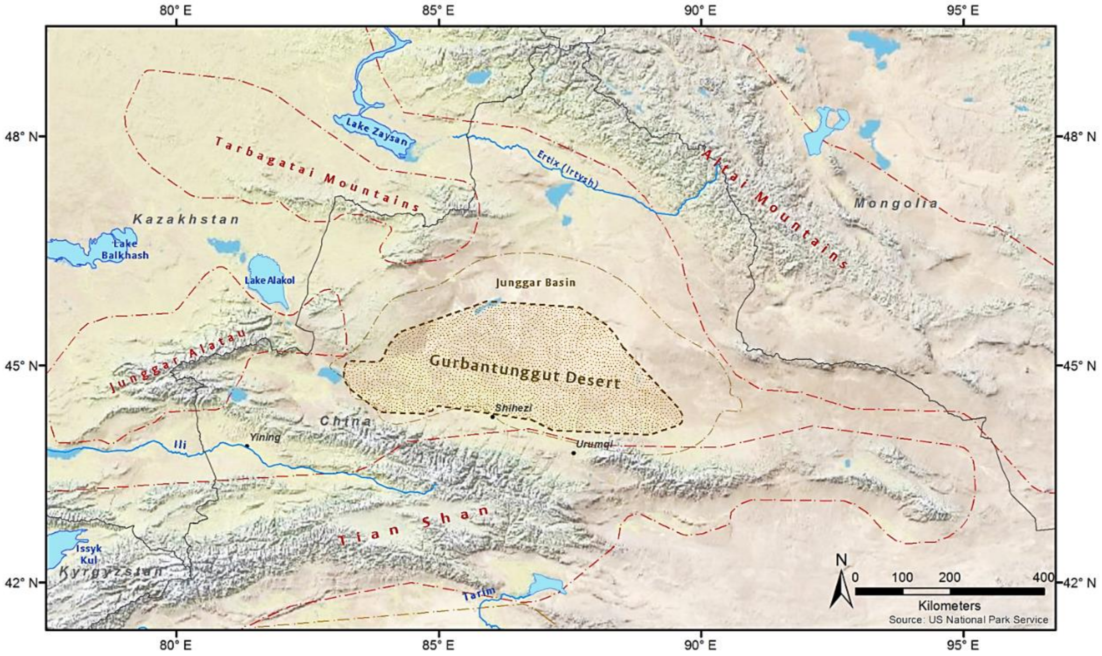

Source: US National Park Service

Figure 2-19. Geographical location of the Gurbantunggut desert in China.

The Gurbantunggut Desert is located in the centre of the semi-closed Junggar Basin with high evaporation (2000–2800 mm a^{-1}) and low annual precipitation of 80 to 160 mm a^{-1}. The runoff is almost non-existent and underground water resources are very deep. In the southern part of the desert, the average number of days with gales exceeds 15 days per year, and dust events occur on 19 days per year (Qian *et al.*, 2007). The general near-surface wind in the Junggar Basin is north-westerly. Dust transported from the Gurbantunggut is deposited on the mountain foothills of northern and eastern Tian Shan (Takeuchi *et al.*, 2008). Loess and loess-like sediments are widely distributed on the northern foothills of east Tian Shan at altitudes of 500 m to 2400 m. Wu *et al.* (2010) showed that among the potential sources, Junggar loess shows much more similar composition characteristics to dust deposited on Urumqi Glacier No. 1, in the eastern Tian Shan, than do the local moraines, suggesting that the primary source of dust for east Tian Shan is dust transported from the Junggar Basin. In their study five main trajectory clusters were identified. The cluster-mean trajectories are shown with their frequencies for air masses at both 100 m and 1000 m above the ground level (Figure 2-20). The modal size of loess particles deposited on the eastern Tian Shan slopes was about 20–40 µm at an altitude of 600 m a.s.l., but this decreases to 5–15 µm when the altitude increases to 2060 m a.s.l.

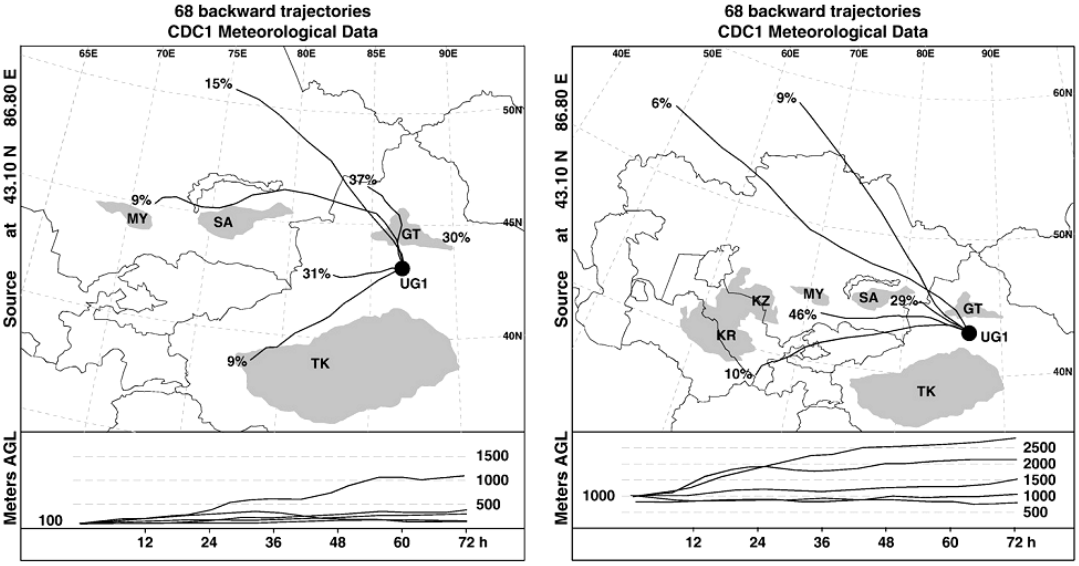

Figure 2-20. Clustering results of HYSPLIT back-trajectories (backward for 72 h) at 100 m (at the left) and 1000 m (at the right) AGL heights for the total 68 fresh snow samples at UG1, ETS. Percentage (%) indicates the frequency for each main air mass trajectory clusters. The shaded areas indicate the deserts, including Taklamakan (TK), Gurbantunggut (GT), Saryyesik Atyrau (SA), Muyun Kum (MY), Kyzylkum (KZ), and Karakum (KR).

2.4.6. Balkhash Depression

The lowlands of the southern Lake Balkhash basin in southeast Kazakhstan contain a number of sandy drylands which cover an area of about 170,000 km^2. The Balkhash Depression (also called Balkhash-Alakol depression) is bounded by Tian Shan Mountains in the south and Junggar Alatau in the east and is bordered by Balkhash Lake to the north (Figure 2-21). The Saryesik Atyrau Desert, located between the Ili and Karatal rivers, is the largest among the deserts in the Balkhash depression. In some literature the name Saryesik is applied for the entire southern area of Lake Balkhash, from Moiynkum desert on the west bank if Ili River to Zhalkum desert on the east bank of Karatal River. Strips of barchans and cellular dunes can be found close to the lake. Sand dunes are oriented in a north-westerly direction and attain a height of around 5 to 10 m (Yedilbayev *et al.*, 2012).

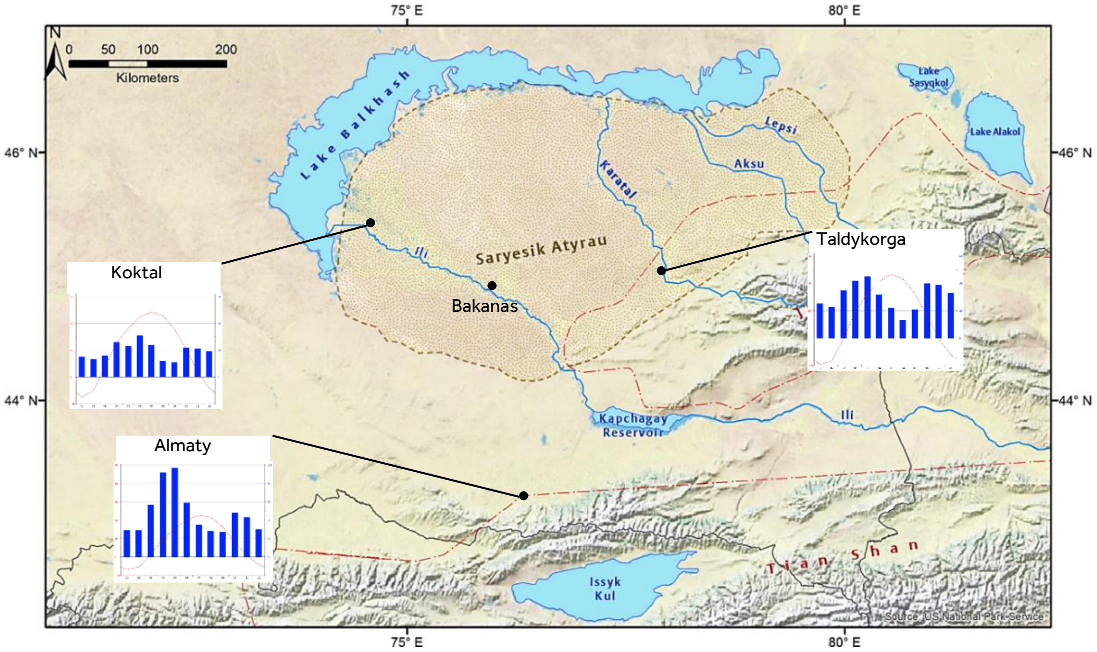

Figure 2-21. Geographical location of the Balkhash depression in Kazakhstan.

The Balkhash depression has a dry continental climate characterized by large daily and annual variations of air temperature, and high levels of solar radiation. Annual precipitation is less than 150 to 200 mm a^{-1} and relative humidity is of about 60%. Average air temperature in January is −16 ℃ in the northern part and −5 ℃ in the southern part of the depression. Mean air temperature is about 20-25 °C in July. The dry climate, along with high summer temperatures and strong winds in Balkhash region, result in a high evaporation rate of 950 mm in cold years and up to 1200 mm in dry years (Issanova *et al.*, 2014).

After the creation of the Kapshagai water reservoir in the 1970s and increasing use of water from the Ili, Karatal, and Lepsi rivers for land development projects and extension of irrigated agriculture, the area of Lake Balkhash reduced to 4,700 km^2 (Issanova *et al.*, 2014). As a result, soil salinization and degradation is a frequent phenomenon around Balkhash Lake. Reduction and regulation of the Ili and Karatal river flow led to desiccation of several lakes, including salty lakes in deltas of these rivers, making them favourable environments for dust emissions.

Dust storms are common in the southern Balkhash basin, which has with sparse vegetation cover and availability of fine grained material on the surface. The long term observations of dust storms in the region were analysed by Issanova *et al.* (2014) using data from four meteorological stations between 1971 and 2010. The most frequent dust storms were observed at the Bakanas weather station located in the western part of the Saryesik Atyrau desert. The number of days with recorded dust events in this station has been decreasing, from more than 90 days a^{-1} in 1974 to about 10 day a^{-1} in 1998. This changed to an increasing trend after 1998, with up to 60 dusty days a^{-1} in 2008. Data from seven meteorological stations observed over the period of 1966-1986 was analysed to determine prevailing dust transport direction, demonstrating that dust transport occurs mainly to the east, south-east and north-east directions. Study of dust sources and their emission rates using MODIS Deep Blue AOD revealed that Balkhash-Alakol depression in eastern Kazakhstan is a significant source of anthropogenic dust (Ginoux *et al.*, 2012), with more than 50% dust occurrence in the eastern part of Lake Balkhash and nearby dry lakes. Atmospheric dust originating from this region is of great importance for reduction of glacier ice surface albedo, as dust from these sources may reach the Tian Shan Mountains which is in a close vicinity of this region.

2.5. Conclusion

In this chapter, a general overview of the main identified dust emission sources surrounding the Tian Shan Mountain system in Central Asia has been presented. The major characteristics of Central Asian deserts and their climate were reviewed. Although the most prominent, well-known deserts have been covered in this chapter, there are still several other dust emission sources, like Ustyurt Plateau and Atrek delta in east coasts of Caspian Sea, Qaidim Pendi in China and Betpaqdala desert in Kazakhstan, which need further investigation. While some research has been carried out on dust source mapping in parts of this region, no single study exists which provide a detailed map of dust sources over the entire region. Previous studies showed that dust emission in this region displays a clear seasonal variation, with highest activities in early spring to late summer (Orlovsky *et al.*, 2005; Indoitu *et al.*, 2012). However, few investigations have studied the transport route of mineral dust originating from these deserts. This indicates a need to understand the climatological aspects of dust entrainment in these arid lowlands.

Apart from global studies like Ginoux *et al.* (2012) and Prospero *et al.* (2002), there is a general lack of research about remote sensing of dust sources in Central Asia. In addition, no research has thoroughly studied the dust in this region by using a combination of satellite remote sensing techniques and climatological analysis over a long period. The evidence from previous studies suggest that a combined procedure for dust source detection using MODIS Deep Blue AOD and high resolution MODIS DEP would be an effective way to study the main dust sources in arid regions of Central Asia. M-DB products (~10 km resolution) enable us to estimate dust emissions over bright surfaces in a quantitative way and detect the regions with most frequency of dust occurrence, while MODIS DEP (1 km resolution) can be used to detect the origin of individual dust plumes.

The initial assessment indicated the great potential of MODIS Deep Blue AOD for studying dust seasonality in this region. AOD can be taken as a proxy for the real process of dust emission (i.e. the uplift of dust from the surface). MODIS Deep Blue AOD retrieval over bright deserts enables production of a detailed inventory of dust erodible surfaces, along with the seasonality of their activity. The spatial resolution of MODIS Level 2 atmosphere products (approximately 10 km for MOD04), is appropriate for comprehensive investigation of seasonal variation of dust activity in Central Asia as well as determining the regions with highest frequency of dust emission. After determining the spatial distribution of dust sources and the seasonal activity, sub-basin scale distribution of dust sources can be investigated using high resolution dust enhancement products obtained from MODIS Level 1 imagery. Taking advantage of the atmospheric reanalysis data and historical archives of high resolution satellite imagery, a thorough investigation of land surface characteristics and synoptic controls of dust emission can be performed.

Chapter 3. Data and Methodology

3.1. Introduction

Observations of dust events in Central Asia have been performed by several researchers using *in-situ* and remote sensing observations (Indoitu *et al.*, 2012; Groll *et al.*, 2013; Xi *et al.*, 2015a). In the previous chapter, a broad selection of publications on dust observation techniques was reviewed, and the advantages and shortcomings of each method discussed. A summary of the most frequently used remote sensing datasets for study of mineral dust and their characteristics and availability is given in Table 2-2. As discussed in the previous chapter, as each type of remote sensing data and analytical methods have their own limitations, a combination of different remote sensing products provides a more robust approach to studying dust emission mechanisms and detecting dust sources. Considering the availability of remote sensing products, and the large spatial extent of dust sources in Central Asia, MODIS products were selected as the primary remote sensing dataset in this project. The main advantages of using MODIS products can be summarised as follows:

(i) Freely available
(ii) Relatively good spatial and temporal resolution
(iii) Continuous availability of data
(iv) Diversity of archived standard products

There are two satellites which carry the MODIS instrument: Terra and Aqua. Both satellites are in sun-synchronous, near-polar circular orbits and cross the Equator at approximately 10:30 A.M. and 1:30 P.M. local time respectively. The MODIS instrument is equipped with a rotating scan mirror that enables the instrument to collect science data in a series of time-ordered scans (Figure 3-1). The MODIS orbit is divided into 5 minutes chunks called 'granules', which cover an area of approximately 2030 km along the path by 2330 km along swath.

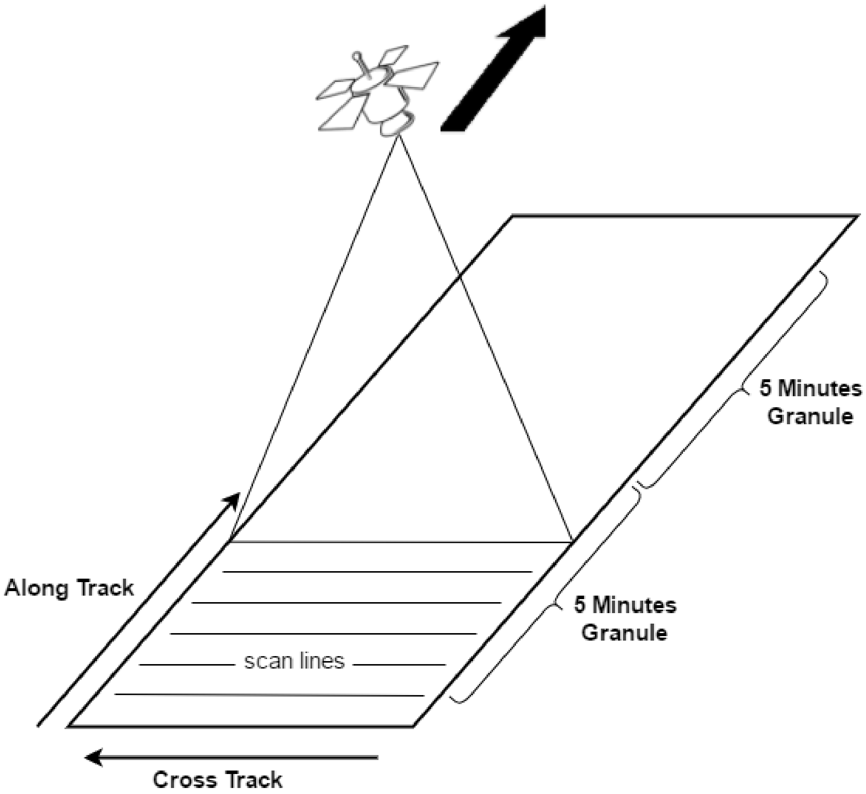

Figure 3-1. Schematic of a MODIS Observation Swath (Toller *et al.*, 2003)

MODIS products are freely available in several processing levels. Figure 3-3 shows the processing architecture for MODIS atmosphere products, their processing levels and naming convention. Daily MODIS atmosphere product are processed at the NASA Goddard Space Flight Centre which provides access to MODIS Level 1, 2 and 3 products, through NASA's Level 1 and Atmosphere Archive and Distribution System (LAADS) website. These products can be accessed either via LAADS web interface (http://ladsweb.nascom.nasa.gov/) or directly from LAADS ftp repository (ftp://ladsweb.nascom.nasa.gov/).

In this study, two types of MODIS products were employed in order to explore the spatial and temporal distribution of dust sources in Central Asia, 1) MODIS L2 aerosol product (MOD04) at the spatial resolution of 0.1° (~10 km), and 2) MODIS L1B calibrated radiance (MOD02) at the spatial resolution of 0.01° (~1 km). The first dataset is used for identification of dust hotspots within the main deserts in Central Asia, and the second dataset is used for generating daily MODIS DEP images in order to pinpoint the dust point sources at the sub-basin scale. The geographical extent of the study area covered by each set of MODIS product is shown in Figure 3-2. In the following sections, a detailed description of each dataset and the methodology for their use in dust source mapping is provided.

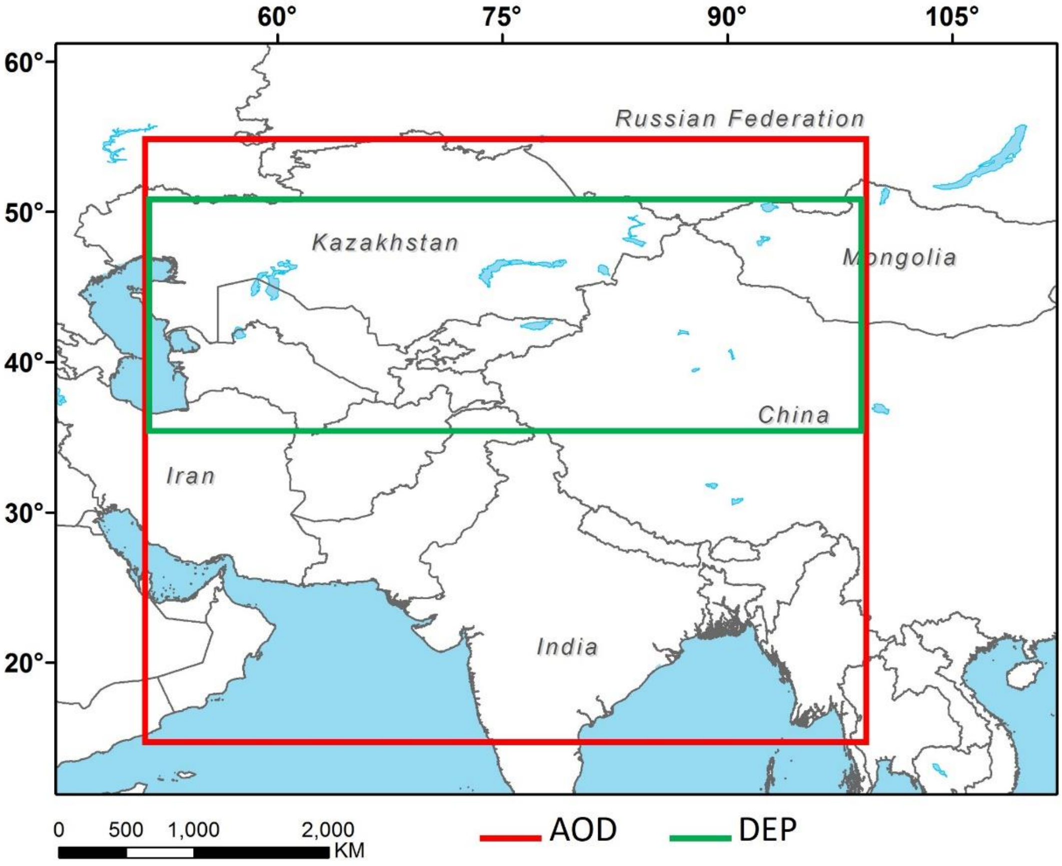

Figure 3-2. Geographical extent of the study area, investigated using MODIS AOD (red) and MODIS DEP products (green).

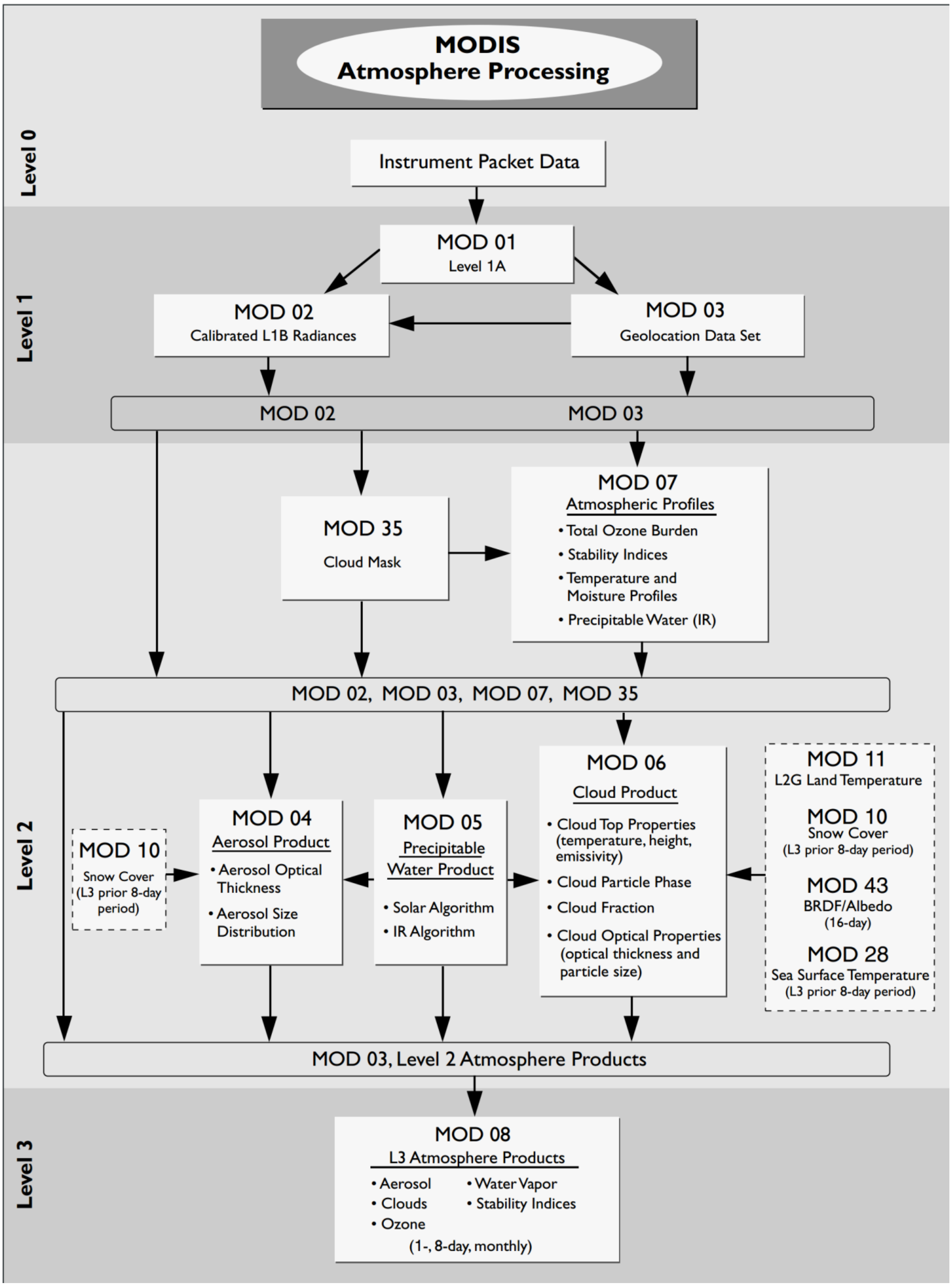

Figure 3-3. MODIS Atmosphere Data Processing Architecture and Products (adapted from Parkinson *et al.*, 2000)

3.2. Aeorosol Optical Depth

Measurement of AOD is a well-established approach to estimate the dust load in atmosphere, which has been used in numerous studies using ground based and remote sensing observations (e.g. Holben *et al.*, 2001; Prospero *et al.*, 2002; Semenov *et al.*, 2005; Peyridieu *et al.*, 2010; Ginoux *et al.*, 2012). AOD and the Angstrom exponent (α), which describes the spectral dependence of AOD over a given wavelength range, are amongst the most commonly retrieved parameters from optical satellite images. For MODIS data, three main AOD retrieval algorithms are developed as part of NASA's MODIS Atmospheres product suite. Over land, these are known as Dark Target (DT) and Deep Blue (DB). The DT algorithm Levy *et al.*, 2010) was developed to retrieve AOD over dense, dark vegetation, while the DB algorithm (Hsu *et al.*, 2004) was originally developed to fill in the gaps in DT dataset by providing coverage over brighter surfaces (such as deserts). A third algorithm (Tanré *et al.*, 1997; Levy *et al.*, 2013) is basically a DT approach to retrieve AOD over water surfaces.

DB retrieval of AOD was first introduced in MODIS collection 5.1 (C5), and its algorithm has been constantly under improvement since then. The DB algorithm enables detection of aerosol properties over brightly reflecting surfaces by employing radiances from the blue channels of MODIS instruments, where surface reflectance is low enough to make AOD retrievals possible (Hsu *et al.*, 2006). In the MODIS C5 collection, static surface databases were used to constrain the DB algorithm to retrieve aerosols over regions with no seasonal vegetation changes. Retrievals were also only performed over bright-reflecting surfaces, leading to insufficient information content for retrievals over regions with mixed vegetated and non-vegetated surfaces (Hsu *et al.*, 2004). Therefore, in order to optimize estimates of surface reflectance and also to expand coverage to all cloud-free and snow-free land surfaces, an extensive effort was made to develop the second generation of the DB algorithm, called Enhanced Deep Blue (eDB), which adopts a hybrid approach to retrieve AOD over more complex surfaces (Hsu *et al.*, 2013).

For the purpose of this research, MODIS eDB AOD, introduced in MODIS Collection 6 (C6), was used for the first time to investigate the dust emission sources in Central Asia. To keep consistency between the observed AODs, only data obtained by the Aqua satellite between January 2003 and December 2014 was used.

3.2.1. Data Access and Pre-Processings

All MODIS L1B and L2 atmospheric products are compressed in the Hierarchical Data Format (HDF; http://www.hdfgroup.org/hdfeos.html), with each variable stored as a Scientific Data Set (SDS). Each granule contains a series of SDSs which hold the product data, along with SDSs holding the geolocation and calibration information. A list of MODIS C6 eDB SDS names and their descriptions is presented in Table 3-1.

Table 3-1. List of SDS Names for MODIS Collection 6 Deep Blue Aerosol Products

SDS Name	Description
Deep_Blue_Angstrom_Exponent_Land	Angstrom Exponent Over Land
Deep_Blue_Aerosol_Optical_Depth_550_ Land	Aerosol Optical Depth at 550 nm Over Land
Deep_Blue_Aerosol_Optical_Depth_550_Land_Best_Estimate	Aerosol Optical Depth at 550 nm Over Land Filtered by Quality (QA= 2,3 only)
Deep_Blue_Aerosol_Optical_Depth_550_Land_STD	Standard Deviation of Individual Pixel-Level Aerosol Optical Depth at 550 nm per Cell
Deep_Blue_Algorithm_Flag_Land	Flag Indicating the Path Taken Through the Algorithm
Deep_Blue_Aerosol_Optical_Depth_550_Land_QA_Flag	Quality Assurance Flag for Aerosol Optical Depth at 550 nm
Deep_Blue_Aerosol_Optical_Depth_550_Land_Estimated_Uncertainty	Estimated Uncertainty in Aerosol Optical Depth at 550 nm
Deep_Blue_Cloud_Fraction_Land	Fraction of Pixels per Cell Where Retrieval was not Attempted
Deep_Blue_Number_Pixels_Used_550_Land	Number of Aerosol Property Retrievals Performed per Cell
Deep_Blue_Spectral_Aerosol_Optical_Depth_Land	Retrieved Aerosol Optical Depth Over Land at 412, 470, and 650 nm
Deep_Blue_Spectral_Single_Scattering_Albedo_Land	Single-Scattering Albedo Over Land at 412, 470, and 650 nm
Deep_Blue_Spectral_Surface_Reflectance_Land	Surface Reflectance Used in Aerosol Retrieval Over Land for 412, 470, and 650 nm
Deep_Blue_Spectral_TOA_Reflectance_Land	TOA Reflectance at 412, 470, and 650 nm

Since the study area covers a very large region, between 15-55 N and 50-100 E, more than 10 MODIS granules were needed to cover the extent of the study area for each day. This means that more than 48,000 MODIS granules, acquired during 12 years, were downloaded. When using the LAADS web interface, the product name, MODIS collection, coordinates of the study area and time period must be specified, and the interface provides the option to order the data with specific post processing. Once the order is placed, the processed data are provided via an ftp address within a few days and users can download it. There are two major problems with using the above method for downloading data for this project. First, there is a limit for number of granules that can be requested on each order. Second, once the data are processed and ready for download, all granules will be placed in an ftp address so the users have to manually download and separate granules obtained on each day and classify them for further processing. There were also complexities in reading from HDF files to raster datasets supported by GIS software packages. Conventional image processing software, e.g. ERDAS Imagine, ENVI and ArcGIS could not be used to directly read SDSs from HDF files and apply geo-referencing parameters to extracted raster datasets.

To overcome these obstacles, a specialized toolkit for downloading and post processing of MODIS atmosphere products was developed. Reading University MODIS Downloader (RUMOD) was developed in Python, to facilitate the download of MODIS products directly from LAADS ftp repository. The Python programing language was chosen because of its ease of use, clear syntax, powerful high level operations and free availability for a wide variety of operating systems. This application allows the user to download all MODIS granules needed to cover the area of interest immediately, without any limit and in a separate folder for each day (Figure 3-4). The main advantage of using RUMOD is that the user does not need to place several orders to get the full archive of the data needed. Limitations associated with number of granule per order are avoided, and the data can be accessed immediately. Also the data for each day are downloaded in separate directories, which is essential for subsequent pre-processing and making mosaics. Without such a tool, accessing the volume of data required for this sort of study would be prohibitively time-consuming.

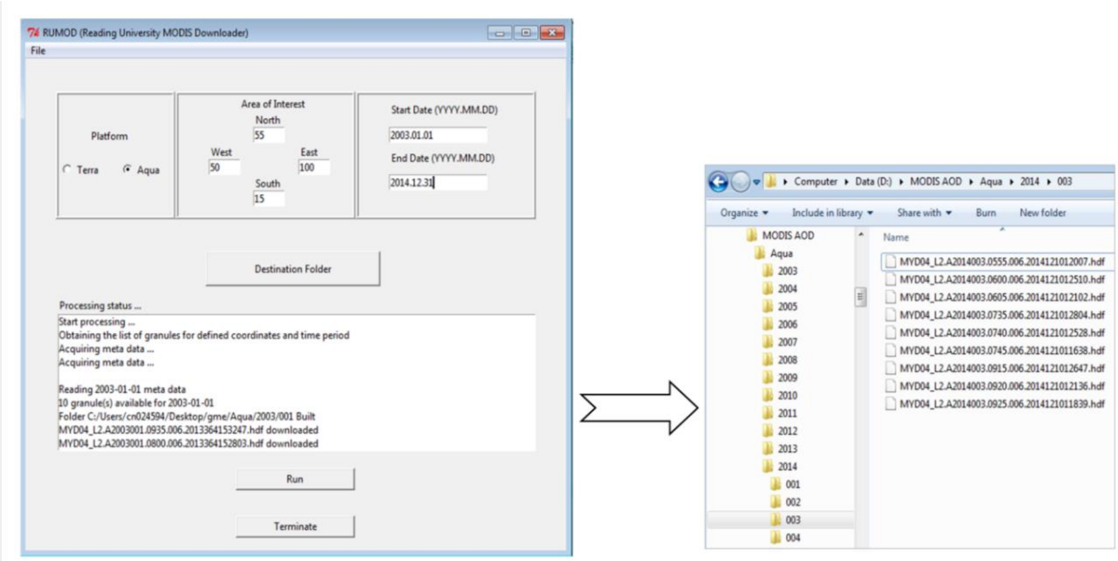

Platform ○ Terra ● Aqua

Area of Interest
North 55
West 50
East 100
South 15

Start Date (YYYY.MM.DD) 2003.01.01
End Date (YYYY.MM.DD) 2014.12.31

Processing status ...

```
Start processing ...
Obtaining the list of granules for defined coordinates and time period
Acquiring meta data ...
Acquiring meta data ...

Reading 2003-01-01 meta data
10 granule(s) available for 2003-01-01
Folder C:/Users/cn024594/Desktop/gme/Aqua/2003/001 Built
MYD04_L2.A2003001.0935.006.2013364153247.hdf downloaded
MYD04_L2.A2003001.0800.006.2013364152803.hdf downloaded
```

```
MYD04_L2.A2014003.0555.006.2014121012007.hdf
MYD04_L2.A2014003.0600.006.2014121012510.hdf
MYD04_L2.A2014003.0605.006.2014121012102.hdf
MYD04_L2.A2014003.0735.006.2014121012804.hdf
MYD04_L2.A2014003.0740.006.2014121012528.hdf
MYD04_L2.A2014003.0745.006.2014121011638.hdf
MYD04_L2.A2014003.0915.006.2014121012647.hdf
MYD04_L2.A2014003.0920.006.2014121012136.hdf
MYD04_L2.A2014003.0925.006.2014121011839.hdf
```

Figure 3-4. RUMOD interface (left) and downloaded data (right)

3.2.2. Dust Hotspot Detection

Previous field studies and remote sensing studies have pointed out that the sources of dust are not homogeneous over large areas and in fact much of the global supply of dust comes from relatively small (compared to the size of deserts) but consistently active dust producing areas, called dust hotspots (Gillette, 1999). AOD data enable the estimation of the aerosol content in the atmospheric column. The Angstrom exponent, an estimate of the aerosol size parameter for the atmosphere column, can also be achieved via spectral variations of the AOD (Hsu *et al.*, 2013). The Angstrom exponent describes the dependency of the AOD on wavelength and has been used in studies of aerosol particle size and for separation of dust from other atmospheric aerosols in satellite optical imagery (e.g. Torres *et al.*, 1998; Ginoux *et al.*, 2010) .

A schematic diagram showing the procedure for detecting dust sources using eDB AOD dataset (adapted from Ginoux *et al.*, 2012), is presented in Figure 3-5. To produce the daily raster images, a series of Python scripts were developed to extract selected SDSs from each MODIS granule, re-project them to the geographic coordinate system and finally generate daily raster mosaics covering the full study region. Three SDSs were extracted from each MOD04 granule: eDB AOD, Angstrom Exponent and Single Scattering Albedo (highlighted in Table 3-1). Extracted SDS were interpolated on a geographic grid with 0.1 ° (~10 km) spacing in latitude and longitude directions. An example of gridded mosaics is presented in Figure 3-6.

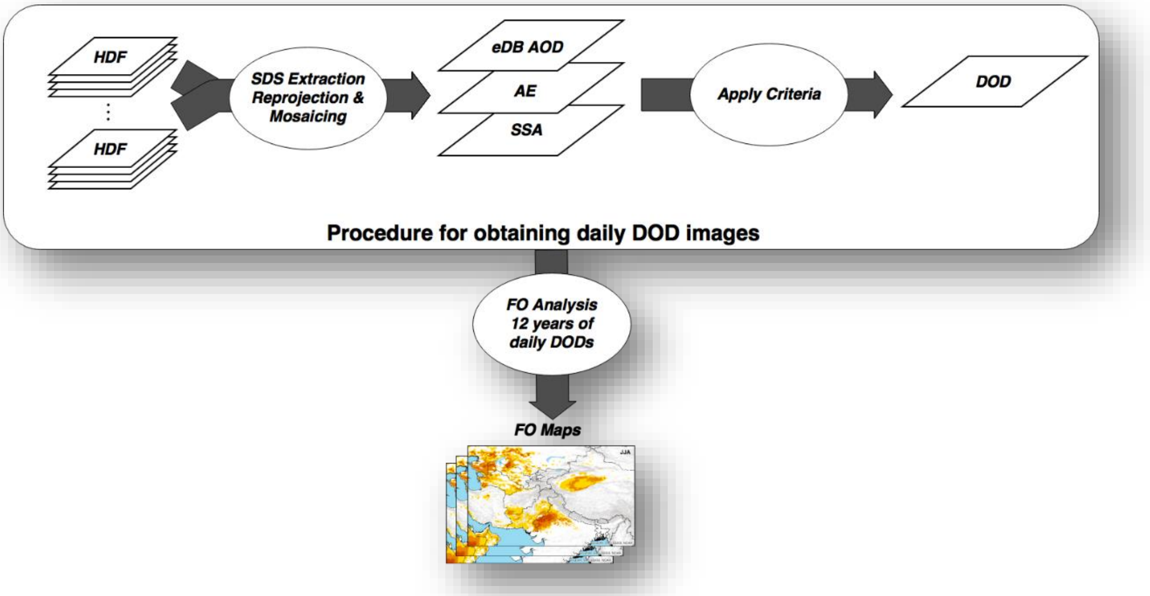

Figure 3-5. Schematic procedure for analysis of eDB AOD dataset.

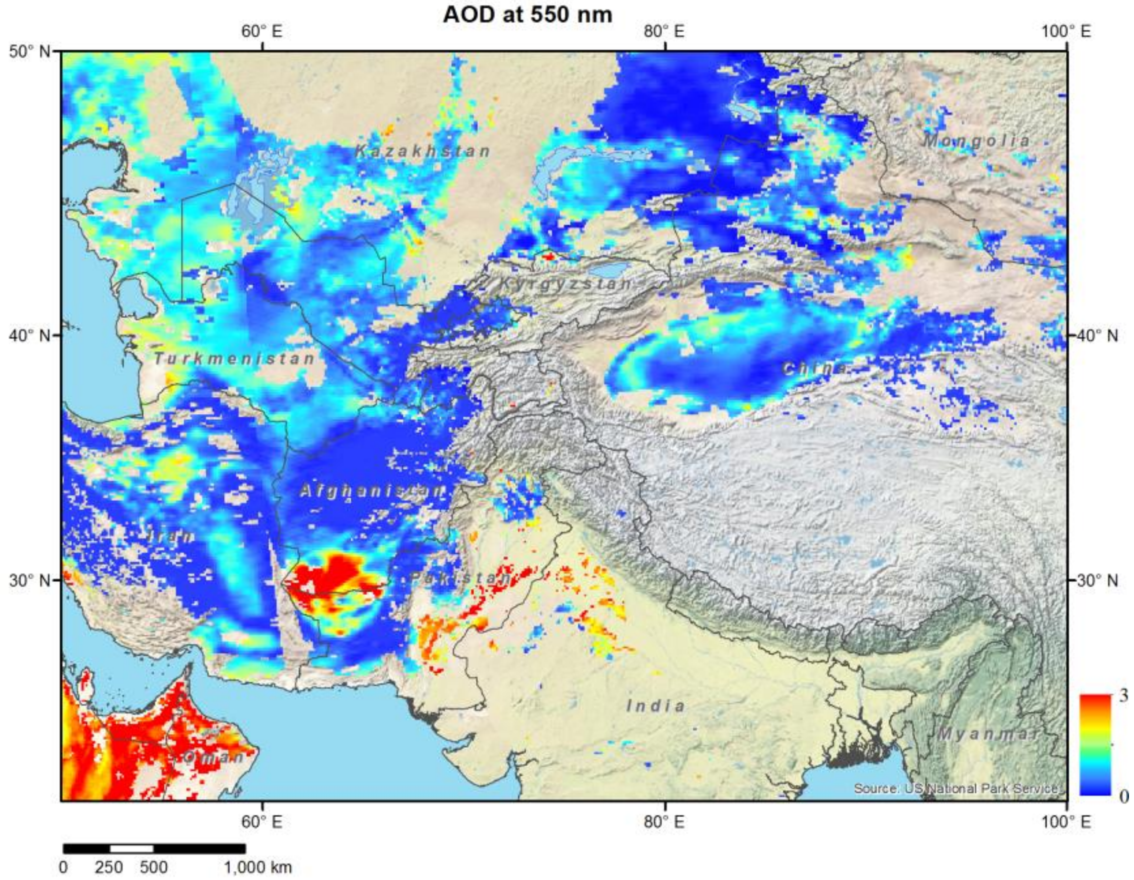

Figure 3-6. Daily Deep Blue AOD at 550 nm on 18 Aug 2009. Areas with missing data because of presence of clouds or low surface reflectivity are filtered out.

In the next step, criteria on size distribution and optical properties of dust were applied to derive dust optical depth (DOD) from eDB AOD. Daily DOD raster datasets were obtained by imposing these three criteria on eDB AOD values:

(i) Angstrom exponent less than 0.5 ($\alpha < 0.5$)
(ii) SSA at 412 nm ($\omega 412$) less than 0.95
(iii) Increasing single scattering albedo with wavelength ($\omega 650 - \omega 412 > 0$)

The first criteria of the screening method is to restrict the AOD observations to larger aerosol particles ($\alpha < 0.5$). Deposition of large dust particles is controlled by gravitational settling; therefore, they are more likely to be very close to the source (Knippertz, 2014). However, this criteria could also be satisfied in coastal regions where concentrations of sea salt coarse particles are high. To filter out sea salt particles, the second criteria was applied based on the fact that the SSA of sea salt are higher than mineral dust (~ 1). The third criteria is grounded on another specific property of mineral dust, which is a positive difference of SSA between 412 and 650 nm. To summarise, mineral dust is always more absorbent at 412 nm than at 650 nm.

After constructing a database of daily DOD raster datasets, the frequency of occurrence (FO) of DOD greater than a threshold optical depth was calculated, and its seasonal and yearly distributions were investigated. In dust related studies, AOD values greater than 0.2 are generally considered as an indicator of presence of dust in the atmosphere (Ginoux *et al.*, 2010). Hence, this threshold was used to calculate FO.

3.2.3. Uncertainties

Although satellite based retrieval of AOD makes a very important contribution to research on spatiotemporal variability of aerosol loading, they suffer from uncertainties inherent in the underlying retrieval algorithms and also the assumptions that are made to model the complex nature of atmosphere and the Earth surface. To account for these uncerainties, each eDB AOD retrieval in MODIS Level-2 atmospheric products is provided with an associated quality assurance (QA) flag. QA is calculated through a series of tests on the 1×1 km resolution AOD within 10×10 km retrieval, with QA=3 indicating the retrieval of highest confidence to QA=1 for the lowest confidence. QA, which can be interpreted as a degree of confidence, is a function of several parameters. The most important parameters considered in QA calculations are cloud contamination and heterogeneity of the scene (Sayer *et al.*, 2013).

Comparison of remotely sensed AOD against Aerosol Robotic Network (AERONET) ground-based sun-photometer observations of AOD is a standard technique for validation of AOD retrievals (Sano *et al.*, 2003; Fan *et al.*, 2009; Schuster *et al.*, 2012; Sayer *et al.*, 2013; Yan *et al.*, 2015). Validation against AERONET suggested that the expected error of MODIS eDB AOD at 550 nm can be stated as $\pm(0.03 + 0.2\tau_m)$ for retrievals with the highest quality flag (QA = 3), where τ_m is the MODIS AOD (Sayer *et al.*, 2013). This is comparable to the nominal uncertainties on other well-used state-of-the-art datasets such as MODIS C5/C6 DT $(0.05 + 0.15\ \tau)$ (Levy *et al.*, 2010), or MISR (0.05 or $0.2\ \tau$) (Kahn *et al.*, 2010). It was also shown that retrievals for the pixels with QA = 2 have a slightly larger uncertainty and so should also be suitable for use in most applications. Contrary to suggestion by Baddock *et al.* (2016) of using AOD products with all QA for detection of dust hotspots, we have only used AOD retrievals with QA = 2&3 in order to minimise the effect of AOD retrieval uncertainties on our FO analysis.

3.3. Dust Enhancement Technique

While it is relatively easy to detect mineral aerosols over ocean and water surfaces in true-colour satellite optical imagery, detecting dust over the land surface, and especially desert regions, in visible channels is very difficult (Baddock *et al.*, 2009). It is mainly due to the similar reflectivity of mineral aerosol and background desert surface in the visible part of the spectrum. In addition, differentiating mineral aerosol from cloud, sea salt, and anthropogenic pollution is also a challenging obstacle in interpreting un-adjusted true-colour images. As a result, several techniques have been developed to facilitate the detection of dust over land by taking advantage of dust optical properties in infrared (IR) and thermal infrared (TIR) wavelengths.

Atmospheric dust can be detected in satellite imagery via dust enhancement techniques, using satellite radiometer measurements in visible/reflective IR (0.4-1.6 μm) (Tanré *et al.*, 1991b), near-IR wavelengths (NIR, 2-5 μm) (Lee, 1989; Wald *et al.*, 1998) or IR/TIR channels (8-12 μm) (Ackerman, 1997; Hansell *et al.*, 2007). Dust enhancement techniques based on brightness temperature difference (BTD) are among the most widely and successfully used techniques for highlighting dust plumes in the remotely sensed imagery (e.g. Ackerman, 1997; Miller, 2003; Hansell *et al.*, 2007; Schepanski *et al.*, 2007; El-ossta *et al.*, 2013). These techniques are based on temperature differences between the hot ground surface and cooler elevated dust plumes.

The ability to differentiate between cloud and dust varies between different BTD methods and different satellite data. Among several satellite optical sensors, MODIS has been extensively used in BTD studies thanks to its wide spectral range, relatively high spatial resolution and daily global coverage. Miller *et al.* (2003) introduced a BTD technique for enhancing desert dust storms in MODIS L1B top-of-atmosphere (TOA) radiance data, which showed a great performance comparing to other dust enhancement techniques developed for MODIS. In the following section a detailed description of this method will be provided, following by the procedure for mapping dust sources using these data.

3.3.1. MODIS Dust Enhancement Products

One of the main drawbacks of BTD techniques is their potential for misidentification of dust because of presence of clouds in the scene. In particular, cirrus clouds, which are cooler than the surface, can be falsely identified as dust when only information from IR/TIR channels are used. To address this issue, Miller *et al.* (2003) combined conventional BTD method with colour information from visible bands to improve visual detection of dust outbreaks over water and land. Unlike traditional BTD binary results (dust/non-dust mask) (e.g. Ackerman, 1997), Millers dust enhancement product (DEP) is a colour composite image, in which the dust is enhanced as shades of pink while clouds/land appear cyan/green. This allows a more accurate interpretation of the features in the scene over regions with a complex surface reflectivity. The ability of the DEP algorithm to separate dust and clouds is especially useful for detection of dust in the higher latitudes where cloud contamination of the scene is more frequent than lower latitude dust source regions such as the Sahara and the Middle East.

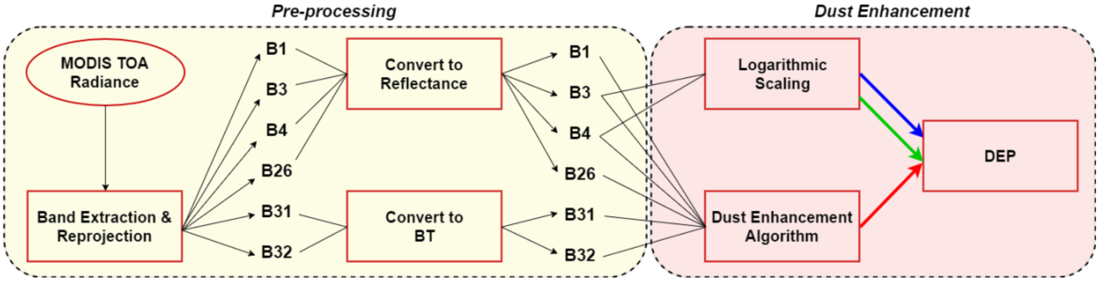

Figure 3-7. Schematic procedure for generating daily DEP images from MODIS

Figure 3-7 shows the diagram for generating daily DEP image from MODIS Aqua and Terra L1B TOA radiance data. For both Aqua and Terra satellites, on average 7 granules were needed to make a mosaic covering the study area between 35-50 North and 50-100 East. Associated MODIS geolocation products (MOD03) were also required for re-projecting the extracted SDSs (bands). We used the RUMOD toolkit (section 3.2.1) to download these granules for a time period of 10 years between 2003 and 2012.

The first step of the pre-processing of MODIS L1B data was to extract six spectral bands from each MODIS granule, from which four bands are reflective solar bands (B1,B3,B4 and B26) and two bands are emissive solar bands (B31,B32). The data for these bands are stored in MODIS native swath projection and need to be re-projected to the conventional geographic projections in order to be used in a GIS environment. The MODIS Re-projection Tool (MRT, https://lpdaac.usgs.gov/tools/modis_reprojection_tool), integrated into the RUMOD Toolkit, was used to re-project each band to the WGS84 system at a 0.01 degree (~1 km) resolution. These data were used to make a mosaic of 5000 km × 1500 km to cover the study region.

MODIS L1B TOA data for each band/pixel are recorded as scaled integer numbers. These values can then be converted to radiance or reflectance values using corresponding scale/offset parameters which are provided as attributes to each solar band. For the 4 reflective bands, reflectance values were calculated using reflectance scale/offset parameters attributed to each band. To convert emissive bands' scaled integer values to brightness temperature (BT), first radiance values were calculated using radiance scale/offset parameters. Then BT values were calculated from radiance by applying Planck's Law.

The second step in producing DEP images from MODIS L1B dataset was to apply the dust enhancement algorithm to the pre-processed bands. Miller's DEP over-land algorithm is based on the following physical hypothesis: (1) elevated dust produces lower brightness temperature against the hot land surface background, (2) dust can be discerned from clouds having the same radiometric temperature based on its coloration properties, (3) dust often produces a positive reverse BTD (12–11 μm), and (4) the additional infrared (1.38 μm) information from MODIS band 26 enables the dust signal to be separated from cirrus clouds.

Each DEP image is an RGB composite, displayed with Red, Green and Blue colour guns. Applying the dust enhancement algorithm, Blue and Green colour guns were loaded with MODIS bands 3 and 4 log-scaled reflectances. For better visualisation, the reflectance values falling within [-1.45, 0.0) are byte-scaled between [0,255]. Finally, the Red colour gun is loaded by over-land dust enhancement values (D_{lnd}), calculated in the following way:

$$D_{lnd} = L1 + L3 + L4 + (1.0 - L2) \tag{3-1}$$

where non-dimensional terms L1–L4 and the normalization bounds are as specified in Table 3-2.

Table 3-2. Terms for over-land dust enhancement

Term	Expression	Normalization Bounds
L1	$BT(32) - BT(31)$	[-2.0 , 2.0]
L2	$BT(31)$	[0.0 , 1.0]
L3	$2R(1) - R(3) - R(4) - L2$	[-1.5 , 0.25]
L4	$\begin{cases} 0 & R(26) > 0.05 \\ 1 & R(26) \leq 0.05 \end{cases}$	(n/a)

BT: Brightness Temperature (Kelvin)
R: Reflectance (W/m2.μm.sr)

A wide variety of dust case studies has been examined to experimentally determine the normalization bounds that optimize the dust contrast. The core of the equation 3-1 is based on BTD between 12–11 μm (L1). The terms L2 and L3 were introduced to exploit the dust contrasting VIS reflective properties when compared to clouds. Term L4 was included as a binary mask, obtained from imposing reflectivity criteria on a water vapour absorption band (band 26, 1.38 μm). This term is applied to filter cirrus clouds which reside at levels above most of the tropospheric vapour (Miller, 2003).

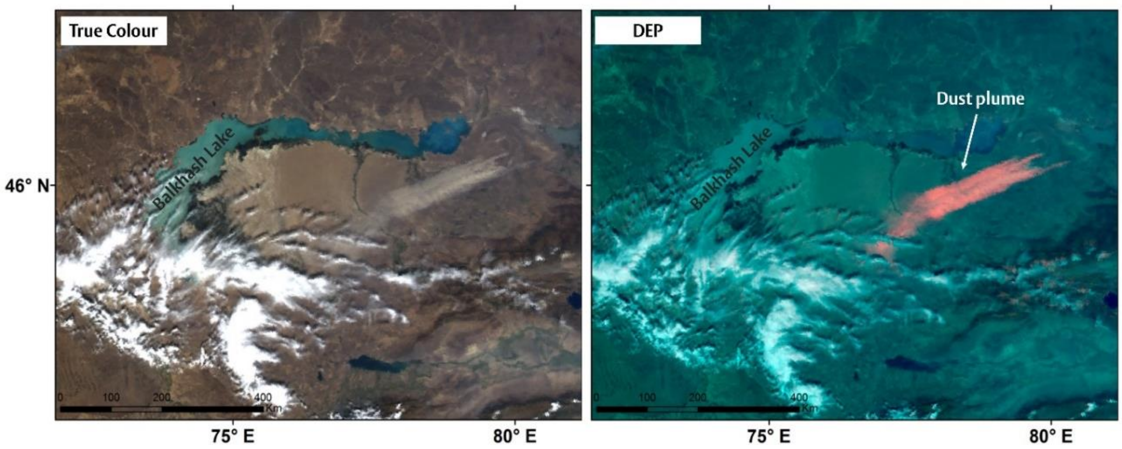

Figure 3-7. Comparison between MODIS true-colour and the DEP images for a dust event in Balkhash Basin region, 28 September 2006.

To highlight the dust plume in the scene, a dust/non-dust threshold should be selected within the range of values of D_{Ind} (between -3 and 3). While Miller (2013) suggested a threshold of 1.3, Baddock *et al.* (2009) showed that the dust/non-dust thresholds for dust enhancement techniques, including Miller's DEP, may need adjusting on a regional and/or event scale. Although there are clear guidelines for positioning thresholds, a considerable amount of informed (but subjective) judgement can be required. They suggested that the users of these techniques should consider adjusting thresholds for each event. Our investigation of dust events captured by MODIS suggested that it is essential to derive event-specific thresholds in order to highlight the boundaries of dust plume in DEP images.

An example of a DEP image is presented in Figure 3-7, comparing the visual appearance of dust in MODIS true-colour and in the DEP. It shows the exceptional ability of the DEP algorithm to separate the dust and cloud over a complex terrain. The dust plume, highlighted as pink in DEP images, can be clearly distinguished from other features of the scene, hence can be used to determine the location of dust point sources which contributed to dust plume formation, assuming the plume has not moved far from the source.

3.3.2. Point Source Detection

To identify and locate the dust producing areas within arid and semiarid regions of Central Asia, 10 years of daily DEP images were visually inspected. Two DEP images were produced for each day from Terra and Aqua overpasses at around 10:30 and 13.30 local time respectively. The approximately 3 hours time difference between the two satellite overpass enabled the investigation of the development of individual dust plumes between the two snapshots and establishing of the location of point sources at the upwind edge of each dust plume.

Along with the visual inspection of dust plumes in DEP images which leads to identification of dust point sources, several auxiliary datasets were utilized in order to cross correlate and verify these observations and record the point sources with a high degree of confidence. These supplementary information consisted of:

I) AOD
II) Wind speed and direction
III) Digital Elevation Model (DEM)
IV) High-resolution satellite optical imagery

For the first item, we have used our MODIS eDB AOD observations (see previous chapter) to confirm the presence of dust in the atmosphere and generate the map of dust hotspots. Although AOD products at ~10 km spatial resolution do not necessarily depict the location of dust point sources, they can be used to narrow down the search for dust sources in a vast region (Figure 3-8 B). Information about the surface wind was obtained from ERA-Interim reanalysis dataset (Dee *et al.*, 2011). 10m wind components, with a temporal resolution of 6 hours, were used to produce the wind fields over the study region. To reconstruct the wind field at the time of satellite overpass as closely as possible, data from two 6 hourly time step (6:00 UTC and 12:00 UTC) were temporally interpolated to 8:00 UTC (Figure 3-8 E). Furthermore, GTOPO30 global digital elevation model was used to investigate the topography of the dust source area (Data available from the U.S. Geological Survey). Using this dataset, shaded relief maps were produced at the spatial resolution of ~1km to highlight the topographic features at the scene (Figure 3-8 F). To investigate the surface features at a very high resolution, the World Imagery basemap (www.esri.com), a collection of high-resolution satellite optical imagery at resolutions of a few meters to sub-meter from Worldview GeoEye, Landsat, SPOT and IKONOS satellites, was used. This collection was accessed through ArcGIS® Version 10.1 (Figure 3-9). Annual composites of Landsat 5 and Landsat 7 ETM+ were also obtained from Google Earth Engine Catalog (https://earthengine.google.com/).

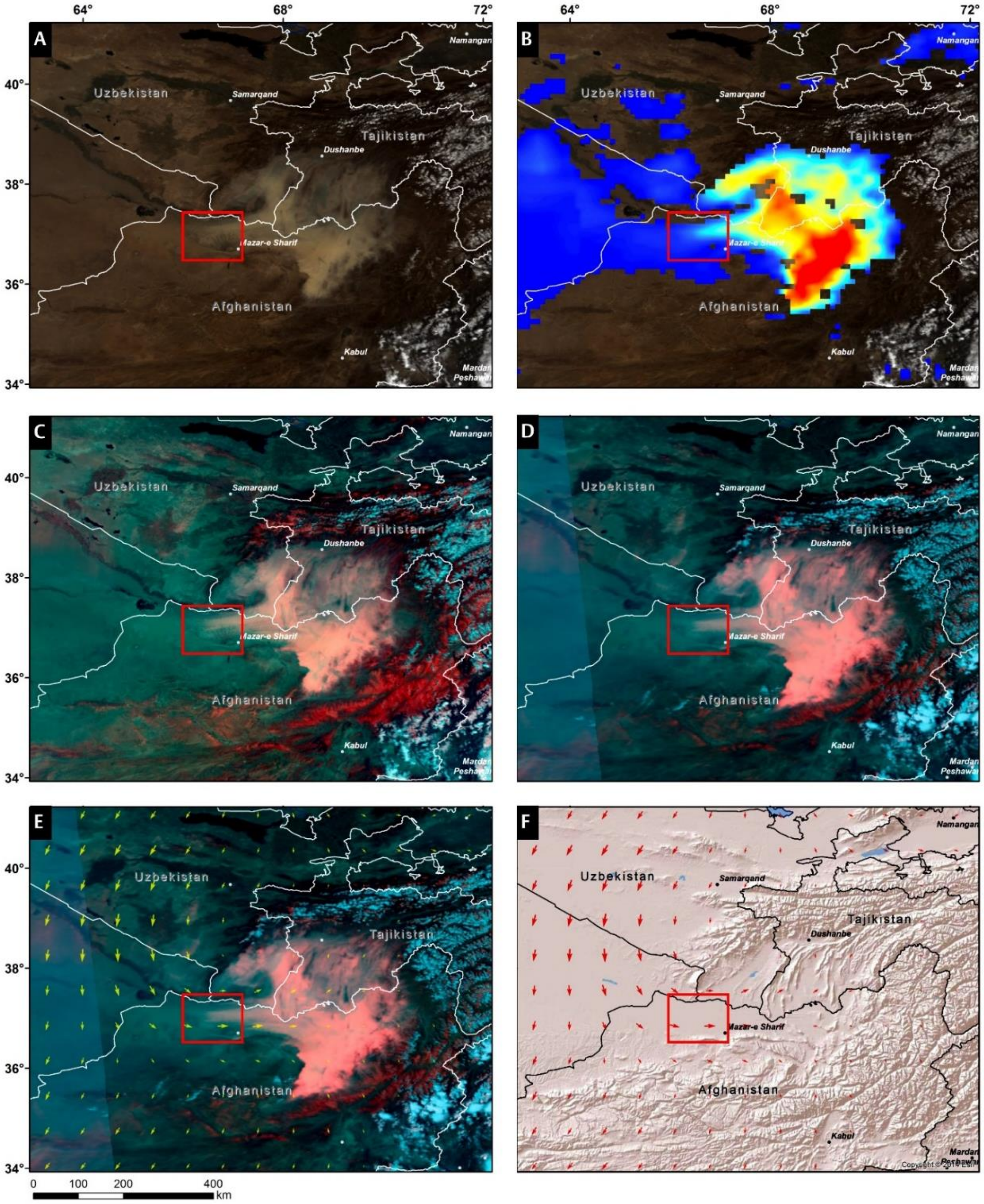

Figure 3-8. A dust outbreak in Northern Afghanistan on 10 August 2008, as it appeared in (A) MODIS Terra true colour image, (B) MODIS eDB AOD, (C) MODIS Terra DEP, and (D) MODIS Aqua DEP. An example of DEP superimposed by ERA-Interim 10m surface wind vectors is shown in (E), and (F) shows the shaded relief obtained from GTOPO30 dataset.

Apart from the auxiliary datasets mentioned above, several historical maps of Central Asia were used, along with previous studies on geomorphology and hydrological conditions of the region. We designed a GIS workspace for simultaneous visualisation of all auxiliary datasets together with DEP images, which enabled the operator to detect the dust plumes relatively quickly and make a decision about the location of point sources that contribute to the dust plumes. A spatial geo-database in a GIS environment was created to be used for recording geographical coordinates of the dust point sources (DPS) as well as meteorological information (wind speed/direction) at the time of observation.

Figure 3-9. Zoomed in subsets over the source of dust plume shown in Figure 3.8, obtained from GeoEye sub-meter resolution images. Images from Esri (www.esri.com).

In the procedure of recording DPS into the database a quality flag (QFlag) was assigned to each DPS, indicating the quality of the observation based on the operator's judgement. The highest quality of observation was indicated by QFlag = 1 and lowest degree of accuracy was indicated by QFlag =3. Different parameters were considered for assigning QFlag to each observation, including the detectability of DPS in both DEP images taken on the same day (from Aqua and Terra), the spectral contrast between dust plume and the background surface, agreement between wind direction/speed and dust plume orientation, etc.

Figure 3-10 and Figure 3-11 show examples of two dust events in which the contributing DPS were detected with varying QFlags. In the first figure which shows a dust event on 3rd August 2008 in the Betpak-Dala desert in Kazakhstan, dust plumes are clearly discernible in the morning overpass image (left) and their dispersion follows the low pressure wind pattern. All DPS are detectable in the afternoon overpass image (right) and hence given a QFlag of 1. However, there is one DPS in the latter which was not active in the morning image but distinctly showing an activated DPS, and hence given a QFlag of 3. Figure 3-11 shows another scenario, where the presence of cloud and overlaying dust plumes in the Aralkum makes it difficult for operator to pinpoint the DPS confidently. Therefore a QFlag of 3 was recorded for the DPS contributing to this dust event.

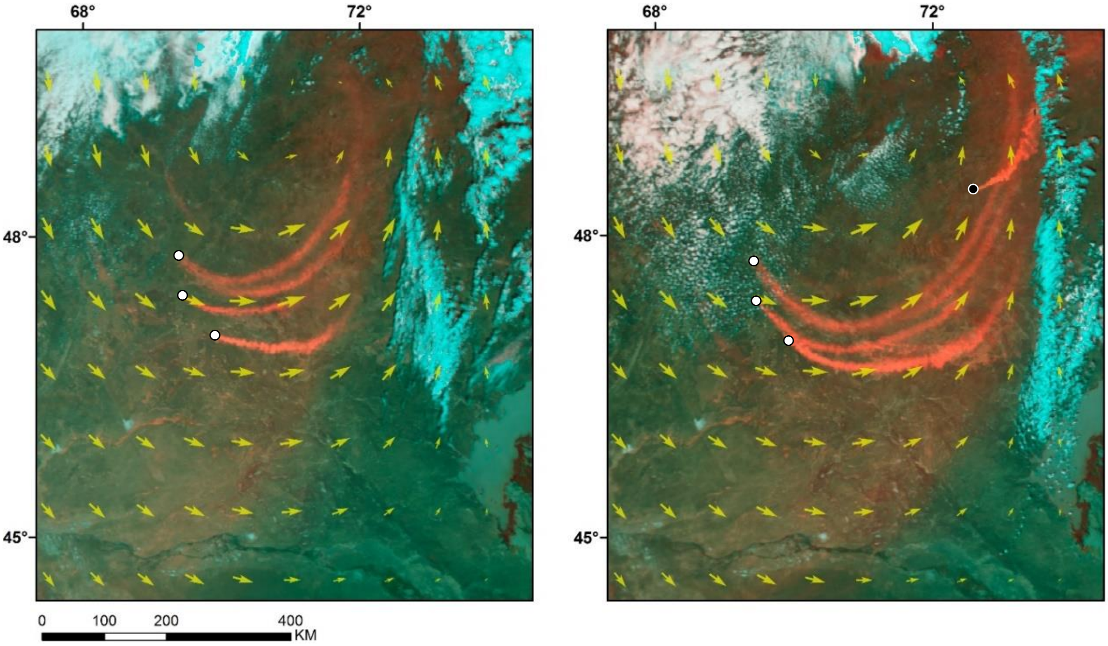

Figure 3-10. DEP images of a dust event in the Betpak-Dala desert on 3rd August 2008, acquired by MODIS Terra (left) and Aqua (right) overpasses. White and black circles represent DPS with QFlag 1 & 3 , respectively. Yellow arrows are wind vector field obtained from ERA-Interim reanalysis dataset.

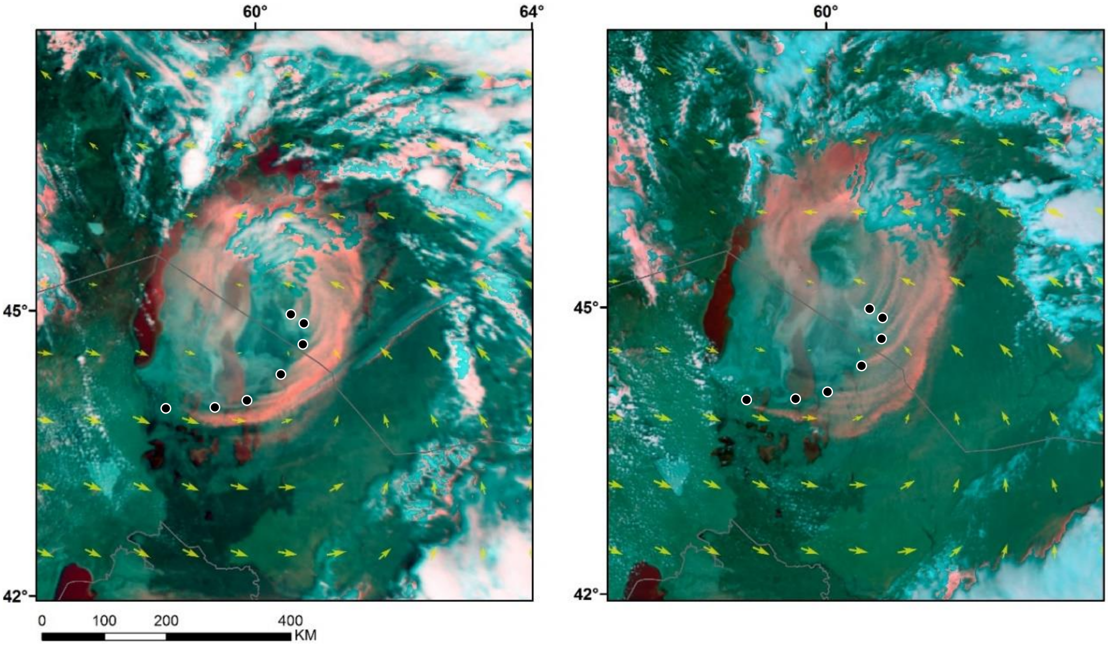

Figure 3-11. DEP images of a dust event in the Aralkum desert on 25 May 2010, acquired by MODIS Terra (left) and Aqua (right) overpasses. Black circles represent DPS with QFlag 3. Yellow arrows are wind vector field obtained from ERA-Interim reanalysis dataset.

3.3.3. Uncertainties

While the DEP method provides a valuable tool to pinpoint dust sources, it is not without its own limitations and caveats. There are several types of uncertainties associated with the datasets and the methodology used for mapping of dust point sources; these can generally be categorised as (A) uncertainties arising from data and methodology, and (B) operator error.

One of the limitations of applying BTD based algorithms, including DEP, for dust enhancement over land is that cold terrain may result in a false enhancement of dust. This limitation is more prominent in wintertime observations, especially over mountain ranges, and in early morning observations (Walker *et al.*, 2009). Another major limitation of using MODIS data has been the coarse temporal resolution of observations. Having two images per day, it is not possible to capture the dust outbreak with any confidence if the onset of dust emission is after satellite overpass and the emission does not last long enough to be captured in the following day's observation.

A key issue for the effectiveness of DEP is that changing of threshold has major implications for where the distal/margin portions of the dust plume are. The upwind edge is of course most sensitive for point source determination. In our investigation of over 36500 daily DEP images we could not define a universal dust/non-dust threshold as it had to be manually tuned for each region and individual cases. The other problem is the fact that only the upwind dust point sources can be precisely located and any additional contributing sources lying under the dust plume could not be detected. Also using these methods, it is still not possible to detect dust beneath clouds (Miller, 2003). Also since the dust point sources are detected manually by visual investigation of DEP images, the operator's error can be introduced into the process of selecting point sources through misidentification of dust plumes or inaccuracy in recording the coordinates.

Chapter 4. Dust hotspot detection using MODIS AOD

4.1. Introduction

In this brief chapter, the results of dust hotspot detection using MODIS eDB AOD products are presented. We first present the FO maps obtained through the procedure outlined in section 3.2.2. These maps provide important information about spatial and seasonal distribution of dust hotspots in Central Asia. Having a detailed map of spatiotemporal variability of dust hotspot is crucial for characterising dust sources and meteorological control of dust emission. It also serves as a guide for our investigations at higher resolution by helping to focus on active hotspots which require further investigation using DEP images. We explore the intra-annual variability of dust loading over detected hotspots to identify the potential trends in dust emission and the magnitudes of dust loadings over the 12-year time period. The chapter concludes by a short summary of our findings.

4.2. Frequency of Occurrence (FO)

As mentioned in the previous chapter, we have used 12 years of daily MODIS eDB AOD products obtained by the Aqua satellite in order to identify the dust hotspots in our study region. We retrieved more than 48,000 MODIS granules directly from LAADS ftp repository using RUMOD toolkit and produced daily raster mosaics for the full extent of study region at the spatial resolution of 0.1°×0.1°. We then generated DOD raster mosaics by applying the screening criteria (Figure 3-5) to the extracted data.

FO analysis was performed for each season during the time period of January 2003 to December 2014. For each season FO at each grid cell is calculated as the number of DOD days greater than 0.2 (threshold for background AOD) to the total number of AOD retrievals for that season during the 12 years, hence:

$$FO(i,j) = \frac{Number\ of\ DOD{>}0.2\ occurances\ at\ grid(i,j)}{Total\ number\ of\ AOD\ retrievals\ at\ grid(i,j)} \qquad (4\text{-}1)$$

To avoid miscalculation over regions with scarce AOD retrievals due to complex background reflectivity (e.g. Tian Shan Mountain), FO calculations for grid cells with less than 100 AOD observations during the whole time period (i.e. less than 10% retrieval) were discarded. This threshold was obtained empirically.

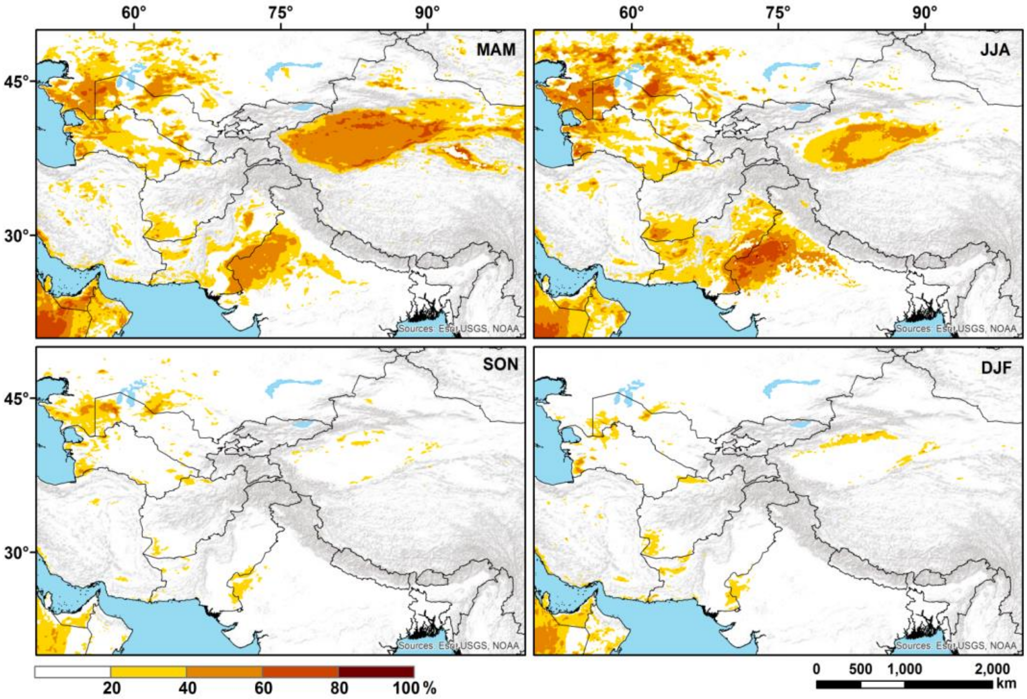

Figure 4-1 Seasonal and spatial distribution of FO of DOD>0.2 for the time period of 2003 to 2014

Analysis of FO distribution enabled detection of active dust sources in the study area and their seasonal pattern of dust emission was revealed. Figure 4-1 presents the spatial and seasonal distribution of FO of DOD > 0.2 during the time period of 2003 to 2014. The first striking observation to emerge from this result was the presence active dust hotspots spreading from eastern shores of Caspian Sea to the Betpakdala desert in Kazakhstan (Figure 4-2 A), with areas reaching FO higher than 80% in north-west of the Aral Sea. The newly formed Aralkum desert is located in the middle of this region. As a result of water diversion from the Amudarya and Syrdarya Rivers for irrigation during the last four decades, the inflow into the Aral Sea was significantly decreased, resulting in loss of almost 74.3% of the surface area of the lake and 90% of the lake water volume which led to formation of Aralkum (Indoitu *et al.*, 2012; Groll *et al.*, 2013). The Aralkum has been reported as a very active source of dust by several studies (Wiggs *et al.*, 2003; Groll *et al.*, 2013). Highest FO in this region was observed during the summer months and to a lesser extent in spring. While dust activity in this region diminishes in autumn and winter, active hotspots remain in some areas, specifically in the delta of the Atrek River and western parts of the Karakum (Figure 4-2 B), where FO is greater than 40%.

As shown in Figure 4-1, the second largest dust hotspot region develops over the Tarim basin in western China. The Taklamakan desert occupies about 323,750 km^2 in the centre of Tarim Basin and contains a series of active sand dunes (Shao *et al.*, 2006). Dust in this basin is mostly attributed to several dried lakes, wadis and fluvial pans that are formed on the periphery of the Taklamakan desert. In particular, desiccated Lake Lop Nur, the remainder of the historical post-glacial Tarim Lake in eastern part of the basin, has been a significant source for dust storms blowing towards the centre of Taklamakan desert (Walker, 1982; Gao *et al.*, 2009). In our analysis, the most active dust hotspots were found in eastern and northern parts of the Tarim basin with peak FO during spring months. This is in a good agreement with previous studies that reported the highest frequency of dust storms in spring months for this region (Yasunori *et al.*, 2002; Wang *et al.*, 2004; Aoki *et al.*, 2005; Che *et al.*, 2013). Our analysis has also revealed some very active sources in the Qaidam Basin in south-east of the Tarim Basin. Similar to the Tarim Basin, the highest FO was observed here in spring season exceeding 80% in some areas. During summer months, however, FO decreases sharply to less than 20% (Figure 4-1) over the Qaidam Basin whereas the Tarim Basin still remains active through this season. The extent of FO of DOD>0.2 in this region significantly shrinks in autumn and winter as a result of less frequent dust outbreaks in these seasons.

One of the least investigated sources identified in our analysis was the upper Amudarya Valley in northern Afghanistan which seems to remain active throughout the year. Very little is published in the literature on characteristics of dust sources in this region (e.g. Smirnov *et al.*, 1993). Apart from dust sources mentioned above, several dust sources with varying seasonal activities were detected at a further distance from the Tian Shan Mountains. The Thar Desert in north-western India was revealed to be one of the largest dust hotspots, spreading over eastern alluvial plains of the Indus River. Mineral dust originated from the Thar Desert has been found to impact extensive areas of snow covered environments in the western Himalaya (Gautam *et al.*, 2013). Several dust sources were also observed in arid and semi-arid central plains of Iran. Active dust sources at Registan Desert at the borders of Iran, Afghanistan and Pakistan were detected.

4.3. Inter-annual variability of dust loading

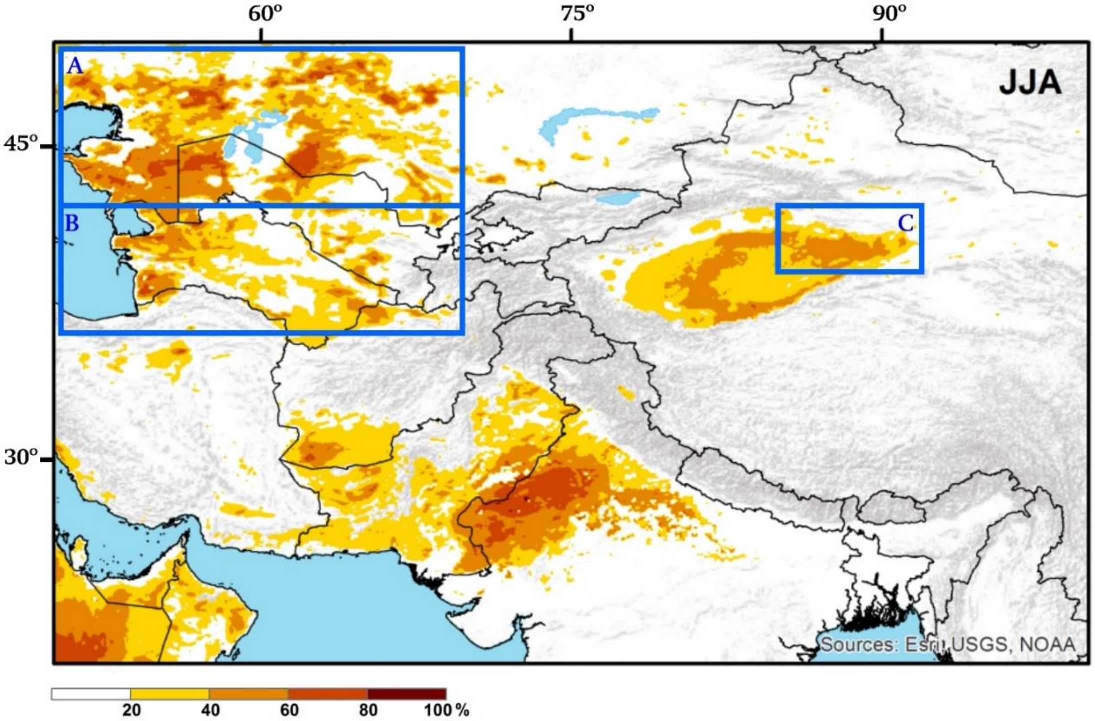

Figure 4-2. Selected regions for investigation of intra-annual variability of AOD, (A) Aralkum and Pre-Aral region, (B) Kyzylkum and Karakum desert and (C) Eastern Taklamakan and Lop Nur

To explore inter-annual variation of dust loading over detected dust hotspots, the mean value of raw AOD (not DOD) over areas with FO higher than 40% (Figure 4-1) were investigated. Three active regions were selected for the investigation of AOD variations, including (A) Aralkum and Pre-Aral region, (B) Kyzylkum and Karakum deserts, and (C) Eastern Taklamakan. Figure 4-2 shows the geographical extent of the selected regions in Central Asia. The Pre-Aral region is a belt of active dust source areas, stretching from the Ustyurt Plateau in the west to the Betpak-Dala and Muyunkum deserts in the eastern part of Aral region. Seasonal distribution of mean AOD values over areas with FO>40% in the Aralkum and Pre-Aral region is shown in Figure 4-3. There has been a steady increase in mean AOD during the time period of 2003 to 2014, especially in the summer season. This can be attributed to increasing dust emission from sources in this region as a result of continuous desiccation of the Aral Sea and surrounding areas, as demonstrated by Micklin (2007).

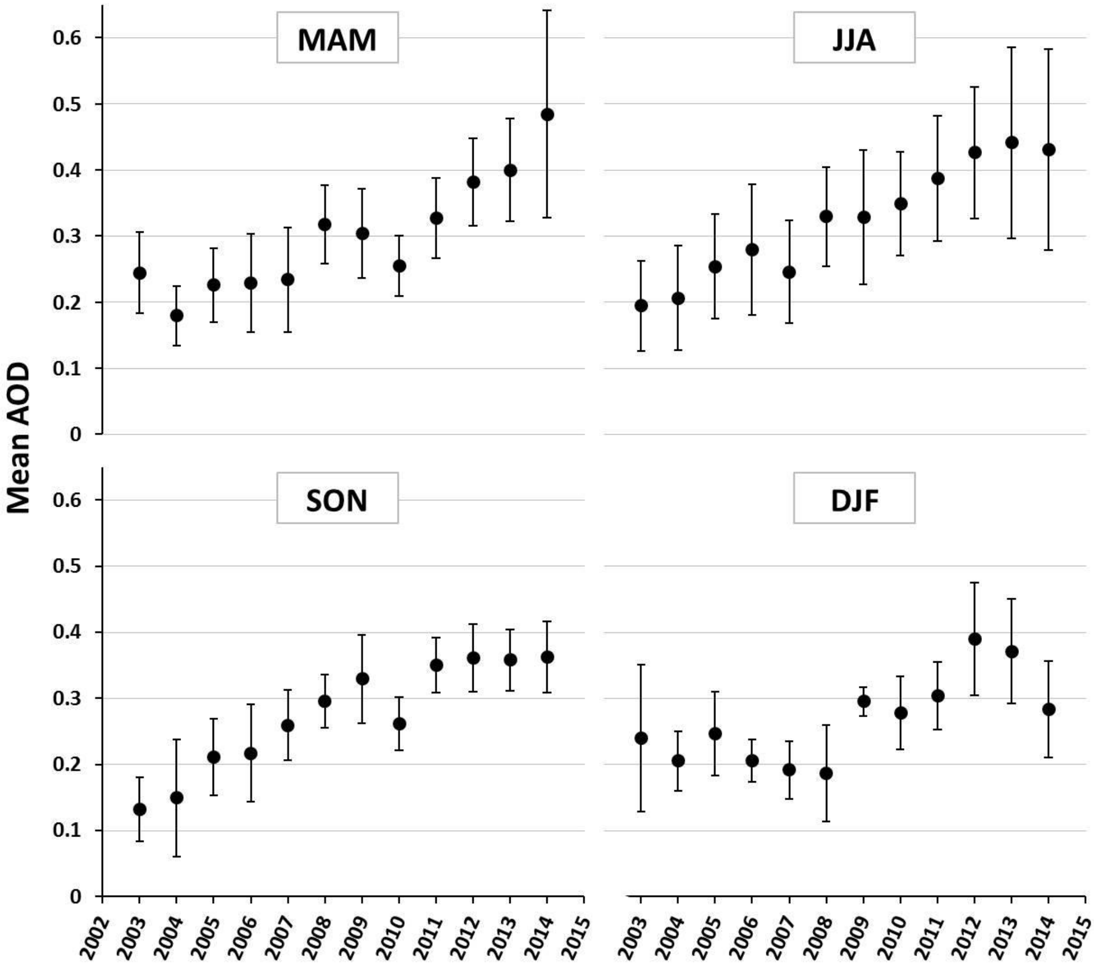

Figure 4-3. Mean AOD (550 nm) over Aralkum and Pre-Aral region between 2003 to 2014. AOD for each season is averaged over areas with FO higher than 40% in Figure 4-1. Vertical error bars and straight red lines represent standard deviation of AOD observations and linear regression respectively.

Mean AOD over Aralkum and Pre-Aral was found to be generally higher in summer and spring seasons, reaching to around 0.5 in the spring of 2014. Standard deviations of AOD observations are also higher during these seasons comparing to autumn and winter when the region is often covered by snow. Frequent snow and cloud cover in autumn and winter results in lesser number of observations and relatively smaller standard deviations.

A less significant increasing trend was found in mean AOD observations over active dust hotspots (FO > 40%) in the Karakum and Kyzylkum deserts. As presented in Figure 4-4, a slightly greater intra-annual variation was observed for mean AOD values over this region. In particular, a relatively sharp decrease was observed in 2010, following by an increase in 2011 for all seasons except winter. In terms of magnitude of AOD observations there is not a significant difference between mean AOD of dusty (spring/summer) and non-dusty seasons (autumn /winter).

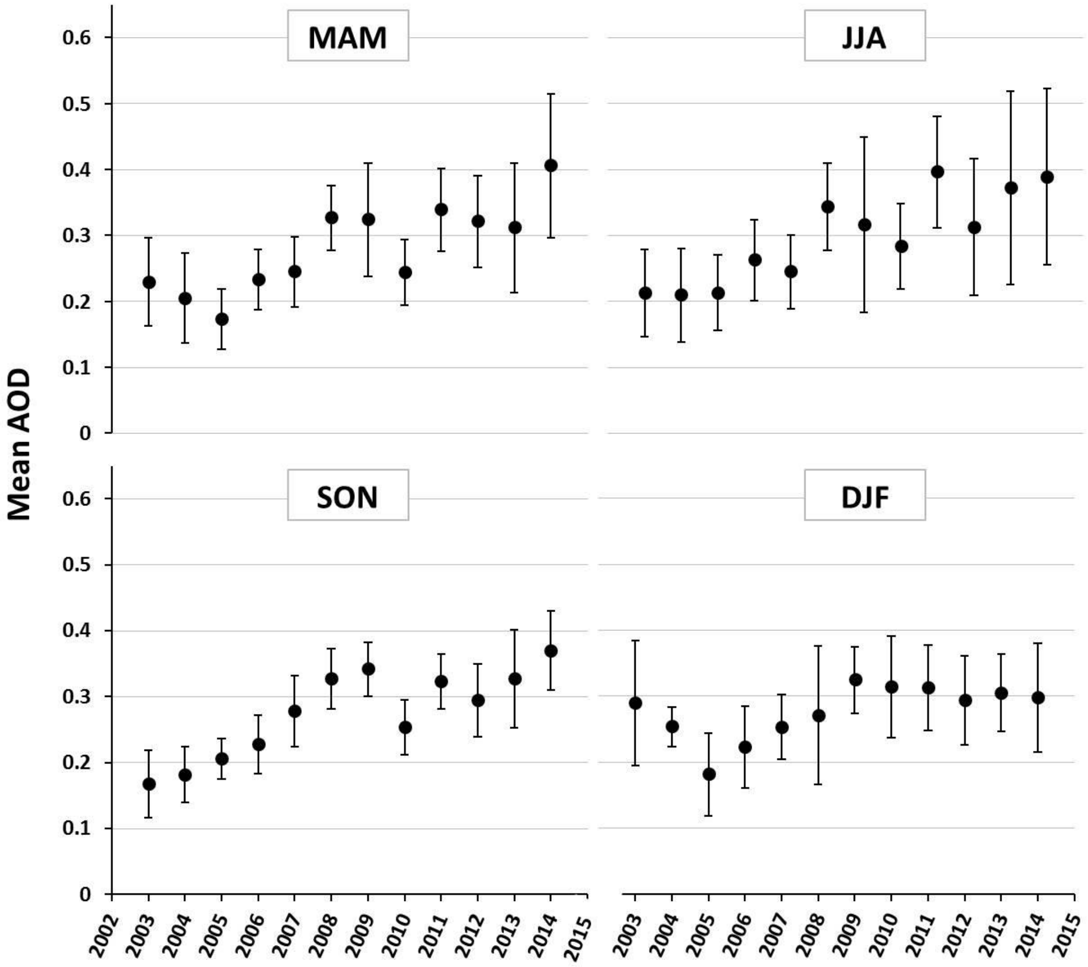

Figure 4-4. Mean AOD (550 nm) over Kyzylkum and Karakum deserts between 2003 to 2014. Annotation the same as Figure 4-3.

In contrast to these two regions, mean AOD over eastern parts of Taklamakan Desert has not shown any significant trend during the study period (Figure 4-5). However, magnitude of mean AOD and its variation over this region are considerably higher than other dust source regions, especially in spring months. The highest dust loadings were observed in spring season, with mean AOD values reaching nearly 1.0 in spring 2006. As suggested by the previous studies on dust activation in this region, a clear decline in the magnitude of AOD was observed for the summer season (Yasunori *et al.*, 2002; Rittner *et al.*, 2016). The number of AOD observations over this region in winter and autumn was low and the AOD data are not shown.

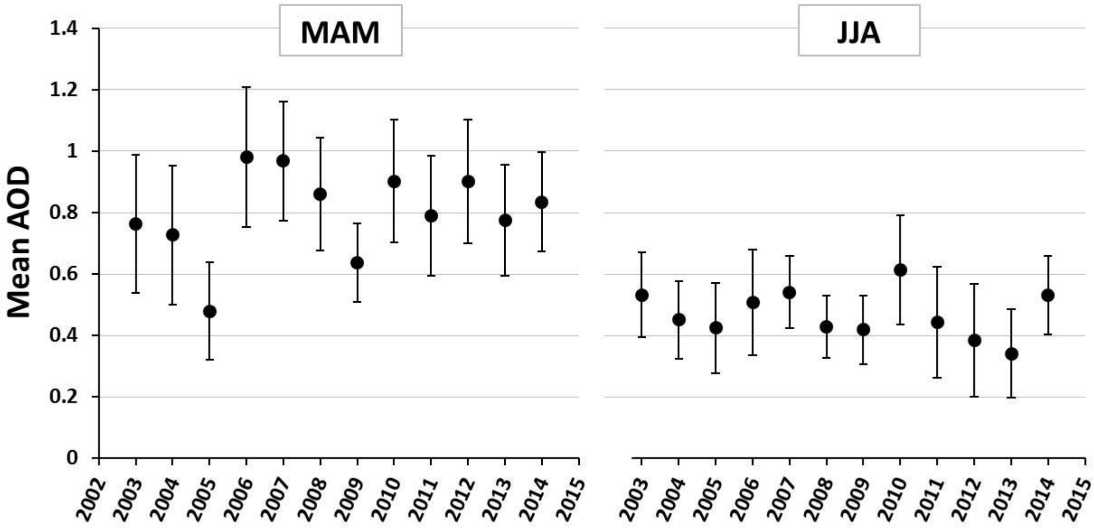

Figure 4-5. Mean AOD (550 nm) over eastern Taklamakan between 2003 to 2014. Annotation the same as Figure 4-3.

4.4. Summary

Analysis of 12 years of daily MODIS Level 2 aerosol products enabled us to obtain an up-to-date map of dust hotspots for a large area extending from the Caspian Sea to Mongolian Plateau in the east and from the Indian subcontinent to high latitudes of Kazakhstan in the north. Our focus, however, was primarily on dust sources in Central Asia. FO analysis revealed several active dust hotspots in this region. Highest activity in spring months was observed in the north-eastern side of Tarim Basin. The most distinctive surface features in this region are floodplains along the lower course of Tarim River as well as several dry lakes including Lop Nur Lake in the eastern sector of the basin. We also investigated the long term trends in mean AOD over those parts of these sources where FO was higher than 40%. The results showed a considerably higher mean AOD in spring months with a higher inter-annual variability. These findings are consistent with previous studies that showed the highest frequency of dust storms in the Tarim Basin in spring (Yasunori *et al.*, 2002; Wang *et al.*, 2004; Aoki *et al.*, 2005; Che *et al.*, 2013). Our results did not suggest a clear trend in AOD for this region over the time period of 2003 to 2014.

During the summer season, the maximum FO frequencies were detected over a vast area lying between the coastal plains of the Caspian Sea in the west and Syrdarya in the east. The highest FO in this region corresponds to the sandy deserts of Ustyurt Plateau in west side of Aralkum and Pre-Aral areas. Our quantitative analysis of dust loading trends during the 12 years highlighted an interesting increase in mean AOD over this region. A constant rise in mean AOD was observed over Ustyurt Plateau and Aral region, with the highest activity in summer. In an investigation of dust deposition in these Central Asian deserts using data from meteorological stations, Groll *et al.* (2013) reported a slight increase in dust deposition activity and intensity between 2003 and 2010. However, their findings did not perfectly represent the spatiotemporal variability of dust emissions due to scarcity of meteorological stations compared to the extent of the region and also associated difficulties in collecting dust samples. A considerable reduction in the extent of dust emitting areas was observed during colder seasons; however, there were still some small active regions throughout these seasons, e.g. the delta of Atrek River in Turkmenistan and northern parts of Tarim Basin.

Although analysis of FO of remotely sensed AOD enabled us to obtain an informative seasonal picture of the most active sources in our study region, there are several shortcomings associated with this procedure. The most important limitation for our analysis was incapability of MODIS sensor to retrieve AOD from cloudy scenes. Like most passive sensors, it is not possible to estimate AOD from MODIS imagery when a dust layer is overlaid or mixed with clouds. This problem is more noticeable in higher latitudes of Central Asia. Another source of limitation was the temporal resolution of MODIS products. Aqua satellite overpasses the mid-latitude regions once a day, therefore short-lived dust outbreaks that happen before or after satellite overpass could not be detected. This effect could be minimized by using MODIS data obtained by Terra satellite, but Terra eDB AOD data was not available after 2007 due to the loss of polarization correction. Hence we preferred to keep consistency by using AOD data collected only Aqua satellite. In addition to other sources of error, e.g. errors inherited from Deep Blue algorithm for estimation of AOD, dominant weather pattern is a key factor affecting the reliability of this procedure for detecting dust sources.

Chapter 5. Dust emission point source inventory

5.1. Introduction

In previous chapter we presented a series of dust hotspot maps obtained by analysis of time series of daily MODIS AOD products. Although it enabled us to provide a good insight into spatial distribution and seasonality of dust emissions in Central Asia, it lacked details regarding the precise location of dust sources. Detailed information about precise location of dust point sources is a key prerequisite for attributing surface characteristics of dust sources, especially over heterogeneous landscape of Central Asian playas. In this chapter we present the results of dust source detection using the methodology described in section 3.3.2. The aim of investigating dust plumes in MODIS DEP images was to pinpoint the precise location of dust point sources (DPS) in order to provide a clear insight into the spatiotemporal characteristics of dust emission, surface characteristics and meteorological controls of dust emission in Central Asia. To achieve this aim, two MODIS DEP images were produced for each day from Terra and Aqua satellites, acquired over a 10 year time period from 2003 to 2012. For every single dust outbreak that has occurred during this time period in this region, we recorded the precise location of each DPS (if detectable), as well as meteorological conditions at the time and location of dust emission. Analysis of the database of DPS provided us with a unique opportunity to develop a detailed inventory of dust emissions sources in this region. We were able for the first time to determine the sources of dust at sub-basin scale, and to investigate the temporal variability of their activation, surface characteristics of source regions, and synoptic conditions for dust emission.

In the following sections, we first present the results of spatiotemporal distribution of DPS in Central Asian drylands. Analysis of the seasonal pattern of dust emission led to categorisation of the major deserts and dust emitting surfaces into several main source regions. A detailed inventory of the most important dust source region is provided and their land surface characteristics, inter-annual and intra-annual variation of dust outbreak frequency and synoptic climatology of dust emissions are investigated. Finally an overview on the main findings is outlined.

5.2. Spatiotemporal distribution of dust point sources in Central Asia

Figure 5-1 shows the spatial distribution of DPS, detected over the 2003-2012 period, grouped within the boundaries of the known dust source emission regions (Section 2.4). The first important result to emerge from a general inspection of this map is that there is a clear link between the major river systems and concentration of DPS. A particular case is the Taklamakan desert, where the majority of DPS were detected along the floodplains of the Tarim River at the northern margins of the Taklamakan desert. The same pattern is apparent in the Karakum and Kyzylkum, with high concentration of DPS on the alluvial plains of the Amudarya and Syrdarya. The floodplain of the Upper Amudarya region in northern Afghanistan, which to date was not discussed in literature, is another noticeable example of a strong link between fluvial systems and dust emission.

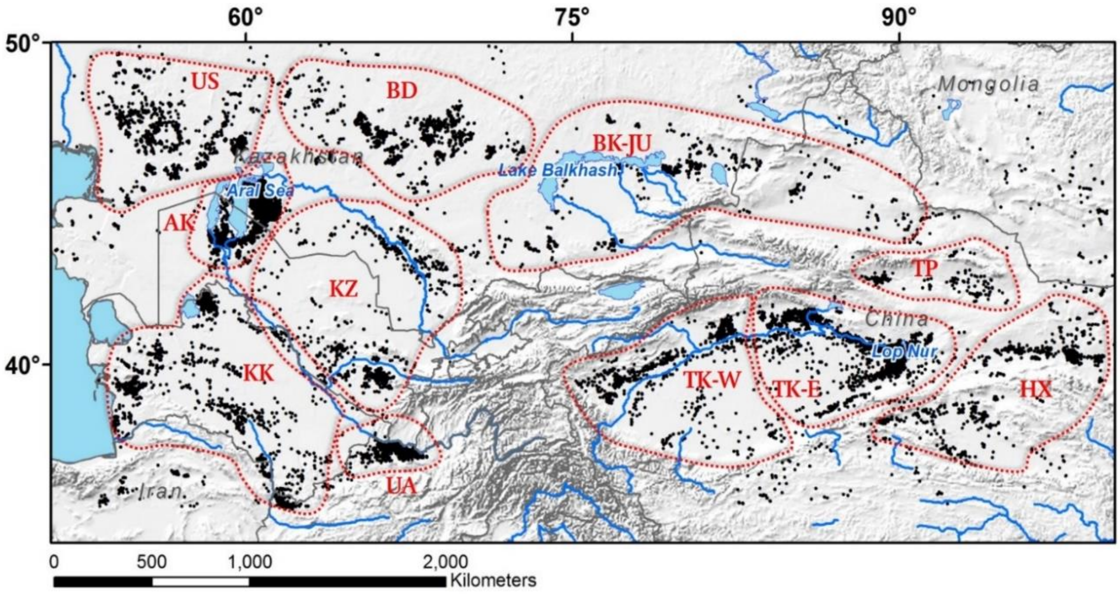

Figure 5-1. Distribution of dust point sources in Central Asia, 2003-2012. The region acronyms stand for: Ustyurt Plateau (US), Betpak Dala desert (BD), Aralkum (AK), Kyzylkum (KZ), Karakum (KK), Upper Amudarya (UA), Balkhash and Junggar basins (BK-JU), Western Taklamakan desert (TK-W), Eastern Taklamakan (TK-E), Turpan depression (TP), and Hexi Corridor (HX). Background is shaded relief generated using GTOPO30 digital elevation model.

In addition to floodplains of the major rivers, desiccated and ephemeral lakes seems to be a very active sources of dust in the region. A high number of DPS were recorded in Aralkum and Sarygamysh Lake located in north of Karakum desert, where availability of deposited alluvial sediments, together with frequent droughts and strong winds make these regions favourable for dust emission. Another distinctive pattern was observed in the Pre-Aral region, which appeared as a belt stretching from the Caspian depression in the west through the Ustyurt Plateau to the Betpak Dala desert in the east.

To further investigate the spatial distribution of detected DPS, we calculated the number of days with a recorded DPS over a 1 degree grid covering the study area. Figure 5-2 shows that the most active sources were located in the eastern part of Tarim basin, where the average number of dusty days reaches to more than 50 per year. The highest number of days with dust emissions in the

Taklamakan desert occurred in the Korla region (highlighted in Figure 5-2). On average, over 25 dusty days per year was recorded in this region. To the east of the Tarim basin, several active dust sources were detected along the Hexi corridor. Strong and gusty alternating easterly and westerly winds are often channelled through this narrow corridor and deflate dust particles from numerous fluvial pans in this region.

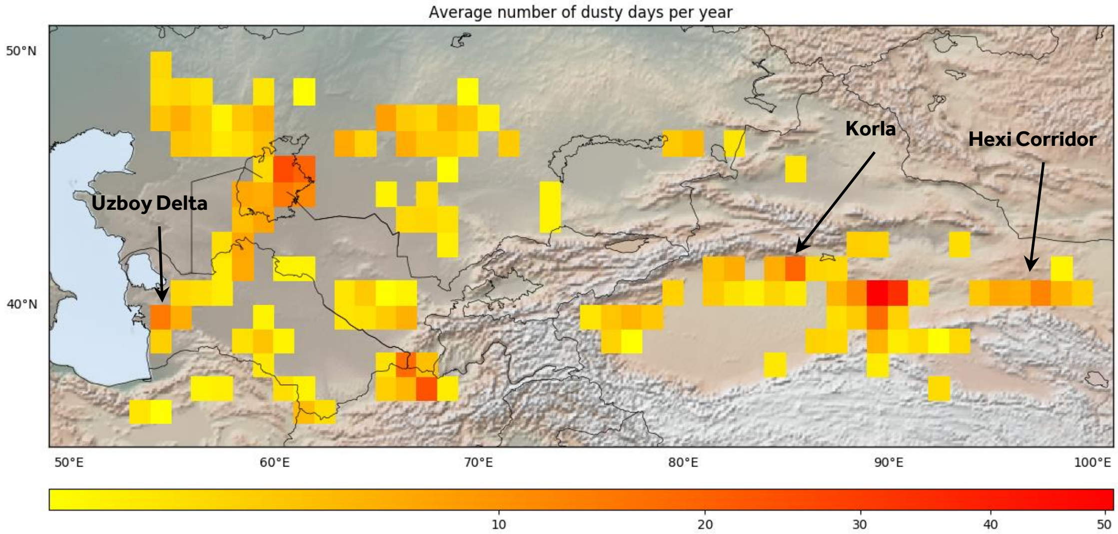

Figure 5-2. Average number of dusty days (defined by presence of DPS) per year. 1°×1° grid cells with less than one dusty day per year are transparent.

The second most active region has been the Aralkum with over 30 dusty days a^{-1} in the central part of the dried lake bed. The exposed bottom of the former Aral Sea is a well-known human made desert which is becoming the dominant source of dust and salt storms in the region (see Figure 4-3). Increasing dust emission from the seashores of the former Aral Sea has been reported in several studies (e.g. Indoitu *et al.*, 2012). A lower but still significant number of dusty days were recorded in the south-western Aralkum, where active sources extend along the channel of the dry River Uzboy. The dry River Uzboy (also Uzboi) was a river which once flew from Sarygamysh Lake towards the Caspian Sea, carrying water surcharge from Aral Sea and western branches of Amudarya River to the eastern coasts of Caspian Sea (Velichko *et al.*, 2002). This 750 km long channel has been dry for at least 800 years. As highlighted in Figure 5-2, a notably high number of dusty days was observed in the delta of this desiccated river.

The Upper Amudarya region in northern Afghanistan (UA in Figure 5-1) is another very active dust source region that experienced a high number of dust outbreaks on which very little information is available (e.g. Middleton, 1986). Very little field studies have been carried out in this part of northern Afghanistan due to long term political instability in this country. It is also due to the fact that many studies on dust emission in Central Asia were mainly focused on Central Asian states of the former Soviet Union namely Turkmenistan, Uzbekistan, Tajikistan, Kyrgyzstan, and Kazakhstan (e.g. Lioubimtseva *et al.*, 2005; Lioubimtseva *et al.*, 2009; Groll *et al.*, 2013; Shen *et al.*, 2016). The average number of dusty days in this region reaches to nearly 30 days per year. Dust source regions with between 10 to 20 dusty days per year were also detected in Pre-Aral region, spreading from the Caspian depression to Betpak-Dala desert (Figure 2-10).

The spatiotemporal distribution of dust emission was investigated by analysis of the average number of dusty days in each season and as a percentage of the total number of annual dusty days. Figure 5-3 illustrates these statistics for each season. The majority of dust source regions are active during the spring season. In particular, frequency of dusty days in the Taklamakan and Aralkum, the two most active regions in the study area, reach their maximum in spring. About 60% of dust emissions from sources in the Taklamakan desert, Aralkum and Balkhash basin have been recorded in spring. The peak of dust emission in the Karakum and Kyzylkum deserts occurs in summer and early autumn. For some areas of these deserts 80% of all days with dust emissions was registered in JJA. The maximum seasonal share of dust emission in the Pre-Aral region has been also recorded in summer. Also many sources in the eastern Taklamakan were active during summer season.

Although some source regions e.g. the eastern Taklamakan, Aralkum and Upper Amudarya still remain active during autumn, especially in September, the overall intensity of dust emissions drops in this season as precipitation increases in October-November (Aizen *et al.*, 2001). Dust emission distinctly diminishes during the winter season, particularly in higher latitude due to persistent snow cover during the cold months.

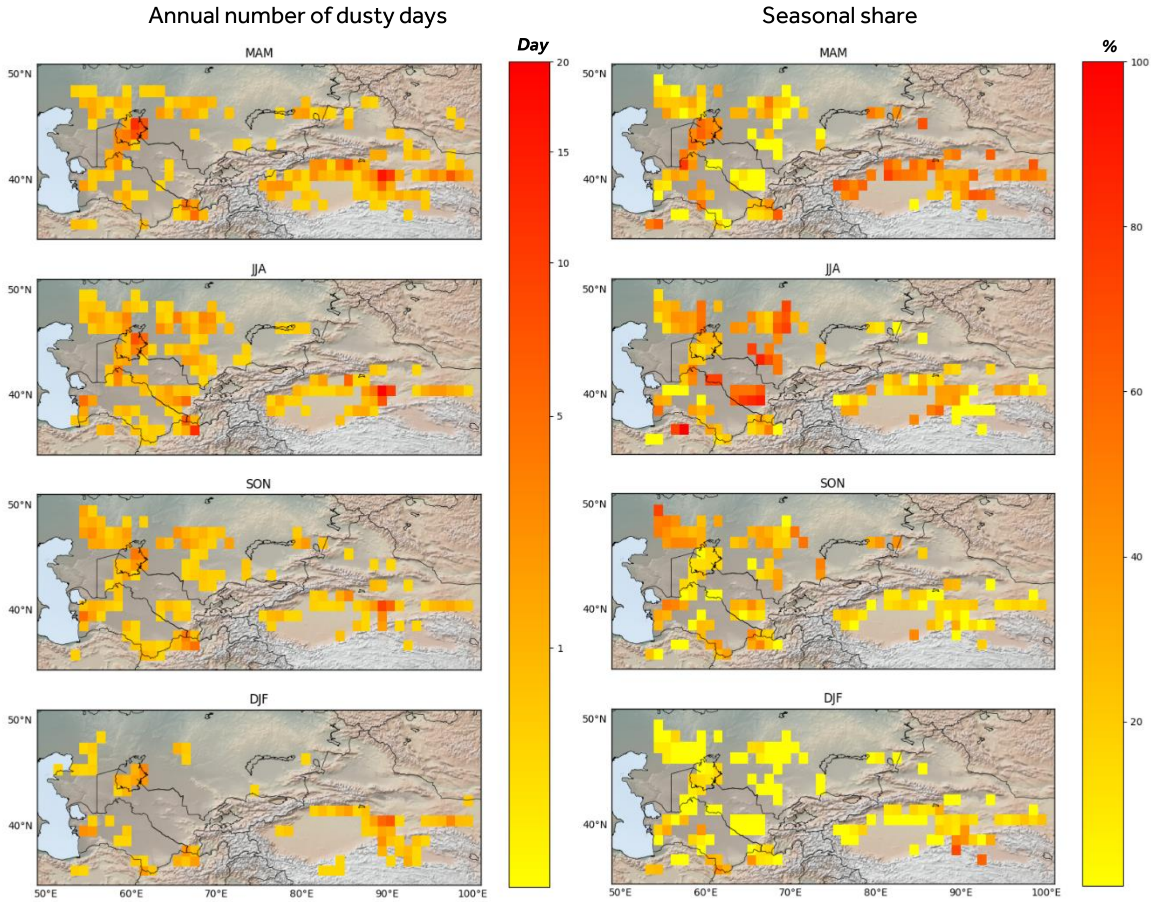

Figure 5-3. Average number of dusty days for each season (left) and their percentage of total number of dusty days (right).

To compare intra-annual cycles of dust emission in Central Asia, a colour-coded heat map whereby regional statistics contained in a matrix are colour-coded, was created (Fig. 5-4). The mean annual number of dusty days, normalized to the range of 0 to 1, for the known dust source regions (Figure 5-1) is shown. Normalization of the number of dusty days allows us to compare the variations in dust emission of different regions. As shown in Figure 5-4, a distinctive general pattern in monthly distribution of dust emission emerges. In six regions, located in the eastern part of the study area, dust activity peaks in spring months. This includes the Taklamakan desert, Balkhash and Junggar basins, Turpan depression, and Hexi Corridor. In contrast, source regions at the western part of the study area experience the highest dust activity in summer. These regions are located in western part of study area, including Upper Amudarya, Ustyurt Plateau, Betpak Dala desert, Karakum and Kyzylkum deserts. The only exception in the western regions was the Aralkum, where dust activity peaks in spring but also remains active in summer.

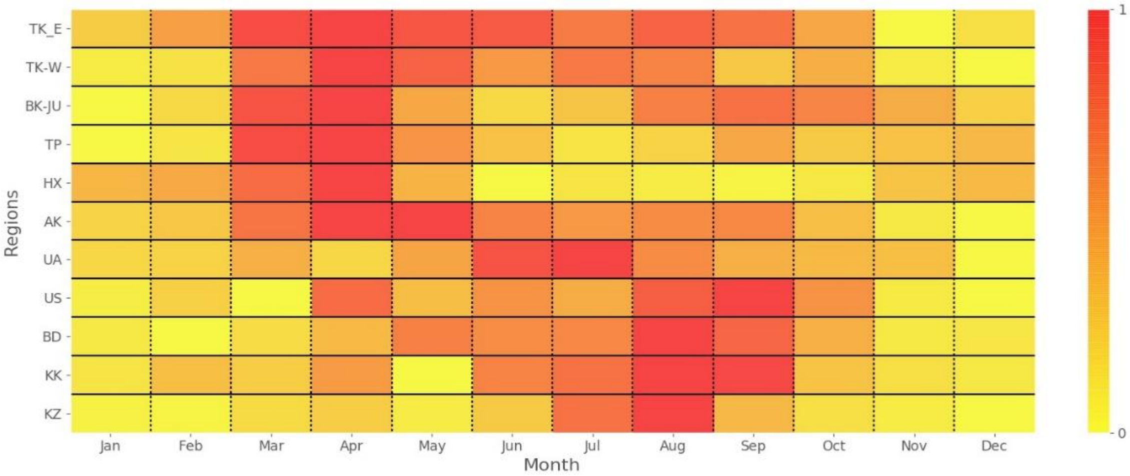

Figure 5-4. Heat map of normalized mean annual dusty days for the dust source regions outlined in Figure 5-1

Valuable information about dust processes in Central Asia can be drawn from the heat map presented in Figure 5-4. It shows that Eastern Taklamakan is a dominant source of dust throughout the year. Dust emission in this region starts in Feburary, peaks in March and April and gradually falls during the following months until October. The same pattern was observed in Western Taklamakan, however dust activity in this region starts later, in March, following by a peak in April. Dust emission from Taklamakan sources seems to be diminished during the cold months, between November and February. In Balkhash and Junggar basins as well as Turpan depression there is very little or no dusty days in January and February due to permanent snow cover, but as snow cover disappears both regions become very active in March and April. A secondary peak in Aug-Oct was also observed in Balkhash and Junggar basins. On the other hand, dust sources in Hexi Corridor, which is located in lower latitudes, seems to be active during cold months but remarkably inactive between June and October.

Apart from Aralkum desert, the maximum number of dusty days in all source regions in the western part of our study area occurs in Jun-Sep. This suggests a different mechanism for dust entrainment in Aralkum comparing to other regions which will be investigated further in chapter 5.3.1. Although summer is the dominant season in terms of dust emission in the western part of the study region, the months in which the maximum dusty days were recorded varies in different regions. Dust emission in the Upper Amudarya region peaks in June, whereas the peak months in Betpak Dala, Ustyurt, Kyzylkum and Karakum are August and September. Dust activities in these regions significantly weaken in cold months, between November and February.

Central Asia is a vast region with varied landscapes and climates, thus dust activities are extremely variable at annual and inter-annual scales. To further investigate the inter-annual and intra-annual variations in dust emission, synaptic controls of dust emission and geomorphological characteristics of dust sources we categorised the main Central Asian dust sources into seven regions. This categorization was made based on their geographical location and similarity of seasonal pattern of dust emission. As shown in Figure 5-4, both the Karakum and Kyzylkum deserts exhibit a similar dust emission seasonality and together form the main part of the Aral Sea basin, hence for the purpose of our analysis they are regarded as one region. The same applies to eastern and western parts of the Taklamakan, where the number of dusty days are highest in spring months and both fall within the Tarim Basin. Also the belt of active dust sources stretched from the Ustyurt Plateau to Betpak Dala desert, is regarded as the Pre-Aral source region. In the following section a detailed analysis on dust emission processes in these regions is presented.

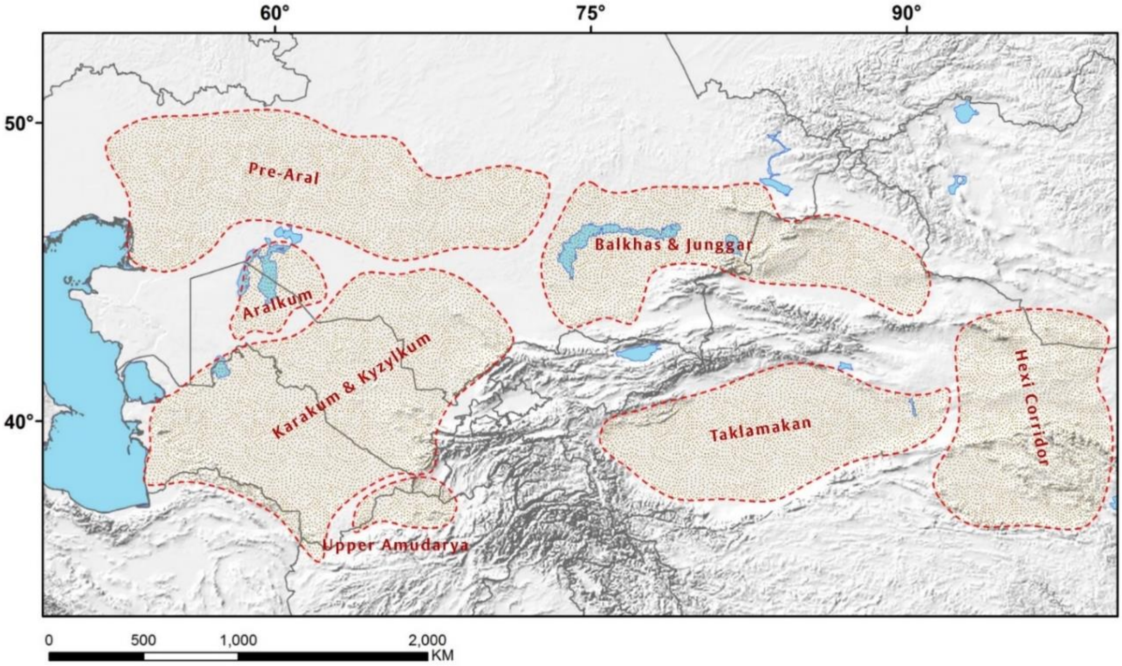

Figure 5-5. The main dust source regions in Central Asia. Background is shaded relief generated using GTOPO30 digital elevation model.

5.3. Dust source regions

The spatial extent of the dust source regions selected for further investigation of dust processes is shown in Figure 5-5. To characterise the dust emission processes in each of these regions, three aspects of dust event formation were investigated: (1) land surface characteristics, (2) inter- and intra-annual variability in dust emission, (3) synoptic controls on dust emission and the direction of entraining winds.

5.3.1. Aralkum

5.3.1.1. Land surface characteristics

The catastrophic desiccation of Aral Sea, once the fourth largest lake in the world, is one of the most well-known examples of environmental disasters caused by human activity. Although strong fluctuations in the Aral Sea levels and configurations of its shores occurred in the Pleistocene and Holocene (Velichko *et al.*, 2002), in the recent past, prior to the 1960s, water level in the Aral Sea was at a relatively stable state as the two main sources of water, the Amudarya and Syrdarya rivers, were flowing naturally into the lake (Micklin, 2007). Water inflow from these two rivers started to decrease sharply in the second half of the 20th Century as a result of excessive use of water for irrigation required by the increasing cotton production in Soviet Central Asia. Although the immediate environmental effect of these developments on the Aral Sea was known to the Soviet scientists, it was in the 1990s when the western world became aware of the ecological disaster (Indoitu *et al.*, 2015). Dust emission in the region intensified as a result of the drastic desiccation of the Aral Sea which led to the development of a new desert, the Aralkum, on the dried sea bed. Since then, several reports and studies confirmed that the exposed bed of Aral Sea has become a new active source of dust and salt storms in the region (Micklin, 1991; Gill, 1996; Waltham *et al.*, 2001; Wiggs *et al.*, 2003; Micklin, 2007; Indoitu *et al.*, 2012; Groll *et al.*, 2013).

The Aral Sea has progressively shrunk during the past 5 decades due to lack of recharge by rivers and high evaporation during summer time. In 1987-1989 the lake separated into two water bodies: a "Small" Aral Sea in the north and a "Large" Aral Sea in the south with a small channel connecting the two parts. The Large Aral Sea was subsequently divided into two parts: a deep western lake and a shallow eastern lake. Following the construction of a 13 km dike in 2005 the water flow from the Small to Large Aral Sea was seized, leading to the increase of salinity level in the eastern lake by as much as 160 g l^{-1} (Aladin *et al.*, 2009). The aftermath effect of discontinuation of flow from Small Aral to Large Aral can be seen in Figure 5-6. This figure illustrates the expansion of Aralkum over the time period of our study, from 2003 to 2012, through a time series of Landsat annual composites acquired from Google Earth Engine catalogue (https://earthengine.google.com/). The shallow eastern part of the Large Aral started to shrink dramatically after 2006 and by 2009 the dried lake bed was completely exposed except a small seasonal pond in the center. Although it partly recovered in 2010 as a result of inflow of drainage and excessive irrigation water from Uzbekistan (Kozhoridze *et al.*, 2012), the shrinkage continued in the following years until 2012.

The land cover of the Aralkum is characterized by high diversity. Solonchaks (salty pans) with high concentration of salt are the dominant land cover of the dried bottom of the lake appearing after the sea's recession (Kozhoridze *et al.*, 2012). Around 22,500 km^2 of the 57,500 km^2 exposed bed is occupied by solonchaks. Wet marsh solonchaks are the first stage of transformation of land cover after the water desiccation. High evaporation rate and surface temperature lead to transformation of marshes into coastal solonchaks and dry solonchaks respectively. Sandy massifs are widely spread across the early dried areas. Periodically, the vegetation cover appears due to the temporal water breaks in the humid years (Kozhoridze *et al.*, 2012).

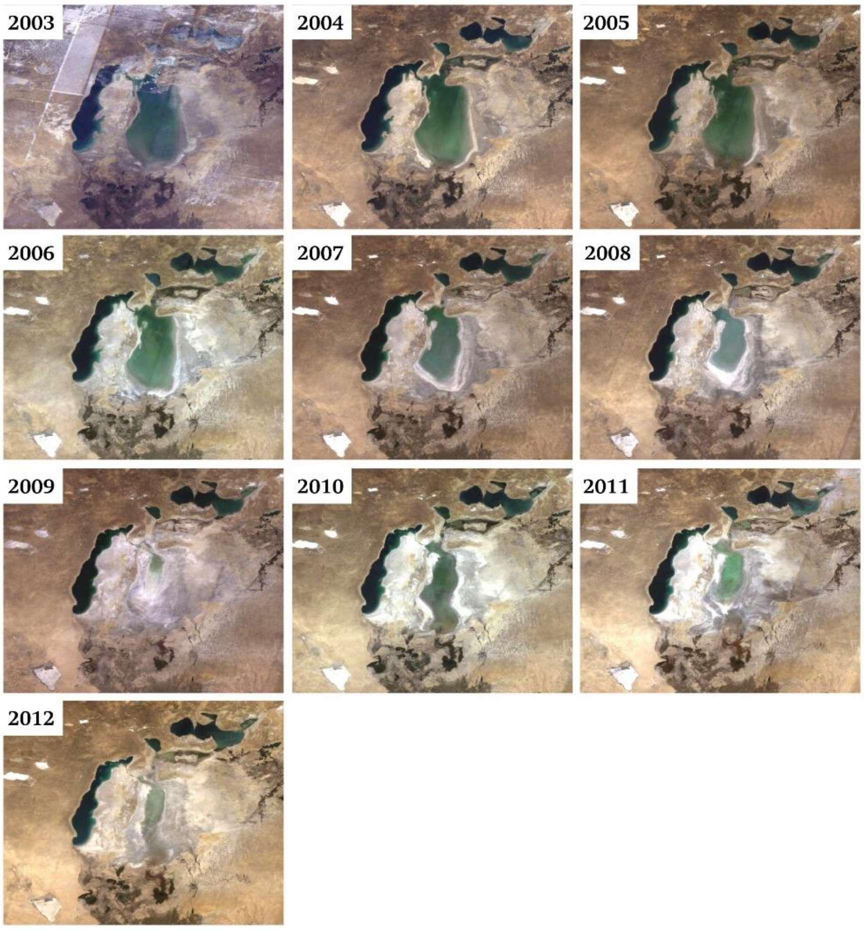

Figure 5-6. Landsat annual composites of surface changes in the Aralkum, 2003-2012.

More than 59% of our DPS observations in the Aralkum were made in northern and eastern parts of the dried lake, where loamy deposits are the prevailing soil type (Kozhoridze *et al.*, 2012). Sandy massifs, combined with dry puffy solonchaks with easily destructible top surfaces, and takyrs forming in the topographic depressions with heavy clay soils, construct the landscape of this very active dust producing part of the Aralkum. Takyrs are formed through submergence of clay soils found in depressions after spring rains which create ephemeral lakes (Babaev, 1994). Around 20% of the observed DPS occurred in the southern and south-eastern parts of the lake where lighter sandy and sandy-loamy soils are found.

The Vozrozhdeniya Island was once a small island of the size of 200 km^2 in the centre of the Aral Sea. As the Aral Sea began drying up in 1960's, this island began to grow in size until it joined the main land in the south and became a peninsula at the beginning of 21st century. These new sand areas as well as termini of the former river channels at the delta of Amudarya river contributed to around 21% of our DPS observations in the Aralkum. The importance of dust emissions from this part of Aralkum is because of the potential risk of contamination of dust by toxic pathogens remained from the development and testing of biological weapons between 1950 and 1990 at the island which hosted bioweapons facilities. It was alleged that the departing Soviet military took measures to decontaminate the island and also a joint clean-up program was carried out in 2002 by the United States and Uzbekistan to ensure the destruction of any surviving weaponized pathogens (Micklin, 2007).

5.3.1.2. Inter- and intra-annual variability in dust emission

Inter-annual and intra-annual variations in dusty days and the number of recorded DPS in the Aralkum region is presented in Figure 5-7. A steady increase in the number of dusty days from 2004 to 2012 is notable, agreeing with trends in AOD (Figure 4-3). The number of dusty days in the Aralkum has increased from 18 in 2004 to more than 60 in 2012. This more than threefold increase in the number of dusty days is in accord with rapid desiccation of the eastern Aralkum as a result of detachment from the Small Aral in 2005. A drop in the number of dusty days in 2011 is probably linked to the temporary rehabilitation of the eastern lake in 2010 (Figure 5-6).

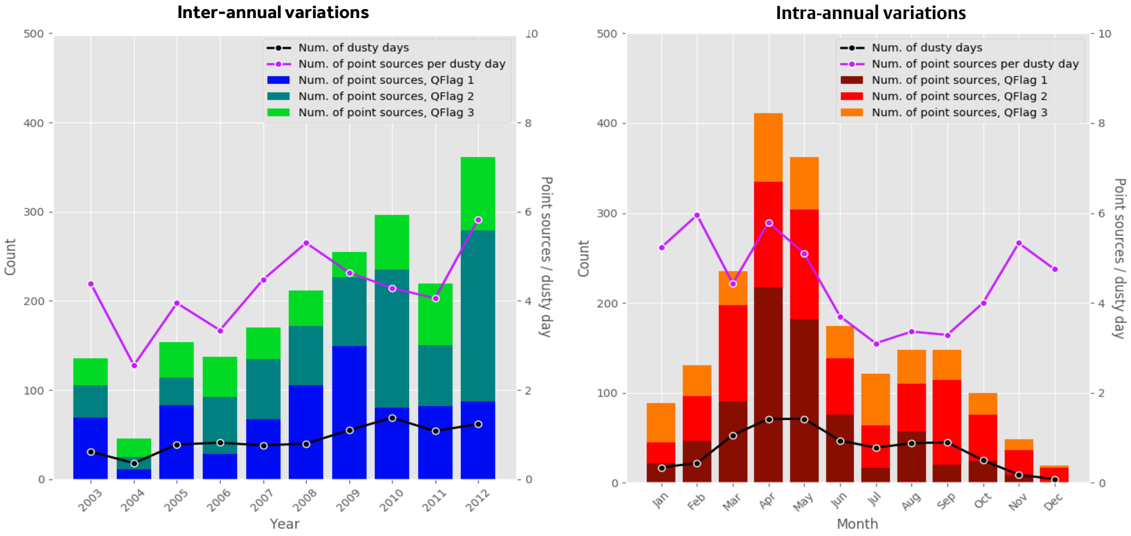

Figure 5-7. Inter-annual and intra-annual variation in dusty days and DPS in the Aralkum. Black line shows the number of dusty days and the purple line shows the average number of DPS per dusty day.

It must be noted that the number of DPS does not necessarily equate to the magnitude of individual dust events. To obtain a proxy measure of the intensity of dust events, the average number of DPS per dusty day for each year was calculated (Figure 5-7). Although there has been some fluctuations in the DPS ratio in the Aralkum between 2003 and 2012, the average number of DPS per dusty day tends to increase towards the end of the period. On average, less than 3 DPS have been activated in each dusty day in 2004, comparing to nearly 6 DPS per dusty day in 2012. This increase is in line with findings of Groll *et al.* (2013) who reported an increase in percentage of high intensity dust deposition events at weather stations around the former shores of Aral Sea, while the number of low dust deposit events decreased considerably.

Investigation of intra-annual variability of the occurrence of dusty days in the Aralkum revealed that the maximum number of dust events occurred in April and May, with more than 70 dusty days in each month during the ten year time period (Figure 5-7). DPS ratio per dusty day has also been the highest in these months (Figure 5-7). This is in contrast to previous studies which suggested the highest dust activities in summer for Central Asian dust sources (e.g. Orlovsky *et al.*, 2004; Orlovsky *et al.*, 2005; Groll *et al.*, 2013; Xi *et al.*, 2015b). We also showed in previous section that number of dusty days in other Central Asian sources, more specifically in the Pre-Aral region and the Karakum-Kyzylkum bordering the Aralkum in the north and south respectively, peak in summer.

In dust modelling a higher threshold wind speed enabling dust emissions is assumed for spring months because of higher soil moisture and also the impact of a short-lived vegetation cover increasing surface roughness (Knippertz, 2014). Ephemeral vegetation cover along with more cohesive soil particles would increase the threshold wind speed, whereas fine dried soil particles of a barren surface can be easily deflated by even light winds with a velocity of less than 5 m s^{-1} at the surface (Sternberg, 2017). Unlike most of the source regions in Central Asia, a vast extent of dust-emitting surfaces in the Aralkum remains entirely free of vegetation because of high salinity of the dried lake bed. On the other hand, Argaman *et al.* (2006) showed that the formation of salt crusts on the solonchak surfaces and fine-grained crusts in the takyr areas of the Aralkum would dramatically increase the threshold wind velocity. The presence of salt solution in the formation process of surface crust would also create a stronger crust, which needs more energy to dislodge surface particles by saltating grains (Rice *et al.*, 1996). Hence it seems that the decrease in the number of dust days in summer might be associated with the fact that stronger surface winds are required to initiate the deflation process, when well-formed crust serves to protect the underlying particles from wind erosion. By contrast, fine-grained material generated by salt weathering and surface disturbance by needle-ice formation in winter creates material that can then be easily deflated by strong winds in spring months (Goudie *et al.*, 2006).

This hypothesis seems to be confirmed by a sharp reduction in the number of DPS per dusty day in summer months. In other words, in spring several DPS become activated at once when the surface wind threshold is met, while in summer season a smaller number of DPS contribute to generating a dust event. This can be explained by the increase in surface crusts in summer which results in less availability of fine-grain particles and smaller number of DPS becoming active when the wind threshold is met.

5.3.1.3. Synoptic controls on dust emission and dust transport pathway

The Siberian high, the strongest semi-permanent high pressure system in the northern hemisphere, is one of the most important circulation systems influencing the climate of Central Asia. Between November and March, Central Asia is influenced by the southwestern fringe of the Siberian High anticyclone, and experiences cold air intrusions from north, northwest and northeast (Lioubimtseva *et al.*, 2005; Orlovsky *et al.*, 2005). The westerly mid-latitude cyclones forming and regenerating over the eastern Mediterranean and the Caspian Sea carry moisture to Central Asia. These are often deflected by the Siberia High and follow trajectories positioned south of the Aral Sea, leading to higher cloudiness and precipitation in winter and spring in this region (Small *et al.*, 1999; Lioubimtseva *et al.*, 2005; Groll *et al.*, 2013). High interannual variability in winter precipitation is strongly correlated with year-to-year changes in the position and intensity of the Siberia High (Small *et al.*, 1999). The frequency of depressions increases over Central Asia in late spring as the Siberian High diminishes and precipitation maximum is observed April - May. Intensive heating of the surface in summer leads to formation of thermal depression over southern parts of the Aralkum, hence cold frontal intrusions from the west and north-west become more frequent. The advection of cold air from the north-west results in strong atmospheric instability and post-frontal dust storms in this region (Orlovsky *et al.*, 2005).

To investigate the links between the circulation patterns and formation of dust storms in Central Asia composite analysis was conducted using two sets of data: (i) mean sea level pressure (MSLP), and (ii) wind components at 10 m height. Both datasets were retrieved from ERA-Interim reanalyses at the spatial resolution of 0.5 degree (~ 50 km) for the period 2003–2012 (Dee *et al.*, 2011). Both MSLP and vector wind were averaged over the identified dusty days for each meteorological season. The composite patterns and anomalies (difference between MSLP of dusty days and seasonal average MSLP) were investigated. It must be noted that average wind speed might not be an appropriate indicator of the wind's real erosive strength. Winds that exceed threshold and raise dust may not be sustained over the 6 hours interval of ERA-Interim reanalysis data. Often only morning wind speed responsible for entreating dust.

Figure 5-8 presents the seasonal MSLP and average 10 m vector wind for the dusty days in Aralkum. It must be noted that for each day the morning time step of the 6 hourly wind data (at 6 UTC) is used for the aggregation. It is shown that dusty days peak in spring months is closely linked with strong easterly winds developing at the south-western periphery of the high pressure system developing over Siberia and extending south towards Central Asia. On the synoptic scale, pressure gradient between the high pressure system centred over eastern Kazakhstan and thermal low over Arabian Peninsula and southeast Iran induces turbulent surface wind over the Aralkum (Xi *et al.*, 2015a). MSLP anomaly of dusty days reveals a high pressure anomaly in northern Aralkum and low pressure anomalies over Gobi desert and Taklamakan (Figure 5-9). It suggests that the majority of dust events in the Aralkum are associated with a shift in the centre of Siberian High towards the west in March to early April, which results in a high pressure anomaly in the northern Aralkum and low pressure anomaly over the Gobi desert.

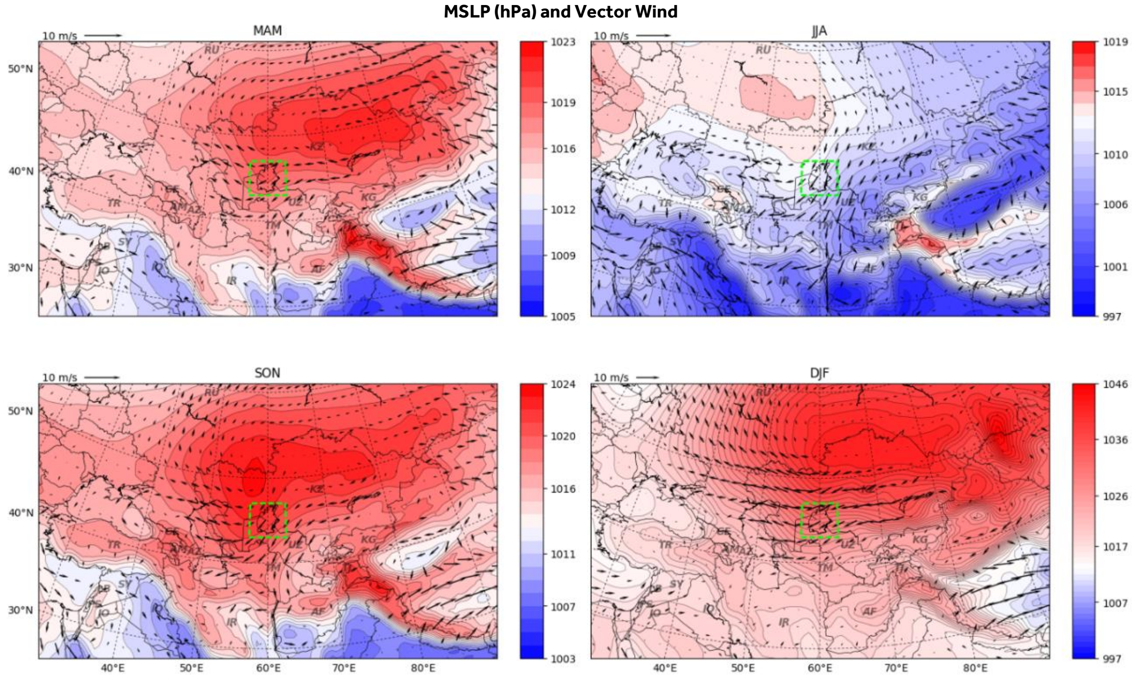

Figure 5-8. MSLP (hPa) for dusty days in Aralkum between 2003 and 2012. Aralkum is depicted by green rectangle.

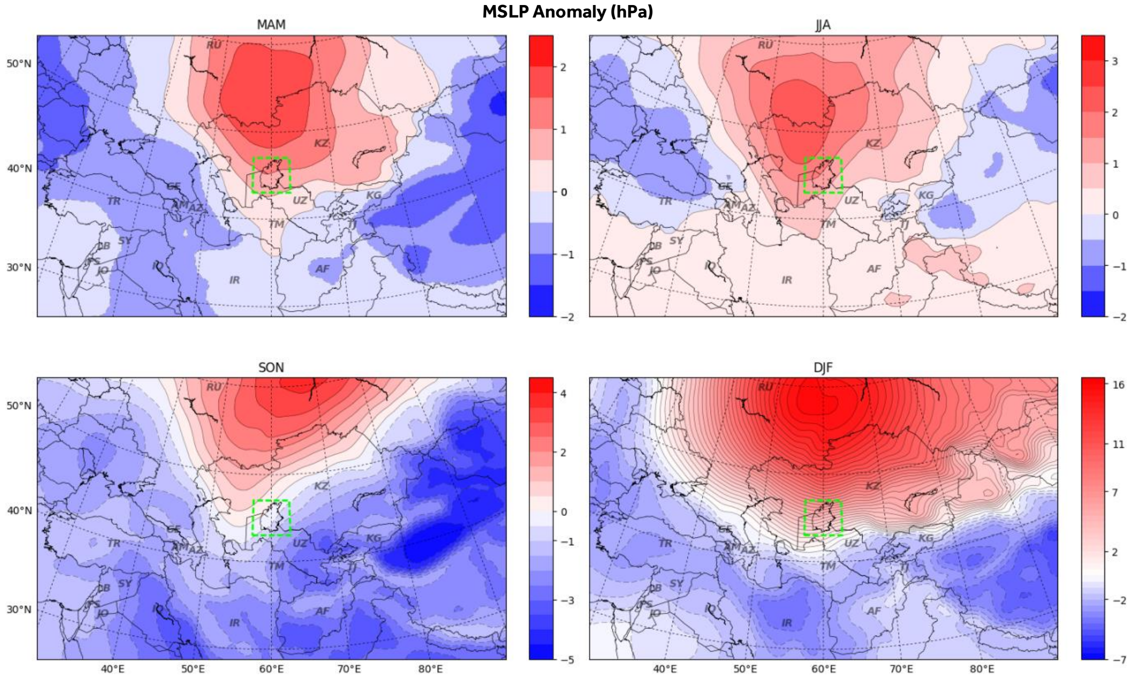

Figure 5-9. MSLP anomaly (hPa) for dusty days in Aralkum between 2003-2012. The Aralkum is depicted by green rectangle.

Circulation patterns noticeably change during summer. The composite MSLP pattern for dusty days features high pressure over European Russia extending towards the Urals and western Siberia reminiscent of a blocking anticyclone similar to that causing drought in 2010 (Cherenkova *et al.*, 2013). Intensification of thermal depression over Central Asia leads to wind direction towards westerly and southwesterly and higher wind speeds at the periphery of the high pressure system. The centre of the high pressure anomaly in summer is roughly over the same region of spring pressure anomaly. However, the low pressure anomalies over the Taklamakan are weaker than spring and also there was no anomaly observed over the regions between Hindu Kush to Arabian Peninsula for dusty days. It implies that despite development of intense depressions in the south, summer dusty days in the Aralkum are mainly associated with the formation of high pressure systems in northwest of the lake and possibly with the blocking pattern.

Regeneration of the semi-permanent high pressure systems in November to February is a prominent feature of weather circulation in the late autumn and winter months. Unlike the spring season, the centre of high pressure for dusty days in autumn and winter is located over western and northern Kazakhstan respectively. Analysis of MSLP anomalies for dusty days in these seasons shows a high pressure anomaly stretching from northern Kazakhstan to Siberia, while a relatively strong negative MSLP anomaly was apparent over southern regions spreading from eastern Europe to Taklamakan region. In particular, in winter months a very strong high pressure anomaly with a sharp pressure gradient over the Aralkum which may play an important role in shaping accelerated easterly and north-easterly winds in this region. Hence it can be concluded that although high pressure systems are dominant during cold seasons, dusty days usually occur when they intensify over Siberia and grow weaker over western China, Iran and eastern Europe.

Near-surface wind speed is one of the most important controls on dust emission (Goudie, 1983; Knippertz, 2014). To investigate the effect of this important factor on dust emissions in the Aralkum, anomalies in 10 m vector wind averaged over the dusty days between 2003 and 2012 were explored (Figure 5-10). As expected, a noticeable wind anomaly was observed over the dusty days in the Aralkum in all seasons. The highest wind anomalies were observed in winter with nearly 4 m s^{-1} in the northwestern Aralkum, which is associated with the dominance of Siberian high all through this season. It was also revealed that wind anomalies in spring months are slightly smaller than in summer. In summer, the intensity of atmospheric circulation over Central Asia significantly weakens (Orlovsky *et al.*, 2005). As a result, the wind speeds are lower and therefore anomalies are higher relative to these lower average wind speeds.

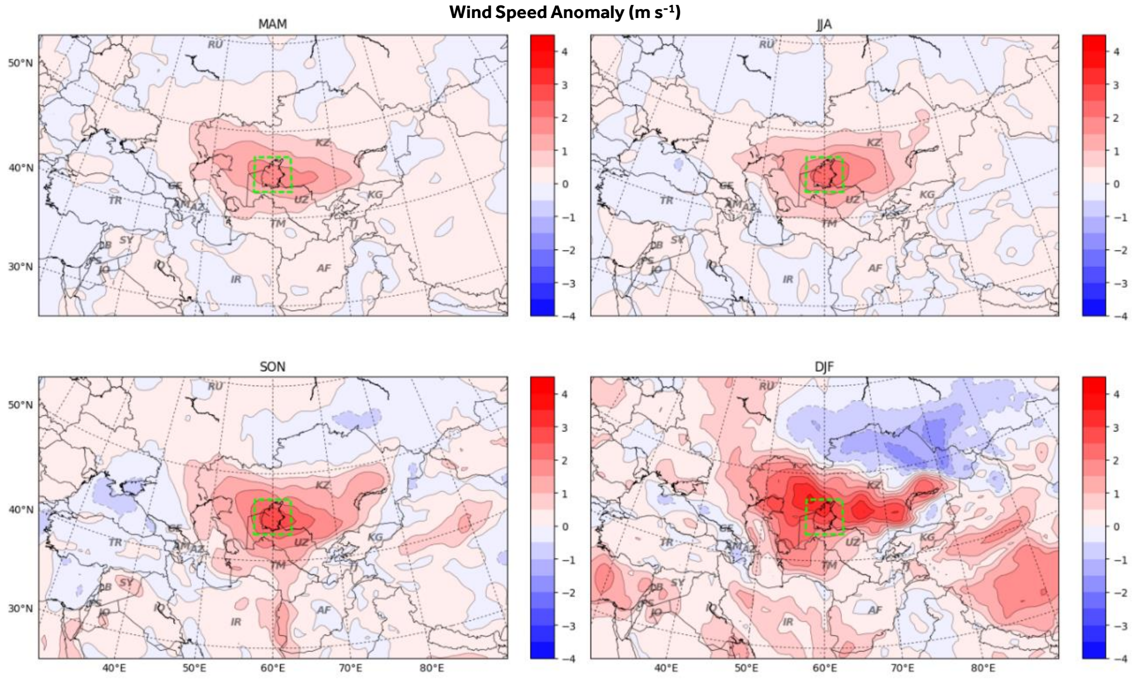

Figure 5-10. Near-surface wind anomaly (m s^{-1}) for dusty days in the Aralkum between 2003 and 2012. The Aralkum is depicted by green rectangle.

In the process of detecting DPS using daily DEP images, 10 m wind speed and wind direction data were interpolated to the location and time of each observed DPS and were recorded in the database. Figure 5-11 shows the distribution of recorded wind speeds for DPS records in Aralkum between 2003 and 2012. It shows that in all seasons, except winter, the majority of DPS in each season were activated by moderate wind speeds of 5 to 8 m s^{-1}. The percentage of above moderate wind speeds (8-10 ms^{-1}) is the lowest in spring (~22%) and keeps increasing in the following seasons to reach to 45% of wind speed records in winter. The same trend is observed for the high wind speed category (>10 ms^{-1}). This trend is in accordance with the increase in soil moisture and occasional frost in cold months which significantly affect the deflatability of soil particles. In contrast, the share of low wind speeds is the highest during spring with around 11% of records, while the percentage decreases in the subsequent seasons to nearly 2% in winter. This can be explained by the lower threshold wind velocity in spring and summer comparing to autumn and winter.

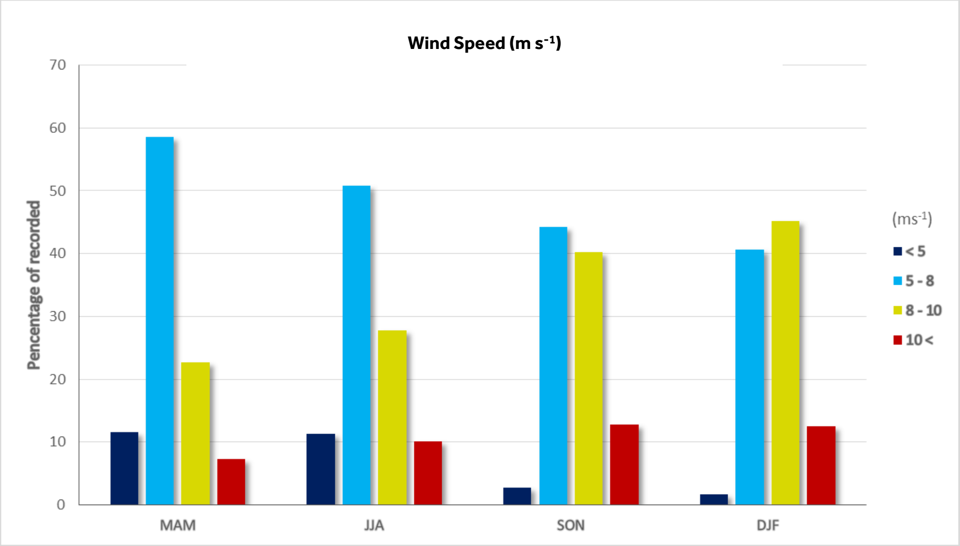

Figure 5-11. Distribution of 10m wind speeds (m s^{-1}) for DPS records in Aralkum between 2003 and 2012.

Analysis of direction of entraining winds showed that the southwest was the dominant wind direction in all seasons during the study period, with the maximum of around 60% of wind records in winter. In general, spring and autumn wind directions are more variable than in summer and winter which seems to be linked to more unstable weather in the former. In summer, the percentage of winds towards south and south-east are noticeably higher than other seasons. It may be the result of more frequent north-westerly intrusions as highlighted by Orlovsky *et al.* (2004) and Groll *et al.* (2013).

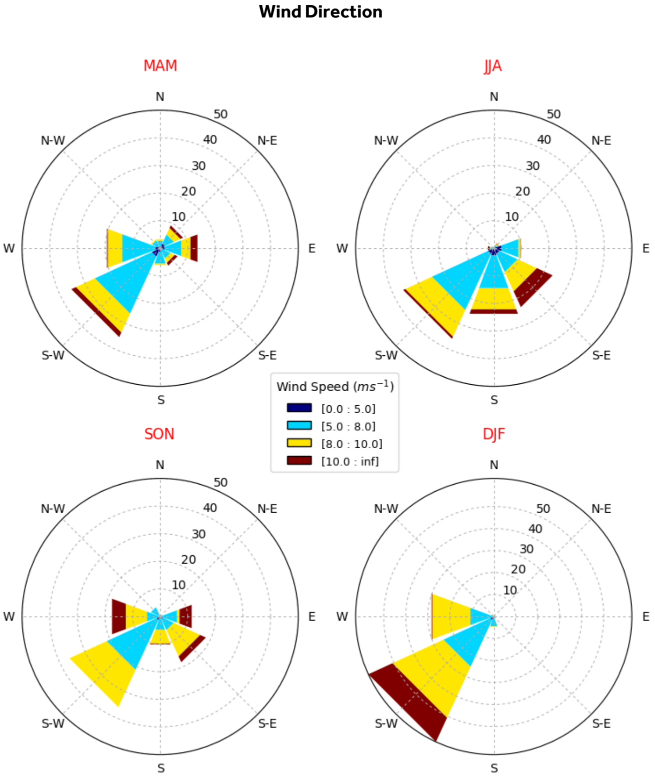

Figure 5-12. Direction of entraining winds for DPS in the Aralkum

5.3.2. Karakum and Kyzylkum

5.3.2.1. Land surface characteristics

Karakum and Kyzylkum deserts occupy the central part of the greater Turan Depression, one of the largest expanses of sand in the world, stretching from south-eastern shores of Caspian Sea to the northern banks of the Syrdarya River. These two desert covers a total area of around 600,000 km² in Central Asian countries of Turkmenistan, Uzbekistan and Kazakhstan (Harris, 2003). The land surface of Karakum and Kyzylkum is characterised by great diversity. Large areas of clay-rich sediments are found in the predominantly sandy deserts of the Karakum and Kyzylkum, in ancient deltas of the Amudarya, Syrdarya, Murghab, Tedzhen and Kashkadarya rivers. Sparsely vegetated sand ridges reaching to up to 90 meters height and sometimes more than 10 km long are the dominant landform in southern Karakum. Takyr pans are commonly found between the sand ridges. Towards the central Karakum, there is a linear chain of depressions, known as Unguz, while to the south-east of Karakum are areas of salt marshes. The Karakum Canal, one of the largest irrigation and water supply canals in the world, extends for nearly 1400 km along the southern edge of the Karakum. Further north is a wind-swept plateau region, including the Sarygamysh depression and central Kyzylkum.

In the Kyzylkum, the altitude is higher and the landscape is more complex. Elevated Monadnocks (remnant tablelands) with altitudes over 500 meters can be found towards the centre of the Kyzylkum (Lewis, 2003). To the south-east, loess deserts cover the transitional zone between the sand expanses of the Kyzylkum and the Tian Shan (Jumashov, 1999). Population density is higher in the southern edges of the Kyzylkum, where industrial and agricultural activities have led to pollution of sands and irrigated lands with pesticides, nitrates, organic pollutants and various heavy metals (Toderich *et al.*, 2001). The Syrdarya River lies in the eastern and northern margins of the Kyzylkum. As a result of high salinization and increasing climate aridity during the past decades, 10 - 15% of the irrigated lands in this area are annually being withdrawn from agricultural use and become potential sources of dust (Baitulin, 2001).

Investigation of the spatial distribution of DPS records between 2003 and 2012 revealed several predominant dust-producing types of land surface, including alluvial fans, floodplains of major rivers, playas and agricultural lands. One of the highest concentration of DPS in the Karakum desert was observed in the drainage basin of Lake Sarygamysh in north-western Turkmenistan (Figure 5-13-b). Sarygamysh is a natural depression in which a lake formed on several occasions in the Holocene. Up until the 17th century, the lake was fed by the Uzboy River, a distributary of the Amudarya River which continued on to the Caspian Sea. The lake dried in the 18th century subsequent to the natural change of the course of the Amudarya towards the Aral Sea (Létolle *et al.*, 2007). Lake formation began again in the 1960s when runoff from the irrigated lands of the Khorezm Oasis in the delta of the Amudarya was re-directed to the Sarygamysh. Drainage basin of the lake is a flat lowland extending to about 70 km to the east of the lake, with an altitude of 58 m a.s.l (Orlovsky *et al.*, 2012).

The Sarygamysh Lake has been progressively increasing in size during the past decades due to the increasing inflow of water used for irrigation (Kostianoy *et al.*, 2014). The salty irrigation water from the fields carries an increasing amount of alluvial sediments as well as biogenic matter, admixtures of pesticides and fertilizers which deposit over a large area of old alluvial and modern sandy and sandy-clay sediments in the eastern side of Sarygamysh Lake (Lioubimtseva *et al.*, 2014). As a result, an increasing number of dust events were recorded in this region. Around 15% of total number of dust plume detected in the Karakum and Kyzylkum were originated from this region (Figure 5-13 b).

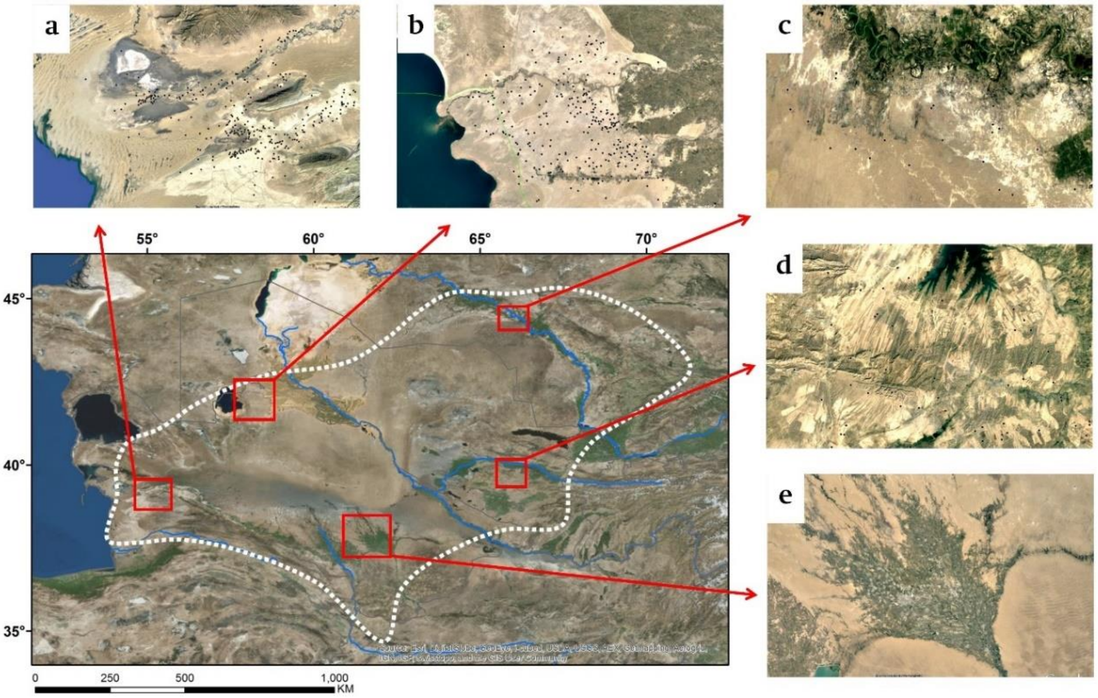

Figure 5-13. Location of active dust source regions in the Karakum and Kyzylkum: (a) Dry River Uzboy delta, (b) Sarygamysh basin, (c) Syrdarya River floodplain, (d) Kattakurgan Reservoir, and (e) Murghab River delta. Images from Google Earth Engine catalog (https://earthengine.google.com).

The sandy-clay plains at the downstream part of the Dry River Uzboy in western Karakum was another active source of dust revealed in our investigation. Although around 17% of DPS records between 2003 and 2012 were identified in this narrow deltaic region, there is a substantial lack of literature about dust processes in this area, mainly because this region is not usually regarded as a part of the Karakum desert in the major dust studies in Central Asia. The Kelkor Solonchak, an area located in flat lowlands between the Great Balkhans Mountains and the Kopetdag Mountains in south western Turkmenistan, was found to be an active source of salt and dust emissions during the study time period (Figure 5-13 a). Land surface in this region features solonchak-clay strips stretching west and north-west to the Gulf of Balkan in the south-east of Caspian Sea (Zonn *et al.*, 2012).

More than 11% of total DPS in the Karakum and the Kyzylkum were detected around inland deltas of the rivers Tejen and Murghab. These two trans-boundary rivers originate from the mountains of Afghanistan, flow westward and then northward to Turkmenistan before disappearing in the southern part of the Karakum desert (Figure 5-13 e). Along their path in southern Turkmenistan, they support agricultural fields within a narrow band of around 2km before forming two typical alluvial fans at the eastern side of the Kopetdag Mountains. For centuries, these fertile alluvial plains have been cultivated and hosted a vast network of historic and modern canals that weave through the alluvial fans (Babaev, 1994). The fans landscape is varied and consists of riparian woodlands and managed agricultural landscapes of the alluvial plain changing to the sparsely vegetated desert environment beyond (Markofsky *et al.*, 2017). The DPS were mainly recorded in the northern margins of the alluvial fans which are largely composed of the sandy-clay deposits of the pra-Amudarya (ancient Amudarya channels), overlain with the deltaic sediments of the Tejen and Murghab rivers. The whole territory is covered by laminated grey sands of very homogeneous composition, with thin inter-beds of dark clays (Zonn *et al.*, 2012).

Agricultural activities are believed to be the main contributor to dust emissions from the southern Kyzylku. In particular, the occurrence of numerous DPS correlates well with land areas under dryland farming in Samarkand region, Uzbekistan. Poor farming techniques can leave the ground vulnerable to wind erosion, especially if the storms strike at a particularly vulnerable time, e.g. the fallowing period when vegetation cover is minimum (Gillette *et al.*, 1988). A clear example of the typical source areas in this region is shown in the satellite snapshot of the Kattakurgan Reservoir and surrounding agricultural lands (~40 km west of Samarkand), acquired by GeoEye-1 satellite in 2008 (Figure 5-13 d).

Towards the north of Kyzylkum, DPS were scattered along the floodplains of Syrdarya River in southern Kazakhstan. During the period between 2003 and 2012, more than 160 DPS were recorded along the nearly 400 km of the river, from Otyrar district in southern Kazakhstan to Kyzylorda region in eastern side of the Aralkum. Landscape in this region is mainly characterised by large irrigated and rain-fed agricultural fields which are constantly exposed to numerous forms of water and wind erosion, leading to loss in soil fertility and reducing arable land (Baitulin, 2001). DPS were detected on both the western side of the river where sandy loam soil formed from the alluvial plain of the Syrdarya, and eastern side between the river valley and piedmonts of the Karatau Mountains (Figure 5-13 c).

5.3.2.2. Inter- and intra-annual variability in dust emission

Figure 5-14 illustrates inter- and intra-annual variations in dust activities in the Karakum and Kyzylkum deserts. Despite high variation in the number of dusty days between 2006 and 2009, there has been a gradual increase in the number of dusty days during the overall study time period. More than 80 dusty days per year were recorded days in 2011 and 2012, comparing to 30 annual dusty days in the first three years. The highest intensity of dust events was also recorded in 2011. Analysis of monthly variations in dust activities in this region shows that the highest number of dusty days were recorded in summer season. Around 45% of dusty days were observed in the three months between July and September with the highest number of dusty days in August. The number of DPS per dusty days however reached its maximum in March, which indicates a potentially stronger dust events in this month.

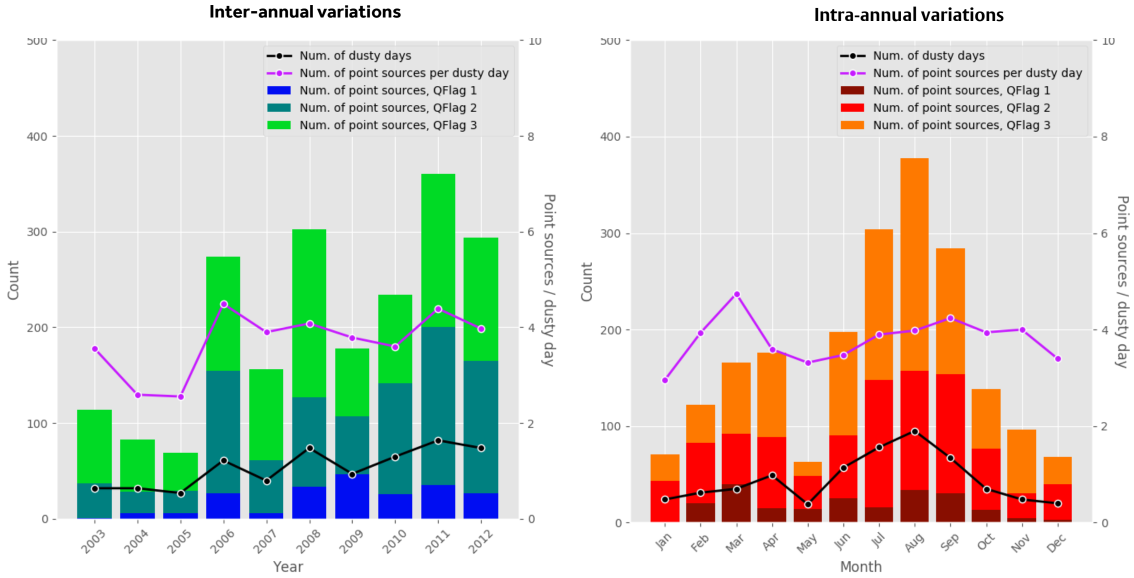

Figure 5-14. Inter-annual and intra-annual variation in the number of dusty days and DPS in the Karakum and Kyzylkum. Black line shows the number of dusty days and the purple line shows the average number of DPS per dusty day.

5.3.2.3. Synoptic controls on dust emission and dust transport pathway

Seasonal synoptic pattern of dusty days in the Karakum-Kyzylkum region is similar to that observed for dusty days in the Aralkum, with a prevailing high pressure system over temperate latitudes in spring, fall and winter (Figure 5-15). As illustrated by Orlovsky *et al.* (2005), climate in this region is significantly influenced by the southwestern peripheries of the eastern anticyclone, and cold air intrusions from north, northwest and northeast are a common characteristics of weather circulations in spring and cold months. MSLP for dusty days in summer shows an intensified low pressure (less than 1000 hPa) characterising the Asiatic thermal depression extending from Arabian Peninsula through Persian Gulf and to northern India. This results in a change in trajectories of westerly cyclones of the temperate zone from west–east to north–south direction in summer, as demonstrated by Lioubimtseva *et al.* (2009) and Groll *et al.* (2013).

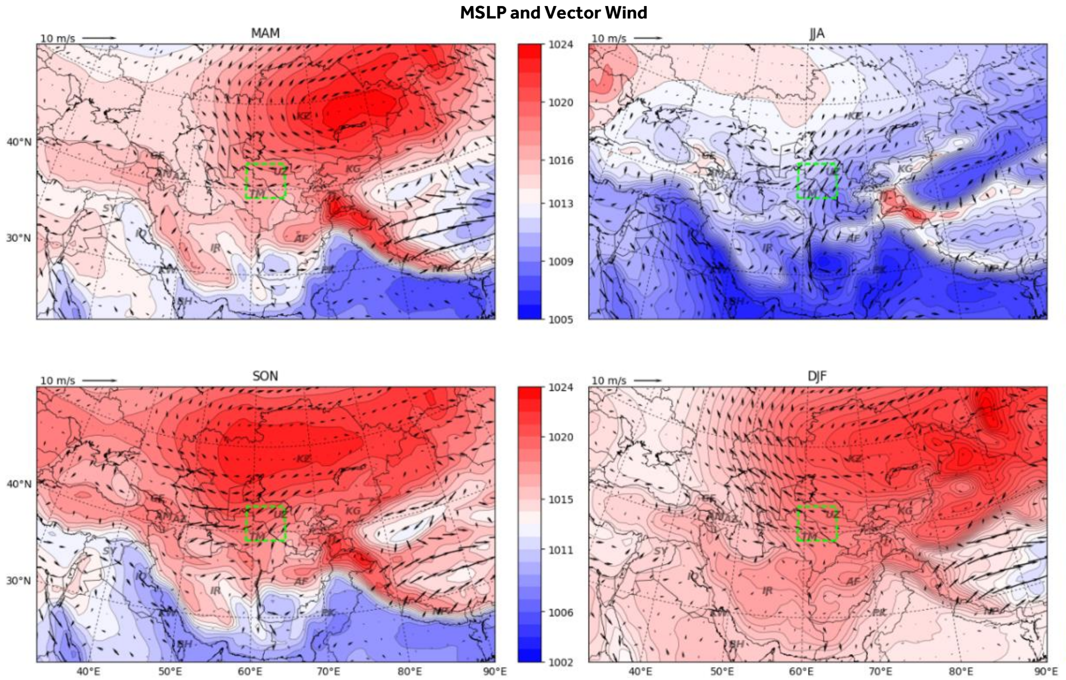

Figure 5-15. MSLP and vector wind for dusty days in the Karakum-Kyzylkum, 2003 - 2012. The centre of region is depicted by a green rectangle.

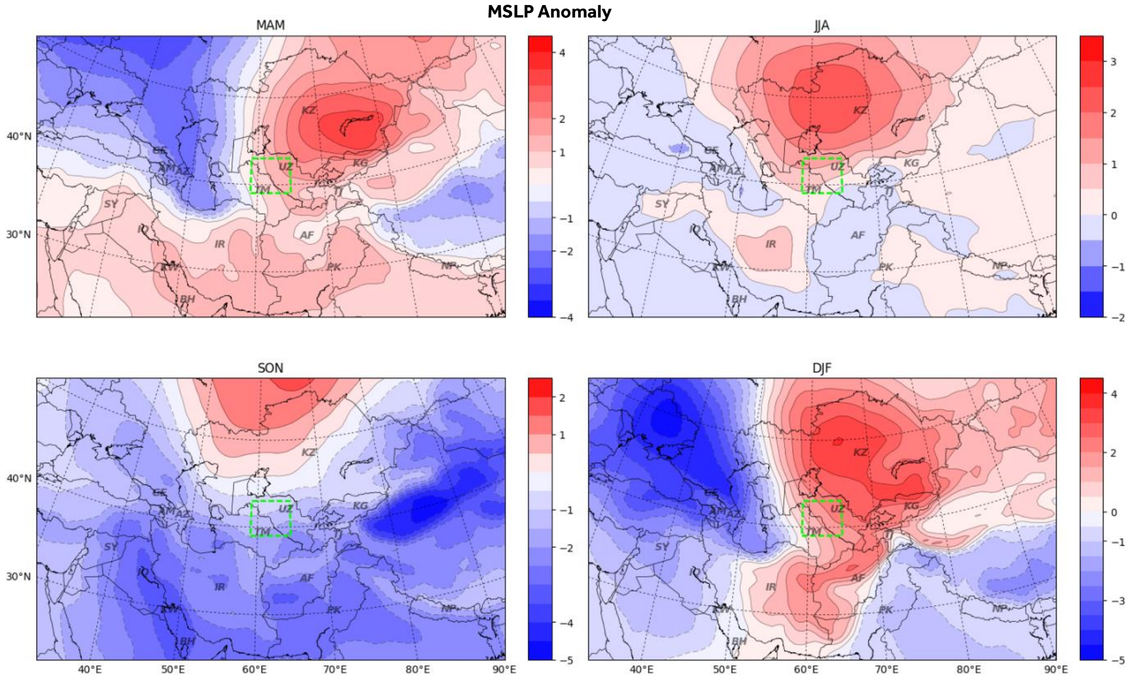

Figure 5-16. MSLP anomaly for dusty days in the Karakum-Kyzylkum , 2003 - 2012. The centre of region is depicted by a green rectangle.

As shown in Figure 5-16, MAM dusty days coincide with a high pressure anomaly centred over Lake Balkhash in eastern Kazakhstan and a low pressure anomaly over Eastern Europe. High gradient of pressure anomaly over the Karakum and Kyzylkum leads to converging surface wind towards the west and north-west (Figure 5-15). The centre of the high pressure anomaly moves to northern Kazakhstan in summer and autumn, causing the change in wind trajectories towards south and south-west. The MSLP anomaly map for summer shows that dust events are associated with high pressure anomalies north of the region. MSLP anomaly pattern for dusty days in in winter is similar to spring anomalies, however the anomaly is notably higher than in spring which may be due to intensification of Siberian High in winter and its effect showing in March MSLP only.

The results of analysis of the wind anomaly of dusty days in Karakum and Kyzylkum are presented in Figure 5-17. It shows that except JJA, the wind anomaly is normally higher in the western and south-western part of the region. North-easterly and north-westerly winds in this part of the region are diverted to west and north-west over the piedmonts of Kopet Dag mountains in south of Karakum desert (Orlovsky *et al.*, 2005). Wind anomaly pattern in the JJA plot is characterised by two high anomaly regions: (i) over the western Karakum which lead to dust emission from the Sarygamysh basin and the Uzboy valley, and (ii) over the eastern and central Kyzylkum, which is responsible for dust uplift from the Syrdarya floodplains and Samarkand region.

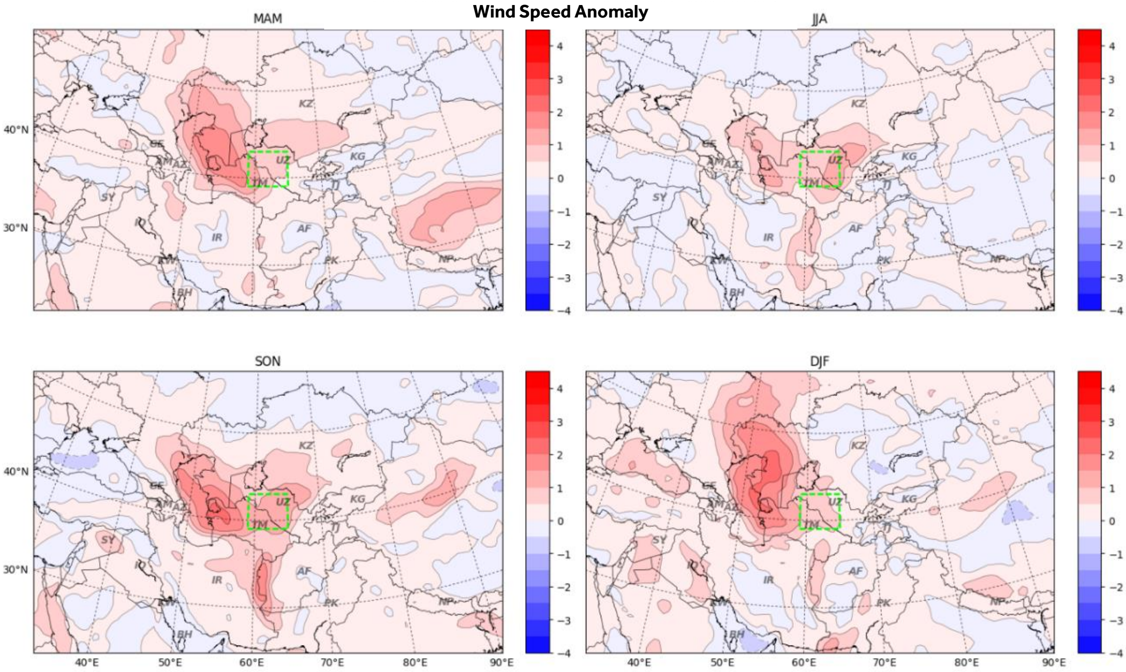

Figure 5-17. The near-surface (10 m) wind speed anomalies for the dusty days in the Karakum-Kyzylkum, 2003 - 2012. The centre of the region is depicted by a green rectangle.

In contrast to the Aralkum, wind speeds initiating dust entrainment in the Karakum and Kyzylkum do not show strong seasonal variations. Wind speeds in the range of 5 to 8 m s^{-1} are responsible for the highest proportion of dust events in all seasons (Figure 5-18). This is followed by the wind speeds of 8-10 m s^{-1}. The highest percentage of strong winds above 10 m s^{-1} was recorded in summer (15%

of days in JJA), which is correlated with the highest number of dusty days in this season (see Figure 5-14).

Analysis of recorded wind directions revealed a dominant direction of westward dust entrainment in all seasons except in summer (Figure 5-19). Wind directions over this region change towards south and south-west in summer along the periphery of the Asiatic thermal depression which dominates the, as demonstrated by Orlovsky *et al.* (2005) and Groll *et al.* (2013).

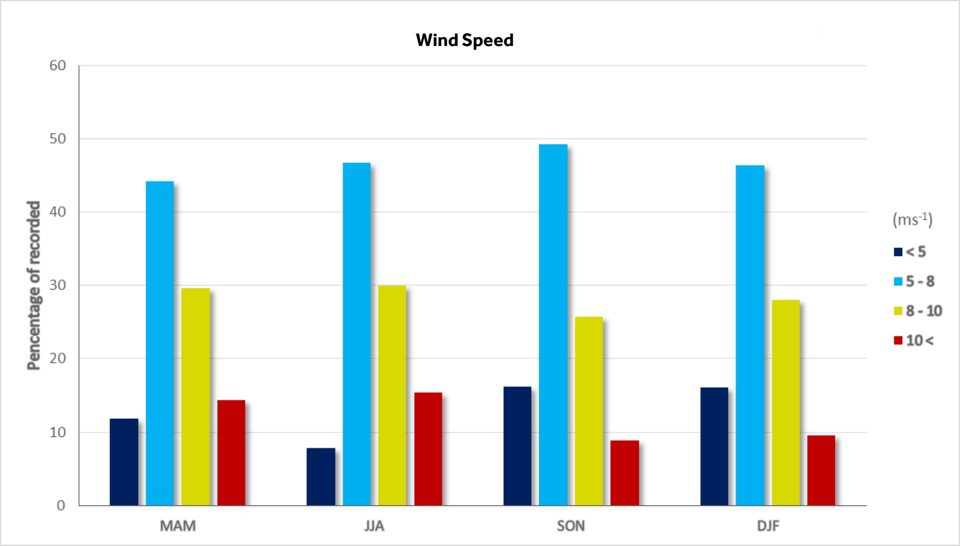

Figure 5-18. Seasonal distribution of 10 m wind speeds for DPS records in the Karakum-Kyzylkum, 2003-2012.

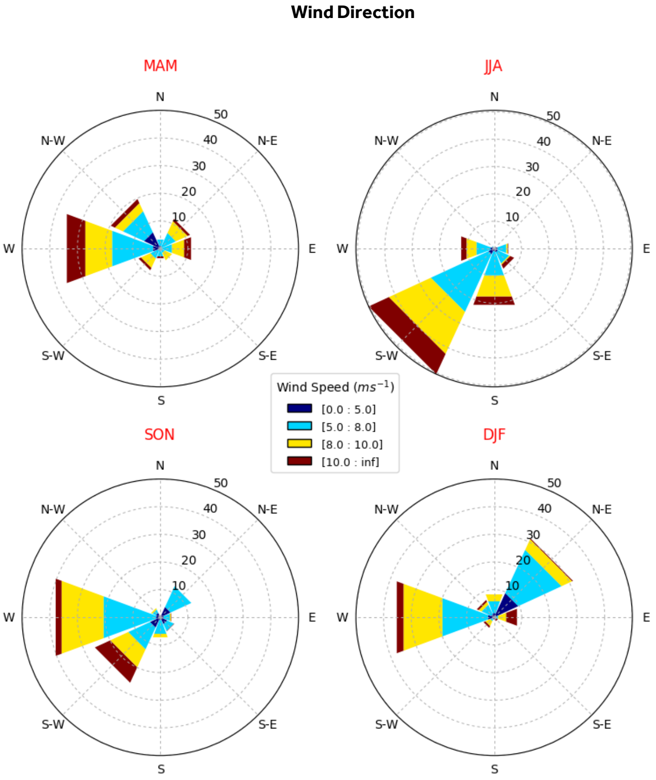

Figure 5-19. Direction of entraining winds for DPS in the Karakum-Kyzylkum region.

5.3.3. Taklamakan

5.3.3.1. Land surface characteristics

The Taklamakan Desert is located in the centre of the Tarim Basin, a terminal basin surrounded by the Pamir Mountains in the west, Tibetan Plateau in the south and the Tian Shan Mountains in the north. It is one of the world's largest sandy deserts, and the largest desert in Asia, with sand dunes that can reach 100 to 300 m high. The complex wind patterns have created a great diversity of sand formations, including longitudinal transverse and star dunes in the region (Harris, 2003). There are some gravel plains and internal mountains in the western part of the Taklamakan, and the water table can be within 2 m of the surface. There are also extensive marginal fans and lake sediments associated with the desiccated lakes (Xuan *et al.*, 2002; Washington *et al.*, 2003; Che *et al.*, 2013).

The Tarim River, the longest inland river in China, runs along the north side of the Taklamakan from west to east. It is fed by three main tributaries: Yarkand which originates from the Karakoram Mountains, Kashgar sourced in the eastern parts of the Pamir Mountains, and the Aksu which has its sources in the Tian Shan Mountains (Figure 5-20). Prior to the construction of reservoirs and irrigation systems in the mid-20th century, the Tarim River emptied in the Lop Nur, a lake system at the eastern opening of the Tarim basin. It is now a salt-encrusted lake bed and the river's waters now drain sporadically into Taitema Lake, which is located about 160 km southwest of the Lop Nur (Middleton *et al.*, 1986).

The highest concentration of DPS in the Taklamakan was observed along the eastern margins of the basin, where strong easterly winds entrain sand and fluvial deposits on the floodplains of the Tarim and Konqi rivers and also the Lop Nur lake bed. The wind-swept yardangs (wind-eroded ridges) and salt crust ranging from 30 cm to 1 m in thickness are the predominant landscape features in this part of the basin. More than 2,200 DPS were recorded in this region between 2003 and 2013, comprising more than 50% of the total DPS records in the Taklamakan region.

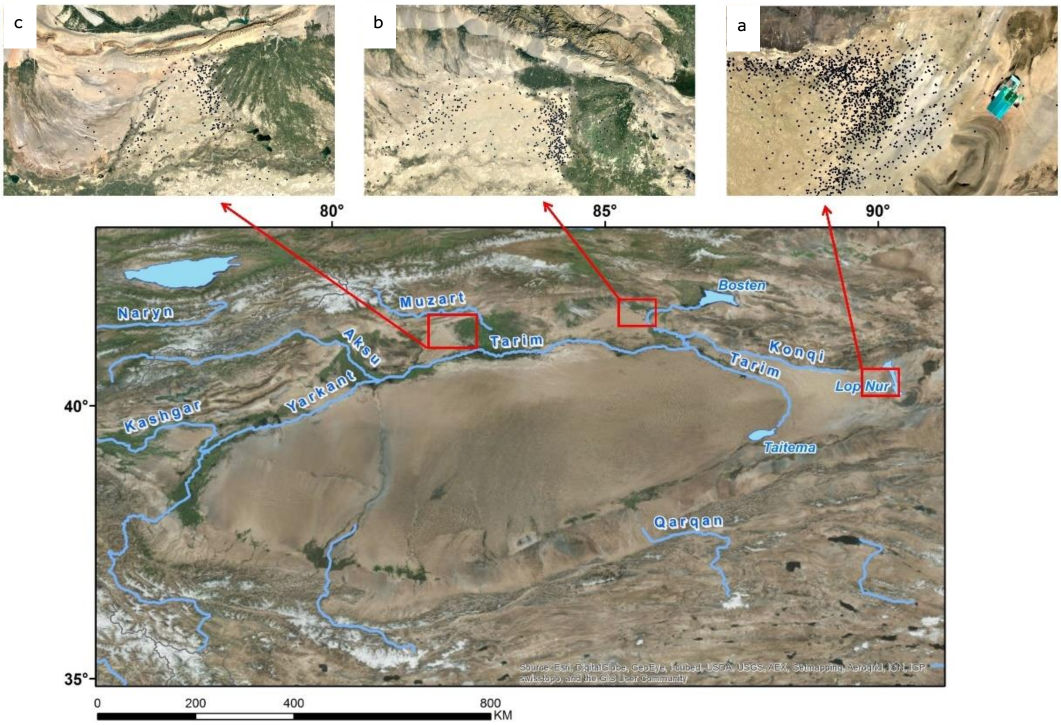

Figure 5-20. Major rivers and lakes in the Tarim Basin. Image subsets are for: (a) Lop Nur lake, (b) Korla region, and (c) Aksu alluvial fans. DPS are shown by black dots in the image subsets. The background image from GeoEye and Landsat, obtained from Esri® and Google Earth Engine catalog (https://earthengine.google.com).

Around 48% of the annual runoff of the Tarim River is supported by glacial melt waters (Rittner *et al.*, 2016), therefore tributaries with glaciated catchments are very important sources of sediment for the basin. 60 - 80% of the Tarim annual runoff occurs in the high-flow season between June and August, carrying more than 80% of its annual sediment load (Ye *et al.*, 2014). During most of the remaining months, a combination of high temperature and falling river stage allows the alluvial fans and flood plains to dry out and become potentially prone to wind erosion. A vast area of dry lands at the margins of the agricultural regions of the Konqi alluvial fan in the north-eastern Taklamakan was one of the most active dust sources in the study (Figure 5-20-b). Around 13% of the total DPS in the

Taklamakan region were identified in this area. The abundant farmland, dried river beds and desiccated drainage channels receive a large volume of alluvial sediment with discharge from the irrigated agricultural fields in the Korla region, as well as several small fluvial systems on the foothills of the Tian Shan Mountains in the north.

The Aksu River drainage basin delivers a significant amount of sediment to the Tarim River while contributing to 70–80% of the annual flow of the river (Kundzewicz *et al.*, 2015). More than 380 DPS (~9%) were recorded over the alluvial plains spreading between the delta of the Aksu and the alluvial fan formed by the Muzart River in the northern part of the Taklamakan (Figure 5-20-c). DPS were observed primarily at the margins of agricultural lands, where the landscape is mainly composed by the abandoned farmland, degraded lands and sand dunes. A strip of semi-active dust-generating surfaces extends from the Aksu basin along the floodplains of the Yarkand River to the delta of the Kashgar River in north-western edges of the Taklamakan desert. Overgrazing and poor farming have rapidly exhausted the semiarid grasslands fringes at the western parts of the Taklamakan contributing to the development of dust storms (Rittner *et al.*, 2016).

5.3.3.2. Inter- and intra-annual variability in dust emission

Figure 5-21 illustrates the temporal variations of dusty days in the Taklamakan between 2003 and 2012. As expected, the number of annual dusty days are significantly higher than in other regions with the peak number of dusty days more than 110 days in 2006. There was no clear trend in the inter-annual variation of dusty days in this region. Analysis of intra-annual variations showed that dust events in this region peak in March and April. Over the ten year period, more than 110 and 120 dusty days were recorded in March and April, respectively.

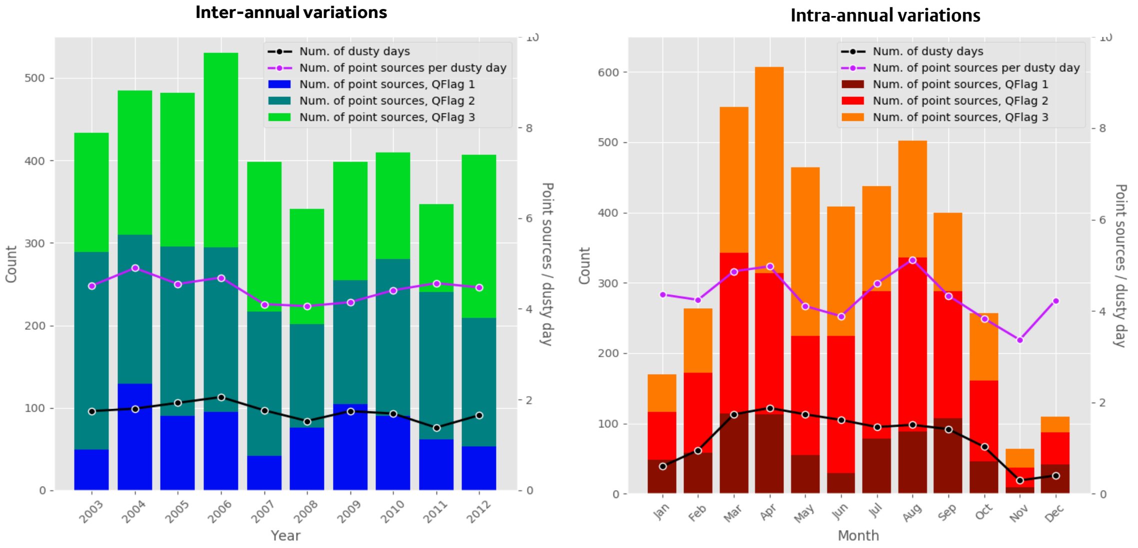

Figure 5-21. Inter-annual and intra-annual variation in dusty days and DPS in the Taklamakan desert. Black line shows the number of dusty days and the purple line shows the average number of DPS per dusty day.

There was also a remarkably high number of dusty days observed in the summer months, with a secondary peak in August. The ratio of DPS per dusty days also peaks in August. It should be noted, however, that only a small fraction of DPS observations are made with a high degree of confidence (QFlag = 1), comparing to lower quality observations. This may be explained by the fact that strong dust storms in this region usually lead to formation of extensive dust clouds which partially mask the down-wind point sources, making it difficult for the operator to distinguish the activated DPS in the DEP images. It is also due to unique nature of dust transport in this closed basin. The elevated dust plumes originated from the eastern parts of Taklamakan usually circulate inside the closed basin for several days, being blocked by the high mountains surrounding the basin. This makes it hard for the operator to establish the precise location of the DPS.

5.3.3.3. Synoptic controls on dust emission and dust transport pathway

Atmospheric circulations and more specifically the near-surface wind speed and wind direction in the Taklamakan are significantly shaped by the topography in this region. Cold air outbreaks from the north and north-west of China are usually funnelled into this basin from its opening in the east, causing large scale dust storms that affect the entire area inside the basin (Xuan *et al.*, 2000; Sun *et al.*, 2001). This circulation pattern is also evident in the westward moving sand dunes formed in the eastern and central parts of the Taklamakan, which indicates prevailing easterly winds in this region (Rittner *et al.*, 2016). Analysis of MSLP composites and vector winds for dusty days in Taklamakan shows the dominance of the anticyclone circulations in MAM which are associated with formation of high pressure systems over the eastern Kazakhstan and western Mongolia region

(Figure 5-22). Strong surface winds forming at the southern peripheries of these anticyclones are channelled into the Tarim basin from its eastern opening, causing strong dust storms in spring season. MSLP anomaly for MAM also shows a gradient between high pressure anomaly in the north of Tian Shan Mountains and low pressure anomaly inside the basin (Figure 5-23). The frequency and intensity of high pressure systems diminish during summer due to the surface heating and thermal depressions formed inside the Tarim basin. MSLP anomalies, however, are similar to those observed in spring exhibiting the same dipole pattern with high pressure anomalies in the north (which are weaker than in spring) and low pressure anomalies in the south (which are stronger than in spring).

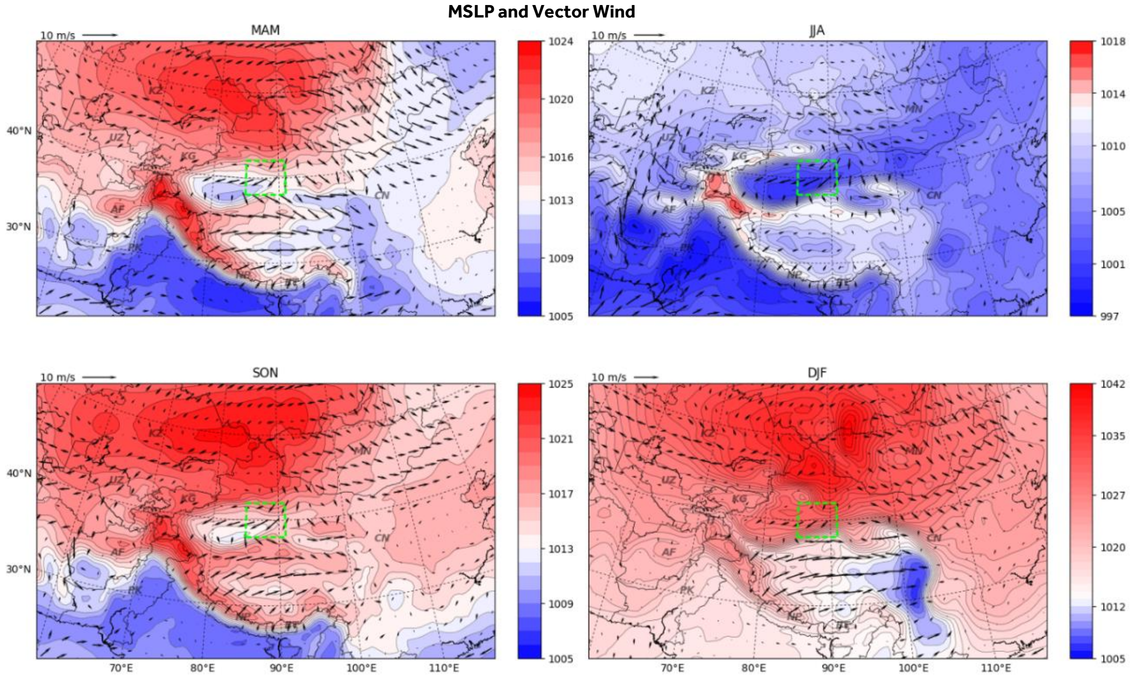

Figure 5-22. MSLP and vector wind for dusty days in the Taklamakan between 2003 and 2012. The eastern Taklamakan is depicted by a green rectangle.

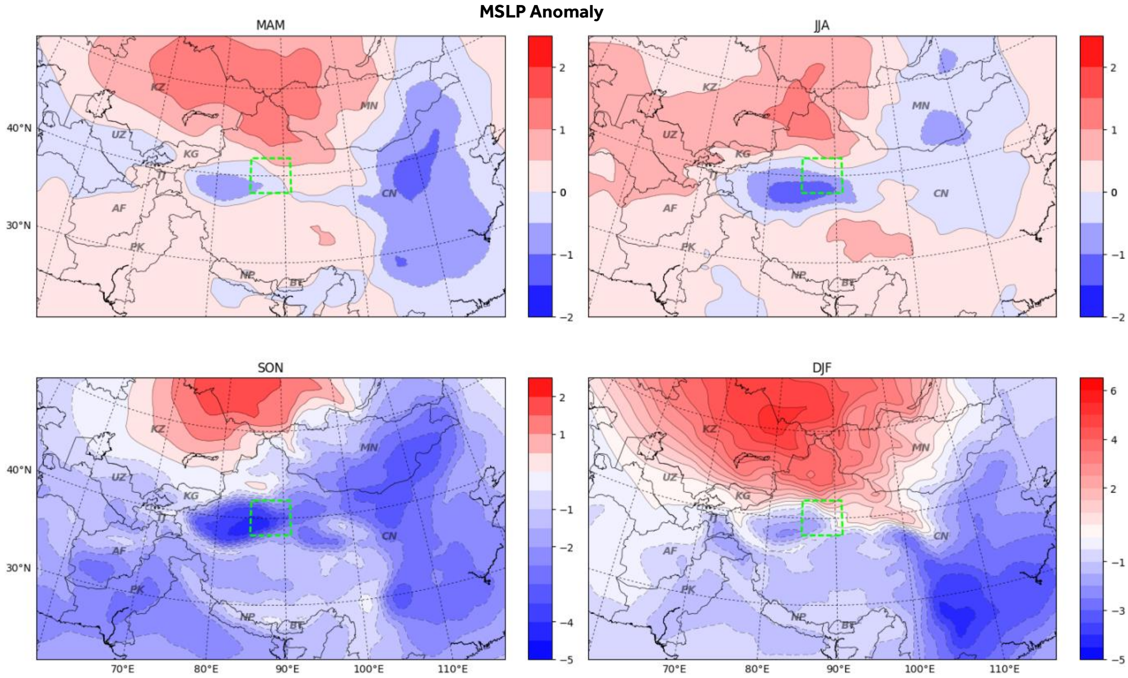

Figure 5-23. MSLP anomaly for dusty days in the Taklamakan between 2003 and 2012. The eastern Taklamakan is depicted by a green rectangle.

The most extreme low pressure anomalies were observed over the Tarim basin in SON with the MSLP anomaly value reaching to -5 hPa. Combined with the intensification of high pressure systems over higher latitudes, it creates strong pressure gradients and leads to strong intrusions of cold air into the basin from the east. The effect of this strong gradient is evident in wind anomaly composites for SON and DJF, where a relatively strong wind speed anomaly was observed over eastern entry of the basin. The same pattern was observed in spring and summer, but with smaller anomaly values (Figure 5-24).

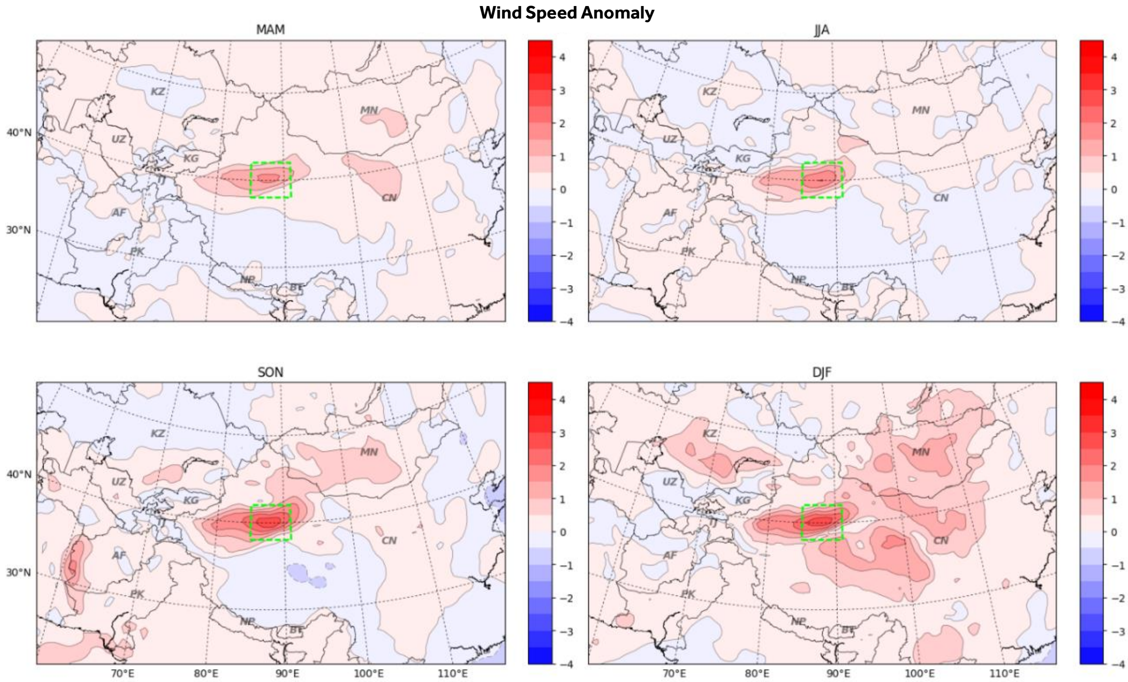

Figure 5-24. Near-surface (10 m) wind speed anomaly (m s^{-1}) for dusty days in the Taklamakan between 2003 and 2012. The eastern Taklamakan is depicted by a green

To investigate thresholds and distributions of speed and direction of wind leading to dust storm formation in Taklamakan, the eastern/northern and western/southern sectors of the Taklamakan were analysed separately. Analysis was performed for these sectors separately because the eastern and northern areas are affected by a different wind pattern than the western and southern areas of the desert. Seasonal cycles of wind speed for the DPS records in these sectors of the Taklamakan desert is shown in Figure 5-25. The most striking result is a low wind speed threshold enabling dust events as shown by a high share of low speed winds in DPS records for all sectors of the Taklamakan. In the east and north of the Taklamakan, nearly 50% of DPS activations in spring and winter were associated with wind speeds less than 5 m s^{-1}. This feature is even more pronounced for DPS records in the western and southern parts of the desert, with low wind accounts for 90% of the observed wind speed records in winter. This is in excellent agreement with the findings of Ginoux *et al.* (2017) who obtained low wind thresholds (< 5 m s^{-1}) for dust sources in Tarim basin. The proportion of stronger winds activating DPS are generally higher in eastern and northern areas than in the western and southern regions. This is because the incoming winds from the eastern opening of the basin slow down as they travel across the Taklamakan basin being also channelled by the high mountains surrounding the Tarim basin.

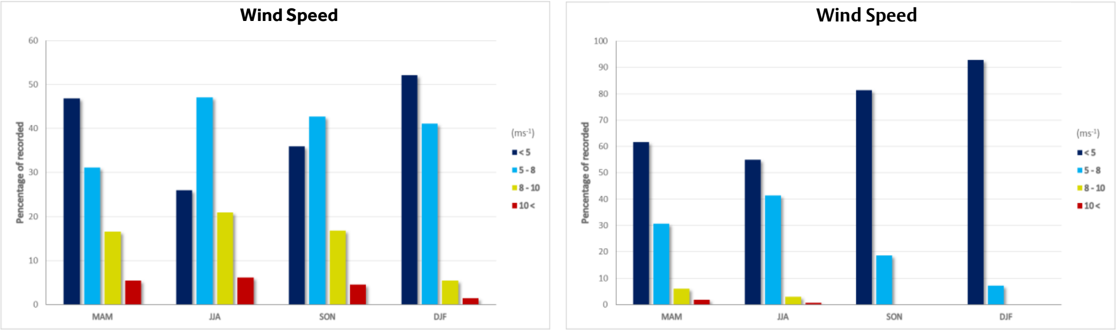

Figure 5-25. Distribution of 10 m wind speeds for DPS records in the east and north of the Taklamakan (left panel) and west and south of the Taklamakan (right panel) between 2003 and 2012.

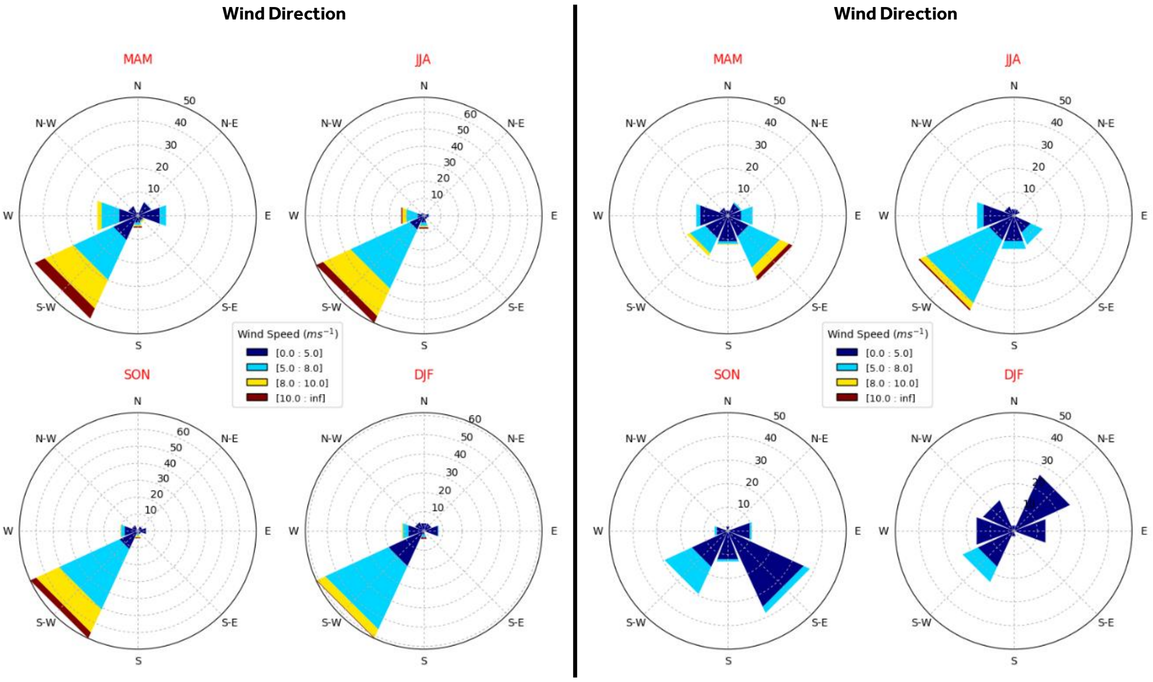

Figure 5-26. Direction of entraining winds for DPS in the east and north of Taklamakan (left panel) and west and south of the Taklamakan desert (right panel).

As shown in Figure 5-26, the dominant direction of entraining winds in the eastern and northern sectors was towards south-west, corresponding to the frequent easterly winds in this part of the region. The distribution of wind directions in the western and southern region however shows a much higher diversity. This is due to the complex atmospheric circulations within this closed basin, as demonstrated by Uno *et al.* (2005) and Aoki *et al.* (2005).

5.3.4. Pre-Aral

5.3.4.1. Land surface characteristics

Vegetation cover has a crucial role in reducing aeolian activities through increasing surface roughness, which results in reducing near surface wind velocities and increase in sediment deposition (Strong *et al.*, 2010). It can also plays an important role in surface stabilization through formation of biological crusts (Belnap *et al.*, 1998). Removal of vegetation cover either by fire or overgrazing can lead to the enhanced wind erosion of the exposed soils. Analysis of spatial characteristics of DPS and investigation of high resolution satellite images revealed that aeolian activities at the Pre-Aral region were mainly associated with degradation of vegetation due to wildfire and grazing in higher latitude regions (46N-50N).

In the 10 year record of observations of daily DPS activations in Central Asia, strong links between extensive degradation of vegetation, caused by wild fire episodes in the Pre-Aral region, and increasing number of DPS records were observed. Figure 5-27 shows MODIS DEP images of one of these fire episodes in the Betpak Dala desert, Kazakhstan, where consecutive dust events and biomass burnings occurred at multiple locations in the course of four days between 20 and 23 June 2004. The biomass burning smoke in DEP images appears in cyan (similar to clouds) and dust is enhanced as shades of red/pink. In addition to clear smoke plumes in the scene, investigation of MODIS Burned Area Monthly L3 (MCD45A1) dataset for June 2004 also confirmed the presence of wildfire episodes in this region (see 22 June 2004 in Figure 5-27).

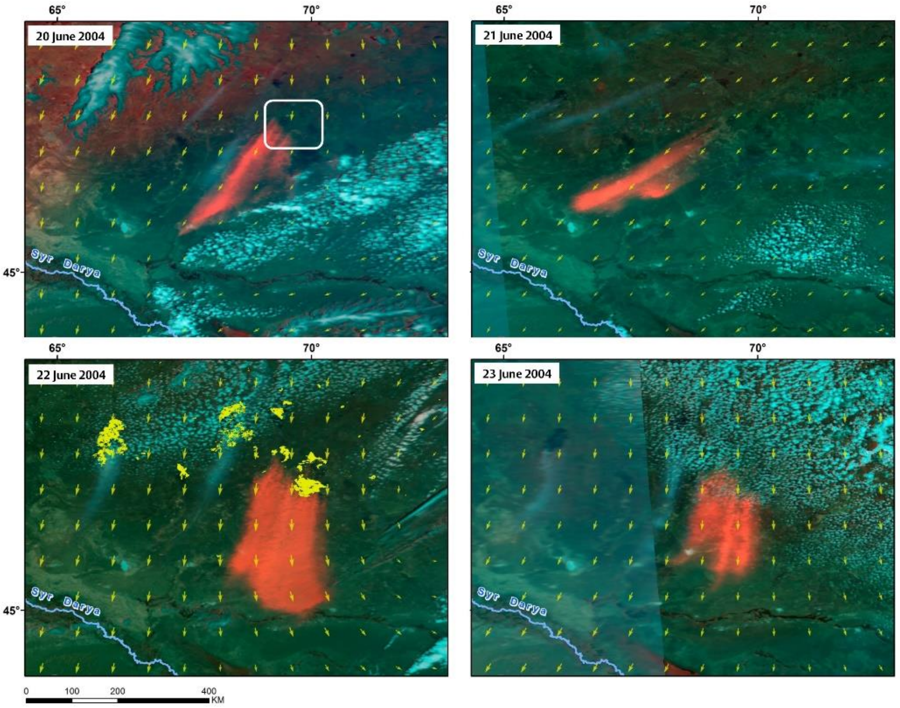

Figure 5-27. DEP images from wildfire and dust events in the Betpak Dala desert, Kazakhstan, 20 - 23 June 2004. The sources of durst storms are shown by white rectangle. The extent of burned area from MODIS Burned area products (MCD45A1) are shown in yellow colour in DEP image for June 22.

Wild fires leave clear scars on the ground (also referred to as fire scars) that are detectible on the satellite and aerial imagery. Visual examination of the annual composites of Landsat 7 ETM+ revealed a series of discernable firescar which emerged right after the wildfire event in June 2004 (Figure 5-28). This event left large fire scars in the area with a size of approximately 17,000 km^2, previously covered by temperate shrublands and grasslands. The amount of time that it takes for the vegetation and biological crust to be restored over the burned areas and stop generating dust storms is determined by a combination of burn severity, soil type and climate (Strong *et al.*, 2010). For this specific event, the burned area remained an active source of dust for 5 years. This long recovery time is evident in satellite images of the fire scars which shows the gradual re-establishment of the vegetation cover during the 5 years after the complete removal of surface vegetation in 2004 (Figure 5-28).

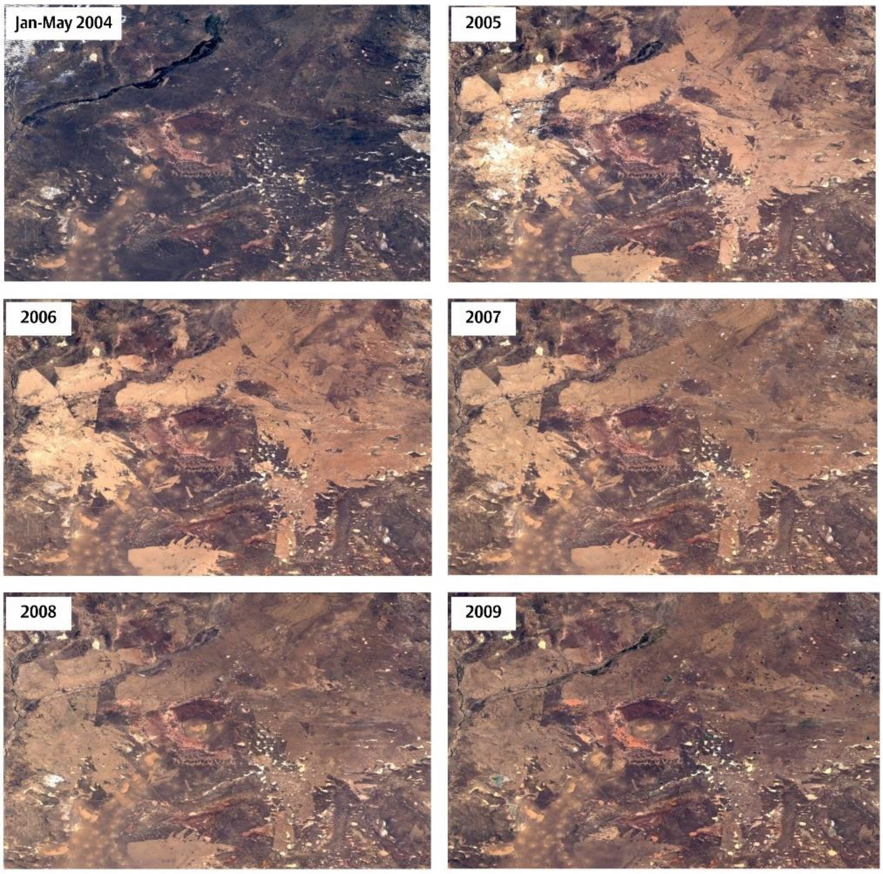

Figure 5-28. True colour Landsat 7 ETM+ annual composites from prior to the wildfire episode (2004; top left) and the following years. Images were acquired from Google Earth Engine Catalog (https://earthengine.google.com).

Developments of wild fires were observed on several occasions in this region during the study period. Except a few burned areas, which regained their vegetation cover shortly after the wet season, they usually remained active sources of dust for several years. The spatial link between DPS activation and removal of vegetation was observed all across the region, from the Kazakh steppes to Caspian lowlands, regardless of the altitude of the region.

5.3.4.2. Inter- and intra-annual variability in dust emission

The results for the inter- and intra-annual trends of dusty days in the Pre-Aral region are presented in Figure 5-29. It shows that from 2003 to 2006 there was a steady increase in the number of dusty days, number of DPS and the DPS ratio in this region. A sharp fall in the number of dusty days was observed in 2007, following by a fluctuating pattern during the rest of the ten year period. The average number of activated DPS reached to over 6 DPS per dusty day, the highest number during the time period. Contrary to the Aralkum, the highest number of dusty days were recorded in August and September, with 74 and 73 dusty days respectively. Although few dusty days were recorded in November (a total of 12 dusty days during 10 year), the highest number of DPS per dusty days were observed in this month. Also more than 90% of DPS records in this month had a high quality (QFlag = 1).

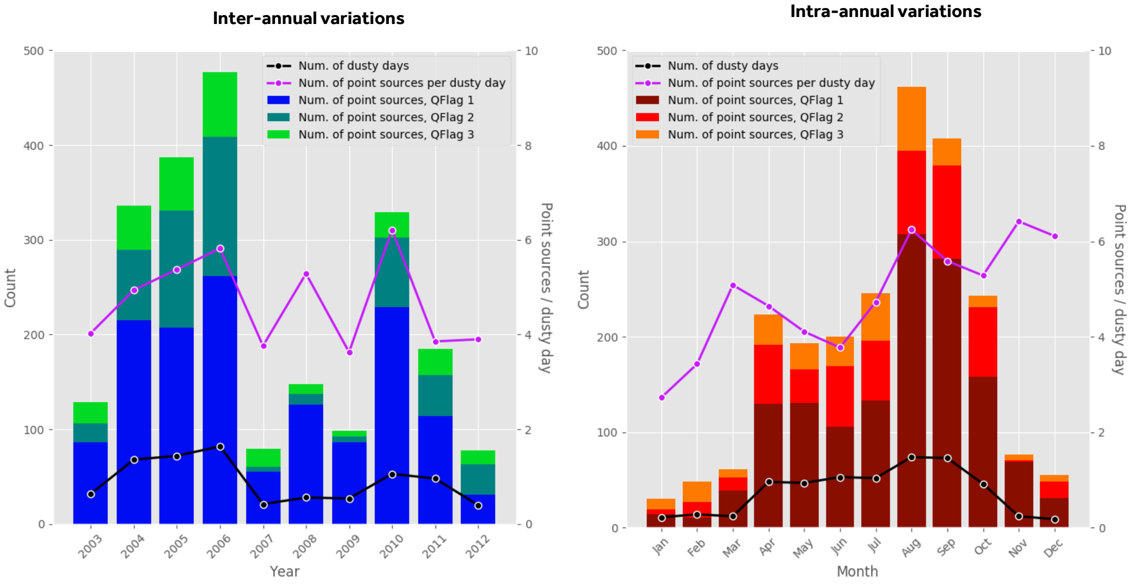

Figure 5-29. Inter-annual and intra-annual variation in dusty days and DPS in the Pre-Aral region. Black line shows the number of dusty days and the purple line shows the average number of DPS per dusty day.

5.3.4.3. Synoptic controls on dust emission and dust transport pathway

Synoptic patterns for dust outbreaks in the Pre-Aral were characterised by high pressure systems centred over eastern Kazakhstan in MAM, SON and DJF, the Asiatic thermal low in JJA, stretching from the Taklamakan to the Arabian Peninsula (Figure 5-30). A strong dipole pattern and a sharp gradient between the high pressure anomalies and low pressure anomalies over the dust source region was observed in all seasons. A noticeable dynamic of the MSLP anomaly for dusty days in this region was the shift in the centre of the high pressure anomaly in JJA towards the west and formation of low pressure anomalies on the east side of the Pre-Aral region (Figure 5-31).

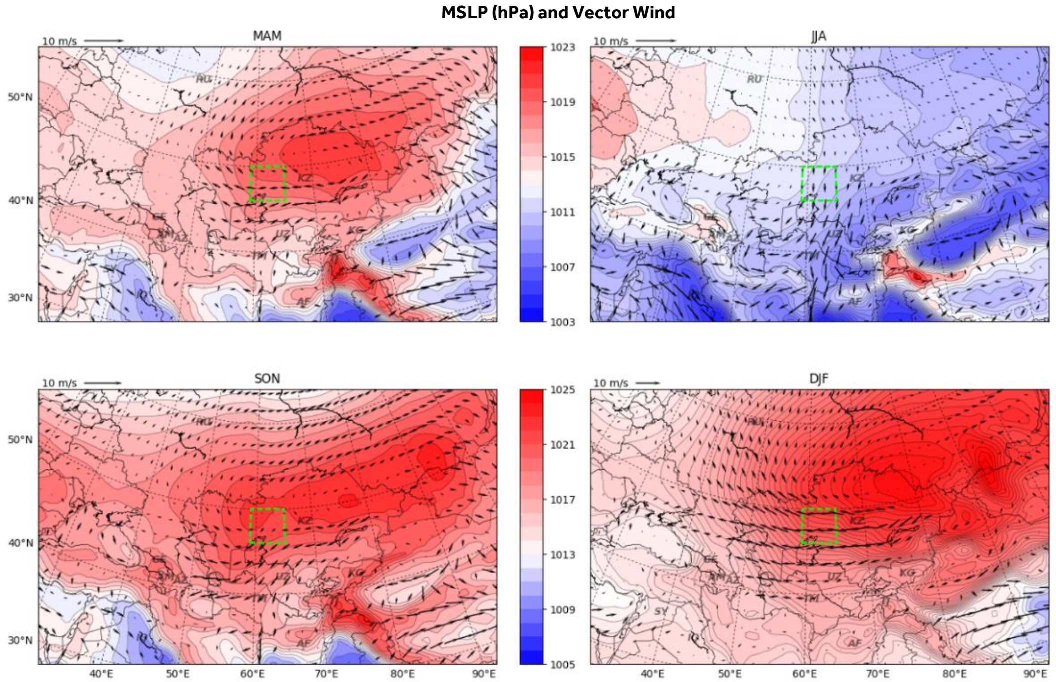

Figure 5-30. MSLP (hPa) and vector wind for dusty days in the Pre-Aral, 2003 - 2012. The centre of region is depicted by green rectangle.

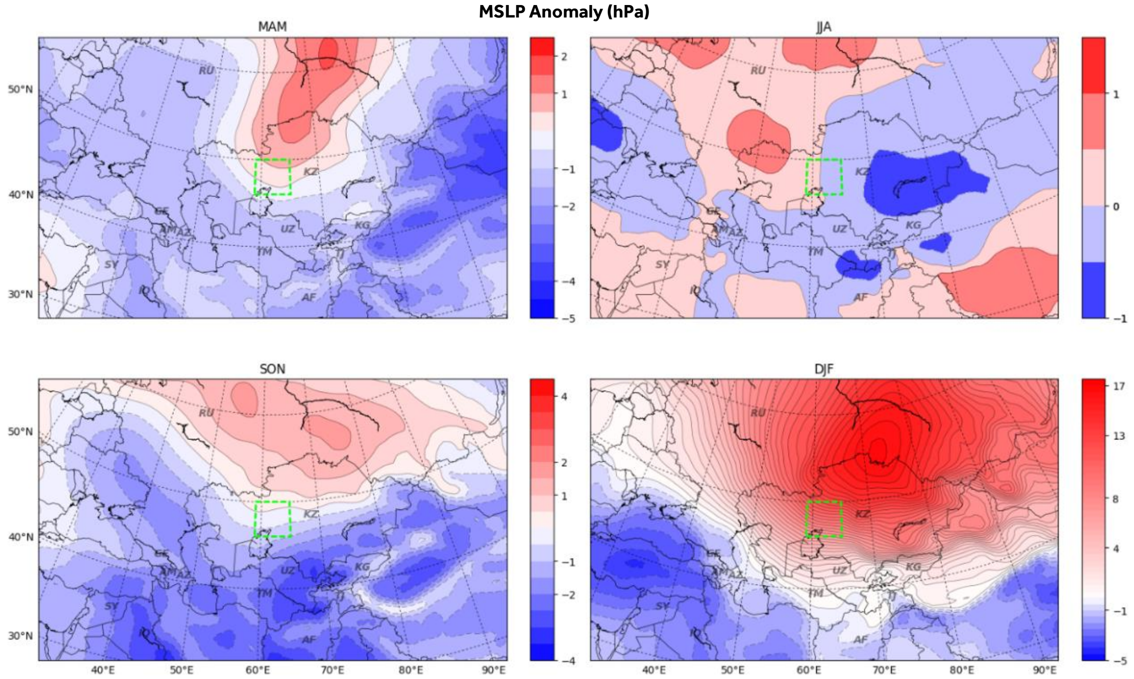

Figure 5-31. MSLP anomaly (hPa) for dusty days in Pre-Aral between 2003 and 2012. The centre of region is depicted by green rectangle.

Spatial and seasonal variations of wind speed anomalies of dusty days in the Pre-Aral region are shown in Figure 5-32. A positive anomaly was observed in this region in all seasons, with the highest values in DJF where eastern part of the region is dominated by a strong wind anomaly of up to 4 m s^{-1}. It is consistent with the high pressure system formed in the eastern side of the region during winter months (Figure 5-31).

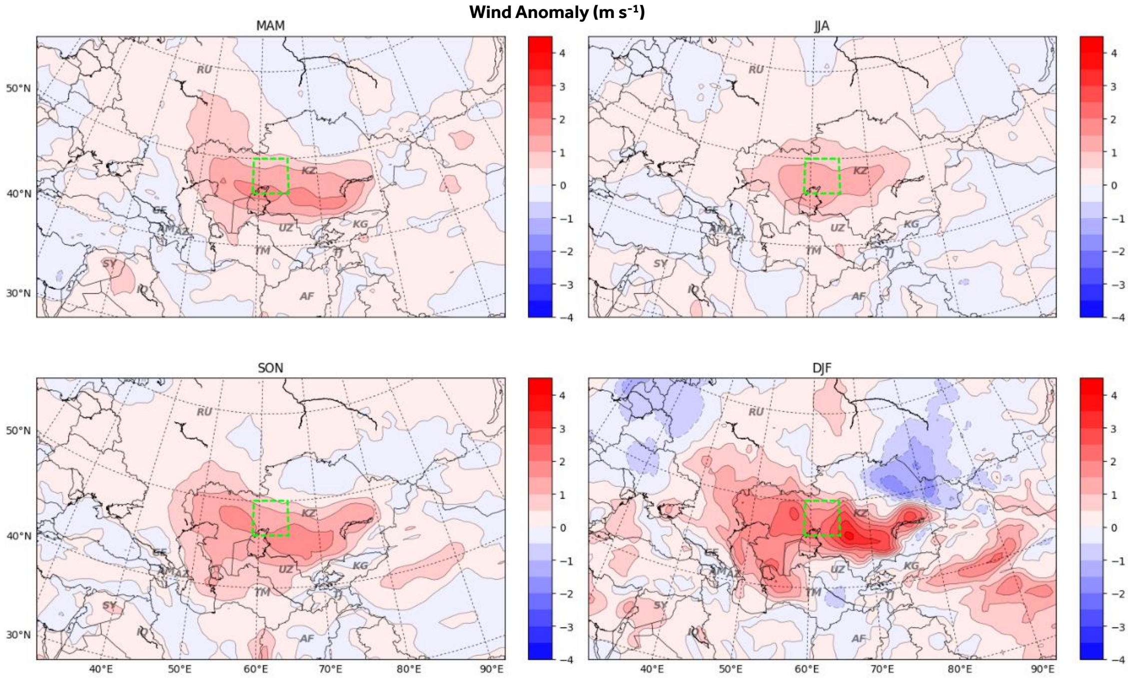

Figure 5-32. Near-surface wind anomaly (m s^{-1}) for dusty days in Pre-Aral between 2003 and 2012. The centre of the region is depicted by green rectangle.

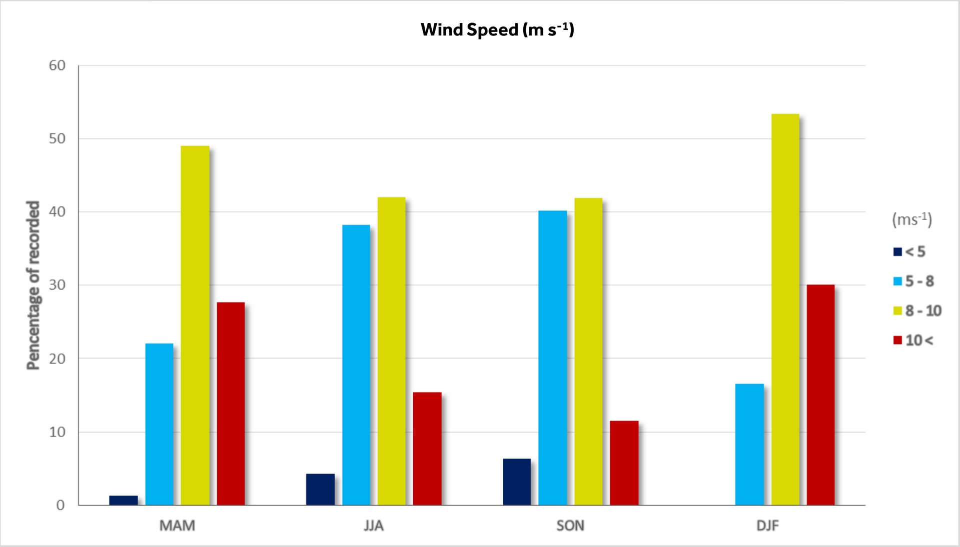

Figure 5-33. Distribution of 10m wind speeds (m s^{-1}) for DPS records in Pre-Aral between 2003 and 2012.

Dust emissions in the Pre-Aral region were found to be mainly associated with above moderate (8-10 m s^{-1}) and strong winds (> 10 m s^{-1}). As shown in Figure 5-33, at least 40% of wind speed records in all seasons were in the range of 8 to 10 m s^{-1}, with a peak of more than 50% in winter. This can be linked to strong easterly winds at the western fringes of the Siberian High, which is the dominant pressure system in this region during winter. The effect of this strong anticyclone on atmospheric circulations over Pre-Aral region is also evident in Figure 5-34, which shows that almost all wind records at the time of dust observation in winter were directed towards west and north-west. Wind directions for DPS records in this region show greater variability during other seasons.

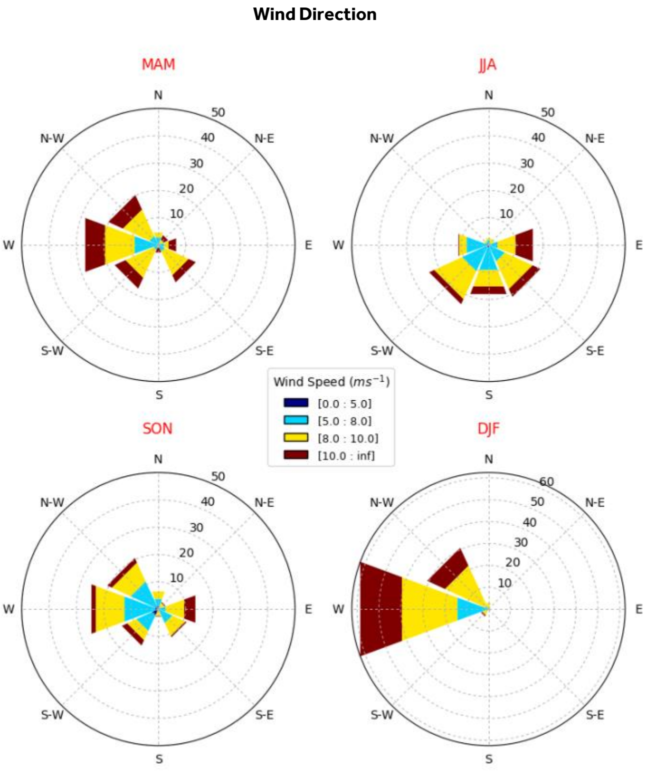

Figure 5-34. Direction of entraining winds for DPS in the Pre-Aral region

5.3.5. Other source regions

Dust source regions in Central Asia are characterised by great diversity in land types, dynamic vegetation cover and different dust entrainment mechanisms. In this section a brief overview on the surface characteristics, temporal variations and meteorological controls of dust emission in the Upper Amudarya, Balkhash-Junggar basin and Hexi corridor are presented.

5.3.5.1. Land surface characteristics

Analysis of spatial characteristics of DPS and investigation of high resolution satellite images revealed that dust emission in these regions is generally associated with two main land surface processes: (i) degradation of vegetation (by wildfire and grazing) in Balkhash-Junggar, and (ii) alluvial processes in lower latitudes, including the Upper Amudarya region in northern Afghanistan and the Hexi corridor in western China.

Post-fire dust emission was the dominant emission mechanism in the Balkha-Junggar region. In many sites the burned areas showed expantion due to consecutive wild fire events. An example of the expansion of fire scars in Balkhash basin is shown in Figure 5-35 and Figure 5-36. In March 2008 a severe dust storm was recorded in the Balkhash depression, with dust being transported hundreds of kilometres downwind towards relatively densely populated agricultural areas of south-eastern Kazakhstan, and lasted for three days. The sources of the dust plumes were traced back to fire scars in the eastern side of the Balkhash depression, near Lake Balkhash. A closer look at the source region using satellite images at higher resolution showed a series fire scars which were frequently expanding during the 10 years prior to the dust event, between 1998 and 2008 (Figure 5-36).

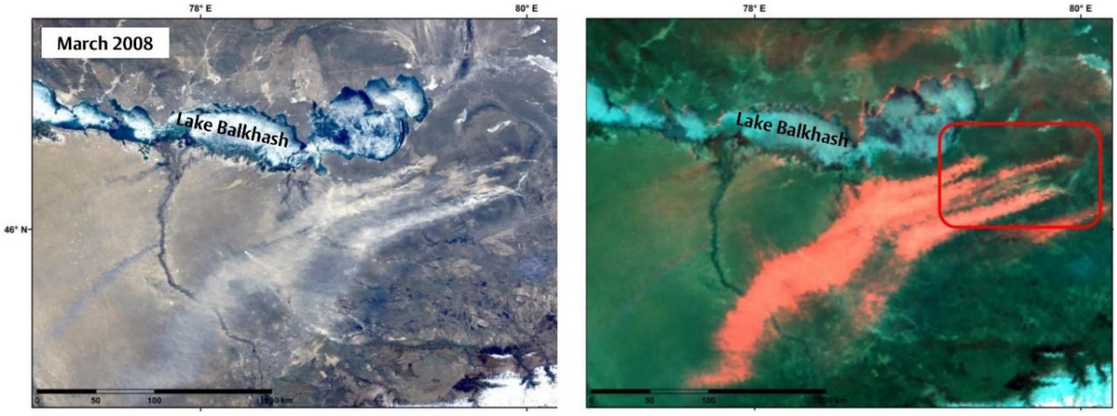

Figure 5-35. Dust storm in the Balkhash depression, south-east Kazakhstan, on 30 March 2008. Satellite images are MODIS true colour surface reflectance (left) and MODIS DEP (right). Dust source area is depicted by red rectangle.

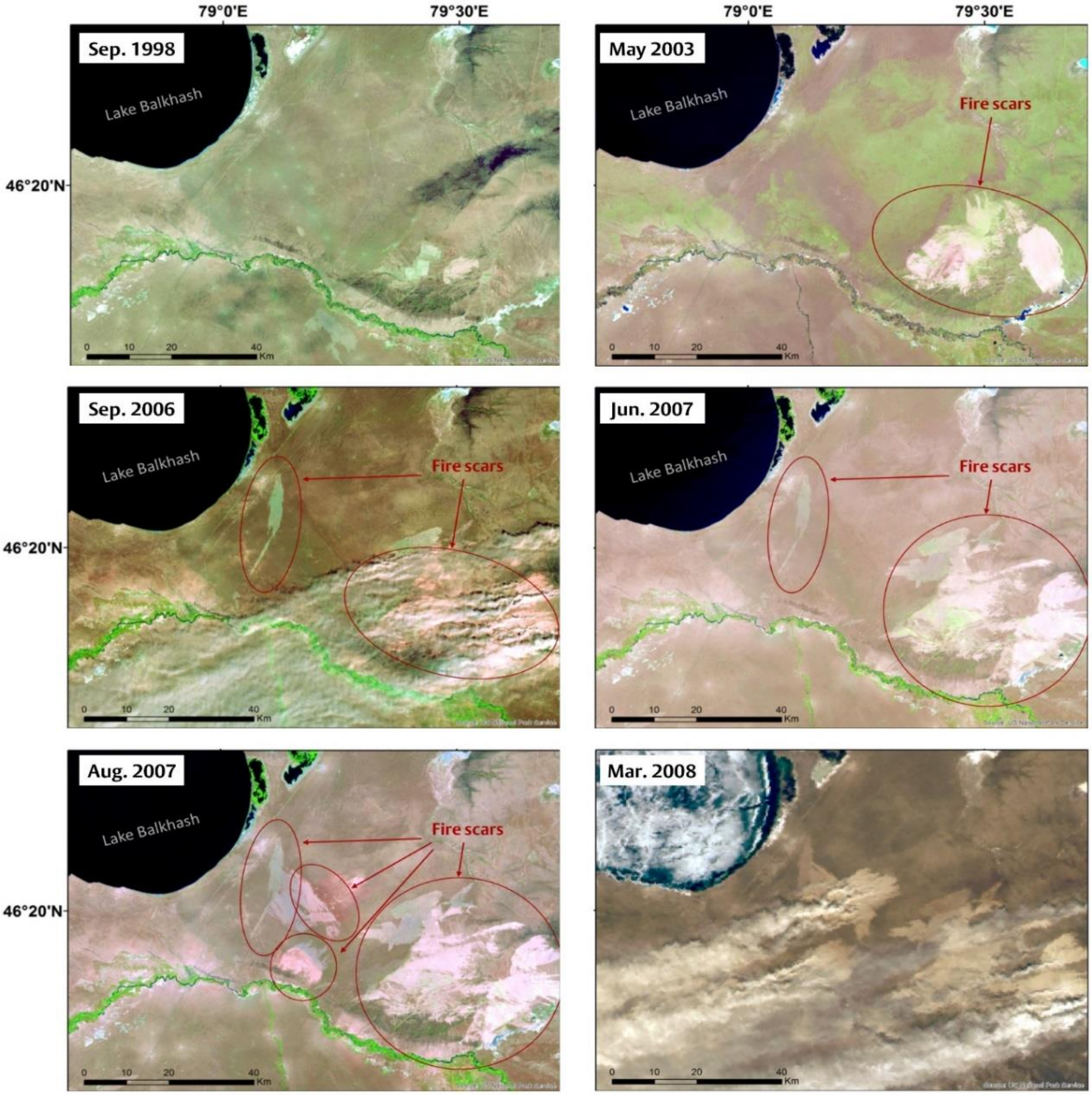

Figure 5-36. Evolution of fire scars in the Balkhash depression, captured by Landsat 5 images acquired between 1998 and 2008. Images obtained from USGS Earth Explorer (https://earthexplorer.usgs.gov/).

Dust emissions in the Upper Amudarya and the Hexi corridor are mainly linked to agricultural activities at the periphery of alluvial fans, which are frequently formed in the lower reaches of the snow- and glacier-fed rivers. One of the active dust sources, associated with agricultural lands, was found in Hexi corridor region, in the delta of the Changma River (Figure 5-37). Alluvial deposits at the lower parts of the fan are partly cultivated in the north-east and mostly exposed in the north-western side of the fan.

In the Upper Amudarya region, north of Afghanistan, almost all DPS were recorded on the margins of alluvial fans, formed at the lower reaches of the Balkh River. Around 950 activated DPS were identified in this relatively small region between 2003 and 2012. Dust activities in this region are of great importance because of proximity of this region to the glacier systems of Pamir and Karakoram

Mountains, which may be affected by the dust from this region, transported by the dominant north-westerly winds in JJA (see Figure 5-54 left panel).

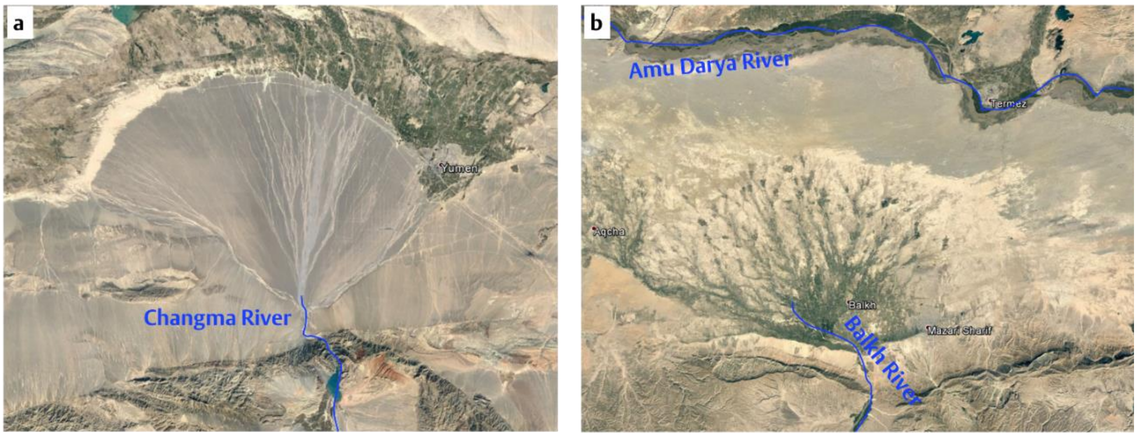

Figure 5-37. Satellite view of alluvial fans at the lower reaches of (a) Changma River in western China, and (b) Balkh River in northern Afghanistan. Images acquired by Landsat 7, obtained via Google Earth Engine Catalog (www.earthengine.google.com).

5.3.5.2. Inter- and intra-annual variability in dust emission

The regions considered in this section, exhibit diverse annual cycles and inter-annual trends in the occurrence of dust storms and occurrence of DPS. In the previous section of this chapter it was shown that the Upper Amudarya region was one of the most active dust sources with a high concentration of DPS in a relatively small area. Number of dusty days and recorded active DPS in Upper Amudarya showed a decreasing trend for the first five years from 2003 to 2007 (Figure 5-38). It was followed by a four-fold increase in 2008. At the peak of dust activity in 2008, more than 180 DPS in 60 dusty days were recorded in this small region. The dust activity increased again in 2011 after a sharp decrease in 2009 and 2010. Considering the extent of this region, high number of DPS per dusty days (more than 5 in 2012) indicates a potentially higher intensity of dust events in this region. The majority of DPS in this region were recorded in June and July, however, the DPS ratio is the highest during March and also November.

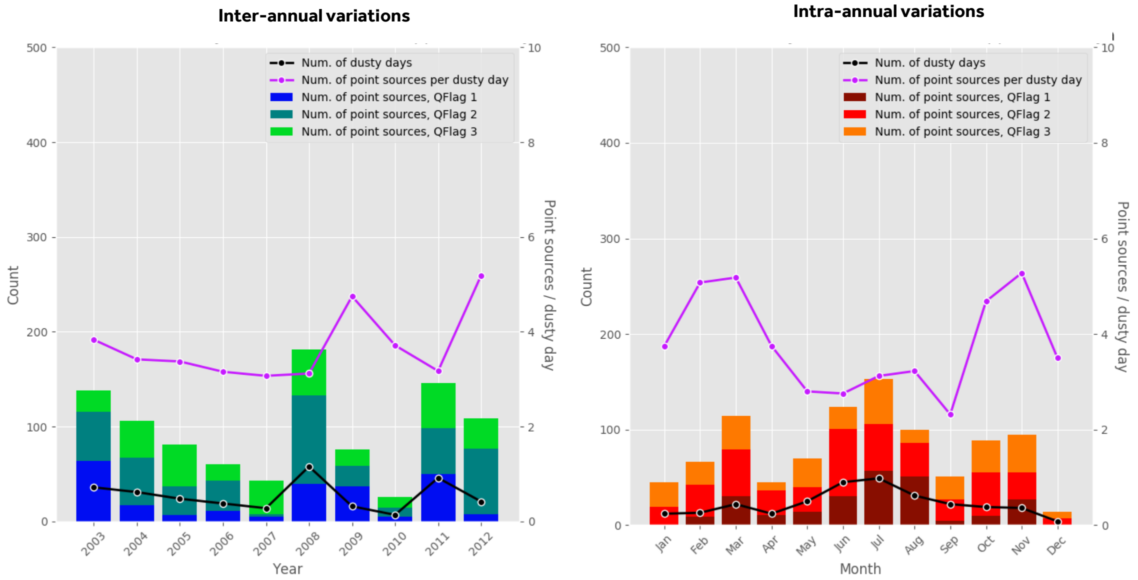

Figure 5-38. Inter-annual and intra-annual variation in dusty days and DPSin the Upper Amudarya region. Black line shows the number of dusty days and the purple line shows the average number of DPS per dusty day.

The last two graphs show the results of analysis of variations in dusty days in the Hexi corridor and the Balkhash-Junggar regions (Figure 5-39 and Figure 5-40). In the Hexi corridor, there was no significant trend in the number of dusty days during the ten year period, similar to inter-annual variability of dusty days in the Taklamakan desert, in the western side of Hexi Corridor (see Figure 5-21). Also in terms of intra-annual variations, a pattern similar to the Taklamakan was observed with April being the month with the highest number of dusty days. Yet the number of recorded DPS in this region is considerably lower than other source regions, e.g. the Taklamakan.

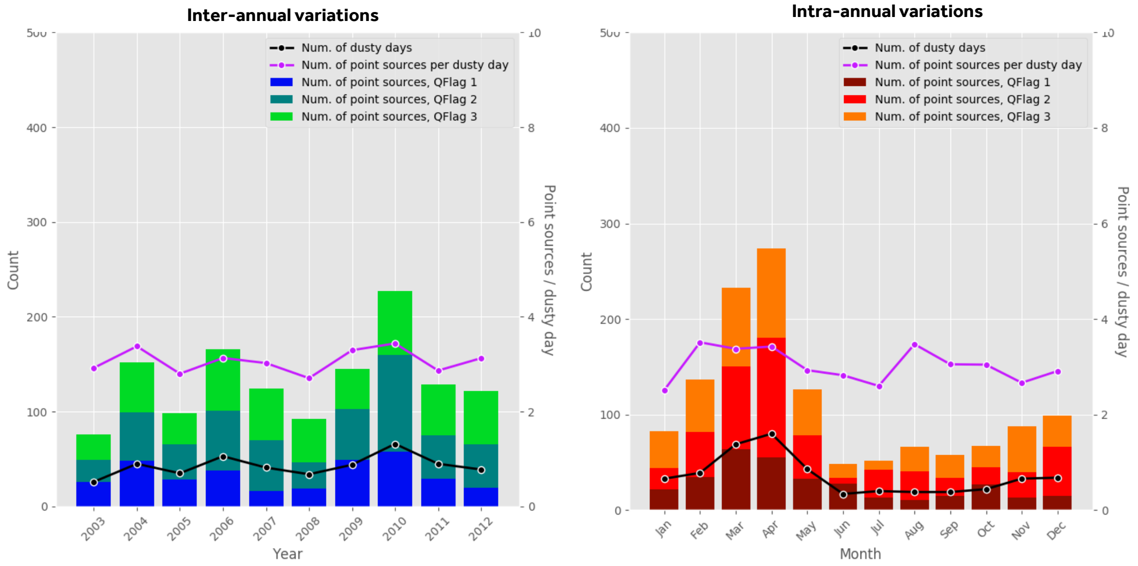

Figure 5-39. Inter-annual and intra-annual variation in dusty days and DPSin the Hexi Corridor. Black line shows the number of dusty days and the purple line shows the average number of DPS per dusty day.

Similar to the Upper Amudarya, the main importance of dust activities in the Balkhash-Junggar region is its proximity to the Tian Shan glacier systems. As discussed in previous chapters, dust deposition on the surface of glaciers in the Tian Shan can significantly alter glacier surface albedo, hence the melt rate of glacier snow and ice, as suggested by Takeuchi *et al.* (2008). It is shown in Figure 5-40 that dust emission from this region is less significant than the other major sources. Number of recorded DPS and dusty days has been gradually falling during the time period of our study. Less than 10 dusty days were recorded in this region in 2011, comparing to above 30 annual dusty days in 2004 to 2006.

The average number of DPS per dusty days also reached its lowest in 2011, following by an increase in 2012. Analysis of intra-annual variation in dusty days revealed that April is the month with the maximum number of dusty days, the highest number of DPS records and the most intense dust events. Dust activities diminish in May to July, and peak again in August. This region stayed moderately active during autumn months. No dust events were recorded in January during the ten year time period, due to permanent snow cover.

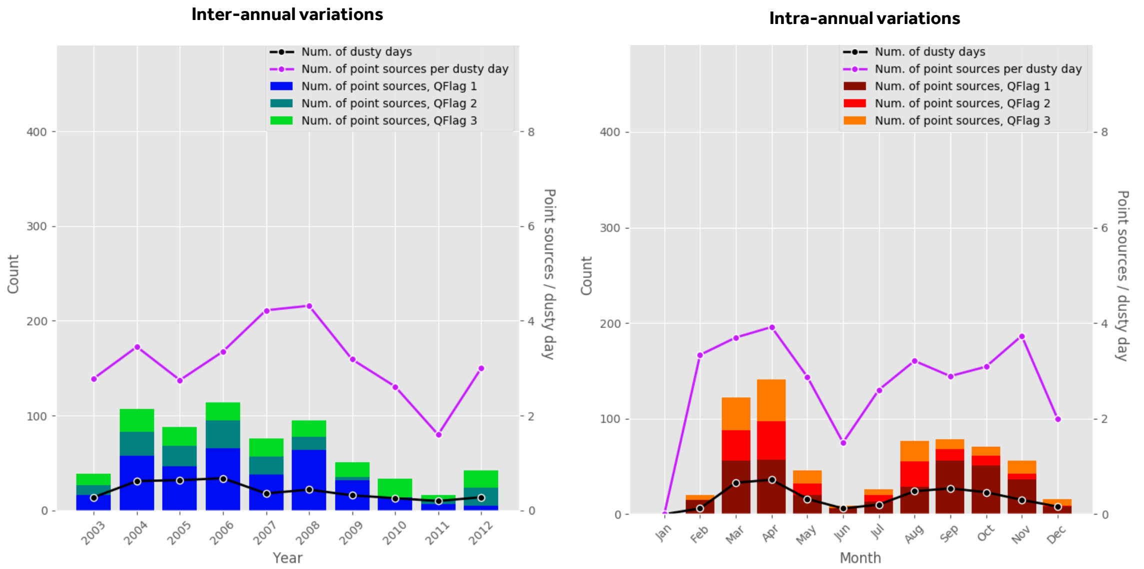

Figure 5-40. Inter-annual and intra-annual variation in dusty days and DPS at the Balkhash-Junggar region. Black line shows the number of dusty days and the purple line shows the average number of DPS per dusty day.

5.3.5.3. Synoptic controls on dust emission and dust transport pathway

MSLP composites for dusty days in these regions showed a close similarity to synoptic patterns of dusty days in other Central Asian sources, e.g. the Aralkum and the Karakum-Kyzylkum. Synoptic patterns for dust outbreaks are influenced by high pressure systems centred over eastern Kazakhstan in MAM, SON and DJF, the Asiatic thermal low in JJA, stretching from the Taklamakan to the Arabian Peninsula (Figure 5-45). Investigation of MSLP anomalies revealed a feature which is common for these regions: a strong dipole pattern and a sharp gradient between the high pressure anomalies and low pressure anomalies over the dust source region. This pattern can be seen in MSLP anomaly composites, shown in Figure 5-31 to Figure 5-46.

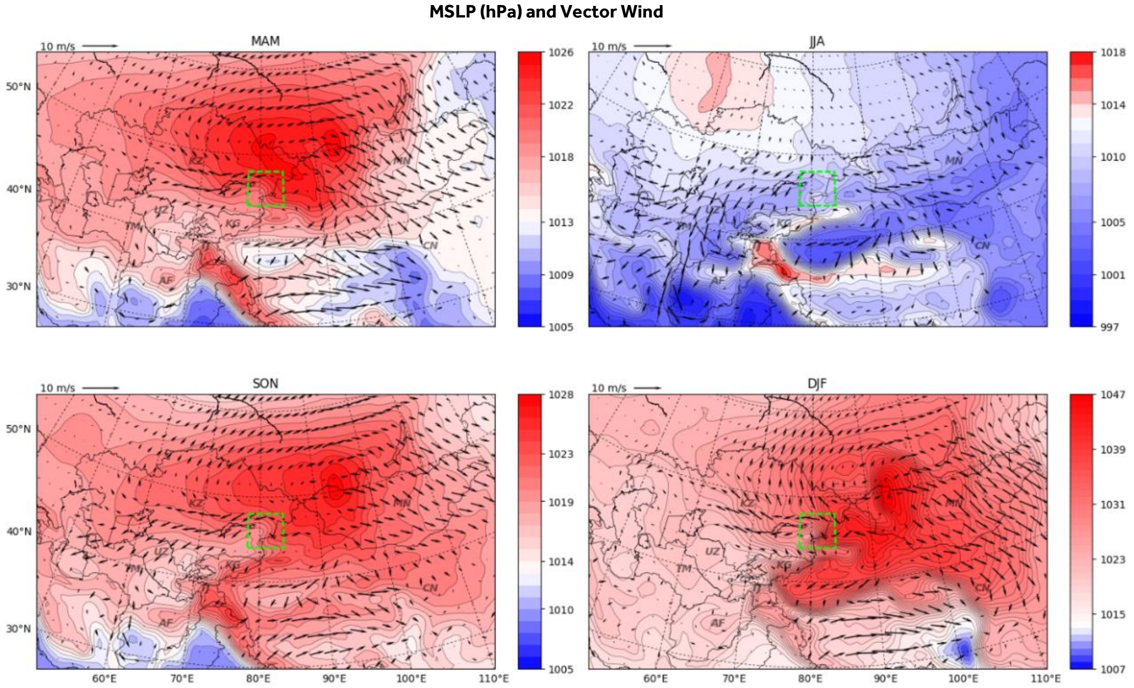

Figure 5-41. MSLP (hPa) for dusty days in Balkhash-Junggar between 2003 and 2012. The centre of region is depicted by green rectangle.

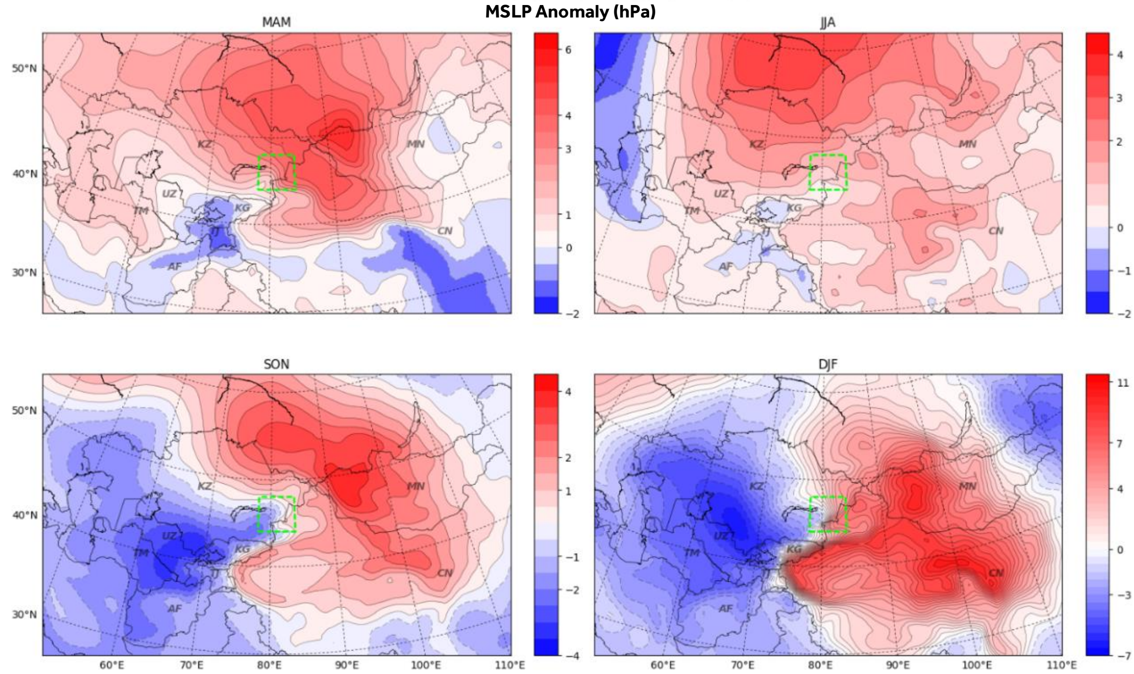

Figure 5-42. MSLP anomaly (hPa) for dusty days in Balkhash-Junggar between 2003 and 2012. The centre of region is depicted by green rectangle.

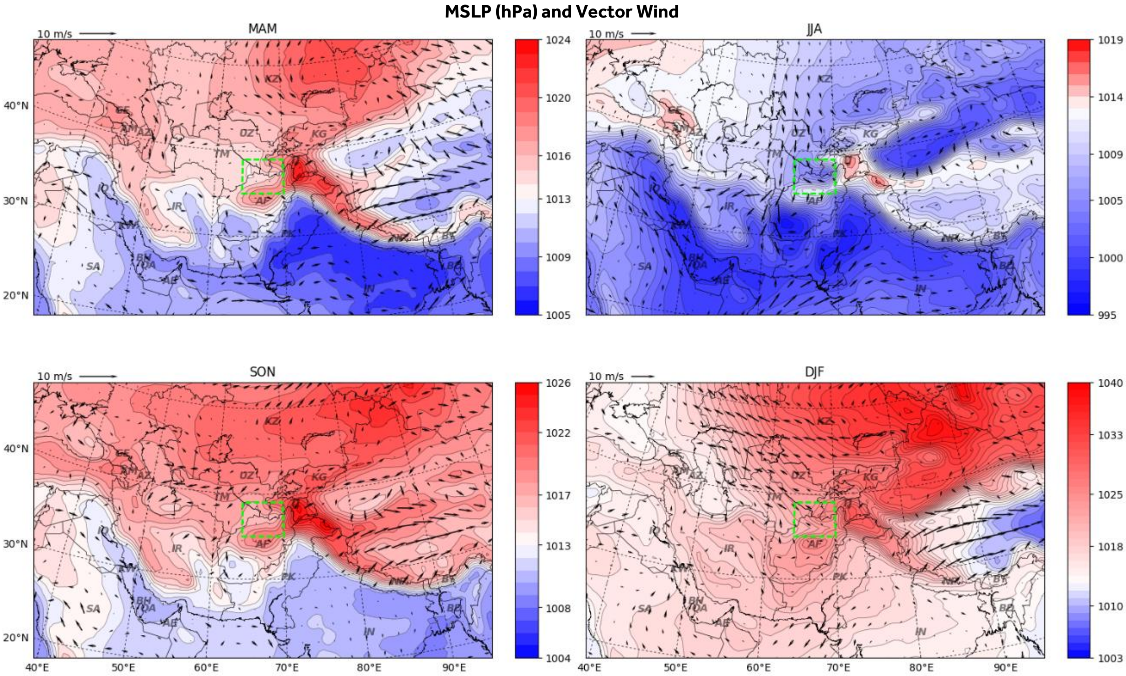

Figure 5-43. MSLP (hPa) for dusty days in Upper Amudarya between 2003 and 2012. The centre of region is depicted by green rectangle.

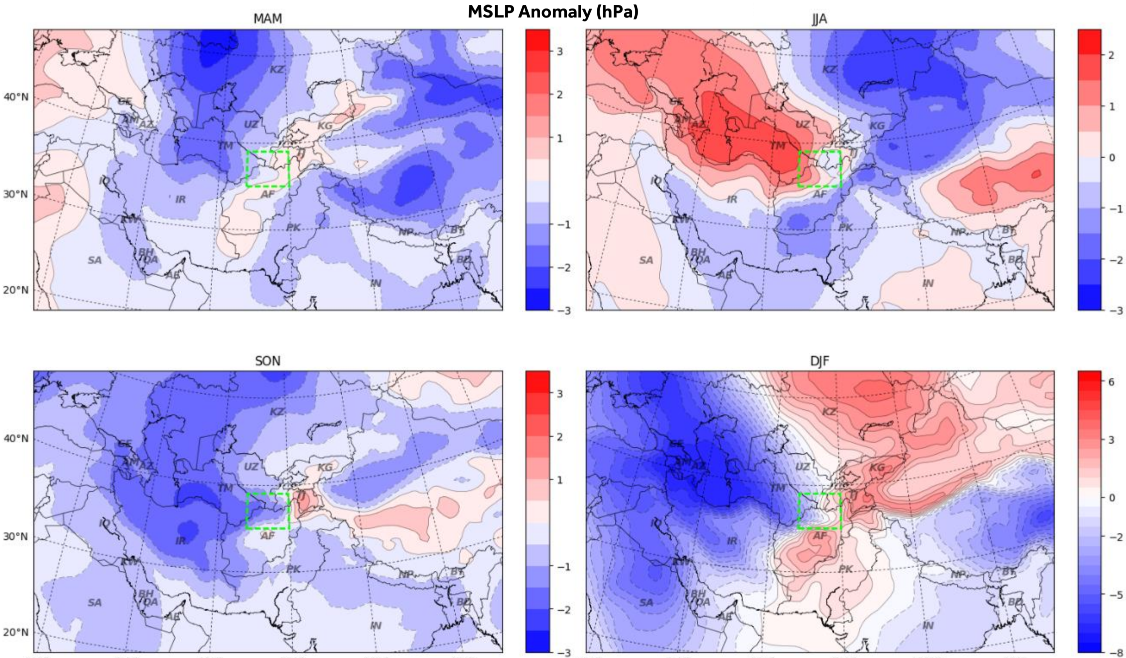

Figure 5-44. MSLP anomaly (hPa) for dusty days in Upper Amudarya between 2003 and 2012. The centre of region is depicted by a green rectangle.

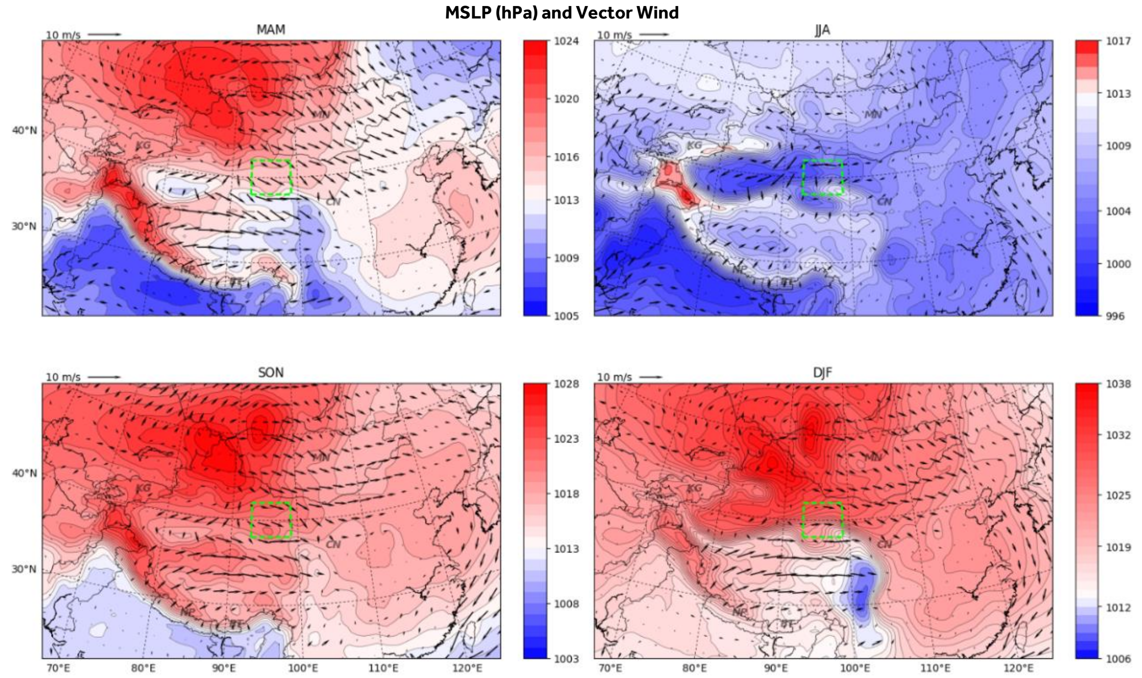

Figure 5-45. MSLP (hPa) for dusty days in Hexi Corridor between 2003 and 2012. The centre of region is depicted by a green rectangle.

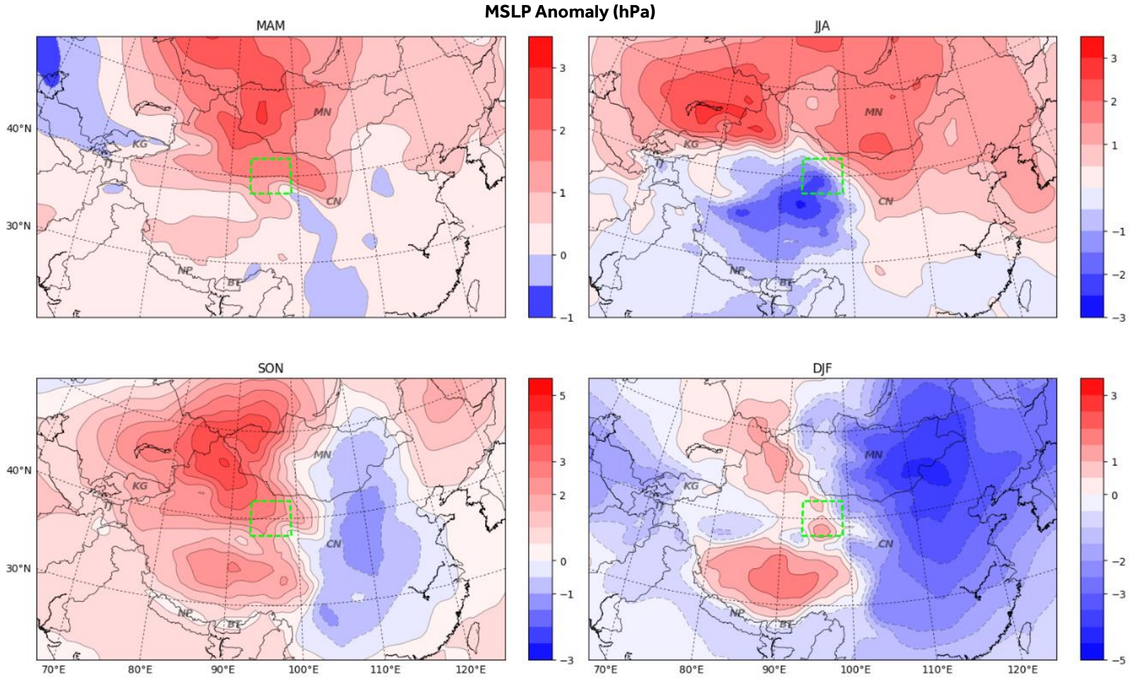

Figure 5-46. MSLP anomaly (hPa) for dusty days in Hexi Corridor between 2003 and 2012. The centre of region is depicted by green rectangle.

A clear link between wind speed and dust emission was established by investigating the wind speed anomaly composites, shown in Figure 5-47 to 49. The highest surface wind anomalies usually occurred in winter, which is most likely due to intensification of the Siberian High over higher latitudes. Although similar wind speed anomaly patterns were observed in these regions, the absolute values of dust generating winds were different for each region, reflecting the differences in wind regime and surface conditions of dust source regions.

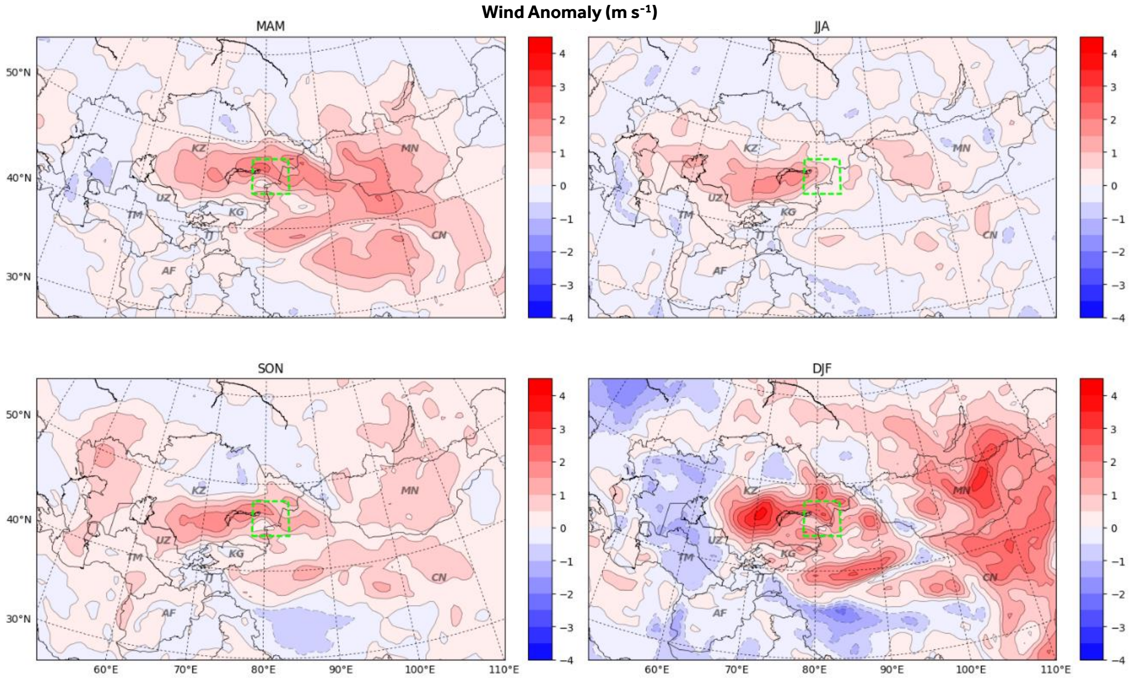

Figure 5-47. Near-surface wind anomaly (m s^{-1}) for dusty days in Balkhash-Junggar between 2003 and 2012. The centre of the region is depicted by green rectangle.

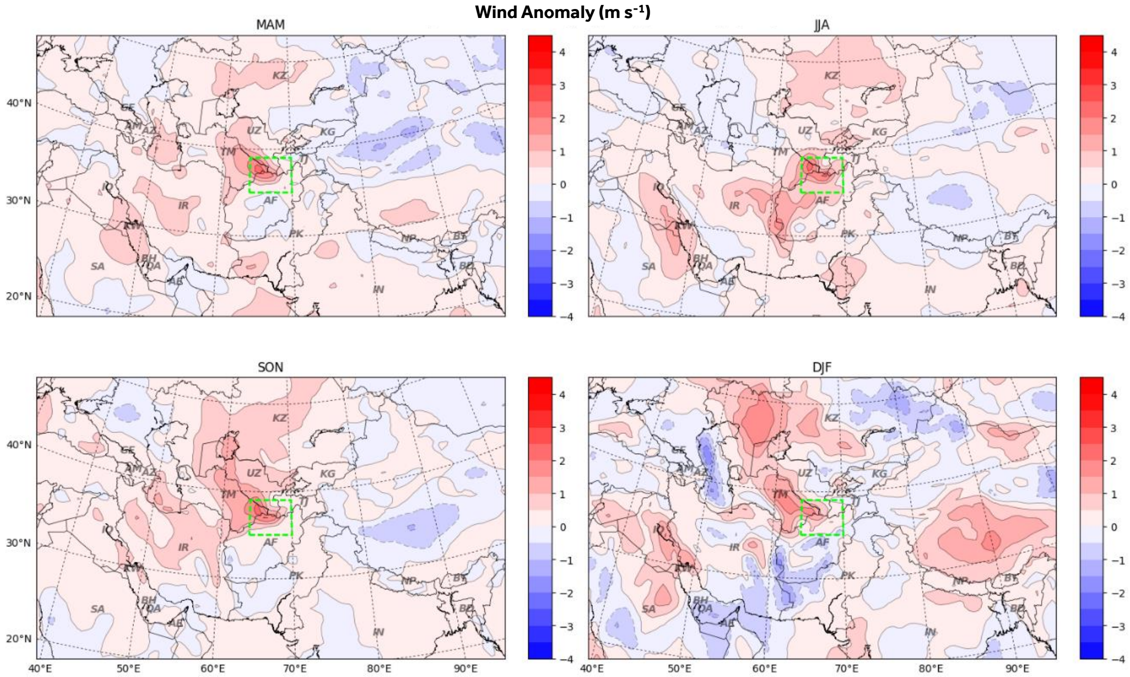

Figure 5-48. Near-surface wind anomaly (m s^{-1}) for dusty days in Upper Amudarya between 2003 and 2012. The centre of the region is depicted by green rectangle.

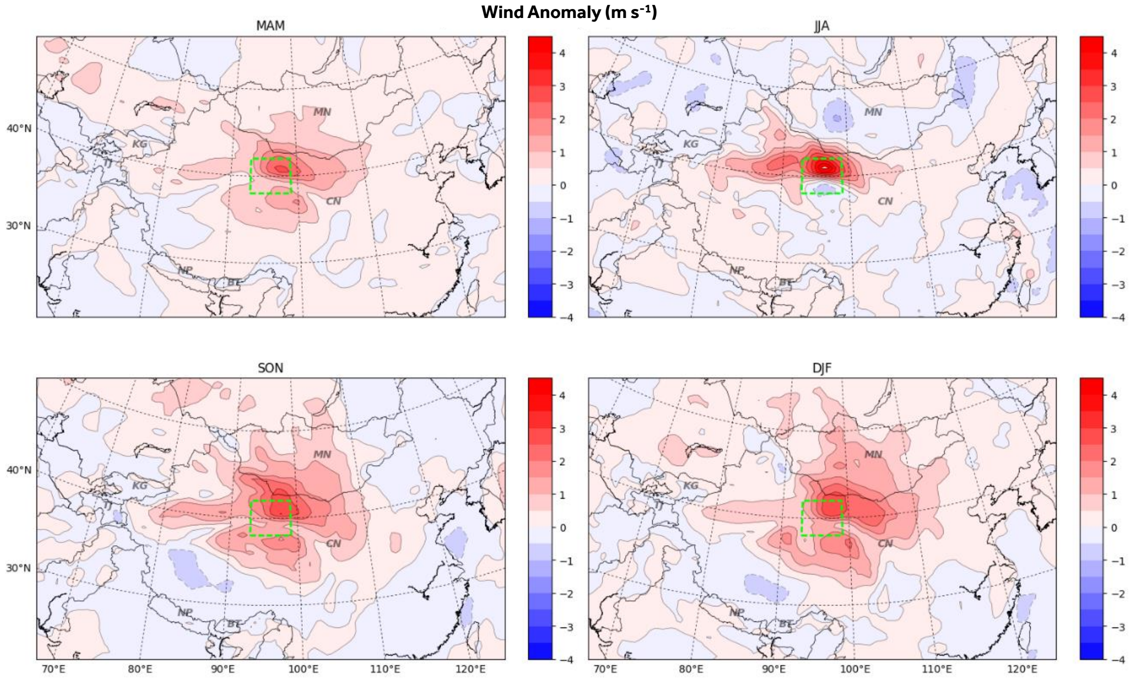

Figure 5-49. Near-surface wind anomaly (m s^{-1}) for dusty days in Hexi Corridor between 2003 and 2012. The centre of the region is depicted by green rectangle.

Moderate wind speeds (8-10 m s^{-1}) were the dominant wind record in Balkhash-Junggar region (Figure 5-50), while low-speed winds were found to be the prevailing wind regime in Upper Amudarya region (Figure 5-51). The wind direction graph for Balkhash-Junggar shows a similar pattern to that of the Pre-Aral region, with high variability in all seasons except in winter (Figure 5-53). In contrast, entraining wind directions in Upper Amudarya shows a more homogeneous pattern. The main direction of surface winds, and consequently the dust entrainment, in Upper Amudarya was towards west in all seasons except in summer, when almost 80% of DPS were activated by north-westerly winds (Figure 5-54).

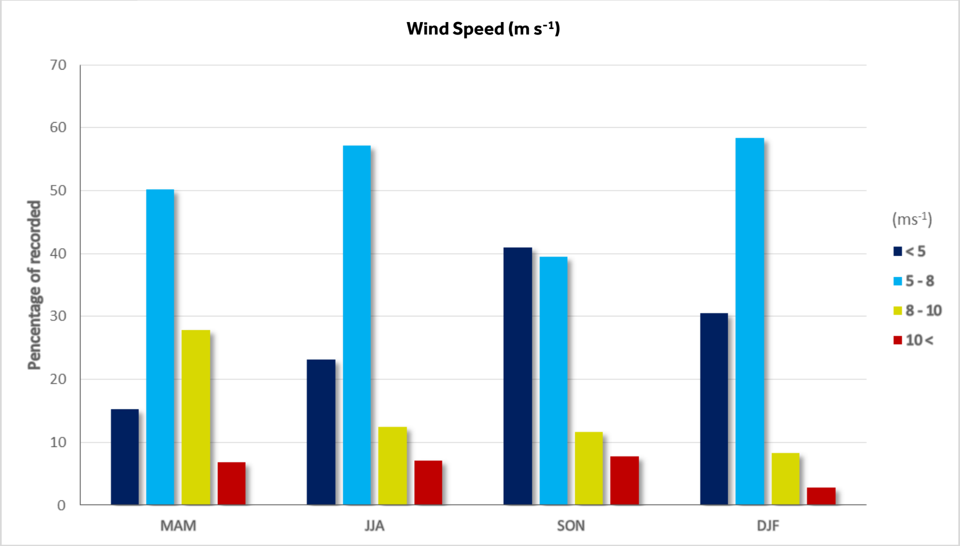

Figure 5-50. Distribution of 10m wind speeds (m s^{-1}) for DPS records in Balkhash-Junggar between 2003 and 2012.

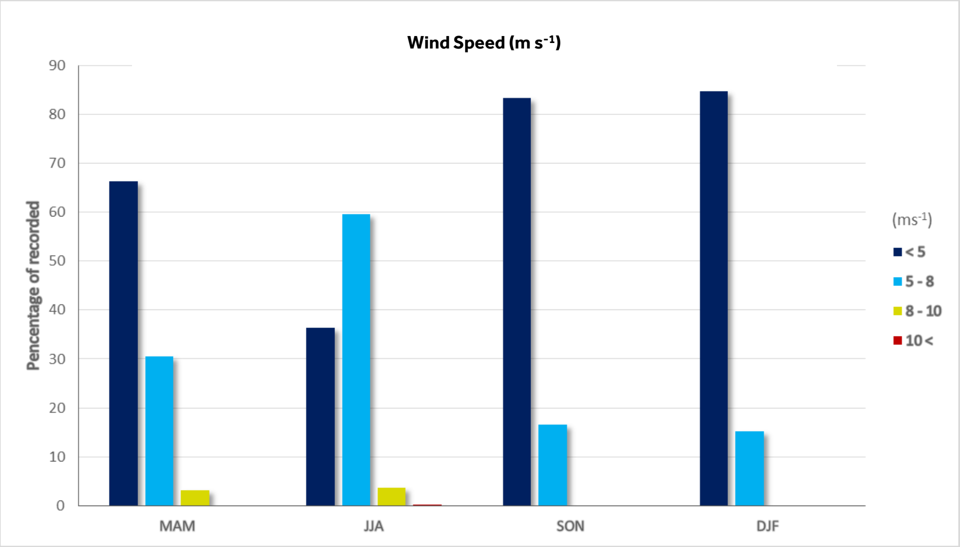

Figure 5-51. Distribution of 10m wind speeds (m s^{-1}) for DPS records in Upper Amudarya between 2003 and 2012.

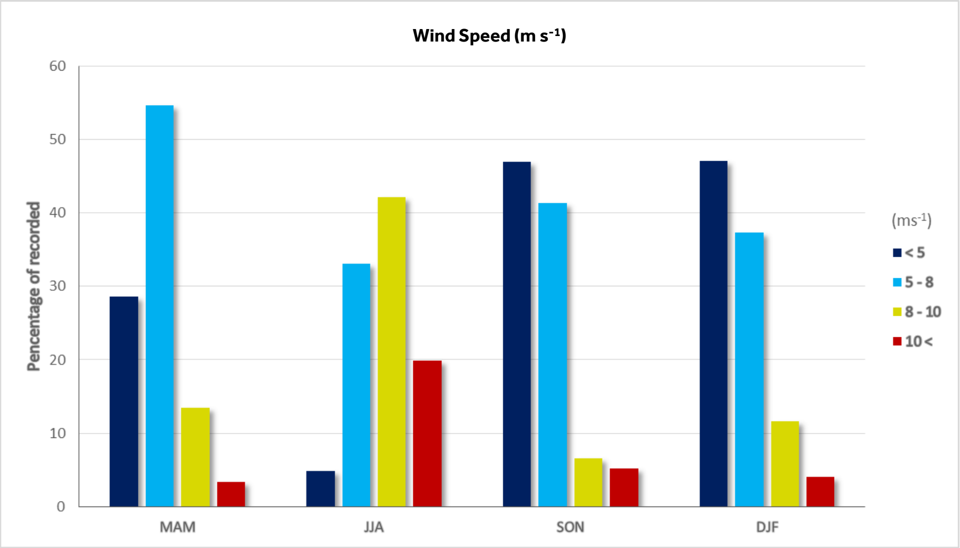

Figure 5-52. Distribution of 10m wind speeds (m s^{-1}) for DPS records in Hexi Corridor between 2003 and 2012.

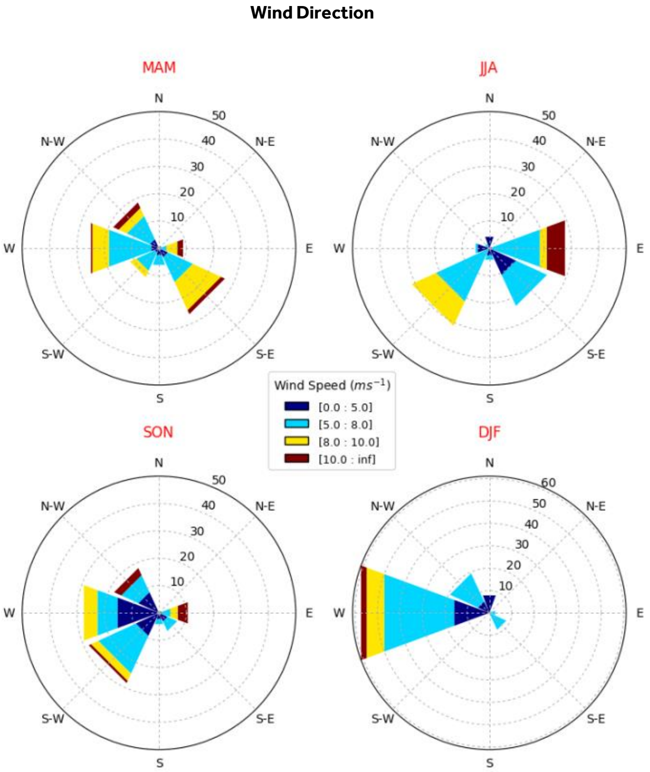

Figure 5-53. Direction of entraining winds for DPS in the Balkhash-Junggar region.

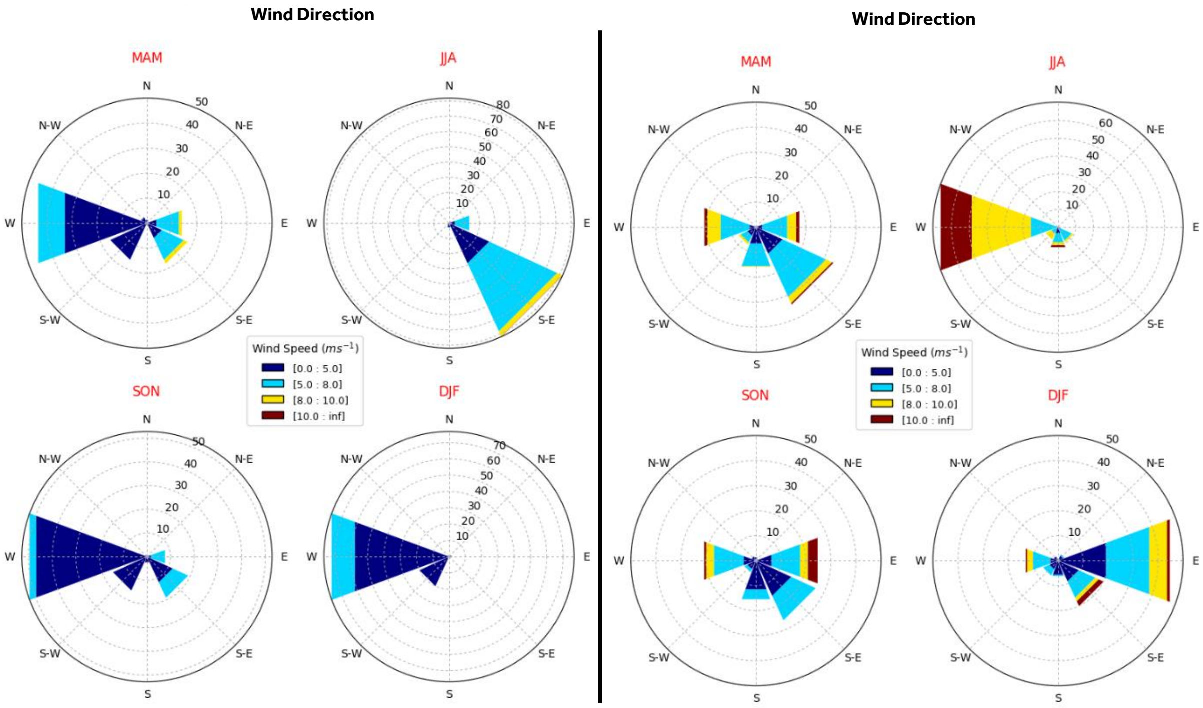

Figure 5-54. Direction of entraining winds for DPS in Upper Amudarya (left) and Hexi Corridor (right).

Chapter 6. Discussion

6.1. Introduction

The Central Asian deserts investigated in this study (Central Asian drylands and the Taklamakan in western China) form the second major source of mineral dust in the world after the Sahara, supplying up to 25% of desert aerosol to the atmosphere (Shao *et al.*, 2006; Ginoux *et al.*, 2012). Mineral dust from this region plays an important role in alteration of surface albedo of glaciers and snow covered surfaces which are the main sources of fresh water for urban and agricultural uses in this region (Painter *et al.*, 2012). Particularly, the glacier systems of the Tian Shan Mountains have been the subject of frequent dust depositions during the past decades (Wake *et al.*, 1992; Takeuchi *et al.*, 2008). Despite this significance as a globally important dust source, very little is known about the nature of the dust processes in this part of the world. While the significance of dust emissions from this region has been highlighted in a number of global studies (e.g. Herman *et al.*, 1997; Washington *et al.*, 2003; Ginoux *et al.*, 2012), to this date there has not been a comprehensive and detailed review on dust sources and spatiotemporal variability of their activation at sub-basin scale using consistent, high-resolution observations.

Precise mapping of the active dust sources is the first step in understanding the driving factors of dust emissions, which is a key part of the dust cycle. One particular benefit of accurate information on spatial variability of dust sources could be in dust modelling. Research has shown that the lack of accurate information on the spatiotemporal variability of dust emitting surfaces can lead to large biases in numerical dust models (Raupach *et al.*, 2004; Shao, 2004). Some of the dust sources investigated in this study have been notably under-researched by the dust research community due to the difficulties in physically accessing the area for conducting research (e.g. the Upper Amudarya region in northern Afghanistan), scarcity of the observation sites (e.g. the Karakum and Kyzylkum) and also lack of research investment. Our investigation on dust emissions in Central Asia led to identification of several major sources of dust which were not discussed in literature before. Some of the identified regions were previously highlighted in literature but without detailed information on temporal and spatial variability of dust sources at sub-basin scale, land surface features associated with dust emissions and meteorological conditions leading to dust emission. Moreover, most of these studies have been either focused on relatively small region, or been concerned with a particular aspect of dust process, e.g. dust deposition rates (Groll *et al.*, 2013) or deflation processes (Issanova *et al.*, 2014).

As a result, the literature is highly fragmented and does not give a full picture of the dust processes in this region.

In this study, for the first time, we provided an up-to-date insight on the spatiotemporal variations of dust emissions in Central Asia and western China at sub-basin scale, by taking advantage of the advanced remote sensing and geo-spatial analysis techniques. A two-step approach was used. We first obtained a map of dust hotspots by frequency analysis of MODIS Enhanced DeepBlue (eDB) AOD products. This enabled us to get a general view on the main dust hotspots and their seasonal activities. In the second phase of the research, a database was established for recording the coordinates of the point sources of every single dust plume discernable in daily MODIS DEP images for the period of 2003 to 2012 in order to stablish the sub-basin variation of the dust point sources. We also recorded the 10 m wind speed and direction, derived from the ERA-Interim reanalysis data, interpolated to match the locations and time of each DPS observation. This extensive work enabled us to present, for the first time, a detailed inventory of the major dust source regions, including the sub-basin distribution of active sources, land surface characteristics, intra and inter-annual variations in dusty days, synoptic controls of dust emissions and the direction of entraining winds.

In this chapter we discuss these results further and try to provide an overarching review of dust source characteristics in this region. In the first section a cross-comparison of the main dust sources is made with regards to their activity, surface characteristics, general climatology of dust emissions and dust entrainment direction. It is followed by a comparison between the two sets of results obtained from by analysis of MODIS AOD and MODIS DEP datasets.

6.2. Comparison of dust source regions

Development and analysis of 10 years of DPS records provided us with a unique opportunity to assess the dynamics of dust sources at the sub-basin level, as well as comparison at the regional scale. Our findings show that the Taklamakan desert was the most active source of dust during the time period of our study, accounting for nearly 35% of DPS record (Figure 6-1). Several dust studies at global and regional scale have highlighted the high frequency of dust events in this region, either as a separate region or together with Gobi desert in north of China (Walker, 1982; Xuan *et al.*, 2000; Washington *et al.*, 2003; Aoki *et al.*, 2005; Shao *et al.*, 2006; Wang *et al.*, 2006). But this is the first time that dust emissions in this region is being compared to other Central Asian dust sources within the same timeframe and using the same methodology. This information is crucial for potential further studies on the effect of dust on glaciated environments of Central Asia, and for modelling of dust processes.

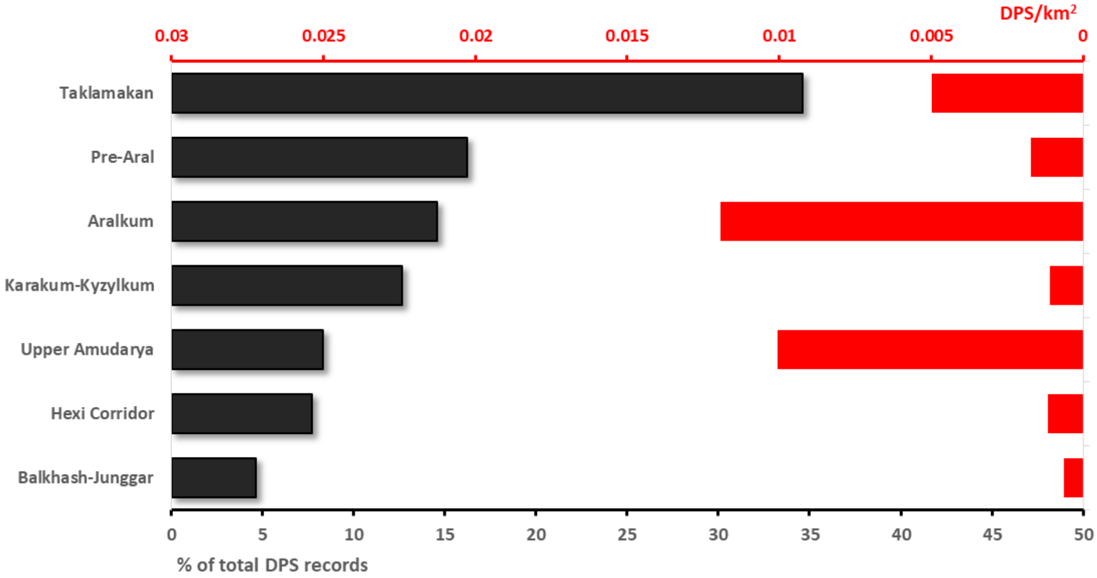

Figure 6-1. Percentage of total DPS records in each region (black bars) and average number of DPS per km^2 of source region area (red bars).

The Pre-Aral region was the second most active source region, accounting for over 16% of all DPS records during the study period. Despite containing more DPS records than the Aralkum, this region is one of the most poorly investigated dust sources in Asia, having drawn very little attention from dust researchers. There is very little literature on the significance of post-fire dust emissions from this region. The Aralkum region, accounting for above 14% of DPS records during the study period, was the third most active region, followed by the Karakum-Kyzylkum (~13%), Upper Amudarya (~9%), Hexi Corridor (~8%) and Balkhash-Junggar region (~5%).

Figure 6-1 also shows the average number of DPS/km^2 for each source region, to assess the variation in concentration of DPS records. It should be noted that the surface area of the dust source regions were calculated approximately, using dust source region definitions from literature. Nevertheless, the average number of DPS would still roughly represent the possible severity of dust events in each region. Our analysis showed that the Aralkum had the highest density of DPS amongst all source regions, with an average of 0.012 DPS/km^2. The Upper Amudarya region in northern Afghanistan was another source region with a remarkably high number of DPS per unit area. It was one of the major findings of our study, especially since information on dust emissions from this region is almost non-existent in the dust research literature. Yet this region is characterized by a low (< 5 m s^{-1}) threshold for activation of DPS (Figure 5-51). The predominant transportation of dust from this source is south-east towards the glaciers of the Pamir and Hindu-Kush in JJA. This requires further investigation of the impacts of this source on the at-surface radiative forcing of dust deposited on snow and ice.

Although the highest number of DPS were recorded in the Taklamakan, it showed a lower density of DPS compared to the Aralkum and the Upper Amudarya regions (~0.005 DPS/km^2). This was because the majority of DPS in the Taklamakan were identified in the margins of the desert and a large part of the central Taklamakan seemed to be considerably less active, with very few DPS observations. The other dust source regions showed a relatively lower DPS density, with the minimum in the Balkhash-Junggar region.

The link between the occurrence and frequency of dust events and the geomorphologic characteristics of dust sources has been investigated in several studies on regional and global scale (Wang *et al.*, 2006; Bullard *et al.*, 2008; Lee *et al.*, 2012a). Bullard *et al.* (2011) developed a geomorphology based conceptual land-surface classification scheme that can be used to characterize the preferential dust sources for dust-cycle modelling. Inspired by this study, we tried to stablish the link between spatial pattern of DPS activity and changes in the surface properties using historical archives of high resolution satellite imagery and exploring the available literature. It should be noted that due to lack of detailed information on land surface characteristics in Central Asia we were not able to reconstruct the identical geomorphic classifications of dust emitting surfaces demonstrated by Bullard *et al.* (2011). Using the available data and literature, the dust emitting land surfaces in Central Asia were classified into 5 main categories, including:

- Lakes: ephemeral or desiccated lakes and water bodies.
- Alluvial and fluvial: high-relief and low-relief alluvial deposits as well as dried up river beds, floodplains and irrigation channels
- Burned: land surfaces devoid of vegetation after wild fires.
- Agricultural: cultivated land surfaces, irrigated or under dryland farming.
- Aeolian: sand sheets and aeolian sand dunes.

Although in many cases a clear link existed between the satellite observation of the land surface and overlapping DPS observations (e.g. fire scars shown in Figure 6-2), the classification of observed DPS was not always straightforward. In areas with complex geomorphology, such as the margins of alluvial fans, where the scene is composed of agricultural lands, fully or partially abandoned farms and uncultivated alluvial plains, it was difficult to identify the dominant surface type. However, these sources accounted for less than 2% of the observed DPS.

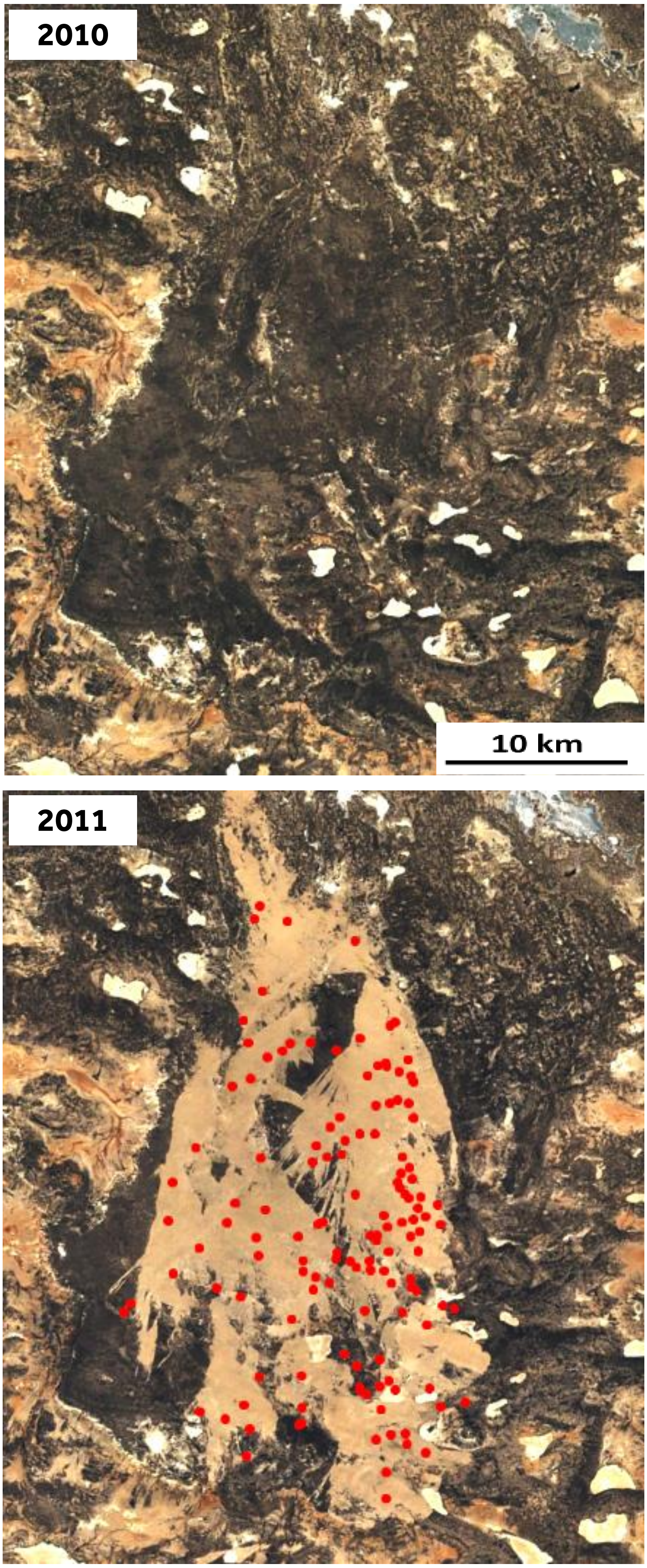

Figure 6-2. The link between land surface changes (fire scars) and DPS activations (red circles) in the Pre-Aral region. Images are Landsat 7 ETM+ annual composites acquired from Google Earth Engine Catalog.

Table 6-1 summarises the estimated contribution of the major land surface types to the dust emissions in Central Asia between 2003 and 2012. The values in this table represent the percentage of the total DPS records. Dust sources in Central Asia are characterised by a great diversity of land surface types and features. Alluvial and fluvial plains account for the highest share of DPS (40.2% of total DPS). This is in contrast with the findings of a similar study by Lee *et al.* (2012) over West Texas and eastern New Mexico which showed only 9% of dust point sources were detected on high and low relief alluvial surfaces. However their study area was limited to a comparably smaller and more homogeneous region. Dry lakes accounted for the second highest share of DPS, with 29.7% of the total DPS records being associated with this type of land surface. They were found to be the most active land surfaces in the Aralkum and the Taklamakan, accounting for 14.6% and 15.1% of total identified DPS respectively. One of the most striking findings of this study was the important role of wildfires in activation of the dust sources in the temperate zone. This is reflected in Table 6-1, which shows that more than 16% of DPS records (~2100 DPS) were associated with post-fire dust emission processes.

Table 6-1. Percentage of total DPS for dust emitting land surface types identified in Central Asia

	Lakes	**Alluvial/Fluvial**	**Burned**	**Agricultural**	**Aeolian**
Aralkum	14.6	--	--	--	--
Karakum-Kyzylkum	--	9.7	--	2.2	0.8
Taklamakan	15.1	15	--	1.5	3.0
Pre-Aral	--	2.6	13.6	--	--
Balkhash-Junggar	--	0.3	2.5	0.7	1.1
Upper Amudarya	--	6.2	--	2.1	--
Hexi Corridor	--	6.4	--	1.1	0.2
Total	29.7	40.2	16.1	7.6	5.1

It must be noted that the primary goal of this study was to provide data on spatiotemporal variations of dust sources at sub-basin scale. Hereby and also to present the first insight into land surface characteristics using satellite observations and available literature. These findings provide the basis for more detailed regional research, and land surface features and processes leading to dust emission should be investigated further in each region.

Cross-comparison of dust source regions with regards to synoptic climatology of dust emissions revealed two major characteristics of synoptic patterns: (i) high pressure systems in higher latitudes are the dominant feature of dusty days in MAM, SON and DJF, while JJA is characterized by strong depressions over lower latitudes, and (ii) a dipole pressure anomaly is typical of the days with dust emissions, whereby a high pressure anomaly and a low pressure anomaly are positioned on two sides of the dust source region with a sharp gradient over the source region, causing strong winds.

In terms of seasonal variations in dust emission, two general patterns could be discerned from our data; (i) peak dust emission in spring, with a secondary peak in summer, in the eastern part of the study region, including Taklamakan, Balkhash-Junggar and Hexi Corridor regions, and (ii) peak dust emission in summer at the western side of the study region, including Pre-Aral, Karakum-Kyzylkum and Upper Amudarya regions. These patterns reflect two different dominant factors operating in the eastern and western regions. The spring peaking emissions are largely caused by meteorological factors, i.e. strong winds associated with pressure anomalies. In summer, MSLP anomalies, although identifiable, are less pronounced and significant changes in vegetation cover become the dominant factor driving the Central Asian dust sources.

Despite high variations in seasonal SLP anomalies, the seasonal patterns of MSLP of dusty days are generally similar across the study region. It indicates that the variations in dust emissions, and the seasons of peak activity, are strongly controlled by the land surface characteristics of each region. The differences between the source regions with regards to the dust generating wind speeds also shows the importance of surface characteristics and topography on the wind erosion thresholds. The highest dust generating wind speeds were recorded in the Pre-Aral region and the lowest wind speeds were observed in the Upper Amudarya region (< 5 m s^{-1}). However, it should be kept in mind that part of these variations in surface wind speeds originates from uncertainties of the ERA-Interim reanalysis, especially in modeled wind components over narrow valleys, such as in the Upper Amudarya region. Validation of ERA-Interim against observational data will improve the quality of analysis in the future.

6.3. Comparison between DEP and AOD results

In this section a comparison between the results reported in chapters 4 and 5 is presented. To visually investigate the spatial correlation between the two datasets and also calculate the spatial statistics, we plotted all DPS (Figure 5-1) over the FO maps (Figure 4-1). Figure 6-3 shows the spatial distribution of all recorded DPS in the Aralkum and the Pre-Aral regions during the time period of 2003 to 2012, superimposed over the FO map of JJA. The FO map for summer season was selected because dust emission in this region reaches its peak in the summer months. A very important result, emerging from this comparison, is a gap in AOD observations over the Aralkum desert where the highest concentration of active DPS was observed. Further investigation and personal communication with the MODIS AOD developing team, based in NASA's Goddard Space Flight Center, confirmed that due to using a static surface reflectance model for the Aral Sea region in DB AOD retrieval algorithm, no AOD retrieval were made available in MODIS C6 over the Aralkum. There was also an apparent discrepancy between the location of dust hotspots derived from AOD and locations of DPS in the Aralkum desert and surrounding regions. The active dust hotspots with FO> 60% were detected in the east and west sides of the Aralkum, whereas very few actual DPS were recorded in these regions. In particular, southern part of the Ustyurt Plateau region, the area between the Aralkum and Caspian Sea, was highlighted as a very active region in our FO analysis, but there was no record of dust plumes originating from this region in our investigation of MODIS DEP images. In the Pre-Aral region, spatial correlation between the two datasets seems to be stronger than in the Aralkum. Density of DPS in the western part of the Pre-Aral is higher in areas with high FO values, but there is less agreement between the two datasets in the eastern part of this region.

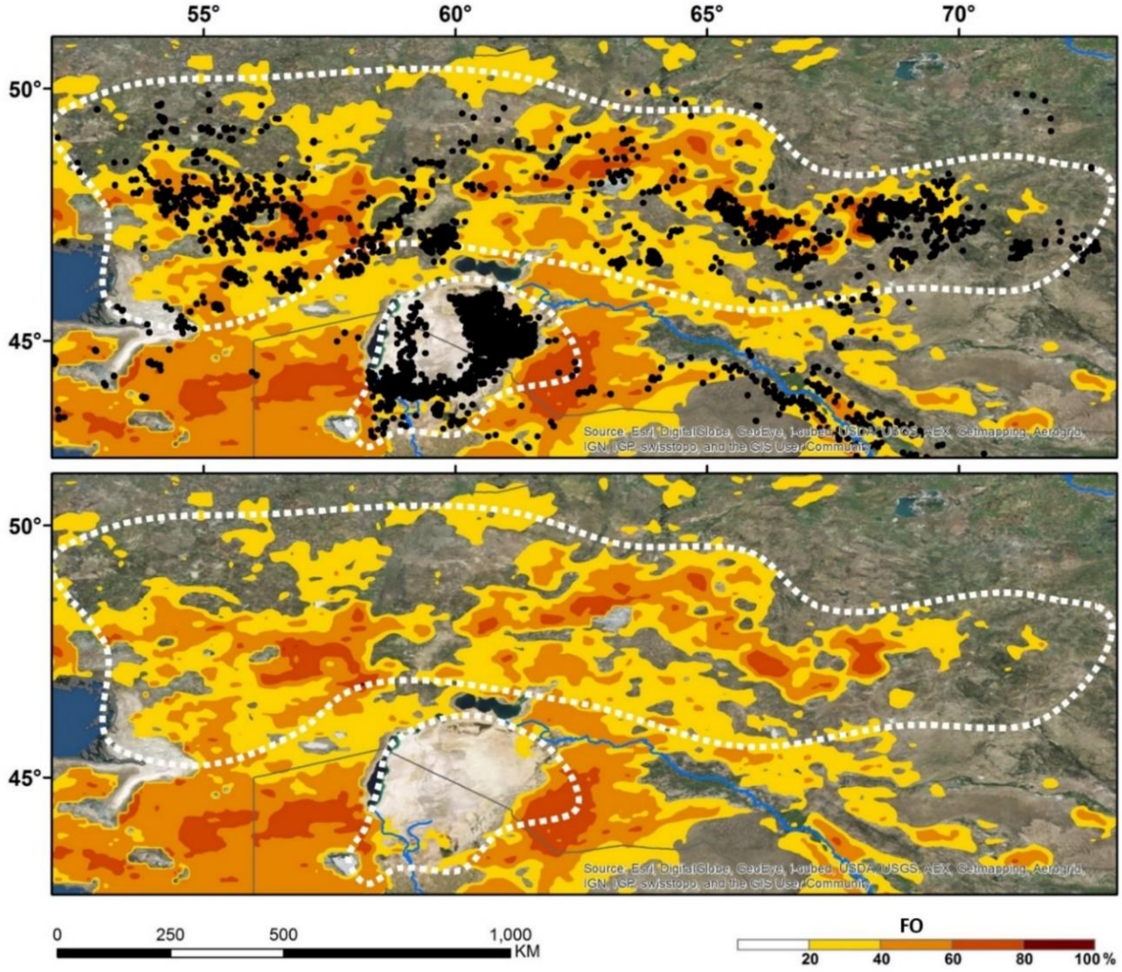

Figure 6-3. Spatial distribution of DPS (black circles), and FO of DOD>0.2 in the Aralkum and the Pre-Aral region. Background image is from Esri Digital Globe.

To provide a statistical view of the spatial correlation between DPS and FO datasets, we investigated the distribution histogram of FO values for the DPS record identified in this region. For this purpose, we first extracted the FO value at the geographical location of each DPS and then plotted the number of DPS records against their corresponding FO value. Therefore, the greater skewness of the distribution histogram towards higher FO values indicates stronger agreement between the two datasets.

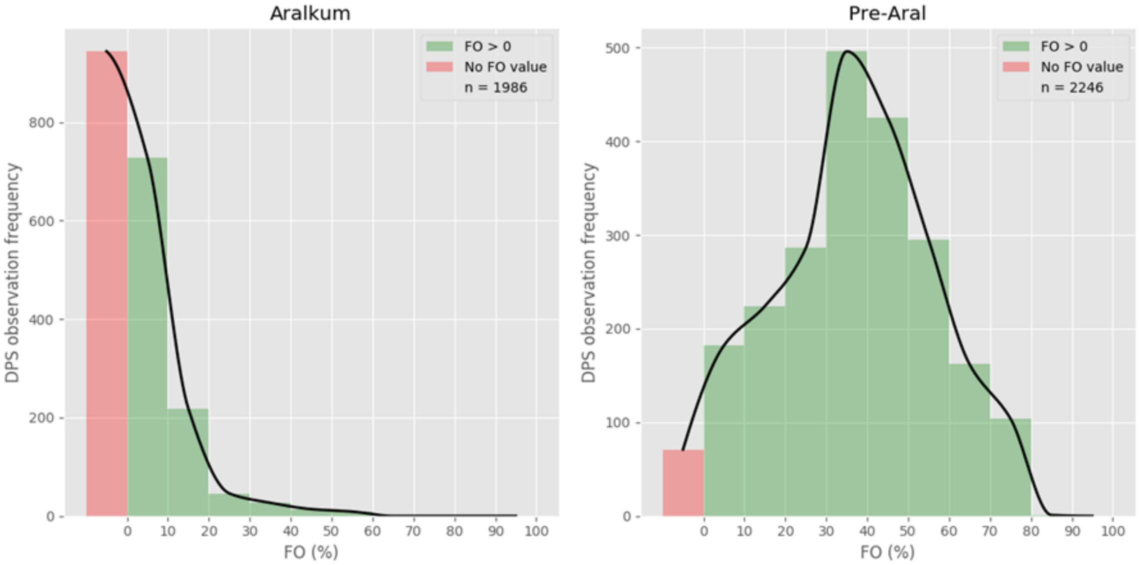

Figure 6-4. Distribution histogram of FO values for DPS records in the Aralkum (left) and the PreAral region (right)

Distribution of FO values for DPS detected in the Aralkum and Pre-Aral region is presented in Figure 6-4. The largest number of DPS records in the Aralkum region was recorded in areas where no AOD observation were available. This confirms our visual observation in Figure 6-3, where the majority of DPS are located inside the boundaries of the former Aral Sea and high FO areas are displaced east and west outside of its main boundaries. The rest of DPS were also located in areas with low FO values (mostly in south-west of the Aralkum desert). The distribution histogram for the Pre-Aral region, however, indicates a better agreement between the DPS and the FO datasets. The highest number of DPS were recorded in the areas with FO values between 30% to 40%.

Spatial distribution of DPS and FO in the Karakum-Kyzylkum and the Upper Amudarya region is shown in Figure 6-5. There seems to be a good agreement between the two datasets in the areas along the Syrdarya River in the north-east of the Kyzylkum desert and in the Samarkand region. Towards the west of the Karakum-Kyzylkum, an area of high DPS density was observed in the drainage basin of Lake Sarygamysh while the FO observations are low or non-existent. In the central part of the Karakum, most of DPS overlapped with low FO areas (FO<40).

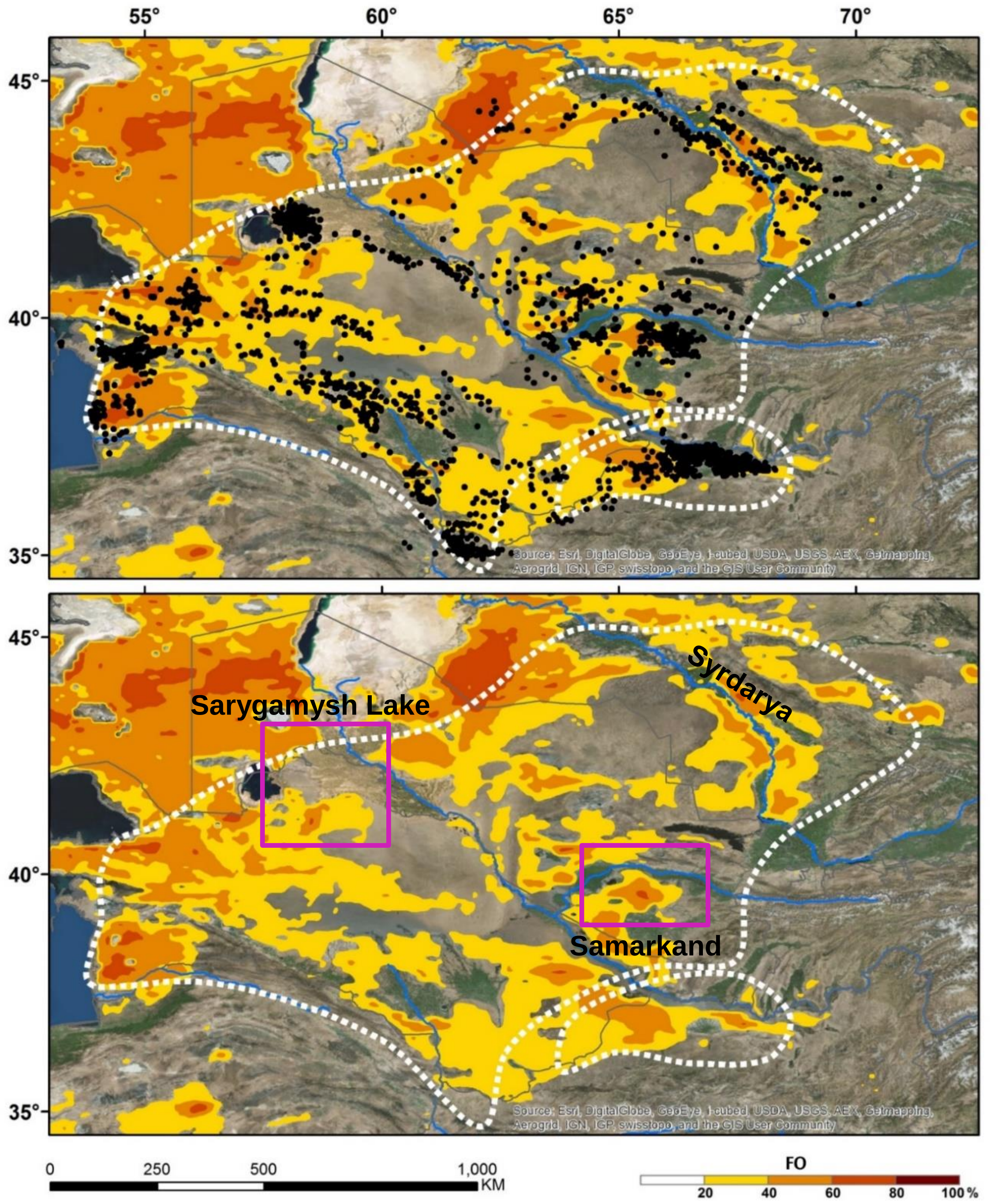

Figure 6-5. Spatial distribution of DPS (black circles) and FO of DOD>0.2 in the Karakum-Kyzylkum and the Upper Amudarya region. Background image is from Esri Digital Globe.

Analysis of distribution histogram for DPS records in the Karakum-Kyzylkum region shows a relatively poor agreement between FO and DPS datasets. As it is shown in Figure 6-6, the highest number of DPS were recorded over the areas with FO values 0 -10 %. Comparing to the Aralkum distribution histogram (Figure 6-4), the wider spread of the histogram indicates a stronger correlation between the FO values and the density of DPS in some areas within the Karakum and Kyzylkum deserts. The distribution histogram for the Upper Amudarya region suggests a good correlation between the FO and DPS datasets over this region. The frequency of DPS in this region peaked in areas with FO values of 40 - 50 %.

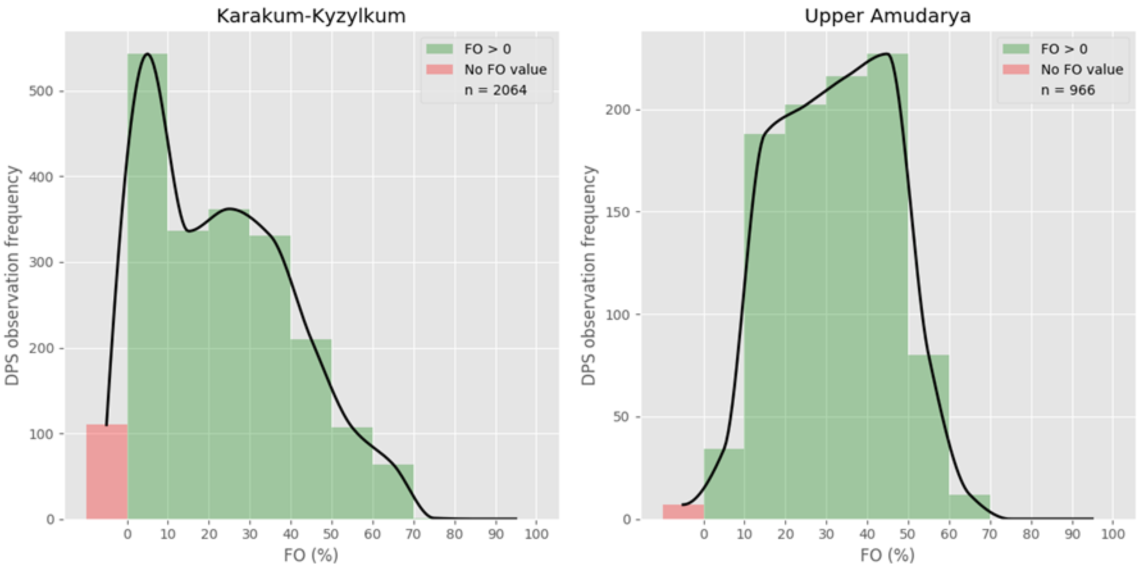

Figure 6-6. Distribution histogram of FO values for DPS records in the Karakum-Kyzylkum (left) and the Upper Amudarya region (right)

Figure 6-7 presents the geographical distribution of DPS records in the other three source regions: Balkhash-Junggar, Taklamakan and Hexi Corridor. It is evident that the spatial distribution of dust hotspots in the Taklamakan closely follows the same pattern of detected DPS, except in the southern part of the desert. There is also a good agreement between active dust hotspots with high FO values and recorded DPS in the Hexi Corridor region. In contrast, in the Balkhash-Junggar basins there seems to be a poor agreement between the two datasets. Most of DPS in this region were identified in areas that were not highlighted by the FO analysis.

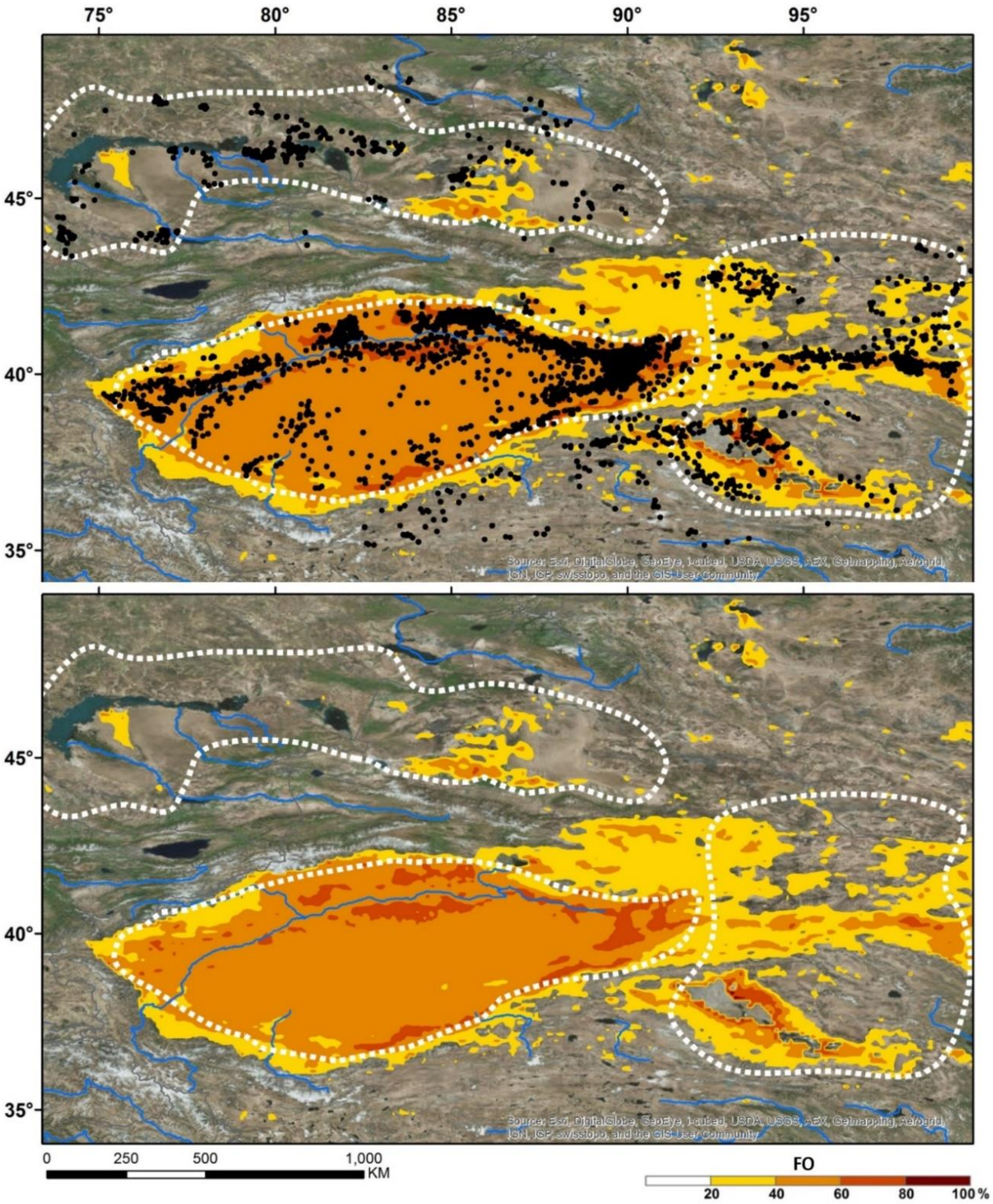

Figure 6-7. Spatial distribution of DPS (black circles), and FO of DOD>0.2 in the Taklamakan, Hexi Corridor and Balkhash-Junggar region. Background image is from Esri Digital Globe.

Distribution of FO values of DPS in the Taklamakan and Hexi Corridor region is presented in Figure 6-8. As expected from visual comparison, a very good agreement between FO and DPS datasets was observed in the Taklamakan. More than 2000 DPS in this region were identified in areas with FO values of 60 -70 %. The narrow spread of the distribution histogram (Figure 6-8, left panel) indicates that there was very small number of DPS in areas with low FO values. Distribution of the FO values for the Hexi Corridor region (Figure 6-8, right panel) shows that although the correlation between FO and DPS datasets are not as significant as in the Taklamakan, there is still a good agreement between them.

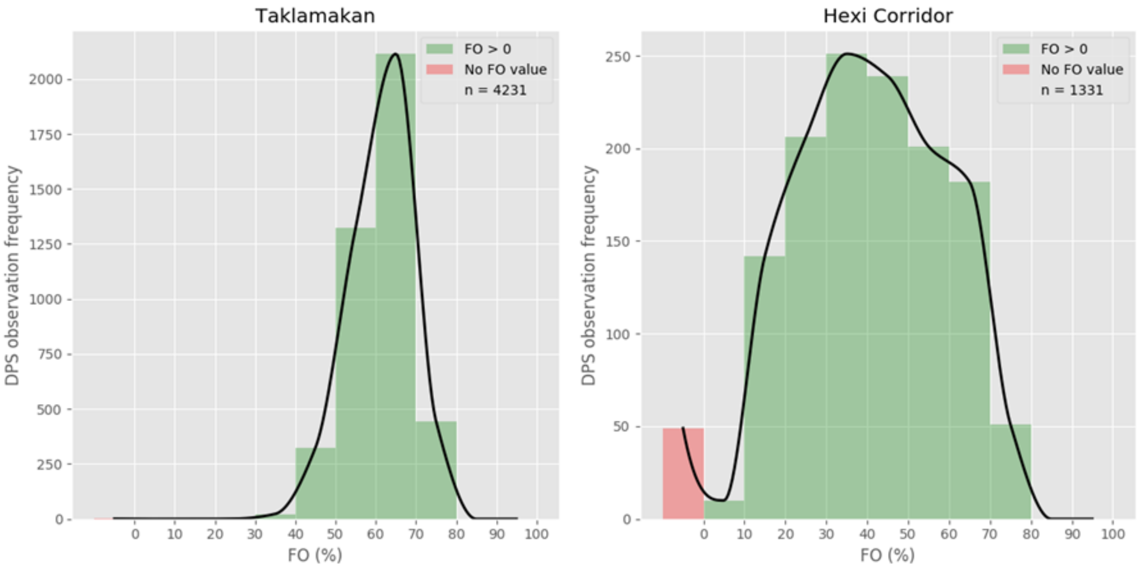

Figure 6-8. Distribution histogram of FO values for DPS in the Taklamakan (left) and the Hexi Corridor region (right).

As it is shown in Figure 6-9, correlation between the two datasets in the Balkhash and Junggar basins was not significant. The greatest number of DPS in this region were overlaid on areas with FO values of 0 to 10 percent. Also there were no AOD observation for a relatively high number of DPS detected in this region.

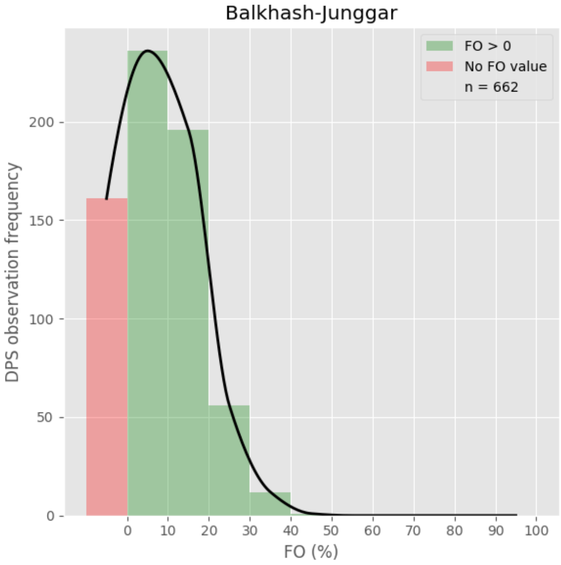

Figure 6-9. Distribution histogram of FO values for DPS records in the Balkhash-Junggar region

6.4. Summary

In this chapter several aspects of dust emissions in identified dust sources were compared. A comparison between the results of AOD analysis and the DPS results was also made and their differences was analysed. This comparison exposed one of the most important shortcomings of the methods that are based on the estimations of atmospheric dust loading, such as MODIS AOD (e.g. Ginoux *et al.*, 2012) and TOMS Aerosol Index (e.g. Prospero *et al.*, 2002; Washington *et al.*, 2003). It was revealed that a distinctive shift exists in the location of dust hotspots obtained from FO analysis of AOD observations, compared to the location of DPS records. We showed that the AOD-based methods have a tendency for incorrectly highlighting dust sources based on the presence of transported dust in the atmosphere. This artefact was more pronounced over areas affected by strong winds such as the Aralkum, where transported dust led to detection of very active dust hotspots away from the dry lakebed (see Figure 6-3). It may also be partially due to not including the low quality data (QA=1) in FO analysis of the AOD data. A recent study by Baddock *et al.* (2016) showed that using QA=1 data for FO analysis might improve the accuracy of dust source detection using this method.

It was also shown that a very small number of DPS were identified in the southern margins of the Taklamakan desert, despite being featured as an active dust hotspot in AOD results (Figure 6-7). This is the result of accumulation of transported dust over the southern part of the Taklamakan, as demonstrated by Rittner *et al.* (2016) and Uno *et al.* (2005), which led to false source detection by our AOD method. It can also be due to the fact that high level of dust loading over the southern margins of the Taklamakan makes it difficult for the operator to detect activated point sources.

The findings of this study indicate that although the conventional methods based on the analysis of station records of dust events (e.g. Middleton, 1986; Issanova *et al.*, 2014) or dust deposition rate (e.g. Lawrence *et al.*, 2009; Groll *et al.*, 2013) provide a useful insight into the temporal variation of dust emissions and their impact region, they can be inaccurate in determining the precise location of dust sources, unless a very careful compositional analysis is performed to determine the provenance of the dust samples, which was not the case for studies carried in Central Asia. For instance, our visual investigation of daily DEP images for 10 years showed that in many cases the dust plumes observed overs central Karakum/Kyzylkum were originated from dust sources in the Pre-Aral region which were activated more than 24 hours before reaching to the Karakum.

This study contributes to our understanding of the spatiotemporal variation of dust emission in Central Asia at sub-basin scale which can play an important role in validation and improvement of regional and global dust models. Many dust modelling studies such as a recent study on modelling of dust emission in Central Asia by Li *et al.* (2017) can benefit from a high resolution map of dust sources for validation of the modelling results and also to improve parametrization of the dust model. Li et al. (2017) developed a dust loading model for Central Asia while accounting for regional climate and land cover and land use changes for the 1950-2010 period in April and reported a low to medium correlation between their results and the average MODIS AOD during the period 200-2014. It is assumed that such modelling results can be validated more accurately using our database of dust sources for Central Asia.

Chapter 7. Conclusions and suggestions for further research

This thesis investigates the characteristics of dust sources in Central Asia and north-western China (35N-50N, 50E-100E) and analyses their spatial and temporal variations through employing remote sensing imagery and GIS tools. The work focuses on four research questions: 1) What are the spatiotemporal characteristics of dust emissions? 2) What are the land surface characteristics of active dust sources? 3) What are the synoptic controls on dust emissions? 4) What are the direction of dust entrainments at the time of dust emission?

In Chapter 3, we described the methodology that was adopted to address these research questions. After undertaking a comprehensive literature review on the dust observation techniques, we selected a multi-scale approach to investigate the dust sources in the study area. The first step was based on the satellite observations of atmospheric aerosol optical depth (AOD). For this purpose 12 years of daily MODIS Enhanced Deep Blue (eDB) AOD products for 2003-2014 were retrieved through NASA's Level 1 and Atmosphere Archive and Distribution System (LAADS). An automated processing chain was designed to generate daily images of dust optical depth (DOD) at 10 km spatial resolution. Finally a frequency of occurrence (FO) analysis was performed to reveal the seasonal and spatial distribution of dust hotspots.

Although using remotely sensed AOD datasets was a useful tool for investigating the seasonality of dust emission and spatial distribution of dust emissions, a more precise method was needed in order to locate the exact location of dust emitting surfaces at sub-basin scale. Hence the second phase was developed based on the visual detection of activated dust point sources (DPS) in higher resolution satellite images. A dust enhancement method, adopted from Miller (2003), was employed to generate dust enhancement products (DEP) from daily MODIS L1B calibrated radiance data at the spatial resolution of 1 km. We designed a GIS-based workflow to visually inspect the daily DEP images, generated for 10 years between 2003 and 2012, and record the identified DPS in a geospatial database. Surface wind speed and direction data from ERA-Interim reanalysis dataset were also spatially and temporally interpolated to the exact location and day of the DPS observation and were recorded in the geospatial database.

Chapter 4 presents the results of dust hotspot detection using MODIS AOD. Analysis of FO of DOD>0.2 revealed several active dust hotspots in the study region. In particular, north-eastern parts of the Tarim Basin were highlighted as a major dust hotspot, with the highest activity in spring months. During summer dust hotspot with high FO (60-80%) were spread over the area between the eastern shores of Caspian Sea to the eastern side of the Aralkum. The highest FO in this region corresponds to stony desert of the Ustyurt Plateau in the western side of the Aralkum and also the Pre-Aral areas. Inter-annual variation of AOD over areas with FO higher than 40% showed a steady increase in mean AOD over the Aralkum, Pre-Aral and Karakum-Kyzylkum regions, while there was no significant trend over the eastern Taklamakan.

In Chapter 5, results of the analyses of spatiotemporal distributions of the identified DPS between 2003 and 2012 were presented. We first analysed spatial distribution of the DPS records in order to obtain a general picture of active sources in Central Asia. Our analysis showed that there is a clear link between fluvial systems and concentration of DPS records, in particular in the Tarim basin, where the majority of DPS were detected along the floodplains of the Tarim River in the northern margins of the Taklamakan desert. The same pattern was apparent in the Karakum-Kyzylkum, with high density of observed DPS along the fluvial plains of the Amudarya and Syrdarya rivers. A large number of DPS were also associated with the major alluvial fans in the region such as those formed at the outlet of the Murghab, Tedzhen and Balkh rivers.

Investigation of monthly variations in the number of dusty days enabled us to categorise the main dust sources into seven dust source regions. Subsequently, three aspects of dust storm formation in these regions were investigated, including land surface characteristics, inter- and intra-annual variability in dust emission, and synoptic controls on dust emission and entraining wind direction. These results were further analysed in Chapter 6 by a cross-comparison of the main dust source regions and also comparison between the spatial patterns of dust sources, obtained from AOD and DEP investigations.

This analysis revealed several previously unidentified or under-reported aspects of dust storm formation in Central Asia, which can be summarized as follows:

- Aralkum has become one of the most important sources of dust in Central Asia. With the westerly prevailing dust transport, towards populated areas of western Asia and Caspian region, dust emissions from this region can potentially affect not only ecosystems but human wellbeing. Detailed modelling of dust transport from this region is required and knowledge of dust source locations will be an important input to future modelling studies.

- A marked increase in dust emission from the Aralkum was observed during the time period of our study. This increase was evident from the analysis of both AOD and DPS observations. A less significant increasing trend was also noted in the Karakum-Kyzylkum region.

- We found a very high density of DPS in Aralkum and Upper Amudarya region, compared to other dust source regions. Upper Amudarya region, in particular, was highlighted for the first time in our study, with more than 10 DPS per 1000 km^2.

- Fire has had a significant effect on developing dust emitting surfaces in the Pre-Aral and Balkhash-Junggar regions. Nearly 80% of dust sources in this region were characterized by radical degradation of vegetation cover due to wildfire events.

- A distinctive shift was noted in the location of dust hotspots obtained from FO analysis of AOD observations, compared to the location of DPS records. This is because AOD values are the highest in the center of dust plume, where the concentration of dust is highest, which is not necessarily the points of dust sources. This shift is more noticeable over source regions that are affected by high wind regimes (e.g. AralKum).

- A very small number of DPS were identified in the southern margins of the Taklamakan desert, despite being featured as an active source of dust in AOD results.

- In terms of climatology of dust emissions, it was found that the dust events are closely linked to the formation of strong dipole patterns with a sharp gradient between the high pressure anomalies and low pressure anomalies over the dust source regions.

This study provided a multi-scale overview of dust source distribution in Central Asia identifying the main regions of dust emissions. Every region requires more in-depth analysis and can be a focus of a further research project which will involve a more detailed characterisation of land surface features, meteorological conditions through the ground-based instrumental observations, and modelling of dust transport from the region. Detailed regional analysis provides potential for improvements in land management and agricultural practices especially in the regions where dust originates from the sources created through anthropogenic activities.

This study merely touched upon dust transportation from the identified source regions. More detailed analysis, involving modelling studies, is required. Dust deposition regions should be examined too with particular focus on the agricultural regions where dust is a stressor affecting crops and reducing yields. Dust deposition on snow- and ice covered mountains of the Tian Shan, Pamir and Hindu-Kush should be examined with a view of analysis of at-surface radiative forcing of dust and its impact on snow and glacier melt.

Chapter 8. References

Abdullaev, S.F., Maslov, V.A., Nazarov, B.I. & Salikhov, T.K. 2014. Variations in parameters of aerosol optical thickness in Dushanbe. *Izvestiya, Atmospheric and Oceanic Physics,* 50**,** 431-434.

Ackerman, S.A. 1997. Remote sensing aerosols using satellite infrared observations. *Journal of Geophysical Research: Atmospheres (1984–2012),* 102**,** 17069-17079.

Aizen, E.M., Aizen, V.B., Melack, J.M., Nakamura, T. & Ohta, T. 2001. Precipitation and atmospheric circulation patterns at mid-latitudes of Asia. *International Journal of Climatology,* 21**,** 535-556.

Aizen, V.B., Aizen, E.M., Melack, J.M. & Dozier, J. 1997. Climatic and hydrologic changes in the Tien Shan, central Asia. *Journal of Climate,* 10**,** 1393-1404.

Aladin, N.V., Plotnikov, I.S., Micklin, P. & Ballatore, T. 2009. The Aral Sea: Water level, salinity and long-term changes in biological communities of an endangered ecosystem-past, present and future. *Natural Resources and Environmental Issues,* 15**,** 177.

Anselmo, T., Clifton, R., Hunt, W., Lee, K., Murray, T., Powell, K., Chomette, O., Viollier, M., Garnier, A. & Pelon, J. 2006. Cloud Aerosol LIDAR Infrared Pathfinder Satellite Observations (CALIPSO). *Data management system and data products catalog, CALIPSO documentation, NASA, release,* 2.

Aoki, I., Kurosaki, Y., Osada, R., Sato, T. & Kimura, F. 2005. Dust storms generated by mesoscale cold fronts in the Tarim Basin, Northwest China. *Geophysical Research Letters,* 32**,** L06807.

Aref'ev, V.N., Kashin, F.V., Krasnosel'tsev, A.V., Semenov, V.K. & Sinyakov, V.P. 2008. Structure of time variations in the atmospheric transparency in Central Eurasia (Issyk Kul monitoring station). *Izvestiya, Atmospheric and Oceanic Physics,* 44**,** 615-620.

Argaman, E., Singer, A. & Tsoar, H. 2006. Erodibility of some crust forming soils/sediments from the Southern Aral Sea Basin as determined in a wind tunnel. *Earth Surface Processes and Landforms,* 31**,** 47-63.

Babaev, A.G. 1994. Landscapes of Turkmenistan. *Biogeography and Ecology of Turkmenistan.* Springer, 5-22.

Baddock, M.C., Bullard, J.E. & Bryant, R.G. 2009. Dust source identification using MODIS: A comparison of techniques applied to the Lake Eyre Basin, Australia. *Remote Sensing of Environment,* 113**,** 1511-1528.

Baddock, M.C., Ginoux, P., Bullard, J.E. & Thomas, G. 2016. Do MODIS-defined dust sources have a geomorphological signature? *Geophysical Research Letters,* 43**,** 2606-2613.

Baitulin, I.O. 2001. National strategy and action plan to combat desertification in Kazakhstan. *Sustainable Land Use in Deserts.* Springer, 441-447.

Belnap, J. & Gillette, D.A. 1998. Vulnerability of desert biological soil crusts to wind erosion: the influences of crust development, soil texture, and disturbance. *Journal of arid environments,* 39**,** 133-142.

Biscaye, P., Grousset, F., Revel, M., Van Der Gaast, S., Zielinski, G., Vaars, A. & Kukla, G. 1997. Asian provenance of glacial dust (stage 2) in the Greenland Ice Sheet Project 2 ice core, Summit, Greenland. *Journal of Geophysical Research: Oceans (1978–2012),* 102**,** 26765-26781.

Brindley, H., Knippertz, P., Ryder, C. & Ashpole, I. 2012. A critical evaluation of the ability of the Spinning Enhanced Visible and Infrared Imager (SEVIRI) thermal infrared red-green-blue rendering to identify dust events: Theoretical analysis. *Journal of Geophysical Research: Atmospheres (1984–2012),* 117.

Brock, B.W., Willis, I.C. & Sharp, M.J. 2000. Measurement and parameterization of albedo variations at Haut Glacier d'Arolla, Switzerland. *Journal of Glaciology,* 46**,** 675-688.

Bullard, J., Baddock, M., Mctainsh, G. & Leys, J. 2008. Sub-basin scale dust source geomorphology detected using MODIS. *Geophysical Research Letters,* 35**,** L15404.

Bullard, J.E., Harrison, S.P., Baddock, M.C., Drake, N., Gill, T.E., Mctainsh, G. & Sun, Y. 2011. Preferential dust sources: A geomorphological classification designed for use in global dust-cycle models. *Journal of Geophysical Research: Earth Surface,* 116**,** n/a-n/a.

Carboni, E., Thomas, G., Sayer, A., Siddans, R., Poulsen, C., Grainger, R., Ahn, C., Antoine, D., Bevan, S. & Braak, R. 2012. Intercomparison of desert dust optical depth from satellite measurements. *Atmospheric Measurement Techniques,* 5**,** 1973-2002.

Casey, K.A. 2012. Supraglacial dust and debris: geochemical compositions from glaciers in Svalbard, southern Norway, Nepal and New Zealand. *Earth Syst. Sci. Data Discuss.,* 5**,** 107-145.

Che, H., Wang, Y., Sun, J., Zhang, X., Zhang, X. & Guo, J. 2013. Variation of aerosol optical properties over the Taklimakan Desert in China. *Aerosol Air Qual. Res,* 13**,** 777-785.

Cherenkova, A., Kononova, A. & Muratova, A. 2013. Summer drought 2010 in the European Russia. *Geography, Environment, Sustainability,* 6**,** 55-66.

Choobari, O.A., Zawar-Reza, P. & Sturman, A. 2014. The global distribution of mineral dust and its impacts on the climate system: A review. *Atmospheric Research,* 138**,** 152-165.

Darmenova, K. & Sokolik, I.N. 2007. Assessing uncertainties in dust emission in the Aral Sea region caused by meteorological fields predicted with a mesoscale model. *Global and Planetary Change,* 56**,** 297-310.

Dee, D.P., Uppala, S.M., Simmons, A.J., Berrisford, P., Poli, P., Kobayashi, S., Andrae, U., Balmaseda, M.A., Balsamo, G., Bauer, P., Bechtold, P., Beljaars, A.C.M., Van De Berg, L., Bidlot, J., Bormann, N., Delsol, C., Dragani, R., Fuentes, M., Geer, A.J., Haimberger, L., Healy, S.B., Hersbach, H., Hólm, E.V., Isaksen, L., Kållberg, P., Köhler, M., Matricardi, M., Mcnally, A.P., Monge-Sanz, B.M., Morcrette, J.J., Park, B.K., Peubey, C., De Rosnay, P., Tavolato, C., Thépaut, J.N. & Vitart, F. 2011. The ERA-Interim reanalysis: configuration and performance of the data assimilation system. *Quarterly Journal of the Royal Meteorological Society,* 137**,** 553-597.

Deuzé, J., Bréon, F., Devaux, C., Goloub, P., Herman, M., Lafrance, B., Maignan, F., Marchand, A., Nadal, F. & Perry, G. 2001. Remote sensing of aerosols over land surfaces from POLDER-ADEOS-1 polarized measurements. *Journal of Geophysical Research: Atmospheres (1984–2012),* 106, 4913-4926.

Dozier, J., Green, R.O., Nolin, A.W. & Painter, T.H. 2009. Interpretation of snow properties from imaging spectrometry. *Remote Sensing of Environment,* 113, Supplement 1, S25-S37.

Dubovik, O., Holben, B., Lapyonok, T., Sinyuk, A., Mishchenko, M., Yang, P. & Slutsker, I. 2002. Non-spherical aerosol retrieval method employing light scattering by spheroids. *Geophysical Research Letters,* 29, 54-1-54-4.

El-Ossta, E., Qahwaji, R. & Ipson, S.S. 2013. Detection of Dust Storms Using MODIS Reflective and Emissive Bands. *IEEE Journal of Selected Topics in Applied Earth Observations and Remote Sensing,* 6, 2480-2485.

Evan, A.T., Heidinger, A.K. & Pavolonis, M.J. 2006. Development of a new over-water Advanced Very High Resolution Radiometer dust detection algorithm. *International Journal of Remote Sensing,* 27, 3903-3924.

Fan, X., Chen, H., Lin, L., Han, Z. & Goloub, P. 2009. Retrieval of aerosol optical properties over the Beijing area using POLDER/PARASOL satellite polarization measurements. *Advances in Atmospheric Sciences,* 26, 1099-1107.

Fan, X., Goloub, P., Deuzé, J.-L., Chen, H., Zhang, W., Tanré, D. & Li, Z. 2008. Evaluation of PARASOL aerosol retrieval over North East Asia. *Remote Sensing of Environment,* 112, 697-707.

Fet, V. & Atamuradov, K.I. 1994. *Biogeography and ecology of Turkmenistan*, Kluwer Academic Publishers.

Gao, H. & Washington, R. 2009. Arctic oscillation and the interannual variability of dust emissions from the Tarim Basin: a TOMS AI based study. *Climate Dynamics,* 35, 511-522.

Gautam, R., Hsu, N.C., Lau, W.K.M. & Yasunari, T.J. 2013. Satellite observations of desert dust-induced Himalayan snow darkening. *Geophysical Research Letters,* 40, 988-993.

Gill, T.E. 1996. Eolian sediments generated by anthropogenic disturbance of playas: human impacts on the geomorphic system and geomorphic impacts on the human system. *Geomorphology,* 17, 207-228.

Gillette, D.A. 1999. A qualitative geophysical explanation for hot spot dust emitting source regions. *Contributions to Atmospheric Physics,* 72, 67-77.

Gillette, D.A. & Passi, R. 1988. Modeling dust emission caused by wind erosion. *Journal of Geophysical Research: Atmospheres,* 93, 14233-14242.

Ginoux, P., Chin, M., Tegen, I., Prospero, J.M., Holben, B., Dubovik, O. & Lin, S.J. 2001. Sources and distributions of dust aerosols simulated with the GOCART model. *Journal of Geophysical Research: Atmospheres,* 106, 20255-20273.

Ginoux, P. & Deroubaix, A. 2017. Space Observations of Dust in East Asia. *In:* BOUARAR, I., WANG, X. & BRASSEUR, G. P. (eds.) *Air Pollution in Eastern Asia: An Integrated Perspective.* Cham: Springer International Publishing, 365-383.

Ginoux, P., Garbuzov, D. & Hsu, N.C. 2010. Identification of anthropogenic and natural dust sources using Moderate Resolution Imaging Spectroradiometer (MODIS) Deep Blue level 2 data. *Journal of Geophysical Research,* 115**,** D05204.

Ginoux, P., Prospero, J.M., Gill, T.E., Hsu, N.C. & Zhao, M. 2012. Global-Scale Attribution Of Anthropogenic And Natural Dust Sources And Their Emission Rates Based On Modis Deep Blue Aerosol Products. *Reviews of Geophysics,* 50(3)**,** 1-36.

Ginoux, P., Prospero, J.M., Torres, O. & Chin, M. 2004. Long-term simulation of global dust distribution with the GOCART model: correlation with North Atlantic Oscillation. *Environmental Modelling & Software,* 19**,** 113-128.

Goudie, A. & Middleton, N.J. 2006. *Desert dust in the global system*, Springer Science & Business Media.

Goudie, A.S. 1983. Dust storms in space and time. *Progress in Physical Geography,* 7**,** 502-530.

Groll, M., Opp, C. & Aslanov, I. 2013. Spatial and temporal distribution of the dust deposition in Central Asia – results from a long term monitoring program. *Aeolian Research,* 9**,** 49-62.

Grousset, F.E., Biscaye, P.E., Revel, M., Petit, J.-R., Pye, K., Joussaume, S. & Jouzel, J. 1992. Antarctic (Dome C) ice-core dust at 18 k.y. B.P.: Isotopic constraints on origins. *Earth and Planetary Science Letters,* 111**,** 175-182.

Hansell, R.A., Ou, S.C., Liou, K.N., Roskovensky, J.K., Tsay, S.C., Hsu, C. & Ji, Q. 2007. Simultaneous detection/separation of mineral dust and cirrus clouds using MODIS thermal infrared window data. *Geophysical Research Letters,* 34**,** L11808.

Harris, N. 2003. *Atlas of the World's Deserts*, Fitzroy Dearborn.

Herman, J., Bhartia, P., Torres, O., Hsu, C., Seftor, C. & Celarier, E. 1997. Global distribution of UV-absorbing aerosols from Nimbus 7/TOMS data. *Journal of Geophysical Research,* 102**,** 16911-16,922.

Holben, B., Eck, T., Slutsker, I., Tanre, D., Buis, J., Setzer, A., Vermote, E., Reagan, J., Kaufman, Y. & Nakajima, T. 1998. AERONET - A federated instrument network and data archive for aerosol characterization. *Remote Sensing of Environment,* 66**,** 1-16.

Holben, B., Tanre, D., Smirnov, A., Eck, T., Slutsker, I., Abuhassan, N., Newcomb, W., Schafer, J., Chatenet, B. & Lavenu, F. 2001. An emerging ground based aerosol climatology: Aerosol optical depth from AERONET. *Journal of Geophysical Research: Atmospheres (1984–2012),* 106**,** 12067-12097.

Hsu, N.C., Jeong, M.J., Bettenhausen, C., Sayer, A.M., Hansell, R., Seftor, C.S., Huang, J. & Tsay, S.C. 2013. Enhanced Deep Blue aerosol retrieval algorithm: The second generation. *Journal of Geophysical Research: Atmospheres,* 118**,** 9296-9315.

Hsu, N.C., Tsay, S.-C., King, M.D. & Herman, J.R. 2004. Aerosol properties over bright-reflecting source regions. *Geoscience and Remote Sensing, IEEE Transactions on,* 42**,** 557-569.

Hsu, N.C., Tsay, S.-c., King, M.D., Member, S., Herman, J.R. & During, A. 2006. Deep Blue Retrievals of Asian Aerosol Properties During ACE-Asia. 44**,** 3180-3195.

Husar, R.B., Prospero, J.M. & Stowe, L.L. 1997. Characterization of tropospheric aerosols over the oceans with the NOAA advanced very high resolution radiometer optical thickness operational product. *Journal of Geophysical Research,* 102**,** 16889-16,909.

Indoitu, R., Kozhoridze, G., Batyrbaeva, M., Vitkovskaya, I., Orlovsky, N., Blumberg, D. & Orlovsky, L. 2015. Dust emission and environmental changes in the dried bottom of the Aral Sea. *Aeolian Research,* 17**,** 101-115.

Indoitu, R., Orlovsky, L. & Orlovsky, N. 2012. Dust storms in Central Asia: Spatial and temporal variations. *Journal of Arid Environments,* 85**,** 62-70.

Issanova, G., Jilili, A. & Semenov, O. 2014. Deflation processes and their role in desertification of the southern Pre-Balkhash deserts. *Arabian Journal of Geosciences,* 7**,** 4513-4521.

Jumashov, A. 1999. Genetic types of deserts in Central Asia. *Desert Problems and Desertification in Central Asia.* Springer, 77-87.

Kahn, R.A., Gaitley, B.J., Garay, M.J., Diner, D.J., Eck, T.F., Smirnov, A. & Holben, B.N. 2010. Multiangle Imaging SpectroRadiometer global aerosol product assessment by comparison with the Aerosol Robotic Network. *Journal of Geophysical Research: Atmospheres,* 115.

Kai, K., Nagata, Y., Tsunematsu, N., Matsumura, T., Kim, H.-S., Matsumoto, T., Hu, S., Zhou, H., Abo, M. & Nagai, T. 2008. The Structure of the Dust Layer over the Taklimakan Deser during the Dust Storm in April 2002 as Observed Using a Depolarization Lidar. *Journal of the Meteorological Society of Japan. Ser. II,* 86**,** 1-16.

King, M.D., Menzel, W.P., Kaufman, Y.J., Tanre, D., Bo-Cai, G., Platnick, S., Ackerman, S.A., Remer, L.A., Pincus, R. & Hubanks, P.A. 2003. Cloud and aerosol properties, precipitable water, and profiles of temperature and water vapor from MODIS. *Geoscience and Remote Sensing, IEEE Transactions on,* 41**,** 442-458.

Knippertz, P. 2014. Meteorological aspects of dust storms. *Mineral Dust.* Springer, 121-147.

Kostianoy, A.G., Lebedev, S.A. & Solovyov, D.M. 2014. Satellite Monitoring of the Caspian Sea, Kara-Bogaz-Gol Bay, Sarykamysh and Altyn Asyr Lakes, and Amu Darya River. *In:* ZONN, I. S. & KOSTIANOY, A. G. (eds.) *The Turkmen Lake Altyn Asyr and Water Resources in Turkmenistan.* Berlin, Heidelberg: Springer Berlin Heidelberg, 197-231.

Kozhoridze, G., Orlovsky, L. & Orlovsky, N. Year. Monitoring land cover dynamics in the Aral Sea region by remote sensing. *In:* Proc SPIE, 2012. 85381V.

Kundzewicz, Z.W., Merz, B., Vorogushyn, S., Hartmann, H., Duethmann, D., Wortmann, M., Huang, S., Su, B., Jiang, T. & Krysanova, V. 2015. Analysis of changes in climate and river discharge with focus on seasonal runoff predictability in the Aksu River Basin. *Environmental Earth Sciences,* 73**,** 501-516.

Kutuzov, S., Shahgedanova, M., Mikhalenko, V., Ginot, P., Lavrentiev, I. & Kemp, S. 2013. High-resolution provenance of desert dust deposited on Mt. Elbrus, Caucasus in 2009-2012 using snow pit and firn core records. *The Cryosphere,* 7**,** 1481-1498.

Lawrence, C.R. & Neff, J.C. 2009. The contemporary physical and chemical flux of aeolian dust: A synthesis of direct measurements of dust deposition. *Chemical Geology,* 267**,** 46-63.

Lee, J.A., Baddock, M.C., Mbuh, M.J. & Gill, T.E. 2012a. Geomorphic and land cover characteristics of aeolian dust sources in West Texas and eastern New Mexico, USA. *Aeolian Research,* 3**,** 459-466.

Lee, S.-S. & Sohn, B.J. 2012b. Nighttime AOT Retrieval for Asian Dusts from MODIS IR Measurements: An Artificial Neural Network Approach. *Journal of the Meteorological Society of Japan. Ser. II,* 90**,** 163-177.

Lee, T.F. 1989. Dust tracking using composite visible/IR images: A case study. *Weather and forecasting,* 4**,** 258-263.

Létolle, R., Micklin, P., Aladin, N. & Plotnikov, I. 2007. Uzboy and the Aral regressions: A hydrological approach. *Quaternary International,* 173**,** 125-136.

Levelt, P.F., Van Den Oord, G.H., Dobber, M.R., Malkki, A., Visser, H., De Vries, J., Stammes, P., Lundell, J.O. & Saari, H. 2006. The ozone monitoring instrument. *Geoscience and Remote Sensing, IEEE Transactions on,* 44**,** 1093-1101.

Levy, R., Mattoo, S., Munchak, L., Remer, L., Sayer, A., Patadia, F. & Hsu, N. 2013. The Collection 6 MODIS aerosol products over land and ocean. *Atmospheric Measurement Techniques,* 6**,** 2989.

Levy, R.C., Remer, L.A. & Dubovik, O. 2007. Global aerosol optical properties and application to Moderate Resolution Imaging Spectroradiometer aerosol retrieval over land. *Journal of Geophysical Research: Atmospheres (1984–2012),* 112.

Levy, R.C., Remer, L.A., Kleidman, R.G., Mattoo, S., Ichoku, C., Kahn, R. & Eck, T. 2010. Global evaluation of the Collection 5 MODIS dark-target aerosol products over land. *Atmospheric Chemistry and Physics,* 10**,** 10399-10420.

Lewis, R. 2003. *Geographic Perspectives on Soviet Central Asia*, Taylor & Francis.

Li, L. & Sokolik, I.N. 2017. Developing a Dust Emission Procedure for Central Asia. *Air, Soil and Water Research,* 10**,** 1178622117711939.

Lioubimtseva, E., Cole, R., Adams, J.M. & Kapustin, G. 2005. Impacts of climate and land-cover changes in arid lands of Central Asia. *Journal of Arid Environments,* 62**,** 285-308.

Lioubimtseva, E. & Henebry, G.M. 2009. Climate and environmental change in arid Central Asia: Impacts, vulnerability, and adaptations. *Journal of Arid Environments,* 73**,** 963-977.

Lioubimtseva, E., Kariyeva, J. & Henebry, G.M. 2014. Climate Change in Turkmenistan. *In:* ZONN, I. S. & KOSTIANOY, A. G. (eds.) *The Turkmen Lake Altyn Asyr and Water Resources in Turkmenistan.* Berlin, Heidelberg: Springer Berlin Heidelberg, 39-57.

Liu, D., Wang, Z., Liu, Z., Winker, D. & Trepte, C. 2008. A height resolved global view of dust aerosols from the first year CALIPSO lidar measurements. *Journal of Geophysical Research: Atmospheres (1984–2012),* 113.

Liu, S.-c., Liu, Q., Gao, M. & Chen, L. Year. Detection of Dust Storms by Using Daytime and Nighttime Multi-spectral MODIS Images. *In:* Geoscience and Remote

Sensing Symposium, 2006. IGARSS 2006. IEEE International Conference on, July 31 2006-Aug. 4 2006 2006. 294-296.

Mares, M.A. 1999. *Encyclopedia of deserts*, University of Oklahoma Press, Norman.

Markofsky, S., Ninfo, A., Balbo, A., Conesa, F.C. & Madella, M. 2017. An investigation of local scale human/landscape dynamics in the endorheic alluvial fan of the Murghab River, Turkmenistan. *Quaternary International,* 437**,** 1-19.

Mcpeters, R.D., Bhartia, P., Krueger, A.J., Herman, J.R., Wellemeyer, C.G., Seftor, C.J., Jaross, G., Torres, O., Moy, L. & Labow, G. 1998. Earth probe total ozone mapping spectrometer (TOMS): data products user's guide.

Micklin, P. 2007. The Aral Sea Disaster. *Annual Review of Earth and Planetary Sciences,* 35**,** 47-72.

Micklin, P.P. 1991. The water management crisis in Soviet Central Asia. *The Carl Beck Papers in Russian and East European Studies***,** 131.

Middleton, N. 1986. A geography of dust storms in South-west Asia. *International Journal of Climatology,* 6**,** 183-196.

Middleton, N., Goudie, A. & Wells, G. 1986. The frequency and source areas of dust storms. *Aeolian geomorphology,* 23.

Miller, R.L., Tegen, I. & Perlwitz, J. 2004. Surface radiative forcing by soil dust aerosols and the hydrologic cycle. *Journal of Geophysical Research: Atmospheres,* 109**,** D04203.

Miller, S. 2003. A consolidated technique for enhancing desert dust storms with MODIS. *Geophysical Research Letters,* 30.

Mona, L., Liu, Z., Müller, D., Omar, A., Papayannis, A., Pappalardo, G., Sugimoto, N. & Vaughan, M. 2012. Lidar measurements for desert dust characterization: an overview. *Advances in Meteorology,* 2012**,** 36.

Oerlemans, J., Giesen, R. & Van Den Broeke, M. 2009. Retreating alpine glaciers: increased melt rates due to accumulation of dust (Vadret da Morteratsch, Switzerland). *Journal of Glaciology,* 55**,** 729-736.

Orlovsky, L., Dourikov, M. & Babaev, A. 2004. Temporal dynamics and productivity of biogenic soil crusts in the central Karakum desert, Turkmenistan. *Journal of Arid Environments,* 56**,** 579-601.

Orlovsky, L., Matsrafi, O., Orlovsky, N. & Kouznetsov, M. 2012. Sarykamysh Lake: Collector of Drainage Water–The Past, the Present, and the Future. *The Turkmen Lake Altyn Asyr and Water Resources in Turkmenistan.* Springer, 107-140.

Orlovsky, L., Orlovsky, N. & Durdyev, A. 2005. Dust storms in Turkmenistan. *Journal of Arid Environments,* 60**,** 83-97.

Orlovsky, N. & Orlovsky, L. 2002. White sandstorms in Central Asia. *Global alarm: dust and sandstorms from the world's drylands. UN Asia Regional Coordinating Unit, Bangkok***,** 169-201.

Painter, T.H., Barrett, A.P., Landry, C.C., Neff, J.C., Cassidy, M.P., Lawrence, C.R., Mcbride, K.E. & Farmer, G.L. 2007. Impact of disturbed desert soils on duration of mountain snow cover. *Geophysical Research Letters,* 34**,** L12502.

Painter, T.H., Bryant, A.C. & Skiles, S.M. 2012. Radiative forcing by light absorbing impurities in snow from MODIS surface reflectance data. *Geophysical Research Letters,* 39**,** L17502.

Painter, T.H., Deems, J.S., Belnap, J., Hamlet, A.F., Landry, C.C. & Udall, B. 2010. Response of Colorado River runoff to dust radiative forcing in snow. *Proceedings of the National Academy of Sciences,* 107**,** 17125-17130.

Pappalardo, G., Wandinger, U., Mona, L., Hiebsch, A., Mattis, I., Amodeo, A., Ansmann, A., Seifert, P., Linne, H. & Apituley, A. 2010. EARLINET correlative measurements for CALIPSO: First intercomparison results. *Journal of Geophysical Research: Atmospheres (1984–2012),* 115.

Parajuli, S.P. & Zender, C.S. 2017. Connecting geomorphology to dust emission through high-resolution mapping of global land cover and sediment supply. *Aeolian Research,* 27**,** 47-65.

Park, S.S., Kim, J., Lee, J., Lee, S., Kim, J.S., Chang, L.S. & Ou, S. 2014. Combined dust detection algorithm by using MODIS infrared channels over East Asia. *Remote Sensing of Environment,* 141**,** 24-39.

Parkinson, C.L., Greenstone, R. & Closs, J. 2000. EOS Data Products Handbook. Volume 2.

Peterson, J. & Junge, C. 1971. Sources of particulate matter in the atmosphere. *Man's Impact on the Climate***,** 310-320.

Peyridieu, S., Chédin, A., Tanré, D., Capelle, V., Pierangelo, C., Lamquin, N. & Armante, R. 2010. Saharan dust infrared optical depth and altitude retrieved from AIRS: a focus over North Atlantic–comparison to MODIS and CALIPSO. *Atmospheric Chemistry and Physics,* 10**,** 1953-1967.

Prospero, J.M., Ginoux, P., Torres, O., Nicholson, S.E. & Gill, T.E. 2002. Environmental characterization of global sources of atmospheric soil dust identified with the Nimbus 7 Total Ozone Mapping Spectrometer (TOMS) absorbing aerosol product. *Reviews of Geophysics,* 40**,** 2-1-2-31.

Qian, Y.-B., Wu, Z.-N., Yang, Q., Zhang, L.-Y. & Wang, X.-Y. 2007. Ground-surface conditions of sand-dust event occurrences in the southern Junggar Basin of Xinjiang, China. *Journal of Arid Environments,* 70**,** 49-62.

Qu, J.J., Xianjun, H., Kafatos, M. & Wang, C. 2006. Asian Dust Storm Monitoring Combining Terra and Aqua MODIS SRB Measurements. *Geoscience and Remote Sensing Letters, IEEE,* 3**,** 484-486.

Raupach, M.R. & Lu, H. 2004. Representation of land-surface processes in aeolian transport models. *Environmental Modelling & Software,* 19**,** 93-112.

Rice, M., Willetts, B. & Mcewan, I. 1996. Wind erosion of crusted soil sediments. *Earth Surface Processes and Landforms,* 21**,** 279-293.

Rittner, M., Vermeesch, P., Carter, A., Bird, A., Stevens, T., Garzanti, E., Andò, S., Vezzoli, G., Dutt, R., Xu, Z. & Lu, H. 2016. The provenance of Taklamakan desert sand. *Earth and Planetary Science Letters,* 437**,** 127-137.

Rosenfeld, D., Andreae, M.O., Asmi, A., Chin, M., De Leeuw, G., Donovan, D.P., Kahn, R., Kinne, S., Kivekäs, N., Kulmala, M., Lau, W., Schmidt, S., Suni, T., Wagner, T., Wild, M. & Quaas, J. 2014. Global observations of aerosol-cloud-precipitation-climate interactions. *Reviews of Geophysics***,** 2013RG000441.

Sano, I., Mukai, S., Yamano, M., Takamura, T., Nakajima, T. & Holben, B. 2003. Calibration and validation of retrieved aerosol properties based on AERONET and SKYNET. *Advances in Space Research,* 32**,** 2159-2164.

Sayer, A.M., Hsu, N.C., Bettenhausen, C. & Jeong, M.J. 2013. Validation and uncertainty estimates for MODIS Collection 6 "Deep Blue" aerosol data. *Journal of Geophysical Research: Atmospheres,* 118**,** 7864-7872.

Schepanski, K., Tegen, I., Laurent, B., Heinold, B. & Macke, a. 2007. A new Saharan dust source activation frequency map derived from MSG-SEVIRI IR-channels. *Geophysical Research Letters,* 34**,** L18803.

Schepanski, K., Tegen, I. & Macke, A. 2012. Comparison of satellite based observations of Saharan dust source areas. *Remote Sensing of Environment,* 123**,** 90-97.

Schepanski, K., Tegen, I., Todd, M.C., Heinold, B., Bönisch, G., Laurent, B. & Macke, a. 2009. Meteorological processes forcing Saharan dust emission inferred from MSG-SEVIRI observations of subdaily dust source activation and numerical models. *Journal of Geophysical Research,* 114**,** D10201.

Schuster, G.L., Vaughan, M., Macdonnell, D., Su, W., Winker, D., Dubovik, O., Lapyonok, T. & Trepte, C. 2012. Comparison of CALIPSO aerosol optical depth retrievals to AERONET measurements, and a climatology for the lidar ratio of dust. *Atmospheric Chemistry and Physics Discussions,* 12**,** 11641-11697.

Schwikowski, B.M., Döscher, A., Gäggeler, H.W. & Schotterer, U. 1999. Anthropogenic versus natural sources of atmospheric sulphate from an Alpine ice core. *Tellus B,* 51**,** 938-951.

Semenov, V.K., Smirnov, A., Aref'ev, V.N., Sinyakov, V.P., Sorokina, L.I. & Ignatova, N.I. 2005. Aerosol optical depth over the mountainous region in central Asia (Issyk-Kul Lake, Kyrgyzstan). *Geophysical Research Letters,* 32**,** L05807.

Shahgedanova, M., Kutuzov, S., White, K.H. & Nosenko, G. 2013. Using the significant dust deposition event on the glaciers of Mt. Elbrus, Caucasus Mountains, Russia on 5 May 2009 to develop a method for dating and" provenancing" of desert dust events recorded in snow pack. *Atmospheric Chemistry and Physics,* 13**,** 1797-1808.

Shao, Y. 2004. Simplification of a dust emission scheme and comparison with data. *Journal of Geophysical Research: Atmospheres,* 109.

Shao, Y. & Dong, C.H. 2006. A review on East Asian dust storm climate, modelling and monitoring. *Global and Planetary Change,* 52**,** 1-22.

Shao, Y., Wyrwoll, K.-H., Chappell, A., Huang, J., Lin, Z., Mctainsh, G.H., Mikami, M., Tanaka, T.Y., Wang, X. & Yoon, S. 2011. Dust cycle: An emerging core theme in Earth system science. *Aeolian Research,* 2**,** 181-204.

Shen, H., Abuduwaili, J., Samat, A. & Ma, L. 2016. A review on the research of modern aeolian dust in Central Asia. *Arabian Journal of Geosciences,* 9**,** 625.

Singer, A., Zobeck, T., Poberezsky, L. & Argaman, E. 2003. The PM10and PM2·5 dust generation potential of soils/sediments in the Southern Aral Sea Basin, Uzbekistan. *Journal of Arid Environments,* 54**,** 705-728.

Small, E.E., Giorgi, F. & Sloan, L.C. 1999. Regional climate model simulation of precipitation in central Asia: Mean and interannual variability. *Journal of Geophysical Research: Atmospheres,* 104**,** 6563-6582.

Smirnov, V.V., Johnson, T.C., Krapivtseva, G.M., Krivchikova, T.V. & Shukurov, A.H. 1993. Synoptic meteorological conditions during the U.S.S.R./U.S. dust experiment in Tadzhikistan in September 1989. *Atmospheric Environment. Part A. General Topics,* 27**,** 2471-2479.

Sodemann, H., Palmer, A., Schwierz, C., Schwikowski, M. & Wernli, H. 2006. The transport history of two Saharan dust events archived in an Alpine ice core. *Atmospheric Chemistry and Physics,* 6**,** 667-688.

Sokolik, I.N. & Toon, O.B. 1996. Direct radiative forcing by anthropogenic airborne mineral aerosols. *Nature,* 381**,** 681-683.

Starodubtsev, V. & Bogdanetz, V. 2007. Formation of the soil cover on the dried bottom of the Aral Sea. *Prob. Desert Dev,* 3**,** 34-40.

Stefanski, R. & Sivakumar, M. Year. Impacts of sand and dust storms on agriculture and potential agricultural applications of a SDSWS. *In:* IOP Conference Series: Earth and Environmental Science, 2009. IOP Publishing, 012016.

Steffensen, J.P., Andersen, K.K., Bigler, M., Clausen, H.B., Dahl-Jensen, D., Fischer, H., Goto-Azuma, K., Hansson, M., Johnsen, S.J. & Jouzel, J. 2008. High-resolution Greenland ice core data show abrupt climate change happens in few years. *science,* 321**,** 680-684.

Sternberg, T. 2017. *Climate Hazard Crises in Asian Societies and Environments*, Taylor & Francis.

Stocker, T.F., Qin, D., Plattner, G.-K., Tignor, M., Allen, S.K., Boschung, J., Nauels, A., Xia, Y., Bex, B. & Midgley, B. 2013. IPCC, 2013: climate change 2013: the physical science basis. Contribution of working group I to the fifth assessment report of the intergovernmental panel on climate change. Cambridge University Press.

Strong, C.L., Bullard, J.E., Dubois, C., Mctainsh, G.H. & Baddock, M.C. 2010. Impact of wildfire on interdune ecology and sediments: An example from the Simpson Desert, Australia. *Journal of arid environments,* 74**,** 1577-1581.

Sun, J., Zhang, M. & Liu, T. 2001. Spatial and temporal characteristics of dust storms in China and its surrounding regions, 1960–1999: Relations to source area and climate. *Journal of Geophysical Research: Atmospheres,* 106**,** 10325-10333.

Takeuchi, N. & Li, Z. 2008. Characteristics of surface dust on Ürümqi glacier No. 1 in the Tien Shan mountains, China. *Arctic, Antarctic, and Alpine Research,* 40**,** 744-750.

Tanré, D., Bréon, F.M., Deuzé, J.L., Dubovik, O., Ducos, F., François, P., Goloub, P., Herman, M., Lifermann, A. & Waquet, F. 2011. Remote sensing of aerosols by using polarized, directional and spectral measurements within the A-Train: the PARASOL mission. *Atmos. Meas. Tech.,* 4**,** 1383-1395.

Tanré, D., Kaufman, Y., Herman, M. & Mattoo, S. 1997. Remote sensing of aerosol properties over oceans using the MODIS/EOS spectral radiances. *Journal of Geophysical Research: Atmospheres,* 102**,** 16971-16988.

Tanré, D. & Legrand, M. 1991a. On the satellite retrieval of Saharan dust optical thickness over land: Two different approaches. *Journal of Geophysical Research: Atmospheres (1984–2012),* 96**,** 5221-5227.

Tanré, D. & Legrand, M. 1991b. On the satellite retrieval of Saharan dust optical thickness over land: Two different approaches. *Journal of Geophysical Research: Atmospheres,* 96**,** 5221-5227.

Tesche, M., Ansmann, A., Müller, D., Althausen, D., Mattis, I., Heese, B., Freudenthaler, V., Wiegner, M., Esselborn, M. & Pisani, G. 2009. Vertical profiling of Saharan dust with Raman lidars and airborne HSRL in southern Morocco during SAMUM. *Tellus B,* 61**,** 144-164.

Toderich, C.N., Goldshtein, R., Aparin, W., Idzikowska, K. & Rashidova, G.S. 2001. Environmental state and an analysis of phytogenetic resources of halophytic plants for rehabilitation and livestock feeding in arid and sandy deserts of Uzbekistan. *Sustainable Land Use in Deserts.* Springer, 154-165.

Toller, G.N., Isaacman, A., Leader, M.T. & Salomonson, V. 2003. MODIS Level 1B Product User's Guide. *Signature*.

Torres, O., Bhartia, P., Herman, J., Ahmad, Z. & Gleason, J. 1998. Derivation of aerosol properties from satellite measurements of backscattered ultraviolet radiation: Theoretical basis. *Journal of Geophysical Research: Atmospheres (1984–2012),* 103**,** 17099-17110.

Torres, O., Tanskanen, A., Veihelmann, B., Ahn, C., Braak, R., Bhartia, P.K., Veefkind, P. & Levelt, P. 2007. Aerosols and surface UV products from Ozone Monitoring Instrument observations: An overview. *Journal of Geophysical Research: Atmospheres (1984–2012),* 112.

Uno, I., Eguchi, K., Yumimoto, K., Takemura, T., Shimizu, A., Uematsu, M., Liu, Z., Wang, Z., Hara, Y. & Sugimoto, N. 2009. Asian dust transported one full circuit around the globe. *Nature Geoscience,* 2**,** 557-560.

Uno, I., Harada, K., Satake, S., Hara, Y. & Wang, Z. 2005. Meteorological characteristics and dust distribution of the Tarim Basin simulated by the nesting RAMS/CFORS dust model. *気象集誌,* 83.

Velichko, A. & Spasskaya, I. 2002. Climatic change and the development of landscapes. *The physical geography in northern Eurasia. Oxford University Press, Oxford***,** 36-69.

Von Holdt, J.R., Eckardt, F.D. & Wiggs, G.F.S. 2017. Landsat identifies aeolian dust emission dynamics at the landform scale. *Remote Sensing of Environment,* 198**,** 229-243.

Wake, C.P., Mayewski, P.A., Ping, W., Qinzhao, Y., Jiankang, H. & Zichu, X. 1992. Anthropogenic sulfate and Asian dust signals in snow from Tien Shan, northwest China. *Annals of Glaciology,* 16**,** 45.

Wald, A., Kaufman, Y., Tanré, D. & Gao, B.C. 1998. Daytime and nighttime detection of mineral dust over desert using infrared spectral contrast. *Journal of Geophysical Research: Atmospheres,* 103**,** 32307-32313.

Walker, A.L., Liu, M., Miller, S.D., Richardson, K.a. & Westphal, D.L. 2009. Development of a dust source database for mesoscale forecasting in southwest Asia. *Journal of Geophysical Research,* 114**,** D18207.

Walker, A.S. 1982. Deserts of China: Deserts now make up more than 13 percent of the land area in China, and various methods are being used to transform them into farmland. *American Scientist,* 70**,** 366-376.

Waltham, T. & Sholji, I. 2001. The demise of the Aral Sea – an environmental disaster. *Geology Today,* 17**,** 218-228.

Wang, H., Zhang, L., Cao, X., Zhang, Z. & Liang, J. 2013. A-Train satellite measurements of dust aerosol distributions over northern China. *Journal of Quantitative Spectroscopy and Radiative Transfer,* 122**,** 170-179.

Wang, X., Dong, Z., Zhang, J. & Liu, L. 2004. Modern dust storms in China: an overview. *Journal of Arid Environments,* 58**,** 559-574.

Wang, X., Zhou, Z. & Dong, Z. 2006. Control of dust emissions by geomorphic conditions, wind environments and land use in northern China: An examination based on dust storm frequency from 1960 to 2003. *Geomorphology,* 81**,** 292-308.

Warner, T.T. 2004. *Desert meteorology*, Cambridge University Press, Cambridge; New York.

Washington, R., Todd, M., Middleton, N.J. & Goudie, A.S. 2003. Dust-Storm Source Areas Determined by the Total Ozone Monitoring Spectrometer and Surface Observations. *Annals of the Association of American Geographers,* 93**,** 297-313.

White, K. 2009. Remote Sensing Of Aeolian Dust Production And Distribution. *Desertification and Risk Analysis Using High and Medium Resolution Satellite Data.* Springer Netherlands, 59-69.

Wiggs, G.F.S., O'hara, S.L., Wegerdt, J., Van Der Meer, J., Small, I. & Hubbard, R. 2003. The dynamics and characteristics of aeolian dust in dryland Central Asia: possible impacts on human exposure and respiratory health in the Aral Sea basin. *Geographical Journal,* 169**,** 142-157.

Winker, D.M., Hunt, W.H. & Mcgill, M.J. 2007. Initial performance assessment of CALIOP. *Geophysical Research Letters,* 34.

Wu, G., Zhang, X., Zhang, C., Gao, S., Li, Z., Wang, F. & Wang, W. 2010. Concentration and composition of dust particles in surface snow at Urumqi Glacier No. 1, Eastern Tien Shan. *Global and Planetary Change,* 74**,** 34-42.

Xi, X. & Sokolik, I.N. 2015a. Dust interannual variability and trend in Central Asia from 2000 to 2014 and their climatic linkages. *Journal of Geophysical Research: Atmospheres,* 120**,** 12,175-12,197.

Xi, X. & Sokolik, I.N. 2015b. Seasonal dynamics of threshold friction velocity and dust emission in Central Asia. *Journal of Geophysical Research: Atmospheres,* 120**,** 1536-1564.

Xu, J., Hou, S., Qin, D., Kang, S., Ren, J. & Ming, J. 2007. Dust storm activity over the Tibetan Plateau recorded by a shallow ice core from the north slope of Mt. Qomolangma (Everest), Tibet-Himal region. *Geophysical Research Letters,* 34**,** L17504.

Xuan, J., Liu, G. & Du, K. 2000. Dust emission inventory in Northern China. *Atmospheric Environment,* 34**,** 4565-4570.

Xuan, J. & Sokolik, I.N. 2002. Characterization of sources and emission rates of mineral dust in Northern China. *Atmospheric Environment,* 36**,** 4863-4876.

Yan, N., Wu, G., Zhang, X., Zhang, C., Xu, T. & Lazhu 2015. Variation of aerosol optical properties from AERONET observation at Mt. Muztagh Ata, Eastern Pamirs. *Atmospheric Research,* 153**,** 480-488.

Yasunori, K. & Masao, M. 2002. Seasonal and regional characteristics of dust event in the Taklimakan Desert. *J. Arid land studies,* 11**,** 245-252.

Ye, Z., Chen, Y. & Zhang, X. 2014. Dynamics of runoff, river sediments and climate change in the upper reaches of the Tarim River, China. *Quaternary International,* 336**,** 13-19.

Yedilbayev, B. & Shokanova, A. 2012. Problems of rational use of water resources and conditions of water pollution on an example of Lake Balkhash. *Civil and Environmental Research,* 2**,** 11-14.

Zonn, I.S. & Esenov, P.E. 2012. The Karakum Desert. *The Turkmen Lake Altyn Asyr and Water Resources in Turkmenistan.* Springer, 23-37.